الجمهورية الجزائرية الديمقراطية الشعبية
République Algérienne Démocratique et Populaire
وزارة التعليم العالي و البحث العلمي
Ministère de l'enseignement supérieur et de la recherche scientifique

Université Mohamed Khider – Biskra

Faculté des Sciences et de la Technologie

Département : **Génie-électrique**

Ref :………………

جامعة محمد خيضر بسكرة
كلية العلوم والتكنولوجيا
قسم: الهندسة الكهربائية
المرجع:………..

Thèse présentée en vue de l'obtention
Du diplôme de

Doctorat LMD en : électronique

Spécialité (Option) : microélectronique

Etude par simulation numérique d'une cellule solaire en a-Si:H/µc-Si:H multijonction (Numerical simulation study of a-Si:H/µc-Si:H multijunction solar cell)

Présentée par :

Kateb Mohamed Nadjib

Soutenue publiquement le ………………

Devant le jury composé de :

Benakcha Abdelhamid	**Professeur**	**Président**	**Université de Biskra**
Tobbeche Souad	**Professeur**	**Rapporteur**	**Université de Biskra**
Saadoune Achour	**Professeur**	**Examinateur**	**Université de Biskra**
Bekhouche Khaled	**Maitre de Conférences 'A'**	**Examinateur**	**Université de Biskra**
Lakhdar Nacereddine	**Professeur**	**Examinateur**	**Université d'El Oued**

Acknowledgement

I would like to express my special appreciation and thanks to my advisor Professor Tobbeche Souad, for the continuous support of my Ph.D study and related research, for her patience and motivation. Her guidance helped me in all the time of research and writing of this thesis.

I would also like to thank my committee members, Professor Benakcha Abdelhamid, Professor Saadoune Achour, Doctor Bekhouche Khaled and Professor Lakhdar Nacereddine.

My sincere thanks also goes to Professor Dehimi Lakhdar, who provided me an opportunity to continue my study. I would also like to thanks Professor Sengouga Noureddine for his help during the past years of my research in the laboratory LMSM.

A special thanks to my family. Words cannot express how grateful I am to my father and my mother for all of the sacrifices that they've made on my behalf. Your prayer for me was what sustained me thus far.

I would also like to thank all of my friends who supported me.

Dedication

I dedicate this work to my father, my mother, my brothers and my sisters.

ملخص

يتناول عمل هذه الأطروحة دراسة الخلايا الشمسية الرقيقة المصنوعة من السليكون القائمة على مفاهيم الوصلات الثنائية والثلاثية باستخدام برنامج Silvaco-Atlas. درسنا أولاً خلية شمسية ثنائية الوصلة متكونة من خليتين فرعيتين، العليا من مادة a-Si:H والسفلى من مادة μc-Si:H مربوطتين على التسلسل ومتصلتين بصريًا وكهربائيًا عن طريق وصلة اعادة الارتباط النفقية أي(n-μc-Si:H/p-μc-Si:H) . تمت مناقشة تصميم و أداء وصلة اعادة الارتباط النفقية بالتفصيل في ابحاثنا هذه. بعد ذلك تم دراسة تأثيرات تركيز ذرات التطعيم و سمك وصلة اعادة الارتباط النفقية على تيار الدارة القصيرة، جهد الدارة المفتوحة، عامل التعبئة ومردود خلية ثنائية الوصلة و قد تم تحسينها عن طريق زيادة تركيز الذرات المانحة لوصلة اعادة الارتباط النفقية. من ناحية أخرى، فإن تركيز الذرات المستقبلة وسمك وصلة اعادة الارتباط النفقية يقللان بشكل أساسي من تيار الدارة القصيرة وعامل التعبئة والمردود بينما تغيرجهد الدارة المفتوحة قليلاً. اظهرت هذه الدراسة عملية وصلة اعادة الارتباط النفقية، وأعلى مردود تحويل بلغ 12.73٪ لوصلة اعادة الارتباط النفقية القصوى ذات تركيزات الذرات المانحة و المستقبلة وسمك قيمهم على التوالي 10^{20} سم $^{-3}$ و $4x10^{19}$ سم $^{-3}$ و 10 نانومتر، عندما تكون ذروة نسبة اعادة الارتباط موجودة تقريبًا في منتصف الطبقة p من وصلة اعادة الارتباط النفقية حيث تكون شبه مستويات Fermi قريبة من بعضها البعض. بعد ذلك، درسنا خلية شمسية رقيقة ثلاثية الوصلات مع خلية عليا من a-Si:H ، خلية وسطى من السيليكون غير المتبلور المهدرج والجرمانيوم (a-SiGe:H) وخلية سفلية من μc-Si:H . مردود التحويل الأولي للخلية الشمسية ثلاثية الوصلات هو 15.79٪. تم تحسين الخلية الشمسية ثلاثية الوصلات بايجاد سمك الخلايا الفرعية العلوية, الوسطى والسفلية الذي يؤدي الى تطابق التيار، مما ادى إلى مردود تحويل عالي بلغ 16.95٪. قمنا بتحسين اضافي مع استعمال نطاقات فجوة واسعة في الخلايا الفرعية العلوية, الوسطى والسفلية ما ادى إلى تحسين مردود التحويل بنسبة وصلت إلى 18.25٪. يعتمد أداء الخلية الشمسية ثلاثية الوصلات بشكل كبير على كثافة عيوب الخلية الشمسية العلوية من a-Si:H ، عن طريق تقليل تركيز الروابط المتدلية في الخلية الشمسية العلوية من a-Si:H ، تم تحسين مردود تحويل الخلايا الشمسية ثلاثية الوصلات بنسبة وصلت إلى 20.3٪. الدراسة الشاملة حول الخلايا الشمسية ثلاثية الوصلات من a-Si:H/a-SiGe:H/μc-Si:H التي تم انجازها في هذا العمل تمكن من توفير و تصنيع خلايا شمسية ثلاثية الوصلات ذات مردود عالي.

Abstract

In this study, thin film silicon solar devices based on double and triple junction's concepts are investigated with the use of the Silvaco-Atlas software. First we investigated a double (tandem) junction solar cell composed of two subcels with p-i-n configurations namely, a-Si:H (top) and µc-Si:H (bottom) junctions stacked in series optically and electrically connected by a tunnel recombination junction (TRJ) (i.e., n-µc-Si:H/ p-µc-Si:H). The development and the design of the TRJ has been addressed in detail in our work. Influence of parameters such as dopant concentrations and thickness of the TRJ on the tandem solar cell are studied. The simulated results indicate that the short-circuit current, the open-circuit voltage, the fill factor and the efficiency of the tandem cell are improved by increasing the donor concentration of the TRJ. On the other hand, the acceptor concentration and the thickness of the TRJ reduce mainly the short-circuit current, the fill factor and the efficiency while the open-circuit voltage changes slightly. This study shows a strong recombination process occurred in the TRJ, the highest conversion efficiency of 12.73% is achieved for un optimal TRJ with donor, acceptor concentrations and thickness of 10^{20} cm^{-3}, $4x10^{19}$ cm^{-3} and 10 nm, respectively when the peak of the recombination rate is approximately located in the middle of the TRJ p-layer where the quasi-Fermi levels are close to each other. Then we investigated a triple junction thin film solar cell of a-Si:H top cell, hydrogenated amorphous silicon germanium (a-SiGe:H) middle cell and µc-Si:H bottom cell. The initial conversion efficiency of the triple junction solar cell is of 15.79%. The optimization of the triple junction solar cell in thicknesses of top, middle and bottom subcells for current matching, leading to a high conversion efficiency of 16.95%. Further optimization with wide band gaps of top, middle and bottom subcells also leads to improved conversion efficiency up to 18.25%. The triple junction solar cell performance depends strongly on the defect density of the a-Si:H top solar cell, by decreasing the concentration of dangling bonds in the top a-Si:H solar cell, the conversion efficiency of the triple junction solar cell is improved up to 20.3%. The overall investigation on a-Si:H/a-SiGe:H/µc-Si:H triple junction solar cells reported in this work can be used to the optimization and development of high efficiency a-Si:H/a-SiGe:H/µc-Si:H triple junction solar cells.

Résumé

Le travail de cette thèse a porté sur l'étude des cellules solaires en silicium en couche mince basées sur les concepts de double et triple jonctions à l'aide du logiciel Silvaco-Atlas. Nous avons d'abord étudié une cellule solaire à double jonction composée de deux sous-cellules, à savoir, la jonction a-Si:H (en haut) et la jonction µc-Si: H (en bas) empilées en série et connectées optiquement et électriquement par une jonction de recombinaison tunnel (TRJ) (c'est-à-dire n-µc-Si: H / p-µc-Si: H). Le développement et la conception de la TRJ ont été abordés en détail dans nos travaux de recherche. Les effets des paramètres tels que les concentrations en dopants et l'épaisseur de la TRJ sur la cellule solaire à double jonction sont ensuite étudiés. Les résultats simulés démontrent que le courant de court-circuit, la tension en circuit ouvert, le facteur de forme et le rendement de la cellule à double jonction sont améliorés en augmentant la concentration des donneurs de la TRJ. D'autre part, la concentration des accepteurs et l'épaisseur de la TRJ réduisent principalement le courant de court-circuit, le facteur de forme et le rendement alors que la tension en circuit ouvert varie légèrement. Cette étude montre un fort processus de recombinaison dans la TRJ, le rendement de conversion le plus élevé de 12.73% pour une TRJ optimale avec des concentrations de donneur, d'accepteur et d'épaisseur de 10^{20} cm^{-3}, $4x10^{19}$ cm^{-3} et 10 nm, respectivement lorsque le pic du taux de recombinaison est approximativement situé au milieu de la couche p de la TRJ où les quasi-niveaux de Fermi sont proches les uns des autres. Ensuite, nous avons étudié une cellule solaire en couche mince à triple jonction avec une cellule supérieure en a-Si:H, une cellule intermédiaire en silicium amorphe hydrogéné au germanium (a-SiGe:H) et une cellule inférieure en µc-Si:H. Le rendement de conversion initial de la cellule solaire à triple jonction est de 15.79%. L'optimisation de la cellule solaire à triple jonction des épaisseurs des sous-cellules supérieure, intermédiaire et inférieure pour l'adaptation de courant, conduisant à un rendement de conversion élevé de 16.95%. Une optimisation supplémentaire avec de larges bandes interdites des sous-cellules du haut, du milieu et du bas conduit également à un rendement de conversion amélioré jusqu'à 18.25%. La performance de la cellule solaire à triple jonction dépend fortement de la densité de défaut de la cellule solaire supérieure en a-Si:H, en diminuant la concentration des liaisons pendantes dans la cellule solaire supérieure en a-Si:H, le rendement de conversion de la cellule solaire à triple jonction est amélioré jusqu'à 20.3%. L'étude globale sur les cellules solaires à triple jonction en a-Si:H/a-SiGe:H /µc-Si:H rapportée dans ce travail peut être utilisée pour l'optimisation et le développement des cellules solaires à triple jonction en a-Si:H/a-SiGe:H/µc-Si:H de haut rendement.

Table of contents

ملخص i
Abstract ii
Résumé iii
Table of contents iv
List of figures ix
List of tables xv

General introduction

General introduction 1
Outline of the thesis 3
References 5

Chapter 1: Basic properties of thin film silicon layers

1.1 Introduction 7
1.2 Crystal structure 7
1.3 Element semiconductors 8
1.4 Conduction in metals, semiconductors, and insulators 8
a) Metals 9
b) Insulators 9
c) Semiconductors 10
1.5 Intrinsic semiconductors 10
1.6 Extrinsic semiconductors 12
1.7 Hydrogenated amorphous silicon 15
1.8 Atomic structure 15
1.9 Density of energy states 17
1.10 Defects and metastability 18
1.11 Depositing amorphous silicon 19
1.11.1 Survey of deposition techniques 19
1.11.2 RF Glow discharge deposition 20
1.12 Optical properties of a-Si:H 21
1.13 Electronic density of states 23

1.14 Amorphous silicon-germanium ... 24
1.14.1 Fabrication ... 24
1.14.2 Structure of a-SiGe:H alloys ... 26
1.14.3 Dangling bonds, density of defect states ... 26
1.14.4 Optical absorption ... 27
1.15 Hydrogenated microcrystalline silicon ... 27
1.15.1 Structure of hydrogenated microcrystalline silicon ... 27
1.15.2 Optical properties ... 29
1.15.3 Defects ... 30
1.16 Transparent conductive oxide ... 30
1.17 Electrical transport mechanisms in amorphous semiconductors ... 31
1.17.1 Conduction through extended states ... 31
1.17.2 Conduction through localized states ... 32
1.17.3 Conduction by hopping around the Fermi level ... 33
1.18 Conclusion ... 33
Chapter 1 References ... 35

Chapter 2: Solar cells fundamentals device

2.1 Introduction ... 36
2.2 Solar radiation ... 36
2.3 Transfer of energy from the photon to the electron ... 37
2.4 Generation of excess carriers by light ... 38
2.5 Recombination mechanisms of excess carriers ... 40
2.5.1 Band-to-band recombination ... 41
2.5.2 Auger recombination ... 41
2.5.3 Shockley Read Hall (SRH) recombination ... 42
2.5.4. Surface recombination ... 43
2.6 Photocurrent and spectral response of solar cells ... 44
2.7 Electrical characteristics ... 49
2.7.1 The ideal solar cell ... 49
2.7.2 Solar cell characteristics in practice ... 52
2.7.3 The quantum efficiency and spectral response ... 53
2.8 Types of solar cells ... 54

2.8.1 Silicon PERL cell 55
2.8.2 Cadmium telluride solar cell (CdTe) 57
2.8.3 Copper Indium Gallium Selenide solar cells (CIGS) 57
2.8.4 Dye-sensitized solar cells 58
2.8.5 Organic Solar Cells 60
2.8.6 Best research cell efficiencies 61
2.9 Tandem device classifications 63
2.9.1 Type A/two-terminal monolithic stack 64
2.9.2 Type B/two-terminal mechanically-stacked 65
2.9.3 Type B/three-terminal monolithic stack 65
2.9.4 Type B/four-terminal mechanically stacked 65
2.9.5 Type B/four-terminal spectrum split 65
2.10 Principle of the two-terminal tandem cell 66
2.11 Recombination tunnel junction 68
2.12 Thin-film silicon solar cell structures 69
2.12.1 Amorphous silicon solar cells 69
2.12.2 Technology of amorphous Si solar cell 71
2.12.3 Microcrystalline silicon solar cells 72
2.12.4 Multijunction solar cells 73
2.12.4.1 a-Si:H based double junction solar cells 74
2.12.4.2 a-Si:H based triple junction solar cells 75
2.13 Conclusion 80
Chapter 2 References 81

Chapter 3: Simulation of a-Si:H, µ-Si:H and a-SiGe:H Based multijunction Solar Cell: Silvaco-Atlas

3.1 Introduction 83
3.2 Basic semiconductor equations 83
3.2.1 Poisson’s equation 83
3.2.2 Carrier continuity equations 84
3.2.3 The transport equations 84
3.2.4 Drift-diffusion transport model 84
3.3 Density of states model of hydrogenated amorphous silicon 86

3.4 Amphoteric defects 87
3.5 Steady-state trap recombination 92
3.6 Trap-assisted tunneling model 93
3.7 Silvaco-Atlas simulation software 95
3.8 Order of Atlas command groups 95
3.8.1 Structure specification 96
a) Mesh 96
b) Region 97
c) Electrodes 98
d) Doping 99
3.8.2 Materials model specification 100
a) Material 100
b) Defects 101
c) Light source 101
d) Models 102
e) Contact 102
f) Interface 102
3.8.3. Numerical method selection 103
3.8.4 Solution specification 103
a) Log 103
b) Solve 104
c) Load and Save 104
3.8.5 Results analysis 104
3.9 Conclusion 106
Chapter 3 references 107

Chapter 4: Results and discussion

4.1 Introduction 108
4.2 aSi:H/µc-Si:H double junction solar cell 109
4.2.1 Device structure of aSi:H/µc-Si:H double junction solar cell 109
4.2.2 Simulation models and parameters 112
4.2.3 Single a-Si:H and µc-Si:H solar cells performances 114
4.2.4 a-Si:H/µc-Si:H double junction solar cell performance 118

4.2.5 Effect of TRJ on double junction solar cell 120
4.2.5.a Effect of donor and acceptor concentrations of the TRJ on double junction solar cell 122
4.2.5.b Effect of TRJ thickness on double junction solar cell 134
4.3 a-Si:H/a-SiGe:H/µc-Si:H triple junction solar cell 138
4.3.1 Device structure and simulation details 138
4.3.2 Single a-Si:H, a-SiGe:H and µc-Si:H solar cells performances 144
4.3.3 a-Si:H/a-SiGe:H/µc-Si:H triple junction solar cell performance 146
4.3.3.a Optimization of thicknesses of triple junction solar cell active i-layers 147
4.3.3.b Optimization of bandgaps of triple junction solar cell layers 152
4.3.3.c Dependence of triple junction solar cell performance on defect states 156
4.4 Conclusion 158
Chapter 4 referances 160

Conclusion

Conclusion 165
Perspectives 167
Publications and conferences 168

List of figures

Chapter 1: Basic properties of thin film silicon layers

Figure 1.1 (a) Diamond lattice, (b) Zinc blende lattice. 7

Figure 1.2 Schematic energy band representations of (a) a conductor with two possibilities (either the partially filled conduction band shown at the upper portion or the overlapping bands shown at the lower portion), (b) a semiconductor, (c) an insulator. 9

Figure 1.3 Intrinsic semiconductor: (a) Schematic band diagram, (b) Density of states, (c) Fermi distribution function, (d) Carrier concentration. 11

Figure 1.4 Schematic bond pictures for (a) n-type Si with donor (arsenic) and (b) p-type Si 13 with acceptor (boron). 13

Figure 1.5 (a) Schematic energy band representation of extrinsic n-type, (b) p-type semiconductors. 14

Figure 1.6 Schematic representation of the atomic structure of (a) single crystal silicon, (b) hydrogenated amorphous silicon. 16

Figure 1.7 The schematic representation of the distribution of density of allowed energy states for electrons for (a) single crystal silicon (b) *a*-Si:H. 18

Figure 1.8 Plot of the defect (dangling bond) density during extended illumination of an *a*-Si:H film as measured by Park, Liu, and Wagner. Data are given for high- and low-intensity illumination; the legend indicates the photocarrier generation rate of each intensity. 19

Figure 1.9 Schematic of a typical RF glow discharge deposition chamber. 21

Figure 1.10 (a) Absorption coefficient as function of photon energy for a-Si:H, *p*-type a-SiC:H and a-SiGe:H [3]. The absorption coefficient of c-Siis shown for reference. (b) Tauc plot with linear extrapolation to determine the Tauc optical band gap for a-Si:H, *p*-type a-SiC:H and a-SiGe:H [3]. 22

Figure 1.11 Density of electronic states *g(E)* in hydrogenated amorphous silicon. The shaded areas indicate delocalized states in the bands; these bands themselves have tails of localized states with an exponential distribution. Midway between the bands are levels belonging to gross defects such as dangling Si bonds indicated by the two peaked bands around E_F. 24

Figure 1.12 Solid-state composition parameter *y* as a function of gas phase composition *x* for a-Si_{1-y} Ge_y:H alloys ($T_S \approx 270$ °C, plasma-deposited, with He-dilution (□), plasma-deposited with H-dilution (o), deposited with the hot wire method ($T_S \approx 360$ °C) (x). 25

Figure 1.13 (a) Atomically ordered Si,Ge alloy, (b) statistical/clustered Si and Ge incorporation. 26
Figure 1.14 Optical gap E_g of (plasma grown) a-SiGe:H alloys as a function of composition y. Substrate temperature was $T_S \approx 210$ °C........ 27
Figure 1.15 Range of film structures (schematic), obtained with different PECVD parameters, for films deposited on glass substrates; the dashed lines indicate the transitions between amorphous and mixed phase material, as well as between mixed phase material and highly crystalline material. 28
Figure 1.16 schematic structural representation of hydrogenated microcrystalline silicon. ... 29
Figure 1.17 Absorption coefficient α as a function of photon energy of a-Si:H and µc-Si:H. 30
Figure 1.18 Electronic transport mechanisms: conduction in extended states, conduction in localized states and hopping at the Fermi energy. 32

Chapter 2: Solar cells fundamentals devices

Figure 2.1 Solar spectral irradiance at air mass 0 and air mass 1.5 and the cutoff wavelength of GaAs and Si........ 37
Figure 2.2 Schematic band diagrams for the photoluminescence processes in (a) A direct gap material, (b) An indirect gap material. 38
Figure 2.3 Absorption coefficient as a function of wavelength of light (bottom abscissa) or energy (top abscissa) for several semiconductors [4]. 40
Figure 2.4 Descriptive diagram of the radiative type recombination process........ 41
Figure 2.5 Descriptive diagram of Auger recombination in a semiconductor. 42
Figure 2.6 Descriptive diagram of trap-assisted recombination........ 42
Figure 2.7 Schematic representation of a silicon p-n junction solar cell. 44
Figure 2.8 (a) Solar-cell dimensions under consideration. (b) Assumed abrupt doping profiles $N_D >> N_A$. (c) Generation rate as a function of distance for long and short wavelengths. (d) Energy-band diagram showing generated electron-hole pair........ 45
Figure 2.9 The external quantum efficiency of a high quality crystalline silicon based solar cell. 49
Figure 2.10 Simplest equivalent circuit, for an “ideal” solar cell; an external load resistance R_L has also been drawn........ 50

Figure 2.11 (a) The I–V characteristic of an ideal solar cell and (b) the power produced by the cell. The power generated at the maximum power point is equal to the shaded rectangle in (a). 51
Figure 2.12 The superposition principle for solar cells. 52
Figure 2.13 Universally used equivalent circuit for a solar cell. 53
Figure 2.14 Effect of (a) the series resistance R_s and of (b) the parallel resistance R_p, as given in the "universal" circuit of Fig. 2.13 on the $J(V)$ characteristics of a solar cell. Values of $(R_s)^{-1}$ and $(R_p)^{-1}$ are given by the slopes of the $J(V)$ characteristics, at the short-circuit point ($V = 0$) and at the open-circuit point ($J = 0$), respectively. 53
Figure 2.15 Classification of photovoltaic cells. 55
Figure 2.16 (a) Passivated emitter rear locally diffused (PERL) cell. (b) Energy-band diagram for the back-surface field. 56
Figure 2.17 Graphic showing the five layers that comprise CdTe solar cells. 57
Figure 2.18 Graphic showing the five layers that comprise CIGS solar cells. 58
Figure 2.19 (a) DSSC cell structure. (b) Energy band diagram and main carrier losses. 59
Figure 2.20 Heterojunction between donor and acceptor facilitates charge transfer by splitting the exciton. 60
Figure 2.21 (a) Bilayer and (b) bulk heterojunction solar cells. 61
Figure 2.22 Timeline for best research and efficiencies for different solar cells reported so far. 62
Figure 2.23 Type A of tandem solar cell device with single TCE and two-terminal monolithic. 63
Figure 2.24 Type B of tandem solar cell device with multiple TCEs and terminal connections: (a) two-terminal mechanically stacked, (b) 3-terminal monolithic stacked, (c) 4-terminal mechanically stacked and (d) 4-terminal spectrum-split. 64
Figure 2.25 Principle of the dual-junction stacked cell or tandem cell. 66
Figure 2.26 Construction of the J-V diagram for a two-terminal tandem solar cell. The short circuit current density of the tandem is slightly higher than the short-current density of the top sub-cell. Actually, it corresponds to the current density of the top sub-cell in a reverse voltage condition. 67
Figure 2.27 Principle of current continuity between top and bottom sub-cells for a two-terminal tandem solar cell, shown here for the example of two *pin*-type sub-cells. The current continuity condition requires that the total flux of electrons or holes exiting from one of the sub-cells has to recombine with the total flux of carriers (of opposite polarity) exiting from the other sub-

cell. This requirement is valid for all types of two-terminal tandem cells, i.e. for *pin*-type and *pn*-type cells, and for both the superstrate (*pin*) and the substrate (*nip*) configurations. 68
Figure 2.28 A single junction p-i-n a-Si solar cell structure. 70
Figure 2.29 Series-interconnected a-Si solar cells deposited on a glass substrate with a rear glass cover bonded using ethylene vinyl acetate (EVA). 71
Figure 2.30 (a) Structure of a μc-Si:H solar cell, (b) Current-voltage characteristics of an n-i-p type microcrystalline silicon cell 73
Figure 2.31 Schematic structure of a microcrystalline/ amorphous tandem cell. 75
Figure 2.32 (a) Schematic structure of the a-Si:H/a-SiGe:H/a-SiGe:H triple-junction solar cell, (b) J-V characteristics of the a-Si:H/a-SiGe:H/a-SiGe:H triple-junction solar cell with an initial efficiency of 14.6% [19] 76
Figure 2.33 Schematics of p-i-n multijunction solar cells with μc-Si:H in the bottom cell. ... 77
Figure 2.34 (a) J-V characteristics and (b) EQE spectra of an a-Si:H/a-SiGe:H/μc-Si:H triple junction solar cell with an initial efficiency of 16.3%. 77
Figure 2.35 The established performance of the a-Si:H/μc-Si:H/μc-Si:H triple-junction solar cell after 1000 h light soaking. This new record was confirmed by NREL. 78
Figure 2.36 The highest efficiency of a-Si:H/a-SiGe:H/μc-Si:H triple-junction solar cells achieved in different research institutions. 79
Figure 2.37 Stabilized I-V curve and parameters of the record module (1.43 m^2)) made by TEL Solar and certified by ESTI. 79

Chapter 3: Simulation of a-Si:H, μ-Si:H and a-SiGe:H Based multijunction Solar Cell: Silvaco-Atlas

Figure 3.1 Atlas inputs and outputs. 95
Figure 3.2 Non-uniform mesh creation using Atlas for a-Si:H solar cell. 97
Figure 3.3 Regions of a-Si:H solar cell. 98
Figure 3.4 Electrodes of a-Si:H solar cell. 99
Figure 3.5 Doping of a-Si:H solar cell. 100
Figure 3.6 I-V characteristic plotted by the instruction TonyPlot. 105
Figure 3.7 P-V characteristic plotted by the instruction TonyPlot. 106

Chapter 4: Results and discussion

Figure 4.1 Structure used in the simulation of a p-i-n (a-Si:H)/p-i-n (µc-Si:H) tandem solar cell mechanically stacked with n-p (µc-Si:H) tunnel recombination junction cell. 110

Figure 4.2 Two-dimensional simulated structure of the a-Si:H/µc-Si:H tandem solar cell with Atlas-Silvaco. 110

Figure 4.3 Mesh of the tandem solar cell with the zoom of the mesh in the TRJ part.......... 111

Figure 4.4 Schematic structure of single a-Si:H top-cell. 115

Figure 4.5 Schematic structure of single a-Si:H top-cell. 116

Figure 4.6 Schematic structure of single µc-Si:H bottom-cell. 116

Figure 4.7 Schematic structure of single µc-Si:H bottom-cell. 117

Figure 4.8 *J–V* characteristics for the single a-Si:H and µc-Si:H solar cells. 118

Figure 4.9 *J–V* characteristics for the a-Si:H top-cell, µc-Si:H bottom-cell and a-Si:H/µc-Si:H tandem solar cell. 119

Figure 4.10 Band diagram explaining tunneling of electrons and holes to midgap states and their subsequent recombination. 121

Figure 4.11 Simulated photovoltaic parameters of the a-Si:H/µc-Si:H tandem solar cell as function of the donor concentration N_D of the TRJ. 124

Figure 4.12 Recombination rate around the TRJ for various donor concentrations N_D of the TRJ under short-circuit condition. 125

Figure 4.13 (a) Band diagram around the TRJ under short-circuit condition for a donor concentration N_D of (a) 10^{19} cm^{-3}, (b) 4×10^{19} cm^{-3} and (c) 8×10^{19} cm^{-3}. 127

Figure 4.14 Simulated photovoltaic parameters of the a-Si:H/µc-Si:H tandem solar cell as function of the acceptor concentration N_A of the TRJ. 130

Figure 4.15 Recombination rate around the TRJ for various acceptor concentrations N_A of the TRJ under short-circuit condition. 131

Figure 4.16 Band diagram around the TRJ under short-circuit condition for an acceptor concentration N_A of (a) 10^{19} cm^{-3}, (b) 4×10^{19} cm^{-3} and (c) 10^{20} cm^{-3}. 133

Figure 4.17 Simulated photovoltaic parameters of the a-Si:H/µc-Si:H tandem solar cell as function of thickness of the TRJ. 136

Figure 4.18 Recombination rate around the TRJ under short-circuit condition for tunnel recombination junction thickness of (a) 10 nm and (b) 30 nm. 138

Figure 4.19 Structure used in the simulation of a p-i-n a-Si:H/a-SiGe:H/µc-Si:H triple junction solar cell with n-p µc-Si:H tunnel recombination junctions. 139

Figure 4.20 Two-dimensional simulated structure of the p-i-n a-Si:H/a-SiGe:H/μc-Si:H triple junction solar cell with Atlas-Silvaco. 140
Figure 4.21 Mesh of the triple solar cell with the zoom of the mesh in the TRJ part. 140
Figure 4.22 Energy band diagram of a-Si:H/a-SiGe:H/μc-Si:H triple junction solar cell simulated under thermodynamic equilibrium conditions. 144
Figure 4.23 Recombination rate of a-Si:H/a-SiGe:H/μc-Si:H triple junction solar cell around the TRJs simulated under short-circuit condition. 144
Figure 4.24 Schematic structure of single a-SiGe:H solar cell. 145
Figure 4.25 *J–V* characteristics simulated for the single a-Si:H, a-SiGe:H, and μc-Si:H solar cells. 145
Figure 4.26 *J–V* characteristics for the a-Si:H top cell, a-SiGe:H middle cell, μc-Si:H bottom cell and initial triple junction solar cell. 147
Figure 4.27 Top cell short-circuit current density as a function of top cell i-layer thickness. 149
Figure 4.28 Bottom cell short-circuit current density as a function of middle cell i-layer thickness. 149
Figure 4.29 Short-circuit current densities of top, middle and bottom cells as a function of top i-layer thickness for (a) middle cell thickness=0.11 μm, (b) middle cell thickness=0.14 μm and (c) middle cell thickness=0.17 μm. 151
Figure 4.30 *J–V* characteristics for the a-Si:H top cell, a-SiGe:H middle cell, μc-Si:H bottom cell and the triple junction solar cell at current matching. 152
Figure 4.31 The variation in the efficiency with the band gap energies of the a-Si:H top and a-SiGe:H middle cells. 153
Figure 4.32 *J-V* characteristic of the improved triple junction solar cell as compared to the initial triple junction solar cell. 154
Figure 4.33 EQE curves of the a-Si:H/a-SiGe:H/μc-Si:H triple junction solar cell. 155
Figure 4.34 Absorptance *A* and reflectance *R* of the triple junction solar cell layers as a function of the wavelength of incident light. The colored areas illustrate the light absorption over the layers. The white area represents the reflected light. 156
Figure 4.35 Conversion efficiency as a function of defect density in only a-SiGe:H middle cell, in only a-Si:H top cell, and in triple junction solar cell. 157

List of tables

Chapter 1: Basic properties of thin film silicon layers

Table 1.1 Portion periodic table related to semiconductors. 8

Table 1.2 Various deposition processes used for depositing amorphous silicon–based materials. 20

Chapter 3: Simulation of a-Si:H, µ-Si:H and a-SiGe:H Based multijunction Solar Cell: Silvaco-Atlas

Table 3.1. Defect states parameters of tail states. 90

Table 3.2. Defect states parameters of Defect pool model and Gaussian model 91

Table 3.3 Atlas command groups with the primary statements in each group. 96

Chapter 4: Results and discussion

Table 4.1 Electrical parameters for tandem solar cell used in this work 113

Table 4.2 Defect states parameters of tail states. 113

Table 4.3 Defect states parameters of Gaussian and DPM distributions 114

Table 4.4 Simulation and experiment photovoltaic parameters of a-Si:H and µc-Si:H solar cells. 118

Table 4.5 Simulation photovoltaic parameters of the top, bottom and tandem solar cells together with experimental results of the tandem solar cell. 120

Table 4.6 Electrical parameters for a-SiGe:H solar cell 141

Table 4.7 Defect states parameters of tail states. 142

Table 4.8 Defect states parameters of Gaussian distributions 142

Table 4.9 Simulation photovoltaic parameters of single a-Si:H, a-SiGe:H and µc-Si:H solar cells. 146

Table 4.10 Simulation photovoltaic parameters of the top, middle, bottom and initial triple junction solar cells. 147

Table 4.11 Simulation photovoltaic parameters of the top, middle, bottom and triple junction solar cells at current matching point 152

Table 4.12 Simulation photovoltaic parameters of the initial and improved triple junction solar cells. 154

General introduction

Due to the development of industry, transport and communication media, growth in global electricity consumption has been observed in recent decades. However, most of the electrical energy is produced by burning non-renewable resources (carbon, oil, gas, nuclear) with an estimated burnout time of a few decades. In addition, this type of energy production is very polluting. The development of renewable and non-polluting sources of energy is therefore topical.

Renewable energy sources include wind, marine and oceanic fluxes, solar (solar cells), etc. The latter is a very powerful source of energy. Indeed, the power of solar radiation at ground level is about 950 W / m^2 [1]. The total amount of solar energy received at ground level for a week exceeds the energy produced by global reserves of oil, carbon, gas and uranium. However, in most cases, a conversion (transformation) of energy from solar radiation into electricity is necessary.

Photovoltaic electricity is obtained by the direct transformation of sunlight into electricity, by means of photovoltaic cells. The most commercialized material in the photovoltaic industry is crystalline silicon (Si) (abundant, easy to manufacture, non-toxic). However, in the cost of the module, the price of the material accounts for about 50% and many studies aim to reduce the costs related to the preparation of substrates [2]. The junctions made with this material make it possible to transform the photons into an electric current.

Thin film solar cells have been of great interest in recent years. Many types of semiconductor materials, such as copper indium gallium diselenide (CIGS) [3-5] and antimony selenosulfide (Sb_2Se_3) [6-9] have been applied as the absorption layers of thin film solar cells and achieved excellent device performance. Research has shown that nanostructures can also be used in kesterite Cu_2ZnSnS_4 (CZTS) solar cells to increase solar cells performances [10] Hydrogenated amorphous silicon (a-Si:H) and its alloys are considered the cheapest sources in thin film solar cell design and potential sources of renewable energy for large-scale terrestrial applications due to abundant material, low costs and the low temperatures at which they are fabricated [11-13]. Main challenges are the limited efficiency and light induced degradation due to the Steabler-Wronski effect [14]. For single junction thin film a-Si:H solar cells, stabilized laboratory efficiencies of 10.22% have been presented [15]. The multijunction approach has been experimentally proven as the main strategy for improving solar cells efficiency. The multijunction solar cell is composed of a number of series connected subcells with decreased bandgaps from the top to the bottom, thereby minimizing losses due to thermalization of hot carriers and transmission of low energy photons. Thus, the solar energy is converted into electricity more efficiently than in single junction solar cells. The tandem cell

configuration using hydrogenated amorphous silicon for the top cell and hydrogenated microcrystalline silicon (µc-Si:H) for the bottom cell is the most commonly fabricated with an efficiency of 12.69% [15]. The highest efficiency of thin film Si solar cells reported in literature is 16.3% for n-i-p type triple junction configuration [16]. It consists of a-Si:H/a-Si:Ge:H/µc-Si:H triple junction structure, the top cell absorber consists of a-Si:H, the middle cell absorber of a-SiGe:H, and the absorber of the bottom cell of µc-Si:H. The highest conversion efficiency of 16.1% is achieved in p-i-n type a-Si:H/a-Si:Ge:H/µc-Si:H [17] and 13.6% in a-Si:H/µc-Si:H/µc-Si:H triple junction configurations [18]. In recent years, a novel a-Si:H/a-Si:H/µc-Si:H/µc-Si:H quadruple junction solar cell has been realized and some promising results have been observed with a conversion efficiency of 13.2% [19]. Furthermore, a conversion efficiency of 15.03% with an a-SiC:H/a-Si:H/a-SiGe:H/µc-Si:H quadruple junction cell structure has been reported [20]. The multijunction solar cell consists of several subcell layers (or junctions), the subcells are electrically connected in series by tunnel recombination junctions (TRJs) providing a higher voltage than single junction solar cells. The current matching between the subcells is the most important task in the design process, this means that the current generated has to be equal in each component cell. Since the subcells are connected in series, the lowest current density determines the overall current density of the multijunction solar cell. If current values are not matched, the excess current in the subcells other than the subcell with lowest current density gets lost as heat. The impact is twofold: firstly, some energy is lost; secondly, the heat generated deteriorates the cell performance further. Double and triple junction solar cells are used for better use of the solar spectrum due to better absorption of different sunlight wavelengths in different layers with different band gaps and, thus, to obtain higher conversion efficiencies of the solar cells.

The structures of the multi-junction solar cells are complex and the numerical simulation is needed to improve the detailed understanding of the device physics and hence optimize the design of the device for improving the multijunction solar cell efficiency.

The aim of this thesis was to investigate multijunction thin film silicon solar cells as well as to understand the influence of the different structural parameters on the cell performance in order to improve their efficiencies and contribute to the development of thin film silicon solar cells technology. In this study, thin film silicon solar devices based on double and triple junction's concepts are investigated with the use of the Silvaco-Atlas software [21]. Triple junction thin film silicon based solar cells have been extensively studied. The goal is to explore the potential of such device structures to achieve high performance.

First, we simulated separately two p-i-n types a-Si:H and µc-Si:H solar cells and then a p-i-n type a-Si:H/µc-Si:H double junction solar cell with optimized parameters. The results of the simulation were validated by comparing simulation results with experimental and confirmed record results reported in the literature [22][15]. The operation characteristics of the µc-Si:H tunnel recombination junction (i.e., n-µc-Si:H/ p-µc-Si:H) as a connection region between the a-Si:H top cell and the µc-Si:H bottom cell has been evaluated. The dependencies of the short-circuit current density (J_{sc}), the open-circuit voltage (V_{oc}), the fill factor (FF), and the conversion efficiency (η) of the double junction solar cell on the TRJ parameters such as dopant concentrations and thickness have also been explored. Next, a thin film silicon solar device based on a triple junction concept with a p-i-n type a-Si:H/a-Si:Ge:H/µc-Si:H configuration is investigated. We present the simulation of single junction a-Si:H, a-SiGe:H and µc-Si:H devices, followed by their incorporation in the a-Si:H/a-SiGe:H/µc-Si:H triple junction solar cell. We present the optimization of the thicknesses of the intrinsic layers of top, middle and bottom cells for matching current. The optimization as the use of wide band gaps of top, middle and bottom subcells is also presented. Finally, we study the effects of defects of a-Si:H and a-SiGe:H subcells on the performance of the triple junction solar cell. Based on our simulation results, the optimized triple junction solar cell has a potential to deliver a high conversion efficiency of 20%.

Outline of the thesis

Chapter 1 concerns the study of the materials classification, conductors, insulators, semiconductors, the physical and optical properties of amorphous semiconductors, in particular a-Si:H. In amorphous semiconductors, such as a-Si:H, there is a continuous defect states in the band gap that act as traps or recombinant centers for free carriers. Similarly, the physical and optical properties of a-SiGe:H and µc-Si:H are studied in this chapter.

Chapter 2 is devoted to cover the physics of solar cell, its operating principle, its photovoltaic parameters as well as the associated technology used. The different types of the solar cell technologies and the different classifications of the tandem solar cells are presented. Theoretical studies of multijunction solar cells based on hydrogenated amorphous silicon are also presented.

Chapter 3 presents the basic semiconductor equations (Poisson's equation, Carrier continuity equations and the transport equations), physical model used for the simulation of density of states of a-Si: H, and steady-state trap recombination and trap-assisted tunneling models for the TRJ. In this work, the simulation software Silvaco-Atlas used for the simulation

of the solar cells and numerical simulations for thin film silicon solar cells of hydrogenated amorphous silicon are also described.

Chapter 4 describes the structures of the solar cells to study, the physical models and the parameters of the materials used in the numerical simulation and presents the results of the simulation of the a-Si:H/µc-Si:H double junction solar cell and the a-Si:H/a-SiGe:H/µc-Si:H triple junction solar cell and their interpretations.

The thesis concludes with a summary of the main findings of the research work and the possible future of work suggested to this study.

References

[1] E. Observ, “Baromètre du solaire photovoltaïque,” *Systèmes Sol*, vol. 160, pp. 69–83, 2004.

[2] N. Oleksiy, “Simulation, fabrication et analyse de cellules photovoltaïques à contacts arrières interdigités,” *Inst. Natl. des Sci. appliquée Lyon*, 2005.

[3] M. Hedayati, S. Olyaee, Proposal of CIGS dual-junction solar cell and investigation of different metal grids effect, Opt. Quantum Electron. 52 (2020) 1–12.

[4] S. Azizifar, M. Imanieh, S. Hassanhosseini, F. Bahadori-Jahromi, Modeling of CIGS single–junction solar cell using multiple quantum well structure with enhanced efficiency, Opt. Quantum Electron. 52 (2020) 1–10.

[5] F. Rasouli, M.R. Madani, Analysis of CIGS-based thin film tandem solar cell with ZnS buffer layers, Opt. Quantum Electron. 52 (2020) 1–10.

[6] J. Zhou, H. Chen, X. Zhang, K. Chi, Y. Cai, Y. Cao, J. Pang, Substrate dependence on (Sb4Se6) n ribbon orientations of antimony selenide thin films: morphology, carrier transport and photovoltaic performance, J. Alloys Compd. 862 (2021) 158703.

[7] Y. Cao, C. Liu, J. Jiang, X. Zhu, J. Zhou, J. Ni, J. Zhang, J. Pang, M.H. Rummeli, W. Zhou, Theoretical Insight into High-Efficiency Triple-Junction Tandem Solar Cells via the Band Engineering of Antimony Chalcogenides, Sol. RRL. 5 (2021) 2000800.

[8] Y. Cao, X. Zhu, J. Jiang, C. Liu, J. Zhou, J. Ni, J. Zhang, J. Pang, Rotational design of charge carrier transport layers for optimal antimony trisulfide solar cells and its integration in tandem devices, Sol. Energy Mater. Sol. Cells. 206 (2020) 110279.

[9] Y. Cao, X. Zhu, H. Chen, X. Zhang, J. Zhouc, Z. Hu, J. Pang, Towards high efficiency inverted Sb2Se3 thin film solar cells, Sol. Energy Mater. Sol. Cells. 200 (2019) 109945.

[10] M.A. Cherif, A. Melliti, Optimization of Si (core)/CZTS/CZTSe (shell) nanowire array for solar cell, Opt. Quantum Electron. 53 (2021) 1–14.

[11] J. Poortmans, V. Arkhipov, Thin film solar cells: fabrication, characterization and applications, John Wiley & Sons, 2006.

[12] B. Yan, J. Yang, S. Guha, Amorphous and nanocrystalline silicon thin film photovoltaic technology on flexible substrates, J. Vac. Sci. Technol. A Vacuum, Surfaces, Film. 30 (2012) 04D108.

[13] M. J. M. de Wild-Scholten, “Energy payback time and carbon footprint of commercial photovoltaic systems,” *Sol. Energy Mater. Sol. Cells*, vol. 119, pp. 296–305, 2013.

[14] D. L. Staebler and C. R. Wronski, “Reversible conductivity changes in discharge-

produced amorphous Si," *Appl. Phys. Lett.*, vol. 31, no. 4, pp. 292–294, 1977.

[15] M. A. Green, K. Emery, Y. Hishikawa, W. Warta, and E. D. Dunlop, "Solar cell efficiency tables (version 48)," *Prog. Photovoltaics Res. Appl.*, vol. 24, no. 7, pp. 905–913, Jul. 2016.

[16] B. Yan, G. Yue, L. Sivec, J. Yang, S. Guha, and C.-S. Jiang, "Innovative dual function nc-SiOx: H layer leading to a> 16% efficient multi-junction thin-film silicon solar cell," *Appl. Phys. Lett.*, vol. 99, no. 11, p. 113512, 2011.

[17] S. Kim, J.-W. Chung, H. Lee, J. Park, Y. Heo, and H.-M. Lee, "Remarkable progress in thin-film silicon solar cells using high-efficiency triple-junction technology," *Sol. Energy Mater. Sol. Cells*, vol. 119, pp. 26–35, 2013.

[18] H. Sai *et al.*, "Triple-junction thin-film silicon solar cell fabricated on periodically textured substrate with a stabilized efficiency of 13.6%," *Appl. Phys. Lett.*, vol. 106, no. 21, p. 213902, 2015.

[19] F. Urbain, V. Smirnov, J.-P. Becker, A. Lambertz, U. Rau, and F. Finger, "Light-induced degradation of adapted quadruple junction thin film silicon solar cells for photoelectrochemical water splitting," *Sol. Energy Mater. Sol. Cells*, vol. 145, pp. 142–147, 2016.

[20] B. Liu *et al.*, "High efficiency and high open-circuit voltage quadruple-junction silicon thin film solar cells for future electronic applications," *Energy Environ. Sci.*, vol. 10, no. 5, pp. 1134–1141, 2017.

[21] A. U. Manual, "Device Simulation Software, Version 5.20. 2," *R, SILVACO Int. St. Clara, CA*, 2015.

[22] T. Matsui *et al.*, "High-efficiency amorphous silicon solar cells: impact of deposition rate on metastability," *Appl. Phys. Lett.*, vol. 106, no. 5, p. 53901, 2015.

Chapter 1:
Basic properties of thin film silicon layers

1.1 Introduction

Amorphous solids are composed of atoms in disordered configuration: There is no order in the arrangement of atoms in contrast to crystalline solids formed by atoms constituting an ordered and periodic lattice. Nevertheless, the amorphous network contains short-range arrangements when considering the atom and its nearest neighbors.

This chapter concerns the study of the materials classification, conductors, insulators and semiconductors. Then the physical properties such as atomic structure, defects density of energy states in hydrogenated amorphous silicon (a-Si:H) and its depositing and optical properties are studied. These properties essentially depend on localized states in the band gap that act as traps or recombinant centers for free carriers. Similarly, we will study hydrogenated amorphous silicon germanium (a-SiGe:H) and hydrogenated microcrystalline silicon (µc-Si:H) and the transparent conductive oxide (TCO). These materials constitute the baseline a-Si:H/µc-Si:H double junction solar cells and a-Si:H/ a-SiGe:H /µc-Si:H triple junction solar cells materials.

1.2 Crystal structure

Most commonly used semiconductors are single crystals with diamond (with Si and Ge) or zinc blende (with GaAs and other compound semiconductors) lattice type as shown in Fig. 1.1.

Both lattices may be viewed as being composed of two interpenetrating face-centered cubic (fcc) sublattices that are displaced by one quarter of the distance along the diagonal of the cube. All atoms in the diamond lattice are identical, while the two fcc sublattices are built of different atoms in the case of III–V compounds such as GaAs. Each atom is surrounded by four close neighbors belonging to the other fcc sublattice [1].

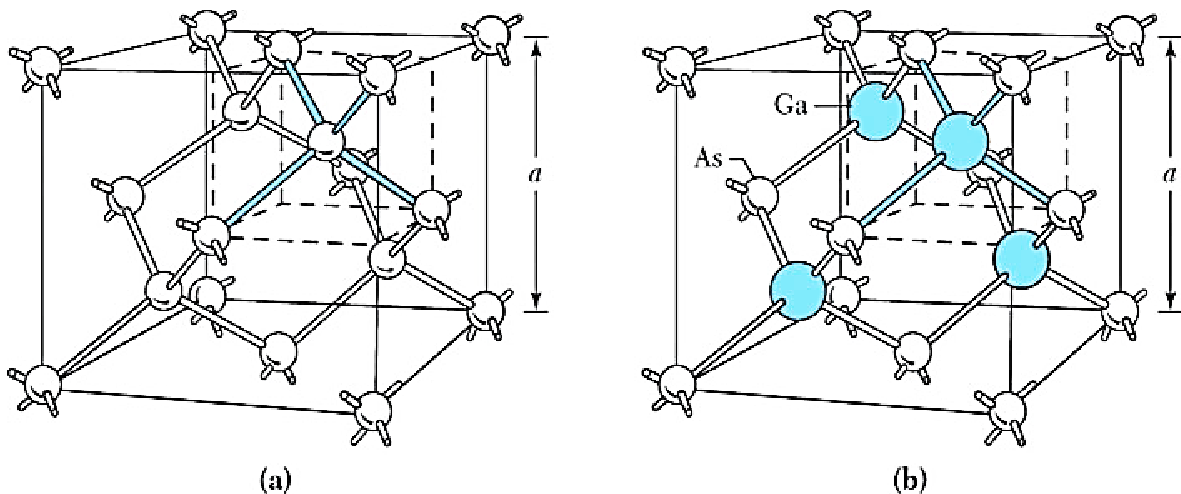

Figure 1.1 (a) Diamond lattice, (b) Zinc blende lattice.

1.3 Element semiconductors

The study of semiconductor materials began in the early nineteenth century. Over the years many semiconductors have been investigated. Table 1.1 shows a portion of the periodic table related to semiconductors. The element semiconductors, those composed of single species of atoms, such as silicon (Si) and germanium (Ge), can be found in Column IV. In the early 1950s, germanium was the major semiconductor material. Since the early 1960s silicon has become a practical substitute and has now virtually supplanted germanium as a semiconductor material. The main reasons we now use silicon are that silicon devices exhibit better properties at room temperature, and high-quality silicon dioxide can be grown thermally. There are also economic considerations. Device-grade silicon costs much less than any other semiconductor material. Silicon in the form of silica and silicates comprises 25% of the Earth's crust, and silicon is second only to oxygen in abundance. Currently, silicon is one of the most studied elements in the periodic table, and silicon technology is by far the most advanced among all semiconductor technologies.

Period	Column II	III	IV	V	VI
2		B Boron	C Carbon	N Nitrogen	O Oxygen
3	Mg Magnesium	Al Aluminum	Si Silicon	P Phosphorus	S Sulfur
4	Zn Zinc	Ga Gallium	Ge Germanium	As Arsenic	Se Selenium
5	Cd Cadmium	In Indium	Sn Tin	Sb Antimony	Te Tellurium
6	Hg Mercury		Pb Lead		

Table 1.1 Portion periodic table related to semiconductors.

1.4 Conduction in metals, semiconductors, and insulators

The enormous variation in electrical conductivity of metals, semiconductors, and insulators may be explained qualitatively in terms of their energy bands. Figure 1.2 shows the energy band diagrams of three classes of solids: metals, semiconductors, and insulators [2].

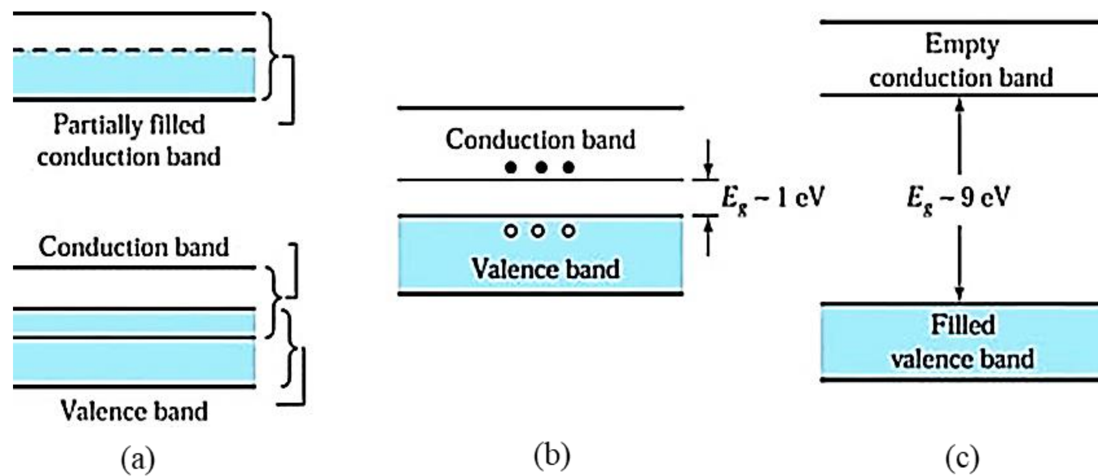

Figure 1.2 Schematic energy band representations of (a) a conductor with two possibilities (either the partially filled conduction band shown at the upper portion or the overlapping bands shown at the lower portion), (b) a semiconductor, (c) an insulator.

a) Metals

The characteristics of a metal (also called a conductor) include a very low value of resistivity and a conduction band that either is partially filled (as in Cu) or overlaps the valence band (as in Zn or Pb) so that there is no bandgap, as shown in Fig. 1.2(a). As a consequence, the uppermost electrons in the partially filled band or electrons at the top of the valence band can move to the next higher available energy level when they gain kinetic energy (e.g., from an applied electric field). Electrons are free to move with only a small applied field in a metal because there are many unoccupied states close to the occupied energy states. Therefore, current conduction can readily occur in conductors.

b) Insulators

In an insulator such as silicon dioxide (SiO_2), the valence electrons form strong bonds between neighboring atoms. Since these bonds are difficult to break, there are no free electrons to participate in current conduction at or near room temperature. As shown in the energy band diagram (Fig. 1.2(c)), insulators are characterized by a large bandgap. Note that electrons occupy all energy levels in the valence band and all energy levels in the conduction band are empty. Thermal energy or the energy of an applied electric field is insufficient to raise the uppermost electron in the valence band to the conduction band. Thus, although an insulator has many vacant states in the conduction band that can accept electrons, so few electrons actually

occupy conduction band states that the overall contribution to electrical conductivity is very small, resulting in a very high resistivity. Therefore, silicon dioxide is an insulator; it cannot conduct current.

c) Semiconductors

Now, consider a material that has a much smaller energy gap, on the order of 1 eV (Fig. 1.2(b)). Such materials are called semiconductors. At $T = 0$ K, all electrons are in the valence band, and there are no electrons in the conduction band. Thus, semiconductors are poor conductors at low temperatures. At room temperature and under normal atmospheres, values of E_g are 1.12 eV for Si and 1.42 eV for GaAs. At room temperature, appreciable numbers of electrons are thermally excited from the valence band to the conduction band. Since there are many empty states in the conduction band, a small applied potential can easily move these electrons, resulting in a moderate current [2].

1.5 Intrinsic semiconductors

Intrinsic semiconductors contain no (in practice, very few) impurities compared with the number of thermally generated electrons and holes. For this condition we shall attempt to estimate the number of free charge carriers (electrons and holes) under equilibrium conditions. The occupation probability for an electronic state is given by the Fermi-Dirac function

$$f(E) = \frac{1}{1 + \exp((E - E_F)/(k_B T))} \tag{1.1}$$

Where E_F, the Fermi energy, is the energy at which the occupation probability of a (possible) state is one half, k is the Boltzmann constant and T is the absolute temperature [1].

The density of free electrons n is obtained by integrating the carrier concentration (Fig. 1.3(d)) given by the product of the density of states N (Fig. 1.3(b)) and the occupation probability $F_n(E)$ (Fig. 1.3(c)) over the conduction band:

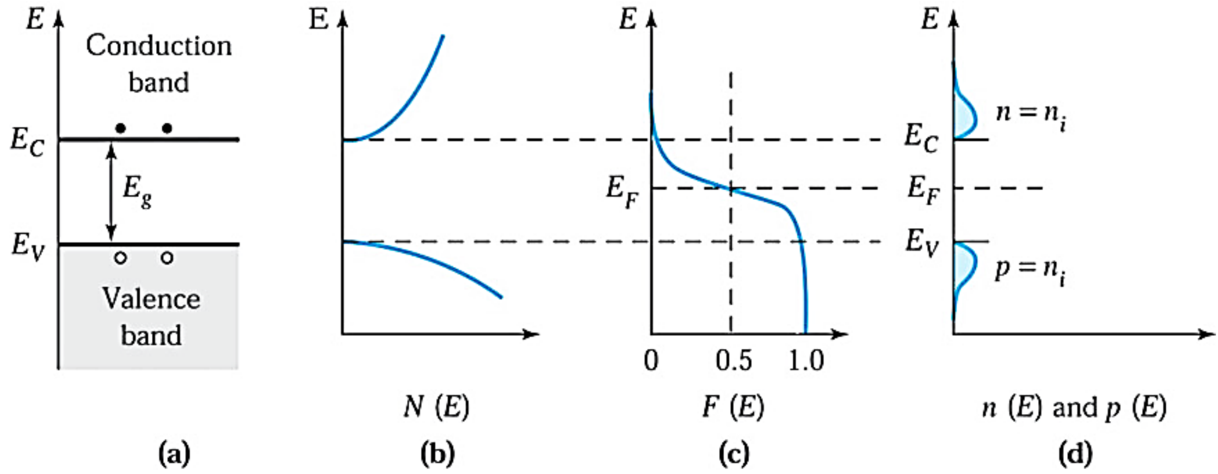

Figure 1.3 Intrinsic semiconductor: (a) Schematic band diagram, (b) Density of states, (c) Fermi distribution function, (d) Carrier concentration.

$$n = 2\left(\frac{2\pi m_n kT}{h^2}\right)^{\frac{3}{2}} e^{-\frac{E_C - E_F}{kT}} = N_C e^{-\frac{E_C - E_F}{kT}} \quad (1.2(a))$$

Similarily for holes, we have:

$$p = 2\left(\frac{2\pi m_p kT}{h^2}\right)^{\frac{3}{2}} e^{-\frac{E_F - E_V}{kT}} = N_C e^{-\frac{E_F - E_V}{kT}} \quad (1.2(b))$$

N_C and N_V are the effective densities of states in the conduction and valence bands respectively. The product of electron and hole concentration, given by $n.p = N_C N_V e^{-\frac{E_C - E_V}{kT}}$, depends on the band gap $E_G = E_C - E_V$ and is thus independent of the Fermi level E_F.

So far the value of the Fermi level E_F has not been specified and equations (1.1) to (1.2) will also be valid for extrinsic semiconductors (to be dealt with in the following chapter). The Fermi level for intrinsic semiconductors E_i can be found from the requirement that the numbers of electrons and holes are equal: $n = p = n_i$. One thus finds that:

$$n_i = \sqrt{N_C N_V}\, e^{-\frac{E_C - E_V}{2kT}} = \sqrt{N_C N_V}\, e^{-\frac{E_G}{2kT}} \quad (1.3)$$

And

$$E_i = \frac{E_C + E_V}{2} + \frac{3kT}{4} \ln\left(\frac{m_p}{m_n}\right) \quad (1.4)$$

where E_i is the Fermi level close to the middle of the band gap, the deviation being due to the unequal effective masses of electrons and holes.

Introducing the intrinsic carrier density n_i and the intrinsic level E_i, one may reformulate the more generally valid (1.2) in the useful form:

$$n = n_i e^{\frac{E_F - E_i}{kT}} \qquad p = n_i e^{\frac{E_i - E_F}{kT}} \tag{1.5}$$

1.6 Extrinsic semiconductors

Intrinsic semiconductors are rarely used in semiconductor devices since it is extremely difficult to obtain sufficient purity in the material. Moreover, in most cases one intentionally alters the property of the material by adding small fractions of specific impurities. This procedure, which can be performed either during crystal growth or later in selected regions of the crystal, is called doping. Depending on the type of added material, one obtains n-type semiconductors with an excess of electrons in the conduction band or p-type with additional holes in the valence band. We will look at extrinsic semiconductors through the simple bond representation and also through a band model.

Figure 1.4(a) shows a two-dimensional schematic bond representation of a silicon crystal with one silicon atom replaced by an arsenic atom with five valence electrons. Only four are used for the formation of covalent bonds with neighboring atoms, while the fifth is not bound to a specific atom but is free for conduction. It should be stressed that the crystal as a whole remains uncharged, since the charge of the free electron is compensated for by the excess charge of the arsenic nucleus bound in the crystal lattice.

If a silicon atom is replaced by an atom with only three valence electrons (Fig. 1.4(b)) one electron is missing in the covalent bonds and a hole is thus created. This hole may be filled by an electron from a neighboring atom, this being equivalent to a movement of the hole. The hole is free for conduction. (That the moving hole is more than a missing electron whose place is filled by a neighboring electron follows from quantum mechanical considerations and is experimentally verified in the Hall experiment) [1].

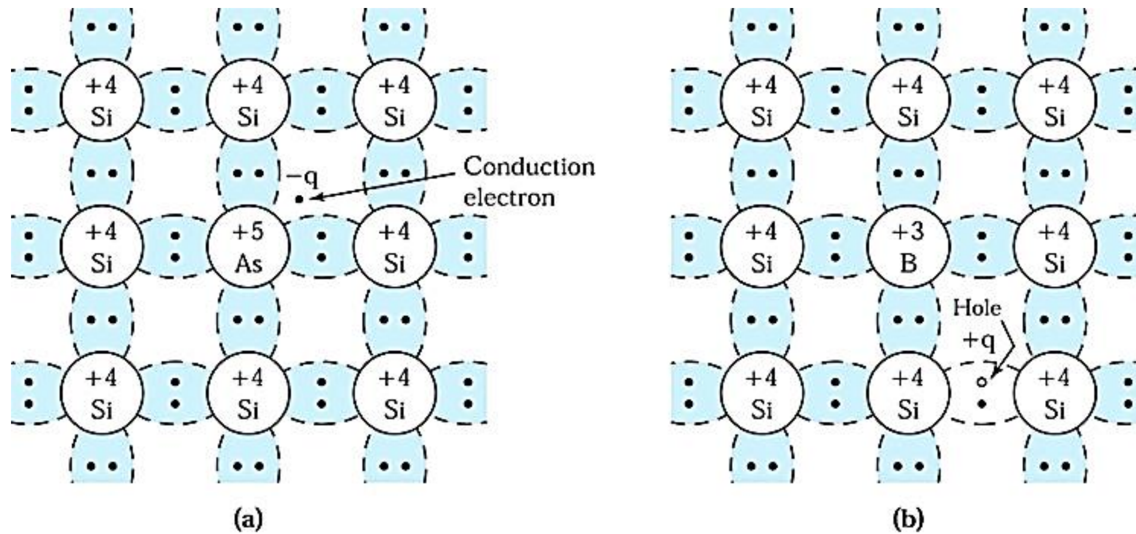

Figure 1.4 Schematic bond pictures for (a) n-type Si with donor (arsenic) and (b) p-type Si with acceptor (boron).

The replacement of a proper atom of the lattice by a different atom is accompanied by the creation of localized energy levels in the band gap. These energy levels may be of the donor (E_D) or acceptor (E_A) type. If donor levels E_D are close to the conduction band, as is the case for phosphorous ($E_C - E_D = 0.045$ eV) or arsenic ($E_C - E_D = 0.054$ eV) atoms in silicon, for instance, these states will be almost completely ionized at room temperature and the electrons will be transported to the conduction band (Fig. 1.5(a)). This is due to the many states with similar energy level nearby in the conduction band, with which the donor states have to share their electrons.

Equivalent considerations hold for acceptor-type states, e.g. boron in silicon ($E_A - E_V = 0.045$ eV). These states will be filled almost completely and holes will be created in the valence band (Fig. 1.5(b)) [1].

The situation that the donor levels are almost completely ionized can be described by a movement of the Fermi level E_F from the intrinsic level E_i towards the conduction band.

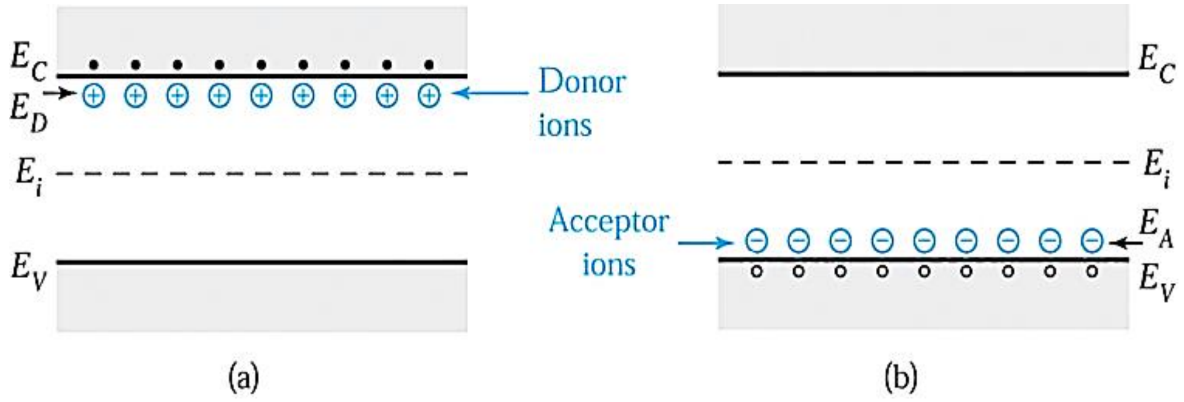

Figure 1.5 (a) Schematic energy band representation of extrinsic n-type, (b) p-type semiconductors.

By setting the electron concentration in the conduction band n equal to the donor concentration N_D, thus:

$$E_C - E_F = kT \ \ln \frac{N_C}{N_D} \tag{1.6}$$

Similarly, one obtains for p-type material and acceptor concentration N_A:

$$E_F - E_V = kT \ \ln \frac{N_V}{N_A} \tag{1.7}$$

A somewhat more complicated treatment is required for the simultaneous presence of donors and acceptors and for very high doping concentrations. It may also be mentioned in this context that the number of donor or acceptor states does not necessarily equal the number of corresponding impurity atoms, since in order to become electrically active doping atoms they have to be properly built into the crystal lattice [1].

The density of free electrons *n* is

$$n = n_i e \frac{E_F - E_i}{kT} \tag{1.8(a)}$$

The density of free holes *p* is

$$p = n_i e \frac{E_i - E_F}{kT} \tag{1.8(b)}$$

The increase of majority carriers (electrons in the case of n-type material) is accompanied by a decrease of minority carriers according to the mass-action law

$$n.p = n_i^2 \tag{1.9}$$

in agreement with (1.8)

1.7 Hydrogenated amorphous silicon

In order to understand design and operation of an a-Si:H solar cell, which is different from a crystalline silicon (c-Si) cell, the material properties of a-Si:H are summarized and compared to the single crystal silicon.

1.8 Atomic structure

Figure 1.6 illustrates the difference in the atomic structure between single crystal silicon and a-Si:H. Figure 1.6(a) shows the structure of single crystal silicon schematically. Each Si atom is covalently bonded to four neighboring Si atoms. All bonds have the same length and the angles between the bonds are equal. The number of bonds that an atom has with its immediate neighbors in the atomic structure is called the coordination number or coordination. Thus, in single crystal silicon, the coordination number for all Si atoms is four; we can also say that Si atoms are fourfold coordinated. A unit cell can be defined, from which the crystal lattice can be reproduced by duplicating the unit cell and stacking the duplicates next to each other. Such a regular atomic arrangement is described as a structure with long range order. A diamond lattice unit cell represents the real lattice structure of single crystal silicon [3].

Figure 1.6(b) illustrates that a-Si:H does not exhibit the structural order over a long range as is the case for single crystal silicon. Nevertheless, there is a similarity in atomic configuration on a local atomic scale, where most Si atoms have covalent bonds with four neighbors. The a-Si:H has the same short-range order as the single crystal silicon but it lacks the long range order. The small deviations in bonding angles and bonding lengths between the neighboring atoms in a-Si:H lead to a complete loss of the locally ordered structure on a scale exceeding a few atomic distances. The resulting atomic structure of a-Si:H is called the continuous random network. Due to the short-range order in the continuous random network of a-Si:H, the common semiconductor concept of the energy states bands, represented by the conduction and valence bands, can still be used [3].

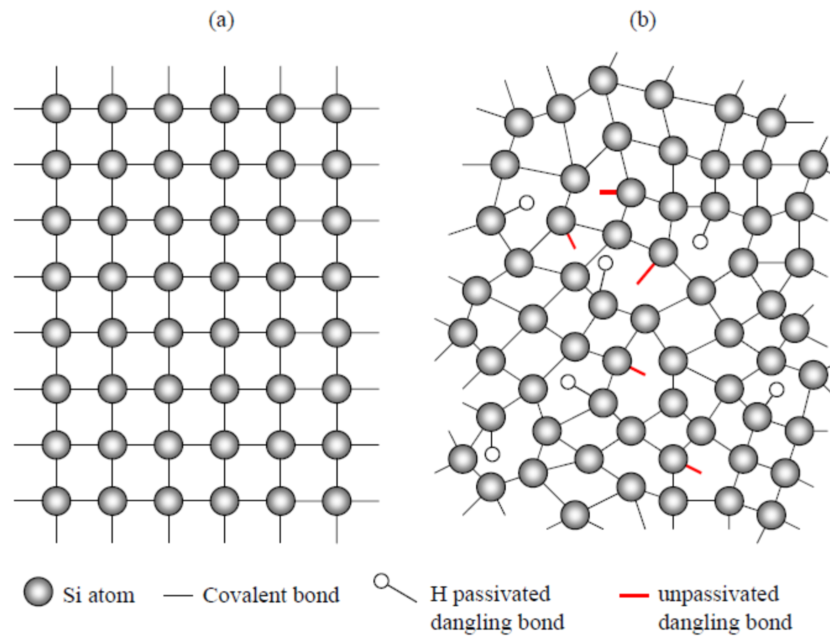

Figure 1.6 Schematic representation of the atomic structure of (a) single crystal silicon, (b) hydrogenated amorphous silicon.

The larger deviations in bonding angles and bonding lengths between the neighboring atoms in a-Si:H result in the so-called weak or strained bonds. The energy of the weak bonds is higher than the energy of optimal silicon covalent bonds in ideal single crystal silicon. Therefore, the weak bonds can easily break and form defects in the atomic network. We note that in the continuous random network, the definition of a defect is modified with respect to the crystal structure. In a crystal any atom that is out of place in a lattice forms a defect. In the continuous random network an atom cannot be out of place. Because the only specific structural feature of an atom in the continuous random network is the coordination to its neighbors, a defect in a-Si:H is the coordination defect [3].

This happens when an atom has too many or too few bonds. In a-Si:H the defects are mainly represented by Si atoms that are covalently bonded to only three Si atoms (threefold coordinated) and have one unpaired electron, a so-called dangling bond. Since this configuration is the dominant defect in a-Si:H, the defects in a-Si:H are often related to the dangling bonds.

When amorphous silicon is deposited in such a way that hydrogen can be incorporated in the network (as in the case of glow discharge deposition from silane), then the hydrogen atoms bond with most of the dangling bonds. We say that the dangling bonds are passivated by hydrogen. Hydrogen passivation reduces the dangling bond density from about 10^{21} cm^{-3} in pure a-Si (amorphous silicon that contains no hydrogen) to 10^{15}-10^{16} cm^{-3} in a-Si:H, i.e. less

than one dangling bond per million Si atoms. In Fig. 1.6(b) some of the defects with unpassivated dangling bonds and with hydrogen passivated dangling bonds are depicted. Device quality a-Si:H contains from 1 to 10 atomic percent of hydrogen. In summary, the short range order in a-Si:H network and the hydrogen passivation of the dangling bonds are responsible for semiconductor properties of amorphous silicon [3].

1.9 Density of energy states

The difference in the atomic structure between single crystal silicon and *a*-Si:H leads to the different distributions of density of allowed energy states as schematically illustrated in Figure 1.7. The periodic atomic structure of single crystal silicon results in the ranges of allowed energy states for electrons that are called *energy bands* and the excluded energy ranges, *forbidden gaps* or *band gaps*. Figure 1.7(a) shows schematically the distribution of density of states for single crystal silicon, in which the valence band and the conduction band are separated by a well-defined band gap, Eg. At room temperature single crystal silicon has a band gap of 1.12 eV. In case of an ideal crystal, there are no allowed energy states in the band gap [3].

As Figure 1.7(b) demonstrates, in case of *a*-Si:H, there is a continuous distribution of density of states and no well-defined band gap exists between the valence band and the conduction band. Due to the long range order disorder in the atomic structure of *a*-Si:H the energy states of the valence band and the conduction bands spread into the band gap and form regions that are called *band tail* states. The band tail states represent the energy states of electrons that form the strained bonds in the *a*-Si:H network. The width of the band tails is a measure for the amount of disorder in *a*-Si:H material. More disorder in *a*-Si:H means that the band tails are broader. In addition, the dangling bonds introduce allowed energy states that are located in the central region between the valence band and conduction band states [3].

The electron and hole wave functions that extend over the whole structure are characteristic for energy states, in which the charge carriers can be considered as free carriers. These states are non-localized and are called *extended states*. The wave functions of the tail and defect states are localized within the structure and therefore these states are called *localized states*. Consequently, mobility that characterizes transport of carriers through the localised states is strongly reduced. This feature of a sharp drop of mobility of carriers in the localised states in *a*-Si:H is used to define its band gap. This band gap is denoted by the term *mobility gap*, E_{mob}, because the presence of a considerable density of states in this gap conflicts the classical concept of the band gap. The energy levels that separate the extended states from the localised states in *a*-Si:H are called the valence band and the conduction band mobility edges.

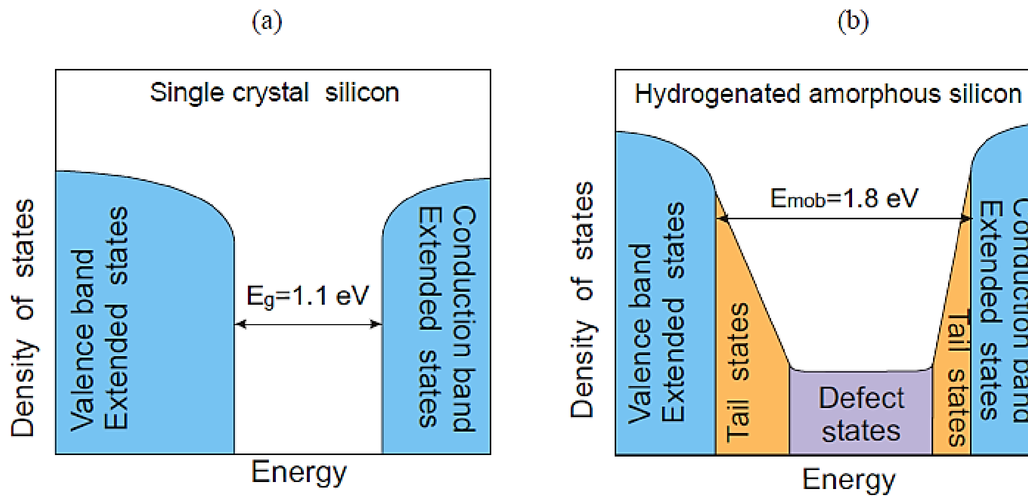

Figure 1.7 The schematic representation of the distribution of density of allowed energy states for electrons for (a) single crystal silicon (b) *a*-Si:H.

The mobility gap of *a*-Si:H is larger than the band gap of single crystal silicon and has a typical value of 1.8 eV. The localised tail and dangling bond states have a large effect on the electronic properties of *a*-Si:H. The tail states act as trapping centres and build up a space charge in a device, the dangling bond states act as very effective recombination centres and affect in particular the lifetime of the charge carries [3].

1.10 Defects and metastability

hydrogen lost from the structure; this effect has been attributed to the evolution of hydrogen from clustered-phase sites, which presumably does not create dangling bonds.

The most intense defect research in *a*-Si:H has not been focused on the direct hydrogen-defect relation, but rather on the light-soaking effects. in Figure 1.8 we illustrate how it increases the defect density. For the high intensity illumination, the defect density reaches a steady state at about $10^{17}/cm^3$. For purposes of engineering and commercial applications, it is very important that *a*-Si:H reaches such a “stabilized” condition after extended light soaking.

Although the defect density is not the only property of *a*-Si:H modified following light soaking, most workers believe that the principal cause of the Staebler–Wronski effect is this increase in dangling bond density after light soaking. The close connection between hydrogen and defects in *a*-Si:H has led to several efforts to understand the defect creation in terms of metastable configurations of hydrogen atoms. The idea is that illumination provides the energy required to shift hydrogen atoms away from their dilute phase sites, thus creating dangling

bonds. The technological importance of establishing the atomic mechanism underlying the Staebler Wronski effect lies in the possibility that this effect can be mitigated in *a*-Si:H by changing its preparation conditions.

An essential feature of the light-soaking effects on *a*-Si:H cells and films is that most of the effects are "metastable" and can be removed nearly completely by annealing of a light-soaked sample at a temperature above 150°C. More generally, the stabilized condition of *a*-Si:H cells and films is quite temperature-dependent [4].

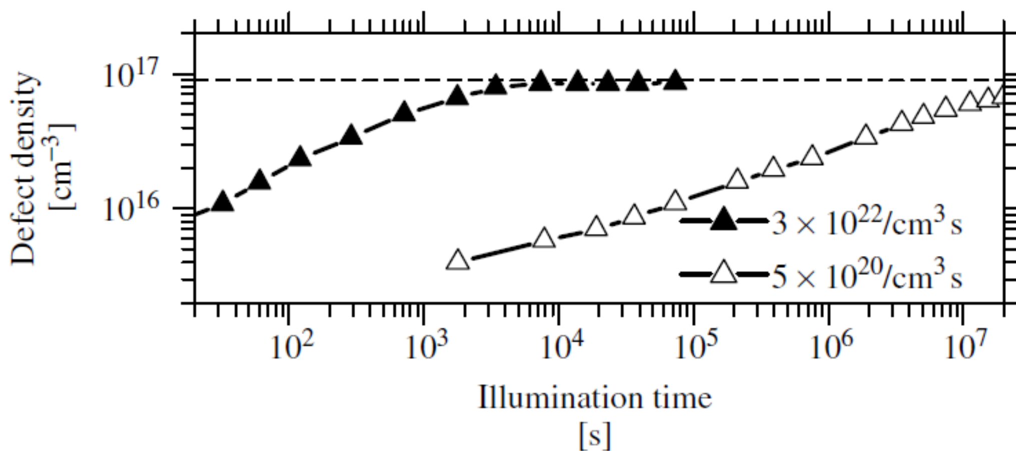

Figure 1.8 Plot of the defect (dangling bond) density during extended illumination of an *a*-Si:H film as measured by Park, Liu, and Wagner. Data are given for high- and low-intensity illumination; the legend indicates the photocarrier generation rate of each intensity.

1.11 Depositing amorphous silicon

1.11.1 Survey of deposition techniques

The first preparations of a-Si:H by Chittick *et al*. and by Spear and LeComber used a silane-based glow discharge induced by radio frequency (RF) voltages; the method is now often termed plasma enhanced chemical vapor deposition (PECVD). Since this pioneering work, many deposition methods have been explored with the intention of improving material quality and deposition rate. Among these methods, PECVD using 13.56-MHz excitation is still the most widely used today in research and manufacturing of a-Si-based materials. However, emerging film deposition methods, mostly toward higher deposition rate or toward making improved microcrystalline silicon films, have been extensively explored in recent years. Table 1.2 summarizes the most extensively studied deposition processes used as well as some of their advantages and disadvantages. Among these, PECVD with very high frequency (VHF) and hot-

wire (HW) catalytic deposition [4]. Table 1.2 summarizes the various deposition processes used for depositing amorphous silicon–based materials.

Processes	Maximum rate [A/s]	Advantages	Disadvantages	Manufacturers
RF PECVD	3	High quality	Slow	Many
DC PECVD	3	High quality	Slow	BP Solar
VHF PECVD	15	Fast	Poor uniformity	None
Microwave PECVD	50	Very fast	Film quality not as good	Canon
Hot-wire	50	Very fast	Poor uniformity	None
Photo-CVD	1	High quality	Slow	None
Sputtering	3		Poor quality	None

Table 1.2 Various deposition processes used for depositing amorphous silicon–based materials.

1.11.2 RF Glow discharge deposition

Figure 1.9 shows a schematic of a typical RF PECVD chamber and related parts. A silicon-containing gas such as a mixture of SiH_4 and H_2 flows into a vacuum chamber that is evacuated by a pump. Two electrode plates are installed inside, and an RF power is applied between them; one option is to ground one of these electrodes. At a given RF voltage across the plates, there is usually a range of gas pressures for which a plasma will occur. The plasma excites and decomposes the gas and generates radicals and ions in the chamber. Various substrates may be mounted on one or both of the electrodes, and thin hydrogenated silicon films grow on the substrates as these radicals diffuse into them. The substrates are heated to achieve optimum film quality; this effect is attributed to thermally activated surface diffusion of adatoms on the growing film [4].

A PECVD system usually consists of several major parts: (1) a gas delivery system (gas cylinders, pressure regulators, mass flow controllers, and various gas valves to direct gas flows); (2) a deposition chamber that has electrodes, substrate mounts, substrate heaters, and the RF power feed through; (3) a pumping system that usually has a turbomolecular pump backed with a mechanical pump; (4) a pressure control system that has a capacitance manometer, ionization gauges, thermocouple gauges, and/or throttle valve to monitor and control the chamber

pressure; (5) an exhaust system for the process gases (typically either with a chemical scrubber to neutralize the gases or with a "burn box" to pyrolyze them). In multichamber systems there is a transfer system to move substrates inside the vacuum system between various deposition

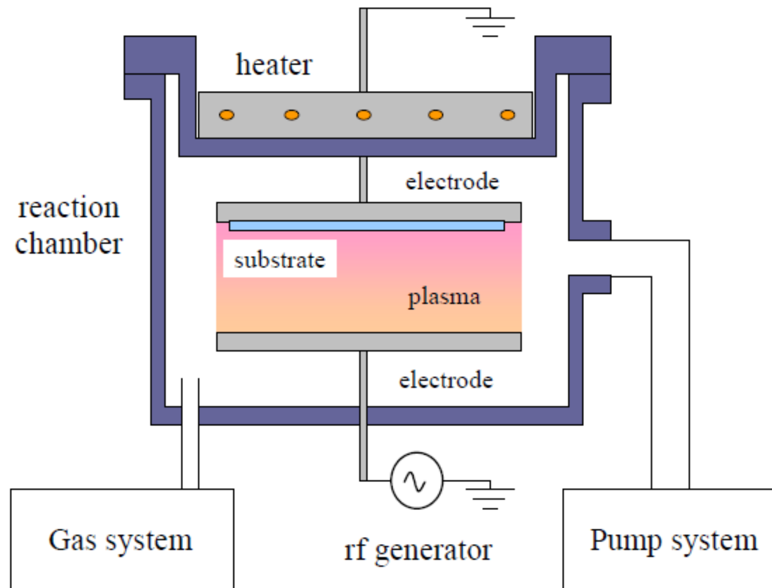

Figure 1.9 Schematic of a typical RF glow discharge deposition chamber.

chambers through appropriate gate valves. Many of these elements are connected to an instrument control panel that contains an RF power supply, impedance matching box, and readouts or controllers for the vacuum gauges, mass flow controllers, throttle valves, pneumatic valves, and turbomolecular pumps [4].

1.12 Optical properties of a-Si:H

The optical properties of a-Si:H are usually characterized by the absorption coefficient and the optical band gap. Figure 1.10(a) shows the absorption coefficient of a-Si:H as a function of photon energy. The absorption coefficient of c-Si is shown for reference. This figure demonstrates that a-Si:H absorbs almost 100 times more than c-Si in the visible part of the solar spectrum. The higher absorption is due to the disorder in the atomic structure of a-Si:H that behaves like a direct gap semiconductor. This means that 1 μm thick a-Si:H layer is sufficient to absorb 90% of usable solar light energy. In practice the thickness of a-Si:H solar cells is less than 0.5 μm that is about 100 times less than the thickness of a typical single crystal silicon cell. This results in important savings in both material and energy in fabrication of a-Si:H solar cells [3].

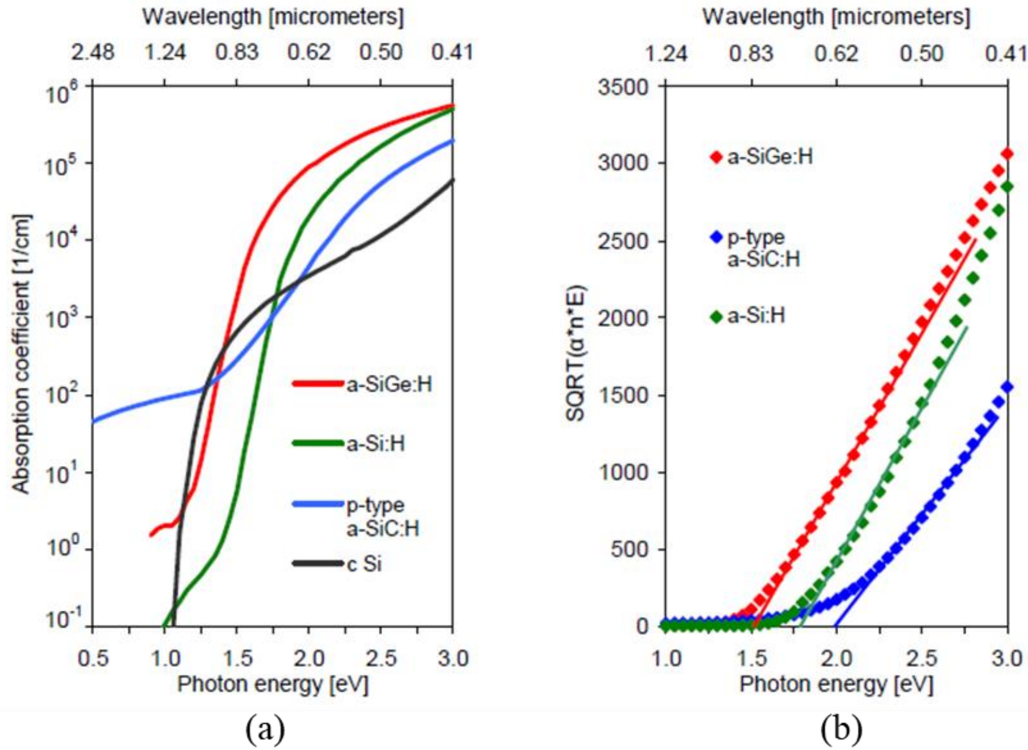

Figure 1.10 (a) Absorption coefficient as function of photon energy for a-Si:H, *p*-type a-SiC:H and a-SiGe:H [3]. The absorption coefficient of c-Siis shown for reference. (b) Tauc plot with linear extrapolation to determine the Tauc optical band gap for a-Si:H, *p*-type a-SiC:H and a-SiGe:H [3].

Another advantage of a-Si:H is that the optical absorption can be slightly changed by varying its hydrogen content, and it can be greatly changed by alloying with carbon or germanium. The absorption coefficient of hydrogenated amorphous silicon carbide (*a*-SiC:H) and hydrogenated amorphous silicon germanium (*a*-SiGe:H) are also shown in Figure 1.10(a). This feature of easy alloying of *a*-Si:H allows to design solar cell structures in which a-Si:H based materials with different absorption properties can be used as active layers [3].

From the absorption coefficient of a-Si:H based materials, the so called optical band gap is determined. The optical band gap is a useful material parameter that allows comparison of a-Si:H based materials regarding their light absorption properties. In general, a material with higher optical band gap absorbs less. The optical band gap, E_{opt}, is determined by extrapolating a linear part of the following function $[\alpha(E)n(E)E]^{1/(1+p+q)}$ vs the photon energy E to $\alpha(E) = 0$ for $\alpha \geq 103$ cm^{-1} [3].

$$(\alpha(E)n(E)E)^{1/(1+p+q)} = B(E - E_{opt}) \tag{1.10}$$

where α (E) is the absorption coefficient, $n(E)$ is the refractive index, p and q are constants that describe the shape of the density of extended states distribution for the conduction band and valence band, respectively, and B is a prefactor. When the density of states distribution near the band edges has a square-root energy dependence (p=q=1/2), as is commonly the case in crystalline semiconductors, Eq. (1.10) describes the so-called Tauc plot and the corresponding optical band gap is called the *Tauc optical gap*. When the distribution near the band edges is assumed to be linear (p=q=1) E_{opt} is called the *cubic optical gap*. The Tauc gap of device quality intrinsic *a*-Si:H is in the range of 1.70 to 1.80 eV, the cubic gap of the same material is usually 0.1 to 0.2 eV smaller than the Tauc gap. The Tauc plot with linear extrapolation to determine the Tauc optical gap for *a*-Si:H (E_{opt}=1.77 eV), *p*-type *a*-SiC:H (E_{opt}=1.95 eV), and *a*-SiGe:H (E_{opt}=1.52 eV) is shown in Figure 1.10(b) [3].

1.13 Electronic density of states

The most important concept used in understanding the optical and electronic properties of semiconductors is the electronic density of states, $g(E)$. The idea is a simple approximation: if a single electron is added to a solid, it may be viewed as occupying a well-defined state (or molecular "orbital") at a particular energy level E. In a range of energies ΔE, the number of such states per unit volume of the solid is $g(E).\Delta E$.

In Figure 1.11 we have illustrated the density-of-states for hydrogenated amorphous silicon as it has emerged primarily from measurements of electron photoemission, optical absorption, and electron and hole drift mobilities. In the dark at low temperatures, the states with energies below the Fermi energy E_F are filled by electrons; above the Fermi energy the states are empty. There are two strong bands of states illustrated: an occupied valence band ($E < E_V$), originating with the Si–Si and Si–H bonding orbitals and an unoccupied conduction band ($E > E_C$), originating with "antibonding" orbitals [4].

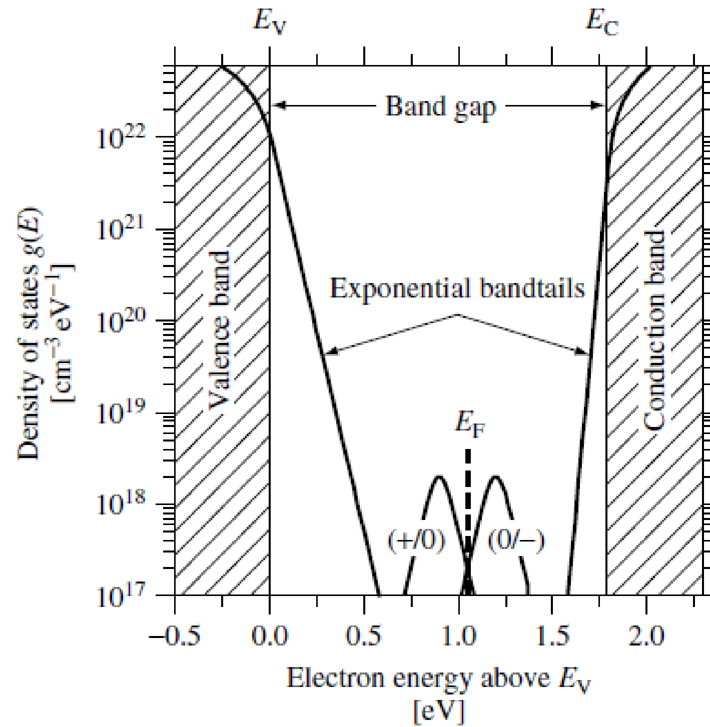

Figure 1.11 Density of electronic states *g(E)* in hydrogenated amorphous silicon. The shaded areas indicate delocalized states in the bands; these bands themselves have tails of localized states with an exponential distribution. Midway between the bands are levels belonging to gross defects such as dangling Si bonds indicated by the two peaked bands around E_F.

1.14 Amorphous silicon-germanium

1.14.1 Fabrication

Amorphous alloys of silicon with other elements of group IV of the periodic table (table 1.1), namely with germanium, have been extensively studied for use within thin-film solar cells. Some attention has also been given to alloys of amorphous silicon with carbon, oxygen, nitrogen and tin. The reason for these investigations was the possibility of substantially varying the bandgap of the resulting thin film layer:

- Towards higher values, by alloying amorphous silicon with carbon (a-SiC:H), oxygen (a-SiO:H) or nitrogen (a-SiN:H).
- Towards lower values by alloying silicon with germanium (a-SiGe:H) or tin (a-SiSn:H).

a-SiGe alloys are usually fabricated by plasma enhanced CVD. One major advantage of the plasma deposition process is the fact that it is very easy to grow a-Si alloys: As an example: just by adding, germane to silane we obtain a-SiGe alloys.

Figure 1.12 shows the alloy composition *y* as a function of gas phase composition *x* for a-SiGe:H alloys prepared by plasma deposition. Hot wire data for a-SiGe:H are also included, for comparison. As one can see, no unique relation between *y* and *x* exists [5].

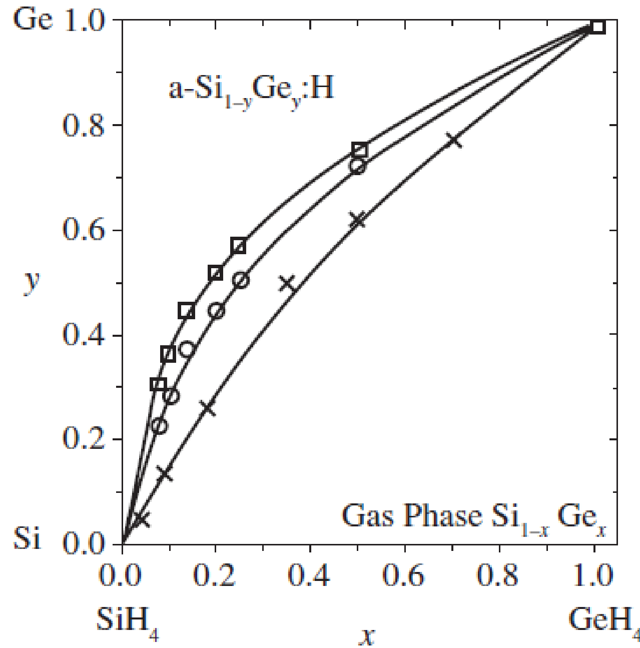

Figure 1.12 Solid-state composition parameter *y* as a function of gas phase composition *x* for a-Si_{1-y} Ge_y:H alloys ($T_S \approx 270$ °C, plasma-deposited, with He-dilution (□), plasma-deposited with H-dilution (o), deposited with the hot wire method ($T_S \approx 360$ °C) (x).

Deposition parameters such as substrate temperature, pressure, gas dilution, plasma power, etc. are expected to play a role in the film composition, as well as the respective binding energies.

The extensive applications of a-SiGe:H origin from its several unique features:

1) it has a very high optical absorption coefficient (>10^5 cm-^{1}) over the majority of visible spectrum, making extremely thin film device possible.

2) a simple low temperature deposition process is applicable.

3) the tunable bandgap of 1.0~1.7eV lies near the energy at which high solar energy conversion efficiencies are expected.

4) the raw materials is abundant.

5) the materials is easy to dope both p-type and n-type using boron or phosphorous respectively.

6) the electronic properties of electrons and holes are adequate for many device applications [6].

a-SiGe:H alloys are used today in commercial thin-film silicon solar cells and modules for the photogenerating intrinsic layers (*i*-layers), in *pin* and *nip* solar cells, in the bottom and middle sub-cells of the triple-junction cells [5].

1.14.2 Structure of a-SiGe:H alloys

An ideal alloy of silicon with germanium would consist entirely of Si-Ge bonds. It would be atomically ordered (see Figure 1.13 (a)). Of course, such a situation can only apply to stoichiometric alloys. In reality, in particular if the alloy is fabricated at rather low deposition temperatures, Ge and Si atoms are incorporated in a random or clustered manner (see Figure 1.13 (b)). One reason is that the binding energies of Si-Ge, Ge-Ge and Si-Si bonds are quite similar, lying between 2.8 and 3.1 eV. Thus, the formation of Si-Ge bonds is barely favored by binding energy effects [5].

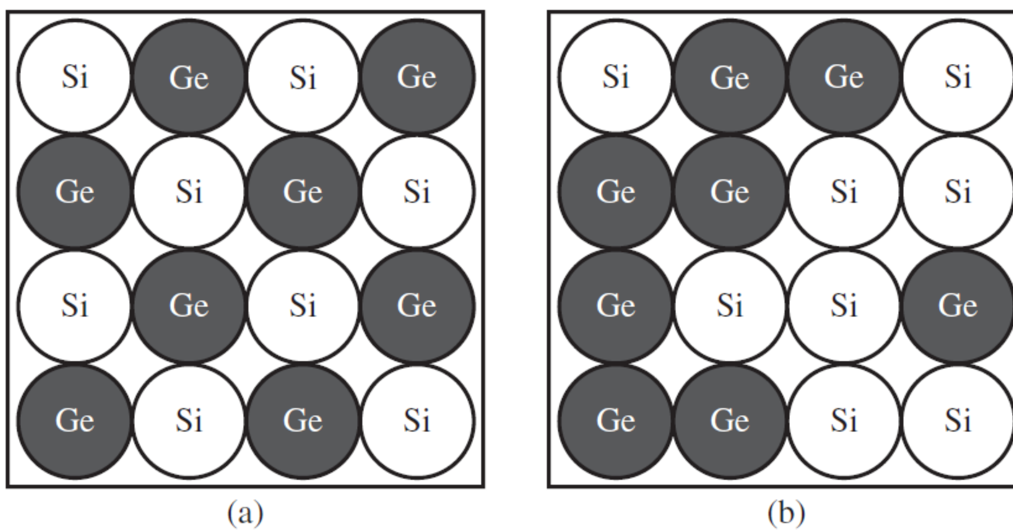

Figure 1.13 (a) Atomically ordered Si,Ge alloy, (b) statistical/clustered Si and Ge incorporation.

1.14.3 Dangling bonds, density of defect states

Upon alloying, quite generally an increase in defect density (i.e. in dangling bond concentration) is observed. Various reasons for this increase in defect concentration have been proposed; the most straightforward one appears to be the formation of void-rich materials where H is unstable at void surfaces and desorbs, resulting in dangling bonds with states near the midgap. The preferential bonding of hydrogen to the alloy component with higher hydrogen binding energy has also been proposed as a possible source of defects in a-SiGe:H alloys [5].

1.14.4 Optical absorption

The influence on the bandgap of alloy formation of silicon with Ge is demonstrated in Figure 1.14. It is often assumed that the bandgap variation is caused solely by the incorporation of a different semiconductor material. One needs to note, however, that in these alloy systems the hydrogen concentration also varies (at fixed deposition conditions), in such a way that the decreased bandgap for a-SiGe:H is partially due to a decreased hydrogen content [5].

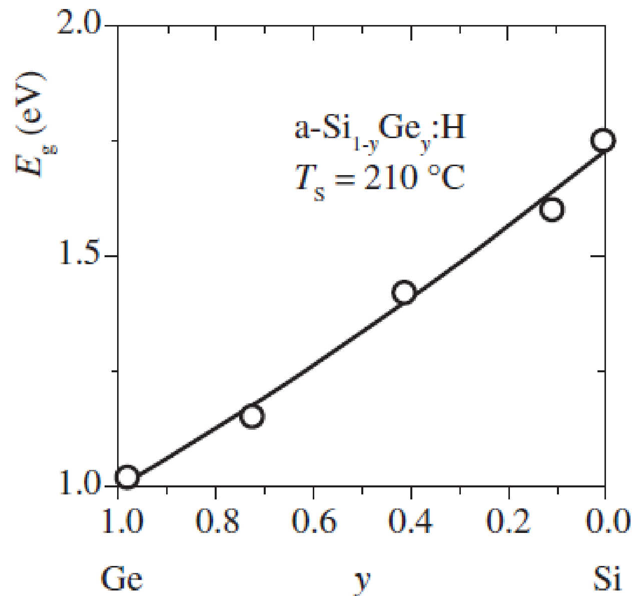

Figure 1.14 Optical gap E_g of (plasma grown) a-SiGe:H alloys as a function of composition y. Substrate temperature was $T_S \approx 210$ °C.

1.15 Hydrogenated microcrystalline silicon

1.15.1 Structure of hydrogenated microcrystalline silicon

Hydrogenated microcrystalline silicon (μc-Si:H), as deposited by PECVD from a mixture of silane and hydrogen, is a mixed-phase material containing a crystalline phase (with tiny crystallites grouped into “conglomerates” or “clusters”), an amorphous phase, and voids (which are very often not real voids but just regions with a lower density). By varying the hydrogen dilution ratio R=[H_2]/[SiH_4] in the plasma deposition (where [H_2] denotes the rate of hydrogen gas flow into the deposition system and [SiH_4] the rate of silane gas flow), one can obtain many different types of layers: (a) at low hydrogen dilution i.e., at low values of R, amorphous layers; (b) by slightly increasing R, layers with mainly an amorphous phase and a low concentration of very tiny crystallites (such as protocrystalline silicon layers); (c) at still

higher hydrogen dilution, layers with about 50% amorphous phase and 50% crystalline phase; and (d) at very high values of R, highly crystalline layers, which tend to have a large concentration of cracks or voids and thus constitute low-density, porous material [7].

When deposited on a glass substrate, the μc-Si:H layers usually start off with an amorphous incubation phase and the nucleation of crystallites only begins later on. This is shown schematically in Figure 1.15. Within μc-Si:H solar cells, the situation is more complex, as the μc-Si:H intrinsic layer is deposited on a p-doped or an n-doped microcrystalline layer, and the latter on a rough substrate. One strives, in fact, to avoid the formation of an amorphous incubation layer (which leads to a reduction in solar cell performance) by starting off the deposition with a relatively high value of R. The value of R at which microcrystalline growth starts depends very much on the deposition parameters, such as plasma excitation frequency, substrate temperature, and deposition pressure. The values of R indicated in Figure 1.15 are merely given as an example and are typical of deposition at relatively high pressures (2 to 3 Torr), with a plasma excitation frequency of 13.56 MHz [7].

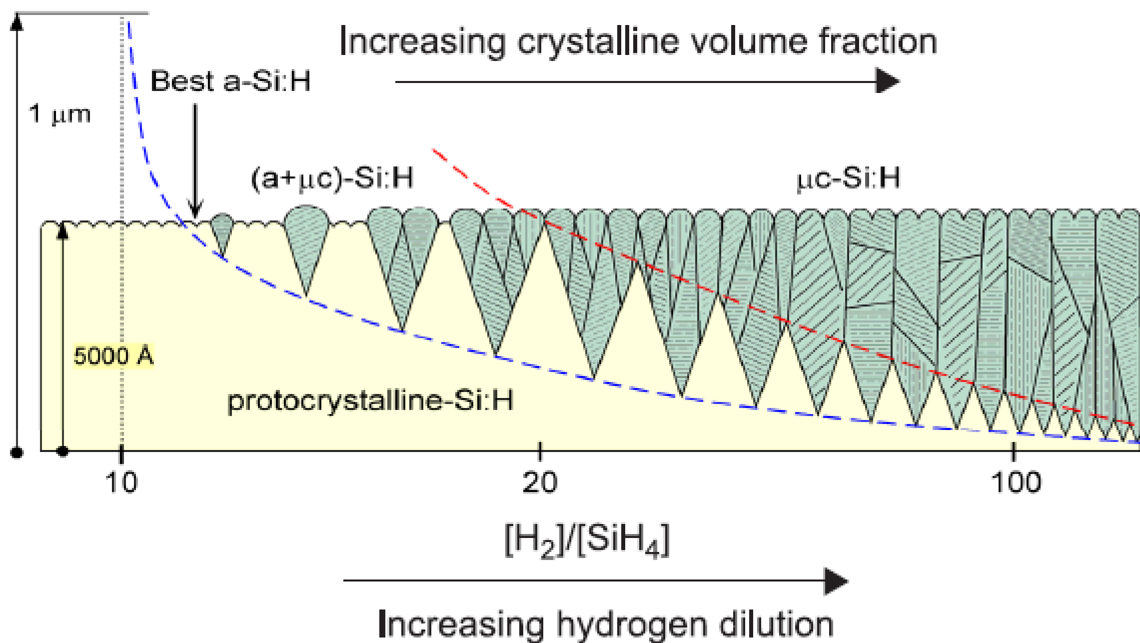

Figure 1.15 Range of film structures (schematic), obtained with different PECVD parameters, for films deposited on glass substrates; the dashed lines indicate the transitions between amorphous and mixed phase material, as well as between mixed phase material and highly crystalline material.

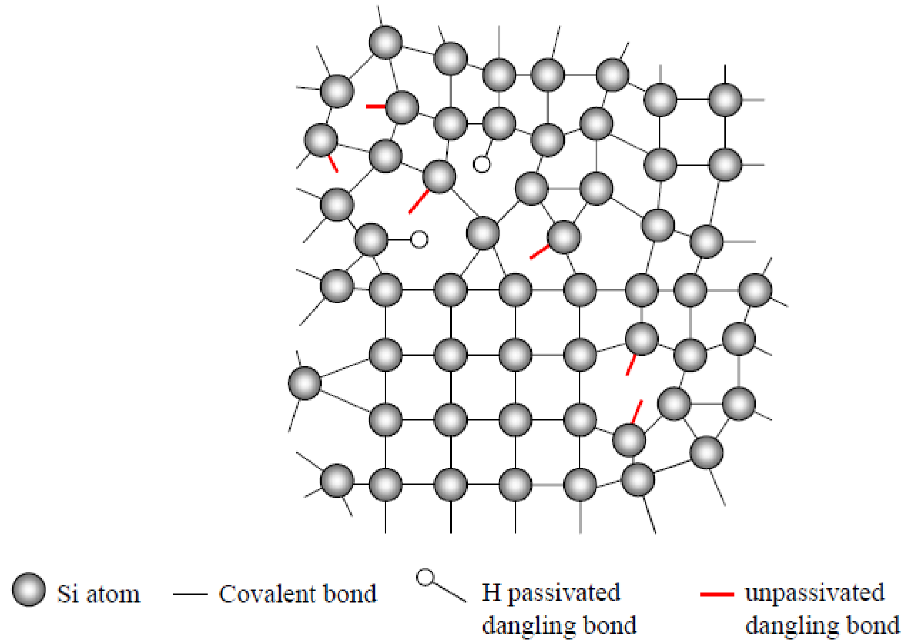

Figure 1.16 schematic structural representation of hydrogenated microcrystalline silicon.

Figure 1.16 shows a schematic structural representation of hydrogenated microcrystalline silicon. Small crystals of highly ordered material in the range of tenths of nanometers are imbedded in the amorphous structure.

1.15.2 Optical properties

Optical properties as shown in Figure 1.17 where μc-Si:H exhibits a lower absorption coefficient α for high photon energies above ~ 1.85 eV as a-Si:H. The band gap varies with crystallinity, but generally amounts to ~ 1.1 eV. Consequently, μc-Si:H absorbs light in the infrared region. Because microcrystalline silicon has an indirect band gap, optical transitions require, additional to photons with suitable energy, the participation of phonons. Therefore, the probability of an optical induced transition is reduced. The overall low α, compared to other thin-film semiconductors with direct band gap like $Cu(In,Ga)Se_2$ and CdTe, makes it necessary to apply rather thick microcrystalline layers [8].

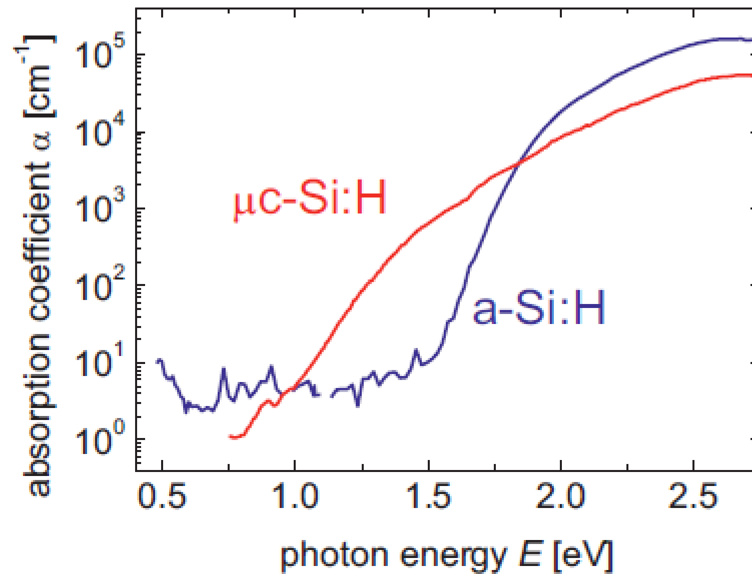

Figure 1.17 Absorption coefficient α as a function of photon energy of a-Si:H and μc-Si:H.

1.15.3 Defects

Band tails are less pronounced than in a-Si:H; one may assign a value of about 30 meV to the exponential fall-off constant E_V^0 of the valence band tail. The fact that the valence band tail is less pronounced in intrinsic in μc-Si:H layers than in intrinsic a-Si:H layers is probably the reason why in μc-Si:H p–i–n-type solar cells can often be illuminated both from the p side as well as from the n side, resulting in both cases in similarly effective photocarrier collection.

Lower defect absorption results from midgap defects (essentially dangling bonds). The defect absorption is taken for in μc-Si:H at a photon energy value of 0.8 eV, whereas it is taken for a-Si:H at a photon energy value of 1.2 eV. If the same calibration factor between defect absorption and defect density would apply in both materials, this would mean that the defect densities in device-quality in μc-Si:H layers would be much lower than in a-Si:H layers [7].

1.16 Transparent conductive oxide

In thin films, a small grid of metal contacts may be unable to collect carriers due to the high density of defects in amorphous silicon. Therefore, a contact covering the entire layer is required. This contact cannot be a metal because light would be reflected instead of reaching the intrinsic layer, thus a different approach is needed.

Transparent conductive oxides are used to avoid the high series resistances of amorphous silicon which do not offer a good lateral conductance for distances over 1 cm. The

most common TCO materials are tin oxide (SnO_2) and zinc oxide (ZnO) because they are economic to produce, abundant in nature and environmentally friendly. Indium-tin oxide is the traditional option however; it is the most expensive of the three because it requires indium which is scarce on Earth. The requirements for a good TCO are summarized as:

1) High conductivity, carrier mobility and transparency in the range of the solar spectrum.
2) Coupling of light with the absorber layer.
3) Texturized surface on both ends of the cell to scatter light.
4) Chemical stability when in contact to silicon.
5) Low cost and environmentally friendly.

In order to produce TCO layers with high conductivity, ZnO and SnO_2 are normally doped with aluminum and fluorine respectively, but gallium and boron can also be used. These dopants produce n-type materials with conductivities between 10^3 and $5x10^3$ $(\Omega.cm)^{-1}$ and mobilities from 30 to 60 $cm^2/V.s$. Unfortunately, a p-type TCO has not been successfully adapted to contact the a-Si:H p-layer and produce a good Ohmic contact yet.

It is compulsory for the band gap of a TCO to be wide because most of the spectrum needs to be able to get through it. For non-doped ZnO and SnO_2 the bandgaps are approximately 3.4 eV and 3.6 eV respectively [9].

1.17 Electrical transport mechanisms in amorphous semiconductors

1.17.1 Conduction through extended states

Just above E_c, the effect of potential fluctuations begins to dominate since the mean free path L is comparable to the interatomic distance a. Therefore, it is no longer valid to consider the model of the free electron. Cohen [10].

proposed diffusive or Brownian motion without thermal activation and obtained the mobility at E_c as:

$$\mu_c = \frac{e.a^2}{6.K.T}.\nu \qquad (1.11)$$

Where ν is the electron frequency of diffusive hopping near E_c.

The conductivity σ_c at E_c is given by

$$\sigma_c = e.\mu_c.g(E_c).K.T.\exp(\frac{\delta}{K}) .\exp(\frac{-E_o}{K.T}) \qquad (1.12)$$

Where $\exp\left(\frac{\delta}{K}\right)$ is a constant associated with the gap reduction as the temperature increases according to equation [11]:

$$E_c - E_f = E_o - \delta T \tag{1.13}$$

Where E_o is the value of E_c-E_f at $T = 0°$ K .

1.17.2 Conduction through localized states

The transport mechanism, when the conduction path energy level E_a lies in the band tail below E_c is electron hopping to the neighbor states with phonon assistance as illustrated in Fig. (1.18).

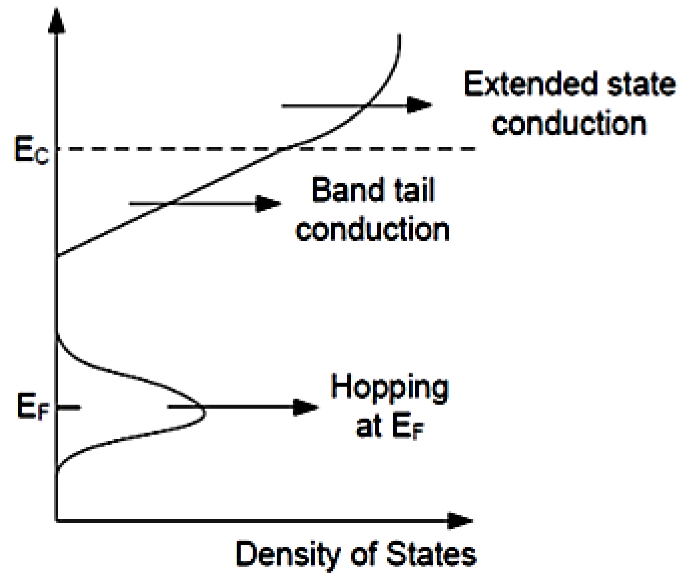

Figure 1.18 Electronic transport mechanisms: conduction in extended states, conduction in localized states and hopping at the Fermi energy.

The hopping mobility is given by [12]:

$$\mu_H = \left(\frac{e.R_o^2}{6.K\,T}\right).\exp\left(-2.\alpha.R_o\right).\nu_{ph}.\exp\left(\frac{-w}{K\,T}\right) = \mu_{Ho}.\exp\left(\frac{-w}{K\,T}\right) \tag{1.14}$$

Which differs from μ_c by the electron hopping rate $\nu_{ph}.exp(-w/K.T)$, ν_{ph} being the phonon frequency and w the energy difference between two neighbors and the overlapping term $exp(-2.\alpha.R_o)$ between two wavefunctions centered at a separating distance R_o with a spatial decay α^{-1}. The corresponding conductivity is:

$$\sigma_{\mathrm{H}} = \mu_{Ho}.K\,T\,.g\,(E_a).\exp\left(\frac{E_f - E_a - w}{K\,T}\right) \tag{1.15}$$

The activation energy change from E_o to E_a-E_f +w indicating the change in the transport mechanism of diffusion through the extended states to the hopping through the localized states was observed around 250 ° K in the first samples of a-Si:H. In the high quality a-Si:H produced much more recently with lower localized states density, the hopping mechanism was observed at much lower temperature (~80°K) [13].

1.17.3 Conduction by hopping around the Fermi level

At low temperature, the major contribution to conductivity takes place around E_f and the electrons move by hopping to the localized states which are not necessarily neighbors to an energy difference $w \sim K.T$ provided by the phonon. This mechanism is called variable range hopping R.

$$\sigma_H\left(E_f\right) = \left(\frac{e.R^2}{6}\right).g\left(E_f\right).\nu_{ph}.\exp\left(-2.\alpha.R - \frac{w}{K.T}\right) \tag{1.16}$$

According to Mott [14], the mechanism is due to a competition between the overlap term and the energy term and the optimal value of R corresponds to the maximum hopping probability, which leads to Mott's law $\sigma \propto T^{-1/4}$.

1.18 Conclusion

This chapter concerns the study of the material classifications, conductors, insulators and semiconductors and the physical and optical properties of thin film silicon layers, in particular hydrogenated amorphous silicon (a-Si:H). The properties of a-Si:H are essentially the presence of defect states in the band gap that act as traps or recombinant centers for free carriers. The ability to deposit the a-Si:H material over large areas, for low cost, at low

temperatures, as well as high optical absorption, has enabled the development of a wide range of devices based on a-Si:H, like solar cells. This material also has the advantage of being resistant to radiation compared to crystalline silicon.

Similarly, the physical and optical properties of a-SiGe:H, μc-Si:H and TCO's materials are also studied in this chapter.

Chapter 1 references

[1] G. Lutz, *Semiconductor radiation detectors*. Springer, 2007.

[2] S. M. Sze and M. K. Lee, "Semiconductor devices: phys-ics and technology. 3-rd edition.-New York, John Wiley and Sons, Inc," 2012.

[3] H. Sterling and R. C. Swann, "THIN-FILM SILICON SOLAR CELLS," 2006.

[4] A. Luque and S. Hegedus, *Handbook of photovoltaic science and engineering*. John Wiley & Sons, 2011.

[5] A. Shah and A. V. Shah, *Thin-film silicon solar cells*. EPFL press, 2010.

[6] Z. Li, "Properties of Amorphous Silicon Germanium Films and Devices Prepared Using Chemical Annealing," 2013.

[7] A. McEvoy, L. Castaner, and T. Markvart, *Solar cells: materials, manufacture and operation*. Academic Press, 2012.

[8] S. Schicho, *Amorphous and microcrystalline silicon applied in very thin tandem solar cells*, vol. 99. Forschungszentrum Jülich, 2011.

[9] A. N. Corpus Mendoza, "Influence of the p-type layer on the performance and stability of thin film silicon solar cells." University of Sheffield, 2017.

[10] M. H. Cohen, H. Fritzsche, and S. R. Ovshinsky, "Simple band model for amorphous semiconducting alloys," *Phys. Rev. Lett.*, vol. 22, no. 20, p. 1065, 1969.

[11] N. K. Hindley, "Random phase model of amorphous semiconductors I. Transport and optical properties," *J. Non. Cryst. Solids*, vol. 5, no. 1, pp. 17–30, 1970.

[12] R. A. Street, *Hydrogenated amorphous silicon*. Cambridge university press, 2005.

[13] W. E. Spear and C. S. Cloude, "Electron and hole transport in the band-tail states of amorphous silicon at low temperatures," *Philos. Mag. B*, vol. 58, no. 5, pp. 467–484, 1988.

[14] N. F. Mott and E. A. Davis, *Electronic processes in non-crystalline materials*. Oxford university press, 2012.

Chapter 2:
Solar cells fundamentals devices

2.1 Introduction

The production of energies is always one of the worries of man. Photovoltaic energy is one of the very promising renewable energies for a clean and unpolluted world. It has the advantage of converting light energy into electrical energy (electron-hole pair generation) and exploiting the entire light spectrum. Several semiconductor materials are used in this conversion and silicon is the most used base material in the world.

This chapter is dedicated to the theoretical study of the solar cell, its operating principle, its photovoltaic parameters as well as its associated technology. Firstly, we will study the solar radiation and how the transfer of energy from the photon to the electron. Then the generation by light, recombinant mechanisms of excess carriers and electrical characteristics $I(V)$ to extract open-circuit voltage, short-circuit current, fill factor and efficiency will be presented. Afterwards, we will describe different generations of solar cell technologies, tandem device classifications and the principle of the two-terminal tandem cell. We will also study amorphous silicon, microcrystalline and amorphous silicon germanium singles and multijunctions solar cells.

2.2 Solar radiation

The radiative energy output from the sun derives from a nuclear fusion reaction. Every second, about $6x10^{11}$ kg hydrogen is converted to helium, with a net mass loss of about $4x10^3$ kg. The mass loss is converted through the Einstein relation ($E = mc^2$) to $4x10^{20}$ J. This energy is emitted primarily as electromagnetic radiation in the ultraviolet to infrared region (0.2 to 3 µm). The total mass of the sun is now about $2x10^{30}$ kg, and a reasonably stable life with a nearly constant radiative energy output of over 10 billion (10^{10}) years is projected.

The intensity of solar radiation outside the earth's atmosphere, at the average distance of its orbit around the sun, is defined as the solar constant and has a value of 1367 W/m^2. Terrestrially, the sunlight is attenuated by clouds and by atmospheric scattering and absorption. The attenuation depends primarily on the length of the light's path through the atmosphere, or the mass of air through which it passes. This "*air mass*" is defined as l/cosϕ, where ϕ is the angle between the vertical and the sun's position.

Figure 2.1 shows two curves related to solar spectral irradiance (power per unit area per unit wavelength). The upper curve, which represents the solar spectrum outside the Earth's atmosphere, is the air mass zero condition (AM0). The AM0 spectrum is relevant for satellite and space vehicle applications. Terrestrial solar cell performance is specified with reference to the air mass 1.5 (AM 1.5) spectrum. This spectrum represents the sunlight at the Earth's surface

when the sun is at an angle of 48° from the vertical. At this angle the incident power is about 963 W/m² [1].

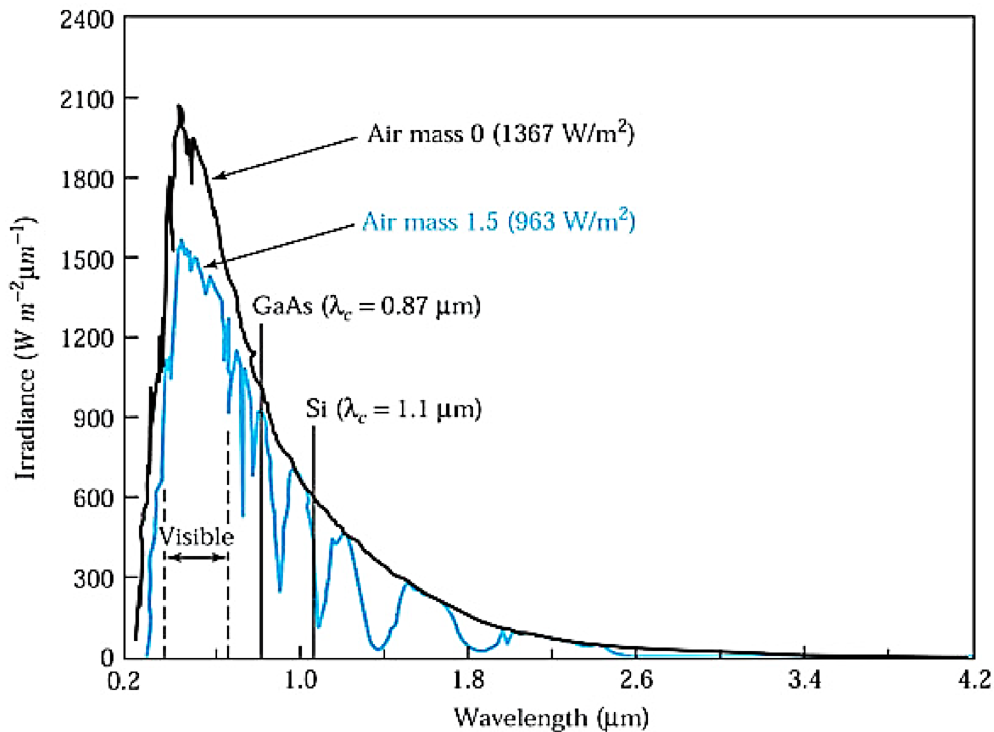

Figure 2.1 Solar spectral irradiance at air mass 0 and air mass 1.5 and the cutoff wavelength of GaAs and Si.

2.3 Transfer of energy from the photon to the electron

Each photon associates a wavelength λ and an energy E_{ph}. The solar cell is sensitive only in a particular wavelength range and only a semiconductor material has the band structure necessary for generating, from solar radiation, usable electron-hole pairs. The generation of electron-hole pairs is generated by absorption of a photon which allows an electron of the valence band to pass into the conduction band leaving a pseudo-positive charge in the valence band named a hole [2].

Figure 2.2 presents the different possible transitions according to the nature of the gap. When the minimum of the conduction band and the maximum of the valence band coincide in the K space, it is a direct gap. Inter-band transitions occur vertically, and are therefore radiative (Figure 2.2(a)). This illustrates the operation of III-V binary semiconductors, such as GaAs, which are widely used in optoelectronics. In the case of silicon (fig 2.2(b)), the gap is indirect: the electronic transitions between the extrema of the bands are oblique and non-radiative.

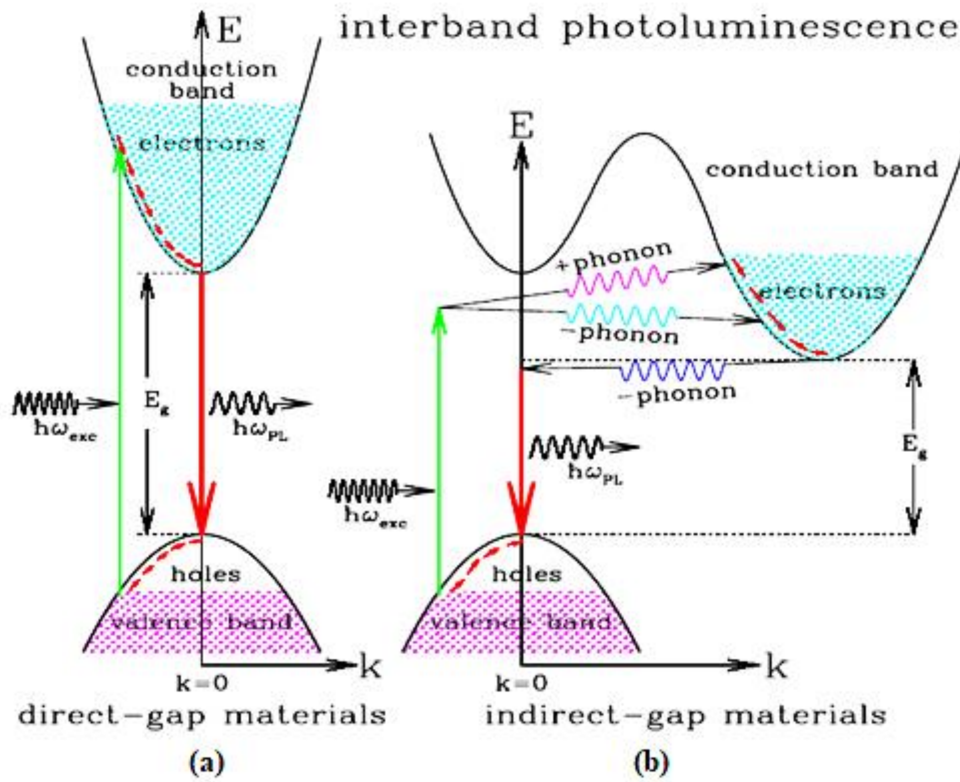

Figure 2.2 Schematic band diagrams for the photoluminescence processes in (a) A direct gap material, (b) An indirect gap material.

The photon/electron interaction within the semiconductor results in the generation of an electron-hole pair. To create an electrical current, it is necessary to dissociate the photogenerated electron-hole pairs and collect them in an external electrical circuit before they recombine within the material.

2.4 Generation of excess carriers by light

The energy of the photon corresponding to a given radiation is related to its wavelength by the relation [3]:

$$E_p = h\nu = \frac{hc}{\lambda} = \frac{1.24}{\lambda} \quad (2.1)$$

Where ν is the frequency of the radiation, λ the wavelength of the radiation in µm, c the speed of light, E_p the photon energy in eV and h is the Plank constant.

A luminous radiation encountering a semiconductor is absorbed according to Lambert-Bouguer's law:

$$I(x) = I(1-R)\exp(-\alpha x) = I_o \exp(-\alpha x) \tag{2.2}$$

Where x is the depth of absorption of the beam in the material from the surface of the semiconductor, R is the reflection coefficient, represents the part of the incident light energy I, reflected on the surface of the material, and α is the absorption coefficient.

The optical behavior of the material is fully described by its optical constants. These are the refractive index n and the extinction coefficient k, which together form the complex refractive index N. n and k depend on the wavelength of the incident light. The refractive index n is related to the propagation speed of the light wave and the coefficient k is a unit of measurement for the wave damping. The complex refractive index is defined as:

$$N = n(\lambda) + ik(\lambda) \tag{2.3}$$

The optical absorption coefficient α is given by:

$$\alpha = \frac{4\pi k}{\lambda} \tag{2.4}$$

Figure 2.3 gives the absorption spectra of some materials. The minimum energy required for the incident photon to cause the electronic transition depends on the band gap E_g of the material.

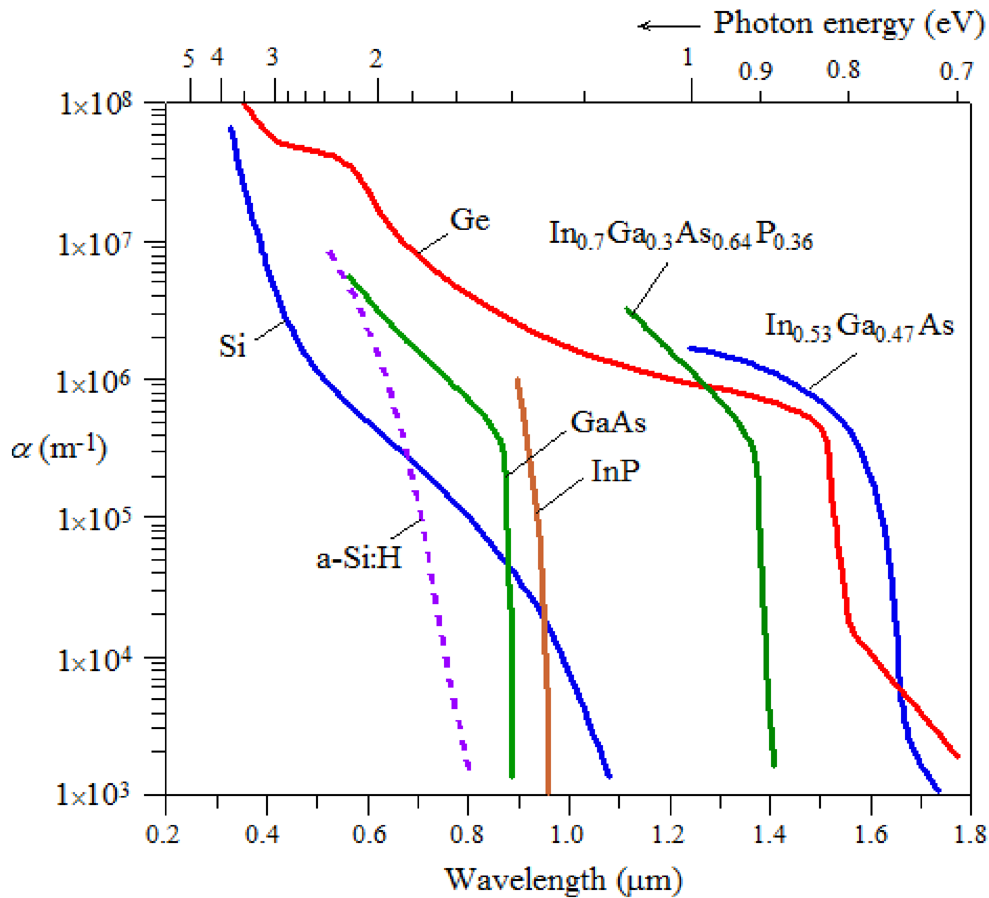

Figure 2.3 Absorption coefficient as a function of wavelength of light (bottom abscissa) or energy (top abscissa) for several semiconductors [4].

The calculation of the generation rate of electron-hole pairs $G(x)$ (cm^{-3}s^{-1}) is carried out as follows. Calling I_o, the flux of photons (cm^{-2}s^{-1}) incident on the illuminated side of the material and α(cm^{-1}) the absorption coefficient of light by the material. At depth x, this generation rate is:

$$G(x) = \alpha(1-R)I_o e^{-\alpha x} \tag{2.5}$$

2.5 Recombination mechanisms of excess carriers

The semiconductor in which the excess carriers were created by photon injection, in accordance with the process described in the previous paragraph, will tend to return to steady state. The disappearance of excess carriers restoring thermodynamic equilibrium occurs via recombination mechanisms.

There are four modes of recombination of the carriers:

2.5.1 Band-to-band recombination

Band-to-band recombination occurs when an electron moves from its conduction band state into the empty valence band state associated with the hole. This band-to-band transition is typically also a radiative transition in direct bandgap semiconductors. Figure 2.4 illustrates the band-to-band recombination process. Band-to-band recombination depends on the density of available electrons and holes. Since both carrier types need to be available in the recombination process, the rate is expected to be proportional to the product of n and p. The net recombination rate can be expressed as:

$$U_{b-b} = b(np - n_i^2) \tag{2.6}$$

where n_i is the density of carriers in thermal equilibrium and b is the bimolecular recombination constant [5].

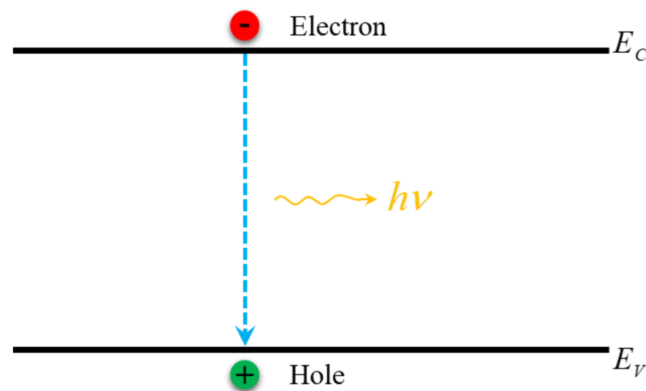

Figure 2.4 Descriptive diagram of the radiative type recombination process.

2.5.2 Auger recombination

Auger recombination involves three particles: an electron and a hole which recombine in a band-to-band transition and give off the resulting energy to another electron or hole (Figure 2.5). The expression for the net recombination rate is therefore similar to that of band-to-band recombination but includes the density of the electrons or hole which receive the released energy from the electron-hole annihilation:

$$U = AUGN\left(pn^2 - nn_i^{\,2}\right) + AUGP\left(np^2 - pn_i^{\,2}\right) \tag{2.7}$$

AUGN and *AUGP* the two terms correspond to the two possible mechanisms [5].

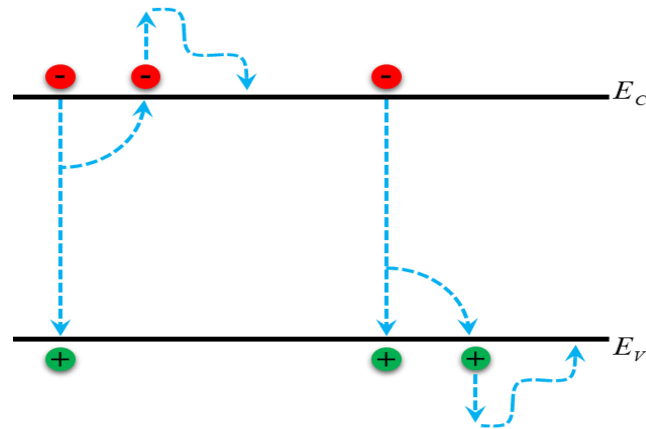

Figure 2.5 Descriptive diagram of Auger recombination in a semiconductor.

2.5.3 Shockley Read Hall (SRH) recombination

Phonon transitions occur in the presence of a trap (or defect) within the forbidden gap of the semiconductor. This is essentially a two steps process, the theory of which was first derived by Shockley and Read and then by Hall [6].

The free electron captured by the center which from the neutral state becomes negative can be re-transmitted to the conduction band. Figure 2.6 shows that an identical process occurs for a captured hole. In total, an electron and a free hole disappear. An electron-hole pair recombined.

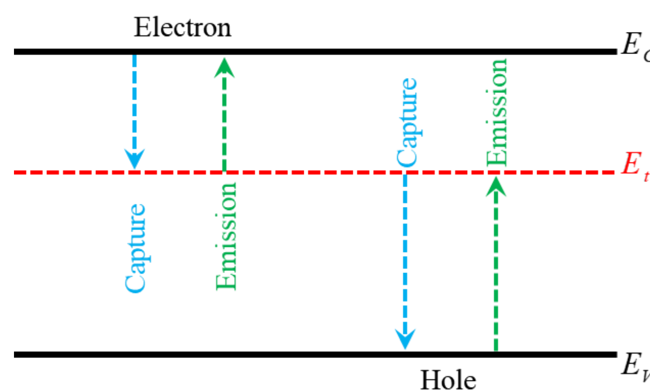

Figure 2.6 Descriptive diagram of trap-assisted recombination.

The Shockley-Read-Hall recombination is modeled as follows:

$$R_{SRH} = \frac{pn - n_i^{\,2}}{\tau_{po}\left[n + n_i \exp\left(\frac{E_{trap}}{kT}\right)\right] + \tau_{no}\left[p + n_i \exp\left(\frac{-E_{trap}}{kT}\right)\right]} \tag{2.8}$$

where E_{trap} is the difference between the trap energy level (E_t) and the intrinsic Fermi level (E_{fi}), T is the temperature in degrees Kelvin and τ_{no} and τ_{po} are the electron and hole lifetimes [6].

2.5.4. Surface recombination

In addition to generation-recombination within the bulk of the semiconductor, electrons or holes may recombine or be generated at interfaces. The rate of surface recombination may be even greater than within the bulk. The standard method is to model interface recombination in a similar manner as the bulk generation-recombination rate where

$$R_{surf} = \frac{pn - n_i^2}{\tau_p^{eff}\left[n + n_i \exp\left(\frac{E_{trap}}{kT}\right)\right] + \tau_n^{eff}\left[p + n_i \exp\left(\frac{-E_{trap}}{kT}\right)\right]} \tag{2.9}$$

Here:

$$\frac{1}{\tau_n^{eff}} = \frac{1}{\tau_n^i} + \frac{d_i}{A_i} S_n \tag{2.10}$$

And

$$\frac{1}{\tau_p^{eff}} = \frac{1}{\tau_p^i} + \frac{d_i}{A_i} S_p \tag{2.11}$$

τ_n^i is the bulk lifetime calculated at node i along the interface and which may be a function of the impurity concentration as well. The d_i and A_i parameters are the length and area of the interface for node i. The S_n and S_p are the recombination velocities for electrons and holes respectively [6].

2.6 Photocurrent and spectral response of solar cells

In this section we derive the photocurrent for a silicon p-n junction solar cell which serves as a reference device for all solar cells. A typical schematic representative of a solar cell is shown in Fig. 2.7. It consists of a shallow *p-n* junction formed on the sur

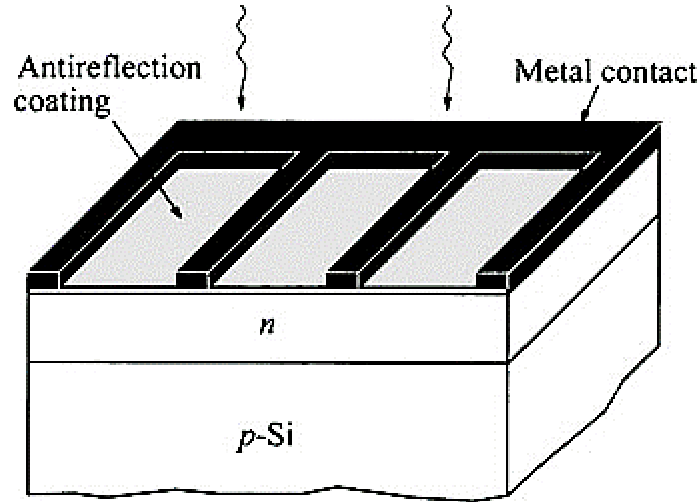

Figure 2.7 Schematic representation of a silicon p-n junction solar cell.

face, front ohmic contact stripes and fingers, an antireflection coating, and a back ohmic contact. The finger grid reduces series resistance, but at the expense of blocking some light, so there is a trade-off for the design. Some use transparent conductors such as IT0 (indium-tin oxide).

When a monochromatic light of wavelength λ is incident on the front surface, the photocurrent and spectral response, that is, the number of carriers collected per incident photon at each wavelength, can be derived as follows. The generation rate of electron-hole pairs at a distance *x* from the semiconductor surface is shown in Fig. 2.8 and is given by

$$G(\lambda, x) = \alpha(\lambda)\phi(\lambda)\left[1 - R(\lambda)\right]\exp\left[-\alpha(\lambda)x\right] \tag{2.12}$$

where $\alpha(\lambda)$ is the absorption coefficient, $\phi(\lambda)$ the number of incident photons per area per time per unit bandwidth, and $R(\lambda)$ the fraction of these photons reflected from the surface. For an abrupt *p-n* junction solar cell with constant doping on each side, Fig. 2.8, there are no electric fields outside the depletion region. Photogenerated carriers in these regions are collected by a diffusion process while that in the depletion region by drift process. We divide

the collection of photogenerated carriers in three regions: the top neutral region, the depletion region of the junction, and the substrate neutral region. We also assume an abrupt one-sided junction with $N_D >> N_A$, so the depletion region at the n-side can be neglected.

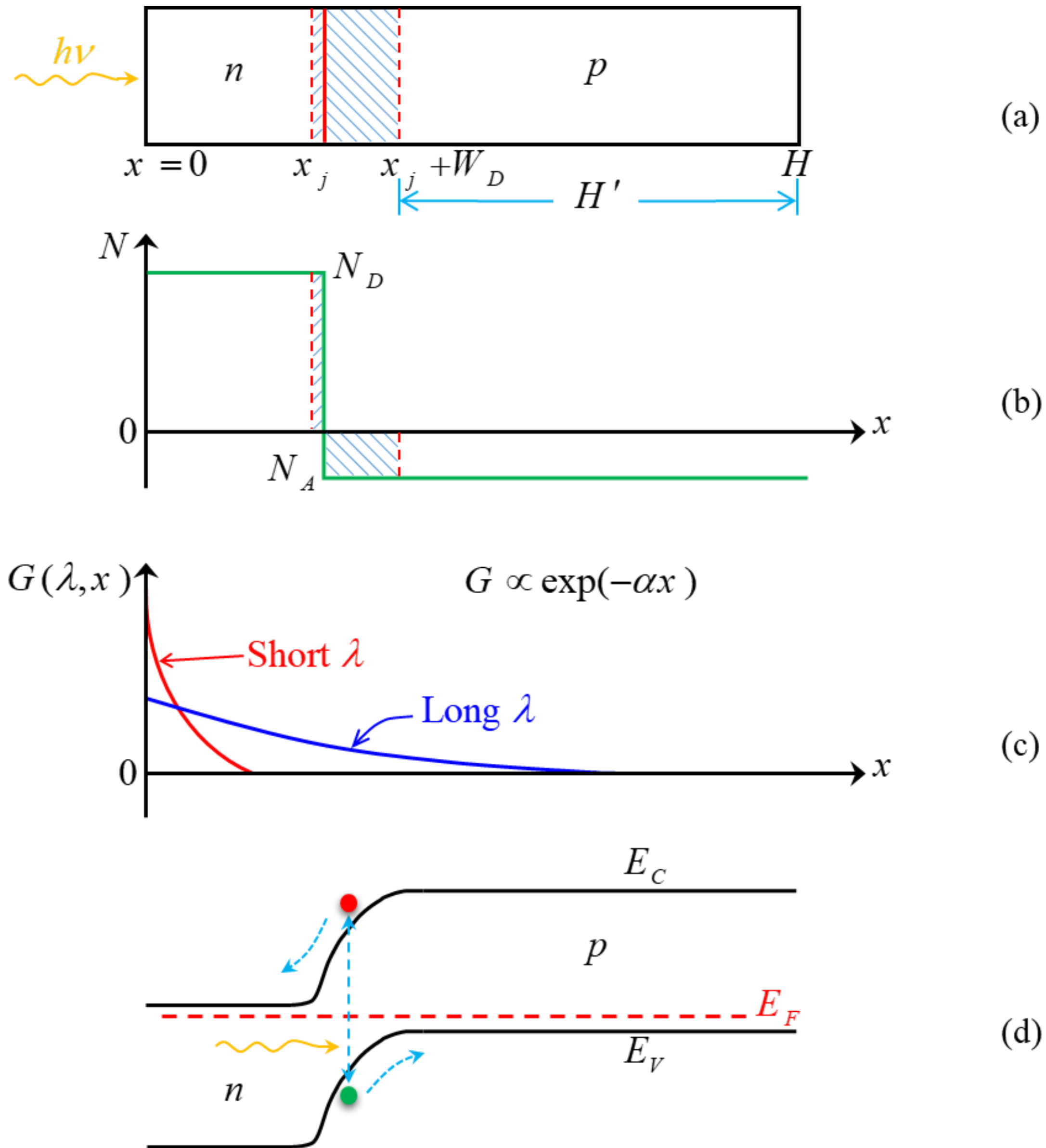

Figure 2.8 (a) Solar-cell dimensions under consideration. (b) Assumed abrupt doping profiles $N_D >> N_A$. (c) Generation rate as a function of distance for long and short wavelengths. (d) Energy-band diagram showing generated electron-hole pair.

Under low-injection condition, the one-dimensional, steady-state continuity equations are:

$$G_n - \left(\frac{n_P - n_{po}}{\tau_n} \right) + \frac{1}{q} \frac{dJ_n}{dx} = 0 \tag{2.13}$$

for electrons in the p-type substrate and

$$G_p - \left(\frac{p_n - p_{no}}{\tau_p} \right) + \frac{1}{q} \frac{dJ_p}{dx} = 0 \tag{2.14}$$

for holes in the n-type layer. The current-density equations are

$$J_n = q\mu_n n_p \xi + qD_n \left(\frac{dn_p}{dx} \right) \tag{2.15}$$

$$J_p = q\mu_p p_n \xi + qD_p \left(\frac{dp_n}{dx} \right) \tag{2.16}$$

For the top *n*-side of the junction, Eqs. (2.12), (2.15), and (2.16) can be combined to yield an expression:

$$D_p \frac{d^2 p_n}{dx^2} \alpha\phi(1-R)\exp(-\alpha x) - \frac{p_n - p_{no}}{\tau_p} = 0 \tag{2.17}$$

The general solution to this equation is

$$p_n - p_{no} = C_2 \cosh\left(\frac{x}{L_p} \right) + C_3 \sinh\left(\frac{x}{L_p} \right) - \frac{\alpha\phi(1-R)\tau_p}{\alpha^2 L_p^2 - 1} \exp(-\alpha x) \tag{2.18}$$

where $L_p = \sqrt{D_p \tau_p}$ is the diffusion length, and C_2 and C_3 are constants. There are two boundary conditions. At the surface, we have surface recombination with a recombination velocity S_p:

$$D_p \frac{d(p_n - p_{no})}{dx} = S_p (p_n - p_{no}) \qquad \text{at } x = 0 \tag{2.19}$$

At the depletion edge, the excess carrier density is small due to the electric field in the depletion region:

$p_n - p_{no} \approx 0 \qquad \text{at } x = x_j$

Using these boundary conditions in Eq. (2.18), the hole density is:

$$p_n - p_{no} = [\alpha\phi(1-R)\tau_p / (\alpha^2 L_p^2 - 1)] \times \left[\frac{\left(\frac{S_p L_p}{D_p} + \alpha L_p\right)\sinh\frac{x_j - x}{L_p} + \exp(-\alpha x_j)\left(\frac{S_p L_p}{D_p}\sinh\frac{x}{L_p} + \cosh\frac{x}{L_p}\right)}{(S_p L_p / D_p)\sinh(x_j / L_p) + \cosh(x_j / L_p)} - \exp(-\alpha x) \right] \tag{2.20}$$

and the resulting hole photocurrent density at the depletion edge is:

$$J_p = -qD_p\left(\frac{dp_n}{dx}\right)_{x_j} = [q\phi(1-R)\alpha L_p / (\alpha^2 L_p^2 - 1)] \times \left[\frac{\left(\frac{S_p L_p}{D_p} + \alpha L_p\right) - \exp(-\alpha x_j)\left(\frac{S_p L_p}{D_p}\cosh\frac{x_j}{L_p} + \sinh\frac{x_j}{L_p}\right)}{(S_p L_p / D_p)\sin(x_j / L_p) + \cosh(x_j / L_p)} - \alpha L_p \exp(-\alpha x_j) \right] \tag{2.21}$$

This photocurrent would be generated and collected in the front side of an n-on-p junction solar cell at a given wavelength, assuming this region to be uniform in lifetime, mobility, and doping level.

To find the electron photocurrent generated in the substrate of the cell, Eqs. (2.12), (2.13), and (2.15) are used with the boundary conditions:

$$n_p - n_{po} \approx 0 \qquad \text{at } x = x_j + W_D \tag{2.22}$$

$$S_n(n_p - n_{po}) = \frac{-D_n dn_p}{dx} \qquad \text{at } x = H \tag{2.23}$$

where W_D is the depletion width and H is the width of the entire cell. Equation (2.23) states that the excess minority carrier density is near zero at the edge of the depletion region, while Eq. (2.24) states that the back surface recombination takes place at the ohmic contact.

Using these boundary conditions, the electron distribution in a uniformly doped p-type substrate is:

$$n_p - n_{po} = \frac{\alpha\phi(1-R)\tau_n}{\alpha^2 L_p^2 - 1}\exp[-\alpha(x_j + W_D)]\left\{\cosh\left(\frac{x'}{L_n}\right) - \exp(-\alpha x') - \frac{(S_n L_n / D_n)[\cosh(H'/L_n) - \exp(-\alpha H')] + \sinh(H'/L_n) + \alpha L_n \exp(-\alpha H')}{(S_n L_n / D_n)\sinh(H'/L_n) + \cosh(H'/L_n)}\sinh(x'/L_n)\right\} \quad (2.24)$$

$(x' \equiv x - x_j - W_D)$ and the photocurrent due to electrons collected at the depletion edge, $x = x_j + W_D$, is

$$J_n = qD_n\left(\frac{dn_p}{dx}\right)_{x_j + W_D} = \frac{q\phi(1-R)\alpha L_n}{\alpha^2 L_n^2 - 1}\exp[-\alpha(x_j + W_D)] \times \left\{\alpha L_n - \frac{(S_n L_n / D_n)[\cosh(H'/L_n) - \exp(-\alpha H')] + \sinh(H'/L_n) + \alpha L_n \exp(-\alpha H')}{(S_n L_n / D_n)\sinh(H'/L_n) + \cosh(H'/L_n)}\right\} \quad (2.25)$$

where H' as shown in Fig. 2.8(a) is the p-substrate neutral region.

Some photocurrent generation takes place within the depletion region as well. The electric field in this region is generally high, and the photogenerated carriers are accelerated out of the depletion region before they can recombine. The quantum efficiency in this region is near 100% and the photocurrent per unit bandwidth is equal to the number of photons absorbed:

$$J_{dr} = q\phi(1-R)\exp(-\alpha x_j)[1 - \exp(-\alpha W_D)] \quad (2.26)$$

The total photocurrent at a given wavelength is then the sum of Eqs. (2.21), (2.25), and (2.26):

$$J_L(\lambda) = J_p(\lambda) + J_n(\lambda) + J_{dr}(\lambda) \quad (2.27)$$

The spectral response (SR) is defined as this sum divided by $q\phi$ for externally observed response or by $q\phi$ *(l - R)* for internal SR:

$$\mathrm{SR}(\lambda) = \frac{J_L(\lambda)}{q\phi(\lambda)[1-R(\lambda)]} = \frac{J_p(\lambda)+J_n(\lambda)+J_{dr}(\lambda)}{q\phi(\lambda)[1-R(\lambda)]} \tag{2.28}$$

An internal SR calculated for a Si *n-p* solar cell is shown in Fig. 2.9.

Once the SR is known, the total photocurrent density obtained from the solar spectral distribution $\phi(\lambda)$.

$$J_L = q\int_0^{\lambda_m} \phi(\lambda)\left[1-R(\lambda)\right]\mathrm{SR}(\lambda)d\lambda \tag{2.29}$$

where λ_m is the longest wavelength corresponding to the semiconductor bandgap [7].

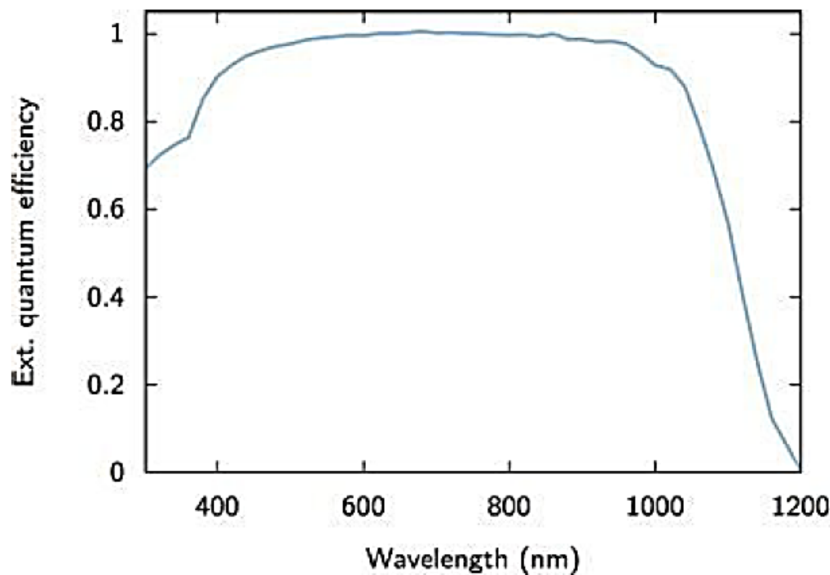

Figure 2.9 The external quantum efficiency of a high quality crystalline silicon based solar cell.

2.7 Electrical characteristics

2.7.1 The ideal solar cell

An ideal solar cell can be represented by a current source connected in parallel with a rectifying diode, as shown in the equivalent circuit of Figure 2.10. The corresponding *I–V* characteristic is described by the Shockley solar cell equation:

$$I = I_{ph} - I_0\left(e^{\frac{qV}{k_BT}} - 1\right) \tag{2.30}$$

where k_B is the Boltzmann constant, T is the absolute temperature, q is the electron charge, and V is the voltage at the terminals of the cell. I_o is the diode saturation current. The photogenerated current I_{ph} is closely related to the photon flux incident on the cell, and its dependence on the wavelength of light is frequently discussed in terms of the quantum efficiency or spectral response [8].

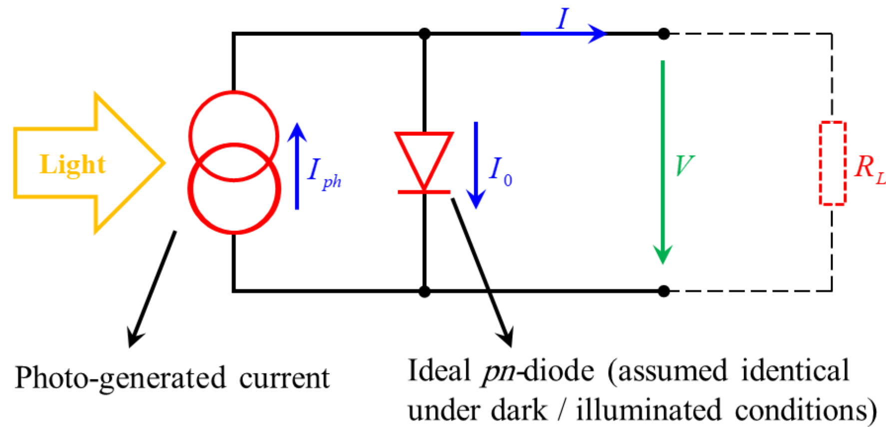

Figure 2.10 Simplest equivalent circuit, for an "ideal" solar cell; an external load resistance R_L has also been drawn.

Figure 2.11(a) shows the *I–V* characteristic (Equation (2.30)). In the ideal case, the short-circuit current I_{sc} is equal to the photogenerated current I_{ph}, and the open-circuit voltage V_{oc} is given by

$$V_{OC} = \frac{k_B T}{q} \ln\left(1 + \frac{I_{ph}}{I_0}\right) \tag{2.31}$$

The power $P=IV$ produced by the cell is shown in Figure 2.11(b). The cell generates the maximum power P_{max} at a voltage V_m and current I_m, and it is convenient to define the fill factor FF by:

$$FF = \frac{I_m V_m}{I_{sc} V_{oc}} = \frac{P_{\max}}{I_{sc} V_{oc}} \tag{2.32}$$

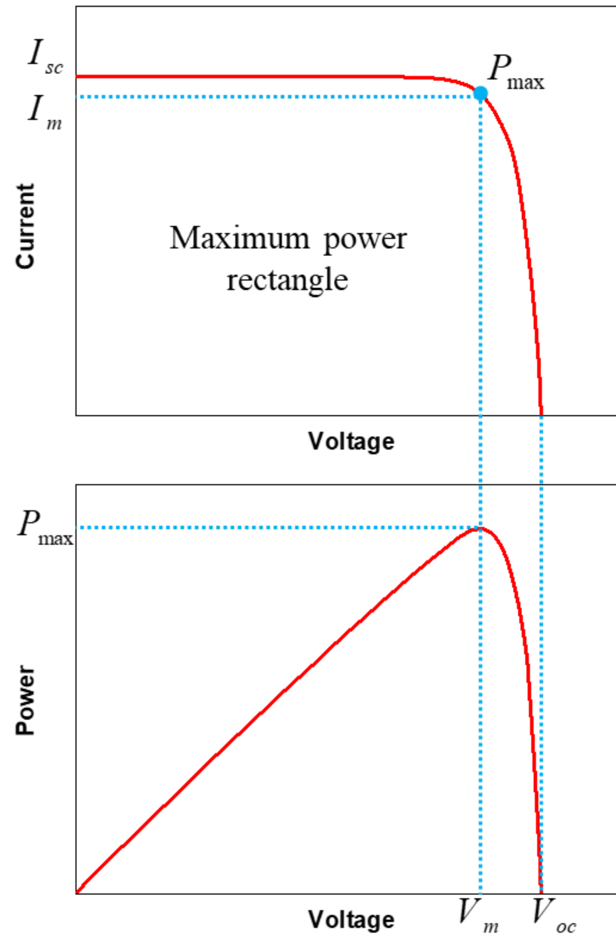

Figure 2.11 (a) The *I–V* characteristic of an ideal solar cell and (b) the power produced by the cell. The power generated at the maximum power point is equal to the shaded rectangle in (a).

The fill factor *FF* of a solar cell with the ideal characteristic (2.30) will be furnished by the subscript 0. It cannot be determined analytically but it can be shown that FF_o depends only on the ratio $v_{oc} = V_{oc} / k_B T$. FF_o is determined by the approximate expression.

$$FF_o = \frac{v_{oc} - \ln(v_{oc} + 0.72)}{v_{oc} + 1} \tag{2.33}$$

The efficiency η, of solar cells refers to the power conversion efficiency. It is defined as the ratio between the maximum power delivered by the cell and the incident light power P_{in}

$$\eta = \frac{P_m}{P_{in}} = \frac{FFV_{co} I_{cc}}{P_{in}} \tag{2.34}$$

P_{in} : the incident light power is equal to the solar power P_{solar} (P_{solar}= 100 mW/cm^2).

The *I–V* characteristics of an ideal solar cell complies with the *superposition principle:* the functional dependence (2.30) can be obtained from the corresponding characteristic of a diode in the dark by shifting the diode characteristic along the current axis by I_{ph} (Figure 2.12).

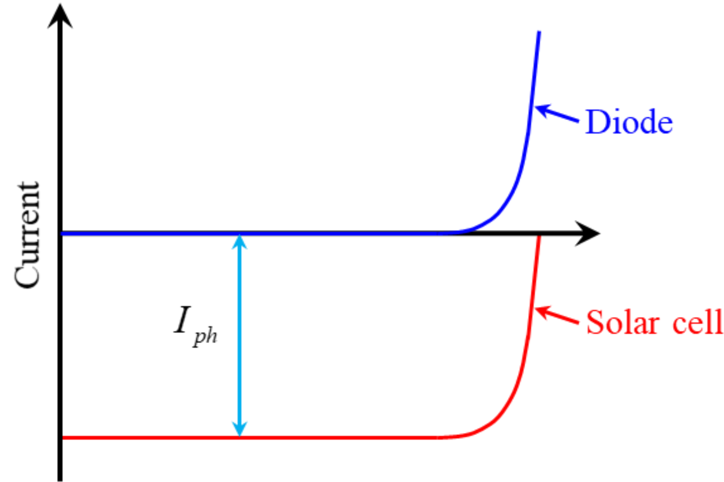

Figure 2.12 The superposition principle for solar cells.

2.7.2 Solar cell characteristics in practice

The *I–V* characteristic of a solar cell in practice usually differs to some extent from the ideal characteristic eq. (2.30). The solar cell (or circuit) may also contain series (R_s) and parallel (or shunt, R_p) resistances, leading to a characteristic of the form [8]:

$$I = I_{ph} - I_0 \left\{ \exp\left(\frac{V + IR_s}{2k_B T} \right) - 1 \right\} - \frac{V + IR_s}{R_p} \tag{2.35}$$

where the light-generated current I_{ph} may, in some instances, depend on the voltage. These features are shown in the equivalent circuit of Figure 2.13. The effect of the series and parallel resistances on the *I–V* characteristic of the solar cell is shown in Figures 2.14. The effect of the series resistance on the fill factor can be writing as:

$$FF = FF_o (1 - r_s) \tag{2.36}$$

where $r_s = R_s I_{sc} / V_{oc}$. An analogous expression exists also for the parallel resistance.

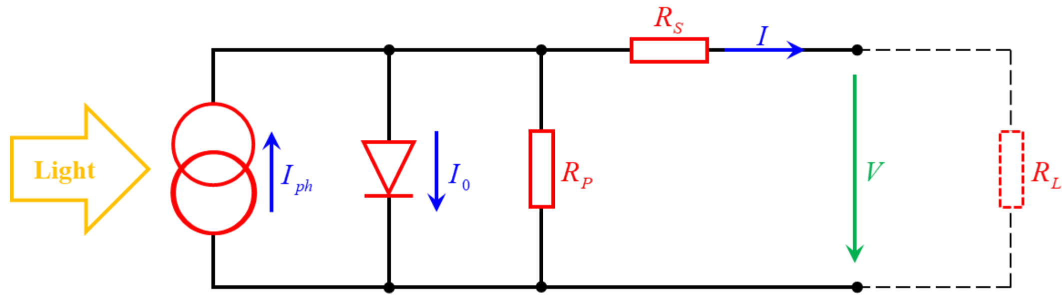

Figure 2.13 Universally used equivalent circuit for a solar cell.

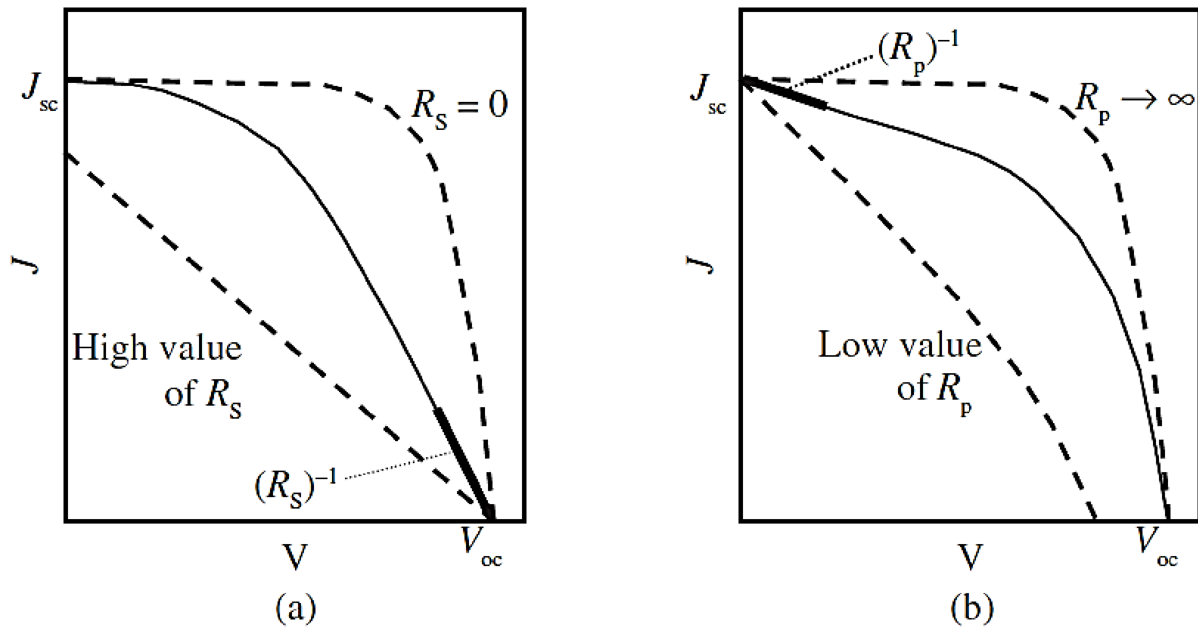

Figure 2.14 Effect of (a) the series resistance R_s and of (b) the parallel resistance R_p, as given in the "universal" circuit of Fig. 2.13 on the $J(V)$ characteristics of a solar cell. Values of $(R_s)^{-1}$ and $(R_p)^{-1}$ are given by the slopes of the $J(V)$ characteristics, at the short-circuit point ($V = 0$) and at the open-circuit point ($J = 0$), respectively.

2.7.3 The quantum efficiency and spectral response

The quantum efficiency of a solar cell is defined as the ratio of the number of electrons in the external circuit produced by an incident photon of a given wavelength. Thus, one can define external and internal quantum efficiencies (denoted by $EQE(\lambda)$ and $IQE(\lambda)$, respectively). They differ in the treatment of photons reflected from the cell: all photons impinging on the cell surface are taken into account in the value of the *EQE*, but only photons that are not reflected are considered in the value of *IQE*.

If the internal quantum efficiency is known, the total photogenerated current is given by:

$$I_{ph} = q \int_{(\lambda)} \Phi(\lambda)\{1 - R(\lambda)\} IQE(\lambda) d\lambda \tag{2.37}$$

where $\Phi(\lambda)$ is the photon flux incident on the cell at wavelength λ, $R(\lambda)$ is the reflection coefficient from the top surface, and the integration is carried out over all wavelength λ of light absorbed by the solar cell.

The spectral response (denoted by $SR(\lambda)$, with the units A/W) is defined as the ratio of the photocurrent generated by a solar cell under monochromatic illumination of a given wavelength to the value of the spectral irradiance at the same wavelength. Since the number of photons and irradiance are related, the spectral response can be written in terms of the quantum efficiency as

$$SR(\lambda) = \frac{q\lambda}{hc} QE(\lambda) = 0.808 \cdot \lambda \cdot QE(\lambda) \tag{2.38}$$

where λ is in micrometres. Spectral response in eq. (2.38) can be either internal or external, depending on which value is used for the quantum efficiency [8].

2.8 Types of solar cells

Solar cells can be classified into first, second and third generation cells. The first generation cells also called conventional, traditional or wafer-based cells are made of crystalline silicon, the commercially predominant PV technology, that includes materials such as polysilicon and monocrystalline silicon. Second generation cells are thin film solar cells, that include amorphous silicon, CdTe and CIGS cells and are commercially significant in utility-scale photovoltaic power stations, building integrated photovoltaics or in small standalone power system. The third generation of solar cells includes a number of thin-film technologies often described as emerging photovoltaics most of them have not yet been commercially applied and are still in the research or development phase. Many use organic materials, often organometallic compounds as well as inorganic substances. Despite the fact that their efficiencies had been low and the stability of the absorber material was often too short for commercial applications, there is a lot of research invested into these technologies as they promise to achieve the goal of producing low-cost, high-efficient solar cells.

"First generation" panels include silicon solar cells. They are made from a single silicon crystal (mono-crystalline), or cut from a block of silicon that is made up of many crystals (multi-crystalline - shown at right).

"Second generation" thin-film solar cells are less expensive to produce than traditional silicon solar cells as they require a decreased amount of materials for construction. The thin-film PV cells are, just as the name implies, a physically thin technology that has been applied to photovoltaics. They are only slightly less efficient than other types but do require more surface area to generate the same amount of power [9]. Fig. 2.15 presents different materials used to make solar cells.

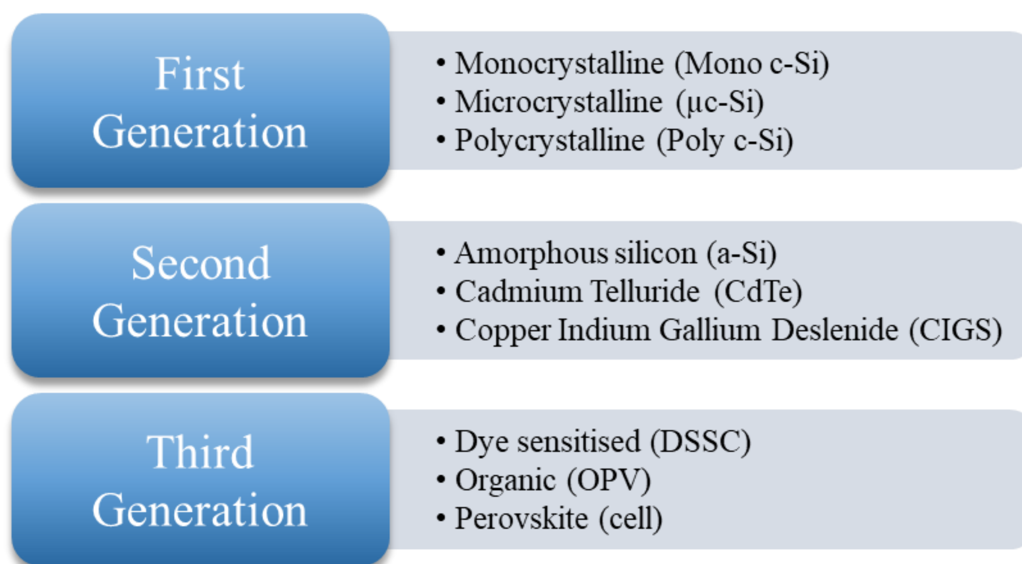

Figure 2.15 Classification of photovoltaic cells.

The following are the different types of solar cells.

2.8.1 Silicon PERL cell

Usually, short-circuit current losses come from metal-finger coverage of the top surface, top-surface reflection loss, and imperfect light trapping in the cell. The voltage losses arise from finite surface and bulk recombination. The fill factor losses come not only from ohmic series resistance loss within the cell, but also from the same factors producing the open circuit voltage loss. The silicon passivated emitter and rear locally diffused (PERL) cell shown in Fig. 2.16(a) is a solar cell design taking all those loss factors into account.

The cell has inverted pyramids on the top that are formed by using anisotropic etches to expose the slowly etching (111) crystallographic planes. The pyramids reduce reflections of light incident on the top surface, since incident light perpendicular to the cell will strike one of the inclined (111) planes obliquely and will be refracted obliquely into the cell. This enhanced light trapping reduces the short circuit current loss.

The cell is characterized by the use of a thin, thermally grown oxide to "passivate" (reduce the electronic activity of) the top surface of Si wafer for a junction diffusion. Then, a shallow, low-sheet-resistivity phosphorus diffusion n-layer is formed. The oxide passivation of the cell surfaces can improve the open-circuit voltage. It can also function as an antireflection coating with refractive index $\bar{n} = 1.46$ to further reduce the total reflection. The rear locally diffused region is formed in the area of the rear point contact.

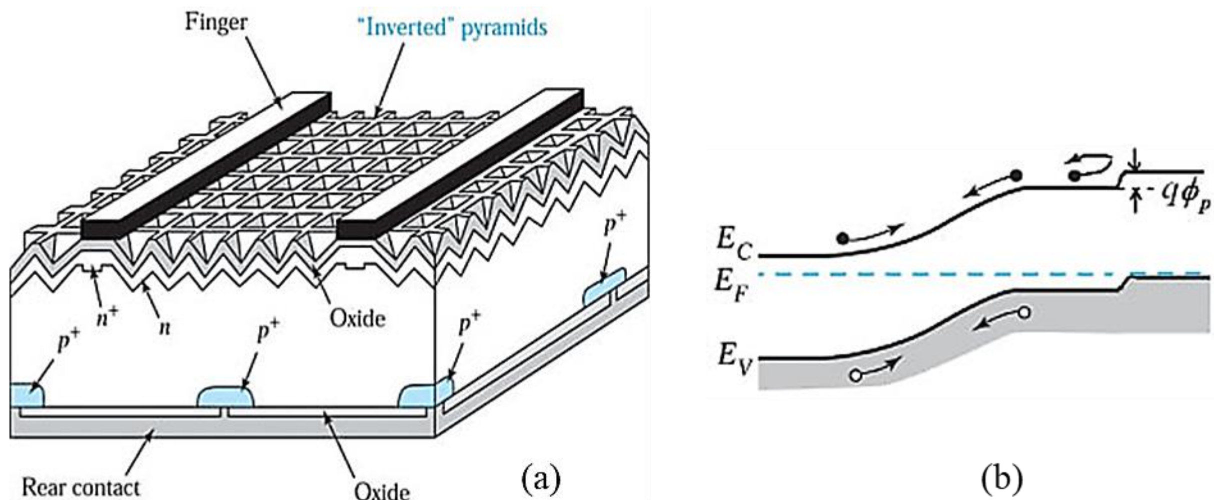

Figure 2.16 (a) Passivated emitter rear locally diffused (PERL) cell. (b) Energy-band diagram for the back-surface field.

The incorporation of a heavily doped layer under the back contact, a so-called "back surface field," is shown in Fig. 2.16(b). The potential energy $q\phi_p$ provides a minority carrier reflecting region between this contact and the substrate. The back surface field also results in a very small recombination velocity at the back. Therefore, the short circuit current will increase. The open circuit voltage is also increased due to the increased short circuit current. It also reduces the contact resistance and improves the fill factor. The rear contact is separated from the silicon by an intervening oxide layer. This gives much better rear reflection than an aluminum layer. To date, the PERL cell shows the highest conversion efficiency of 24.7%.

2.8.2 Cadmium telluride solar cell (CdTe)

Cadmium telluride (CdTe) photovoltaics describes a photovoltaic (PV) technology that is based on the use of cadmium telluride, a thin semiconductor layer designed to absorb and convert sunlight into electricity. Cadmium telluride PV is the only thin film technology with lower costs than conventional solar cells made of crystalline silicon in multi-kilowatt systems.

On a lifecycle basis, CdTe PV has the smallest carbon footprint, lowest water use and shortest energy payback time of all solar technologies. CdTe's energy payback time of less than a year enables for faster carbon reductions without short-term energy deficits. The toxicity of cadmium is an environmental concern mitigated by the recycling of CdTe modules at the end of their life time, though there are still uncertainties and the public opinion is skeptical towards this technology. The usage of rare materials may also become a limiting factor to the industrial scalability of CdTe technology in the mid-term future. The rare abundance of tellurium of which telluride is the anionic form—is comparable to that of platinum in the earth's crust and contributes significantly to the module's cost [9]. Figure 2.17 shows structure of CdTe solar cell.

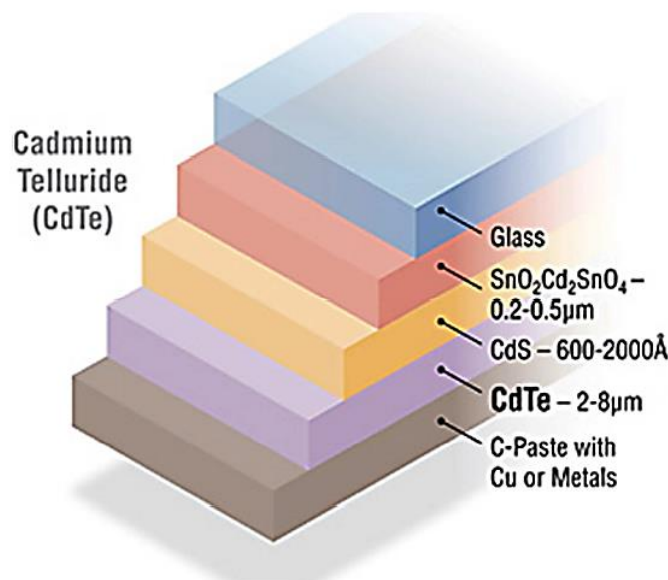

Figure 2.17 Graphic showing the five layers that comprise CdTe solar cells.

2.8.3 Copper Indium Gallium Selenide solar cells (CIGS)

One of the most interesting and controversial materials in solar is Copper-Indium-Gallium-Selenide, or CIGS for short. A copper indium gallium selenide solar cell (or CIGS cell, sometimes CI(G)S or CIS cell) is a thin film solar cell used to convert sunlight into electric power. They are manufactured by depositing a thin layer of copper, indium, gallium and

selenide on glass or plastic backing, along with electrodes on the front and back to collect current. Because the material has a high absorption coefficient and strongly absorbs sunlight, a much thinner film is required than of other semiconductor materials. Figure 2.18 shows structure of CIGS solar cell.

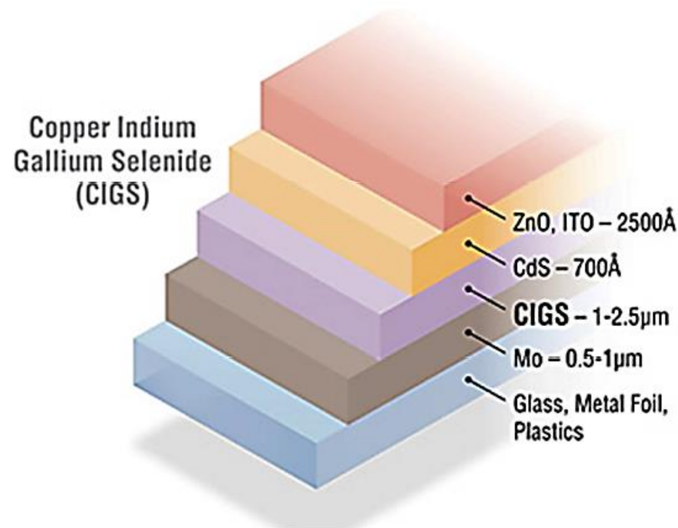

Figure 2.18 Graphic showing the five layers that comprise CIGS solar cells.

CIGS is one of three mainstream thin-film PV technologies, the other two being cadmium telluride and amorphous silicon. Like these materials, CIGS layers are thin enough to be flexible, allowing them to be deposited on flexible substrates. However, as all of these technologies normally use high-temperature deposition techniques, the best performance normally comes from cells deposited on glass. Even then the performance is marginal compared to modern polysilicon-based panels. Advances in low temperature deposition of CIGS cells have erased much of this performance difference. It is best known as the material for CIGS solar cells a thin-film technology used in the photovoltaic industry. In this role, CIGS has the advantage of being able to be deposited on flexible substrate materials, producing highly flexible, lightweight solar panels. Improvements in efficiency have made CIGS an established technology among alternative cell materials [9].

2.8.4 Dye-sensitized solar cells

The cell in Fig. 2.19(a) has a layer of transparent conductive oxide (TCO) [usually fluorine-doped tin oxide (SnO_2:F)] deposited on glass used as anode. On the conductive plate is a layer of titanium dioxide (TiO_2), formed into a highly porous 3-D Structure with an extremely high surface area for holding large numbers of dye molecules. The plate is then

immersed in a mixture of a photosensitive ruthenium-polypyridine dye solution. The dye molecules are quite small (nanometer sized). In order to capture a reasonable amount of the incoming light, the layer of dye molecules covalently bonded on highly porous 3-D nano-structured TiO_2 surface needs to be fairly thick. A separate backing is made with a thin layer of the iodide/iodine electrolyte spread over a conductive platinum sheet [1].

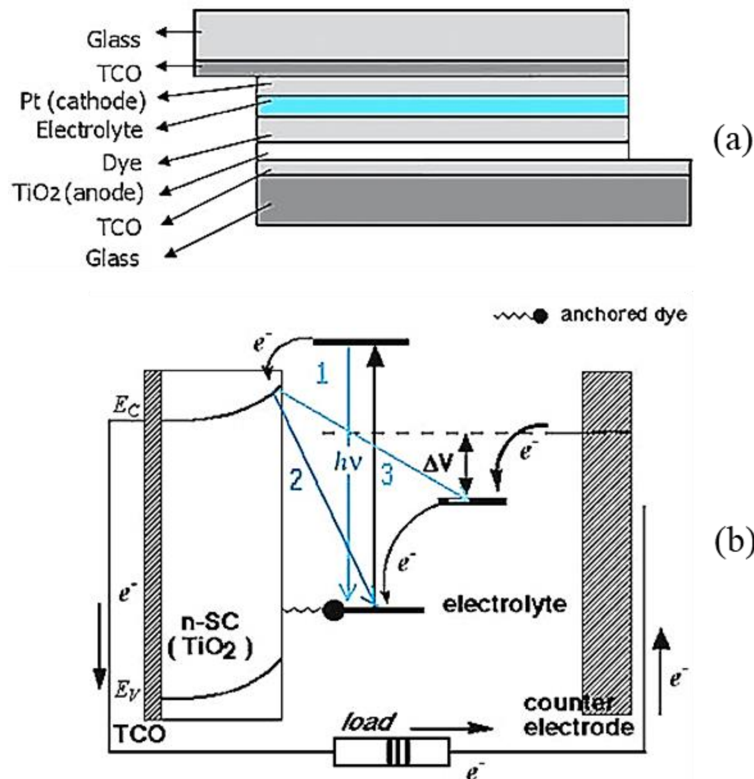

Figure 2.19 (a) DSSC cell structure. (b) Energy band diagram and main carrier losses.

The bulk of the semiconductor (TiO_2) is used solely for charge transport; the photoelectrons are provided from a separate photosensitive dye. Charge separation occurs at the surfaces between the dye, semiconductor, and electron in the conduction band has a probability to go back to valence band of the dye as the loss path 1. The excited electron can be injected directly into the conduction band of the TiO_2, and from there it moves by diffusion to the anode. Meanwhile, the dye molecule strips one electron from iodide in electrolyte, oxidizing it into triiodide. This reaction occurs quite quickly compared to the time for the injected electron to recombine with the oxidized dye molecule, which is the loss path 2 shown in Fig. 2.19(b). The triiodide then recovers its missing electron by diffusing to the counter-electrode, which

reintroduces the electrons after flowing through the external circuit. The third loss is from the recombination of injected electron with the electrolyte (path 3).

The dye is highly efficient in converting photons into electrons, but only those electrons with enough energy can cross the TiO_2 bandgap and result in photocurrent. DSSCs offer slightly higher V_{oc} than the silicon solar cell (about 0.6 V). The fill factor is about 70%, and the quantum efficiency is about 11% [1].

2.8.5 Organic Solar Cells

Carrier mobilities are very low because their transport processes are dominated by carrier hopping in organic semiconductors. However, organic semiconductors show strong absorption in UV and visible regions and the penetration depth of the incident light is typically 80-200 nm. Thus, only a 100 nm thick organic active layer is sufficient for effective absorption. Currently, the power conversion efficiency is only 5.7 % but organic solar cells attract high interest due to their large-area, low-cost potential.

Solar cells with a heterojunction between donor and acceptor molecules can efficiently dissociate

photogenerated excitons into free carriers at the interface and exhibit superior performances. After photoexcitation of an electron from the HOMO to the LUMO shown in Fig. 2.20, the electron can jump from the LUMO of the donor (with the higher LUMO) to the LUMO of the acceptor if the potential difference $\Delta\Phi$ between the ionization potential of the donor and the electron affinity of the acceptor is larger than the exciton binding energy. However, this process of so-called photo-induced charge transfer can lead to free charges only if the hole remains on the donor with the higher HOMO level [1].

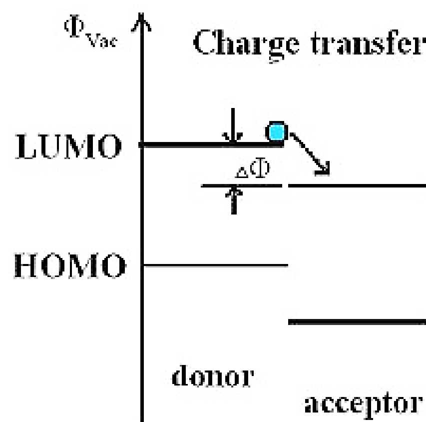

Figure 2.20 Heterojunction between donor and acceptor facilitates charge transfer by splitting the exciton.

Moreover, the space between donor and acceptor should be in the range of the exciton diffusion length for efficient transfer and dissociation. A heterojunction can be prepared with donor and acceptor bilayers shown in Fig. 2.21(a). This bilayer geometry guarantees directional photoinduced charge transfer across the interface, and the recombination losses are reduced. However, the interfacial area and thus the exciton dissociation efficiency are limited. Higher interfacial area and thus the improved exciton dissociation efficiency can be achieved if a mixture layer contains both electron donor and electron acceptor (so-called bulk heterojunctions) shown in Fig. 2.21(b), but needs a percolating pathway for the separated charge carriers to reach their corresponding electrodes. Both approaches can be carried out either by sublimation of small molecules or by spincoating of polymers [1].

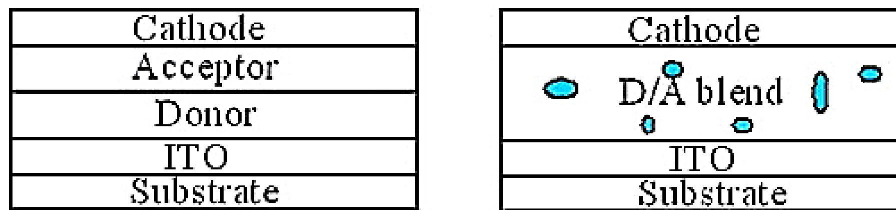

Figure 2.21 (a) Bilayer and (b) bulk heterojunction solar cells.

2.8.6 Best research cell efficiencies

Figure 2.22 shows us the conversion efficiencies of the best research solar cells worldwide from 1976 through 2020 for various photovoltaic technologies; efficiencies determined by certified agencies/laboratories [10].

Cell efficiency results are provided within different families of semiconductors: (1) multijunction cells, (2) single-junction gallium arsenide cells, (3) crystalline silicon cells, (4) thin-film technologies, and (5) emerging photovoltaics. Some 26 different subcategories are indicated by distinctive colored symbols.

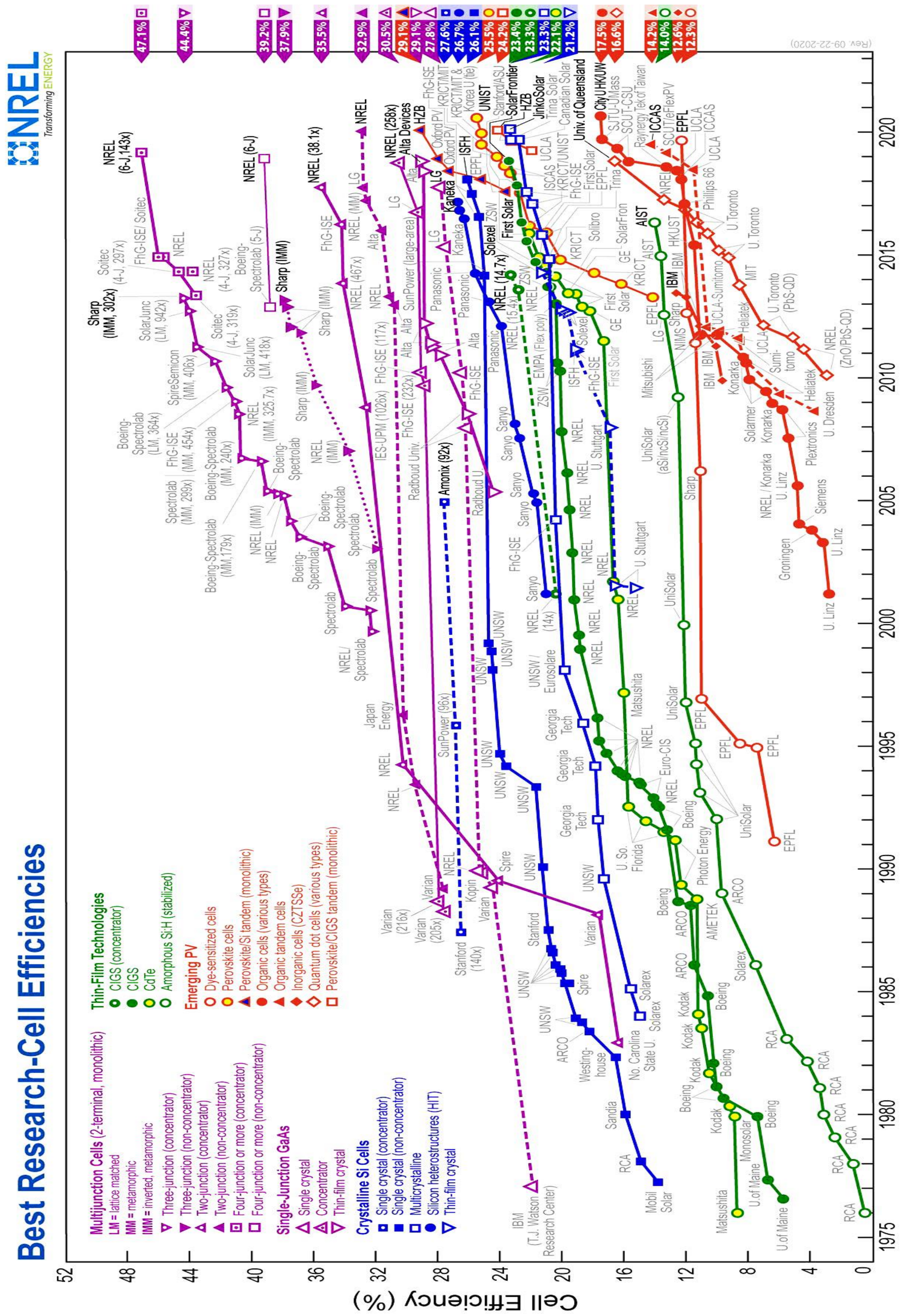

Figure 2.22 Timeline for best research and efficiencies for different solar cells reported so far.

2.9 Tandem device classifications

Multi-junction solar cells have their advantages for efficiently absorbing a wider range of the solar spectrum. For optimal absorption, p–n junctions with a higher band-gap are stacked on top of those with a lower bandgap. The multiple p–n junctions are electrically connected via tunnel junctions or a shared electrode, resulting in a series electrical connection.

There are several types of tandem solar cells depending on the fabrication sequence and interconnection scheme used. They classify them as type A and B based on the number of transparent conductive electrodes (TCEs) and the number of their contact terminals that ranges from two to four [11].

Type A tandem is a monolithic series interconnected device grown on a single substrate that employs one TCE (Fig. 2.23), which implies that it is a two-terminal (2-T) tandem device. This is the configuration almost exclusively used in commercial products because it involves a minimum number of processing steps, substrates, layers and interconnections. Because these are essentially two back to front solar cells monolithically stacked on top of one another, the performance of the tandem relies on the efficiency of the charge transport layer at the interface between the two solar cell components [11].

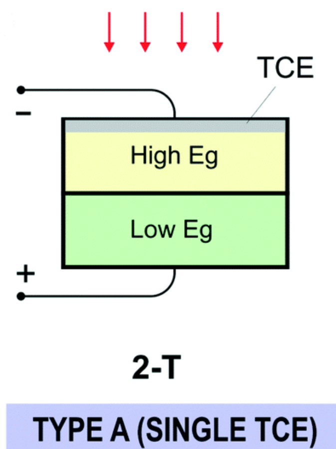

Figure 2.23 Type A of tandem solar cell device with single TCE and two-terminal monolithic.

Type B tandem solar cells (Fig. 2.24(a–c)) use additional transparent conductive layers and substrates; this type includes a 2-T (two terminal) mechanically stacked device, 3-T, and 4-T tandems. This way the individual devices from the stack can be fabricated independently, thereby also significantly expanding the processing tolerance window as well as simplifying the full device characterization [11].

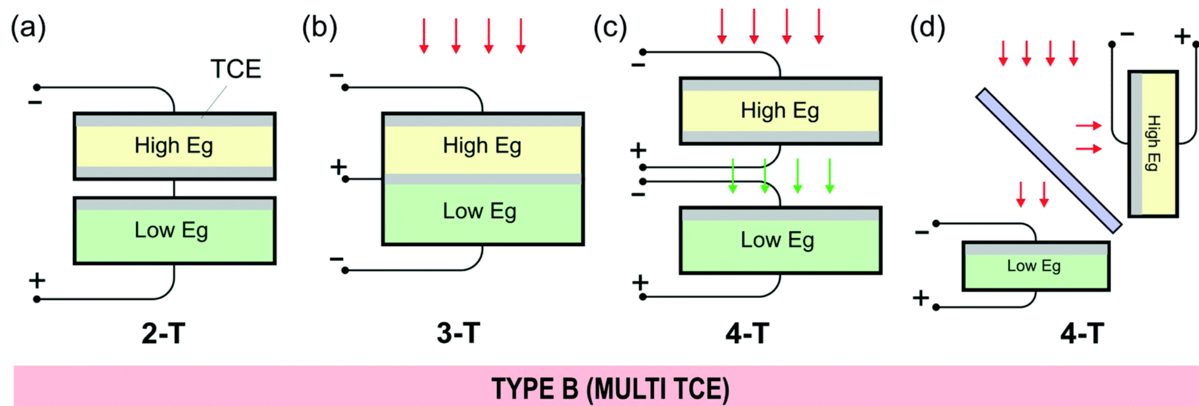

Figure 2.24 Type B of tandem solar cell device with multiple TCEs and terminal connections: (a) two-terminal mechanically stacked, (b) 3-terminal monolithic stacked, (c) 4-terminal mechanically stacked and (d) 4-terminal spectrum-split.

While the type B tandem is convenient for research and feasibility demonstration purposes, it is impractical for large scale manufacturing. The single transparent TCE layer is one of the most critical components for large-scale applications from both a manufacturing and a performance perspective. Research and development of type A solar cell is extremely challenging because it requires compatibility of every processing step with all preceding layers and interfaces as well as precise optical and current matching between individual devices. Naturally, type B is the configuration of choice for most research focused on non-traditional tandem solar cell concepts [11].

2.9.1 Type A/two-terminal monolithic stack

As described in the introduction, this tandem device is constructed from a monolithically integrated bottom and top cell with a single transparent conductive layer. A recombination or tunneling layer is formed between the two devices. The main electrical limitation in these devices is the current matching condition i.e. the performance of the device is limited by the cell with the lowest current. However, this architecture is attractive in terms of simplicity for commercial deployment as only two terminals are required and a monolithic series interconnection of narrow device architectures on a single substrate is feasible with the standard scribing technology thus reducing the series resistance losses associated with large-area modules [11].

2.9.2 Type B/two-terminal mechanically-stacked

The tandem device is constructed as a stack of two separate top and bottom cells but they are serially connected with two terminal output. This type of tandem has the advantage where the need for interfacial tunneling is eliminated and the current matching condition can be relaxed by adjusting different areas of the solar cell. However, these devices require as many as three TCE layers and thus impose severe optical losses [11].

2.9.3 Type B/three-terminal monolithic stack

Similar to the two-terminal tandem, the device is constructed from a monolithically integrated bottom and top cell however, a third intermediate terminal is provided. This terminal adds another degree of freedom in the electrical connection to relieve the circuit from the current matching condition. This can be done by adding a matching resistive load to either the top or bottom cell. This type of device is not frequently explored (for the reason explained in the next section) but nevertheless they have been demonstrated in a tandem a-Si solar cell, GaAsP/SiGe device and polymer solar cell [11].

2.9.4 Type B/four-terminal mechanically stacked

The tandem device is constructed from two separately developed cells that allow a fabrication process that yields optimum performance. However, bifacial transparent electrodes are needed on the top cell to allow some light transmission to the bottom cell. Each cell produces independent electrical output thus requiring 4 terminal connections. While efficiency can be maximized, the interconnection and module integration could become more costly. A recent example of this type of perovskite tandem device has reached an efficiency of 25.2% and 18.6% with perovskite–silicon and perovskite–CIGS tandem, respectively [11].

2.9.5 Type B/four-terminal spectrum split

This architecture is essentially still a four terminal device; however, a dichroic filter is used to split the light spectrum. This system offers advantages in terms of flexibility of individual device fabrication i.e. each device can be optimized as if it operates as a stand-alone solar cell and only requires two TCEs (instead of three as in the standard 4-T tandem) thus reducing the optical loss. However, the added cost of filter and four terminals limits the commercial potential of this architecture. An example of this type of tandem has been demonstrated by Uzu et al. with an impressive total potential efficiency of 28.0% [11].

2.10 Principle of the two-terminal tandem cell

The principle of the dual-junction stacked cell or tandem cell is presented in Fig. 2.25

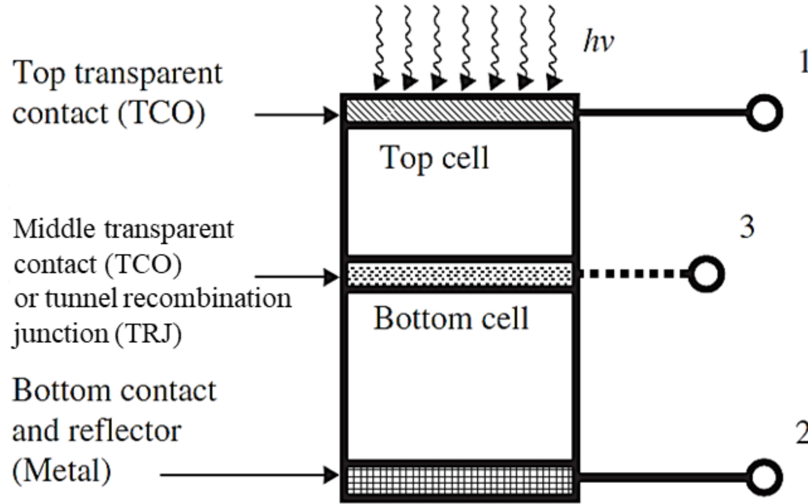

Figure 2.25 Principle of the dual-junction stacked cell or tandem cell.

In a two-terminal tandem cell, both the top sub-cell and the bottom sub-cell are electrically in series. If we use the following symbols [12]:

J_{top}, V_{top} top sub-cell current density and voltage.

J_{bottom}, V_{bottom} bottom sub-cell current density and voltage.

J_{tandem}, V_{tandem} tandem cell current density and voltage.

we will then have:

$$J_{\text{tandem}} = J_{\text{top}} = J_{\text{bottom}} \tag{2.39}$$

$$V_{\text{tandem}} = V_{\text{top}} + V_{\text{bottom}} \tag{2.40}$$

The construction of the corresponding diagram for $J_{tandem}(V_{tandem})$ is shown in Figure 2.26. It is easy to convince oneself from this figure that:

$$J_{sc\ \text{tandem}} \approx \text{Min}\left\{J_{sc\ \text{top}}, J_{sc\ \text{bottom}}\right\} \tag{2.41}$$

$$V_{oc\ \text{tandem}} \approx V_{oc\ \text{top}} + V_{oc\ \text{bottom}} \tag{2.42}$$

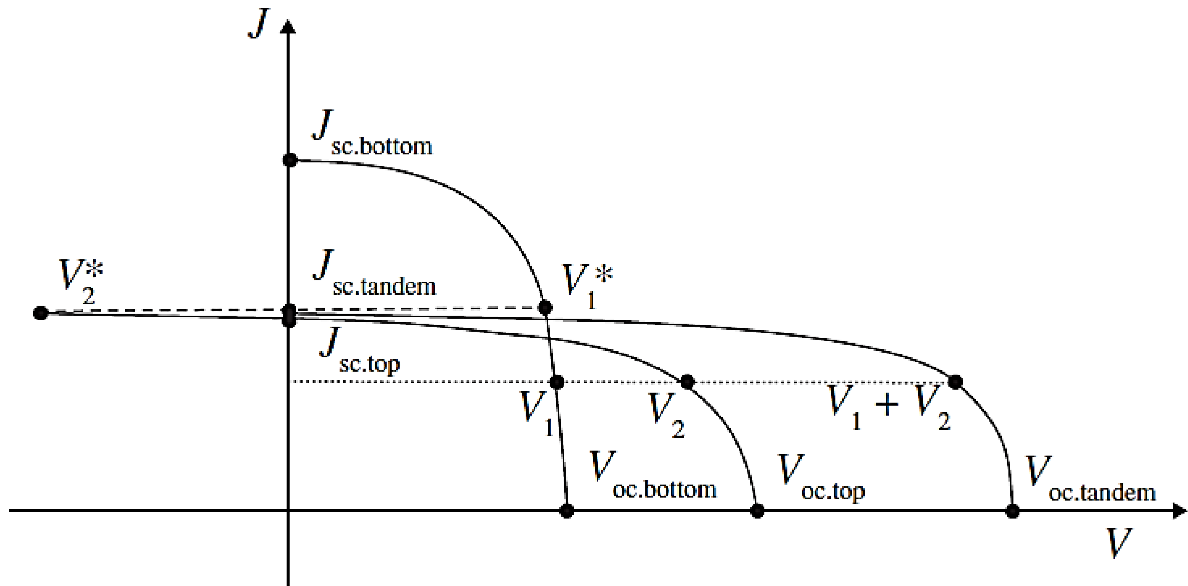

Figure 2.26 Construction of the *J-V* diagram for a two-terminal tandem solar cell. The short circuit current density of the tandem is slightly higher than the short-current density of the top sub-cell. Actually, it corresponds to the current density of the top sub-cell in a reverse voltage condition.

Equation 2.39 leads to the *current-matching condition*; for optimal performance one should have:

$$J_{sc\ \mathrm{top}} \approx J_{sc\ \mathrm{bottom}} \tag{2.43}$$

If, on the other hand, there is a large difference between $J_{sc.top}$ and $J_{sc.bottom}$, the short-circuit current density of the tandem will be given by the smaller of the 2 short circuit current densities of the sub-cells. The sub-cell with the higher short- circuit current density will then not be using its full current potential [12].

The fill factor *FF* of the tandem cell merits a special comment. If we do have current-matching, the *FF* may be considered to lie within the fill factors of the top and of the bottom sub-cells. However, if the currents are not matched, the *FF* of the tandem is very often quite a bit higher. On the other hand, we will, by such a current mismatch, certainly be losing more in current than we will be gaining in *FF*, so that it is not worthwhile to try to obtain mismatch conditions when attempting to increase tandem cell efficiency [12].

2.11 Recombination tunnel junction

In Figure 2.27, the detailed structure of a thin-film silicon tandem solar cell is shown for the superstrate configuration. We can see that current continuity between the two sub-cells can only be maintained when electrons which exit from the *n*-layer on the bottom part of the top sub-cell recombine with holes exiting from the *p*-layer, or top layer of the bottom sub-cell. This means practically that it is advantageous to include, between the two sub-cells, a highly doped and very thin layer (*n*- or *p*-layer) with enhanced recombination, i.e. with a large density of "midgap defects" or "dangling bonds". If this layer is too thick, it will lead to optical losses by absorption.

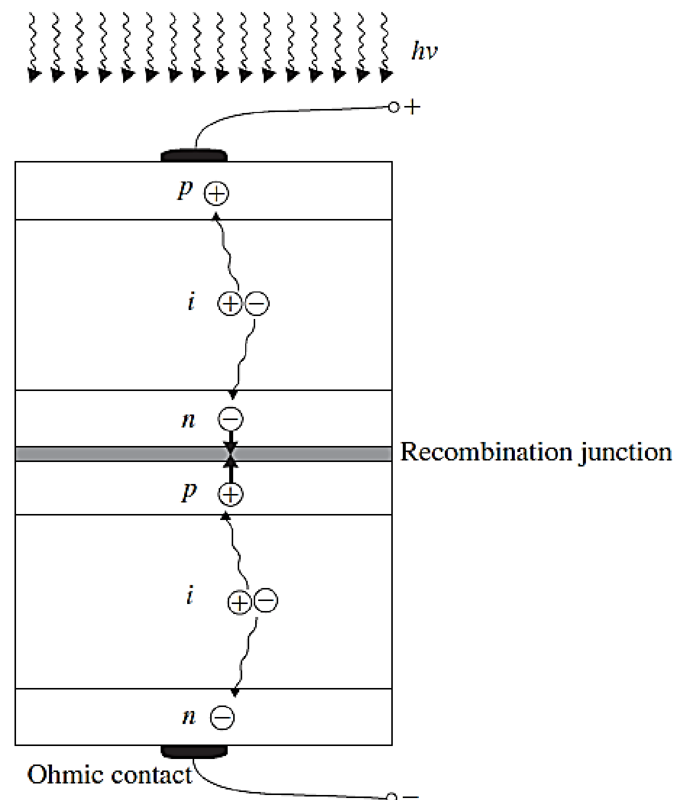

Figure 2.27 Principle of current continuity between top and bottom sub-cells for a two-terminal tandem solar cell, shown here for the example of two *pin*-type sub-cells. The current continuity condition requires that the total flux of electrons or holes exiting from one of the sub-cells has to recombine with the total flux of carriers (of opposite polarity) exiting from the other sub-cell. This requirement is valid for all types of two-terminal tandem cells, i.e. for *pin*-type and *pn*-type cells, and for both the superstrate (*pin*) and the substrate (*nip*) configurations.

In order for the electrons from the *n*-layer of the top sub-cell to recombine with the holes from the *p*-layer of the bottom sub-cell, (at least) one of the two charge carriers should be transported to the zone where the other type of carriers is in majority. With the help of tunneling, this transport can be enhanced. Tunneling becomes possible when the corresponding layer is heavily doped, i.e. when the Fermi level E_F is shifted very near to the band edge. Such a shift is easier to obtain for microcrystalline silicon layers than for amorphous silicon layers. For this reason, at least one of the doped layers which form the tunnel/recombination junction within a thin-film silicon tandem solar cell should be microcrystalline (and not amorphous) [12].

2.12 Thin-film silicon solar cell structures

2.12.1 Amorphous silicon solar cells

In a-Si:H, the diffusion length of the charge carriers is much shorter than in crystalline silicon. In device quality intrinsic a-Si:H the diffusion length ranges from 0.1 to 0.3 μm. In doped a-Si:H layers, in which the defect density due to doping is two or three orders of magnitude higher than in intrinsic a-Si:H, the diffusion length of the minority carriers is even lower. A solar cell structure based on the transport of the minority carriers in the quasi-neutral regions of the p-n junction as in the case of crystalline silicon does not work for a-Si:H. Due to the very short diffusion length the photogenerated carriers would virtually all recombine in the doped a-Si:H layers before reaching the depletion region of the p-n junction. Therefore, an a-Si:H solar cell is designed differently compared to the standard p-n junction of a crystalline silicon cell [13].

A schematic structure of a single junction a-Si:H solar cell is shown in Figure 2.28. The active device consists of three principal layers: p type a-SiC:H layer, intrinsic a-Si:H layer, and n type a-Si:H layer, which form a p-i-n junction. This structure is called the single junction a-Si:H solar cell. The doped layers are usually very thin: a p type a-SiC:H layer is ∼10 nm thick, and an n type a-Si:H is ∼20 nm thick. The doped layers have two functions in an a-Si:H solar cell. First, they set up an internal electric field across the intrinsic a-Si:H layer. The electric field should be high enough to ensure that the photogenerated carriers in the intrinsic a-Si:H layer are collected. The strength of the electric field depends on the doping level in the doped layers and the thickness of the intrinsic layer. Second, the doped layers establish low loss ohmic electrical contacts between the a-Si:H part of the solar cell and the external electrodes. Therefore, a sufficiently high electrical conductivity is required for both p and n type layers in order to form a high built-in voltage across the p-i-n function and low resistance contacts with the electrodes. The intrinsic layer with an optical bandgap of about 1.75 eV serves as an

'absorber' layer. The electron–hole pairs that are generated in the absorber layer experience the internal electric field, which facilitates separation of electrons and holes. The material quality of the intrinsic layer and the strength and profile of the internal electric field determine the collection of the photogenerated charge carriers and thus the solar cell performance. The electric field profile in the absorber layer strongly depends on the defect density and its distribution in the bulk of the intrinsic layer and at the interfaces with the doped layers. The photogenerated carriers move towards the doped layers (electrons towards the n type layer and holes towards the p type layer) and are collected by the electrodes [13].

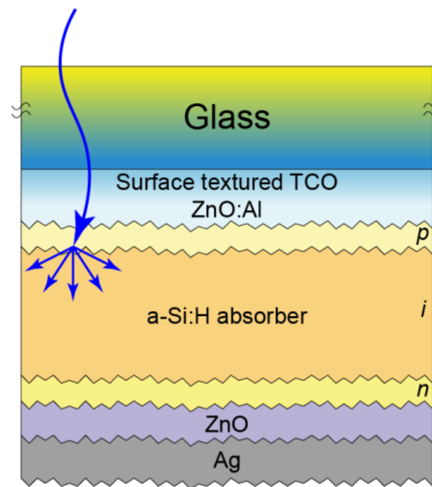

Figure 2.28 A single junction p-i-n a-Si solar cell structure.

The dominant transport mechanism of the photogenerated carriers is drift in the internal electric field, and therefore, an a-Si:H solar cell is often denoted in the literature as a drift device. Determining the optimal thickness of the intrinsic a-Si:H layer in the solar cell is the crucial part of the solar cell structure design. The thickness of the intrinsic layer is a delicate trade-off between the absorption, which is higher in a thicker layer, and the collection, which improves when the layer gets thinner. Since the collection depends on the drift of the photogenerated carriers in the internal electric field, it is the magnitude of the electric field across the intrinsic layer and the mobility and lifetime of the carriers that determine the collection.

However, the electric field is not uniform across the intrinsic layer but strongly depends on the distribution of the space charge in this layer. The space charge in this intrinsic a-Si:H layer, resulting from trapped carriers in the gap states, cannot be neglected as is often possible in crystalline silicon solar cells. Due to the large density of the localized states in the bandgap,

the charge trapped in these states substantially contributes to the overall charge in the device and determines the electric field profile. The presence of large defect densities at the interfaces with the doped layers can lead to a strong electric field in these interface regions, while in the bulk of the intrinsic layer, the electric field is relatively low [13].

2.12.2 Technology of amorphous Si solar cell

Amorphous silicon (a-Si) thin films can be deposited directly on low-cost large-area substrates. In amorphous silicon, the distribution of bond lengths and bond angles disturb the long-range order of the crystalline silicon lattice and change the optical and electronic properties. The optical energy gap increases from 1.12 eV of single crystalline silicon to about 1.7 eV. The apparent optical absorption is nearly an order of magnitude higher than in the crystalline material.

The basic cell structure for a series interconnected a-Si solar cells is shown in Fig. 2.29. A layer of SiO_2 followed by a transparent conducting layer of a large bandgap, degenerately doped semiconductor such as SnO_2 is deposited onto a glass substrate and patterned using a laser. The substrate is then coated by a p-i-n junction stack of amorphous silicon by the decomposition of silane in a radio-frequency plasma-discharge system. After deposition, the a-Si layers are patterned by a laser system. A layer of aluminum is sputtered onto the rest of the silicon and this layer is also patterned by laser. This technique forms a series of interconnected cells, as shown in Fig. 2.29. The cell has the lowest manufacturing cost but a modest efficiency of 6% [1].

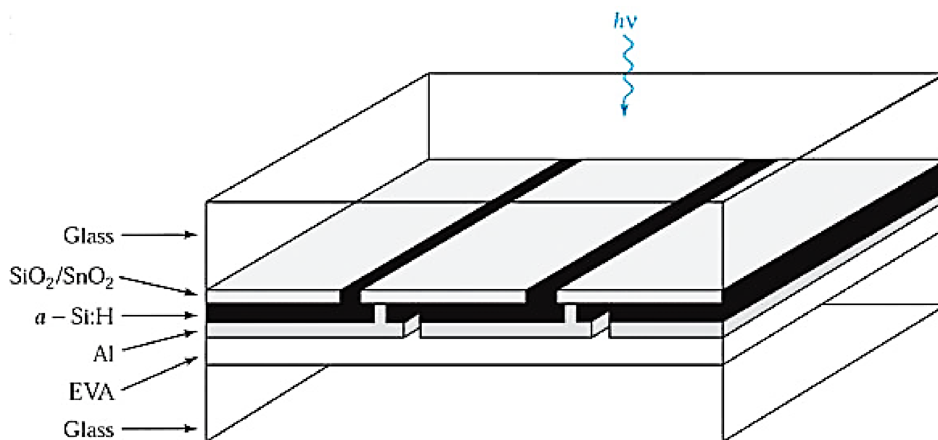

Figure 2.29 Series-interconnected a-Si solar cells deposited on a glass substrate with a rear glass cover bonded using ethylene vinyl acetate (EVA).

The amorphous silicon obtained by this process is incorporated with a fairly large concentration of hydrogen. The hydrogen atoms tie up dangling silicon bonds and decrease the density of localized states in the energy gap. These localized states play a dominate role in determining the carrier transport properties of amorphous silicon. The typical deposition temperature is below 300 °C, otherwise no hydrogen is incorporated in the film.

In larger outdoor "power" modules, the beneficial effect of the hydrogen upon the amorphous-Si properties deteriorates under illumination. A steady drop of output efficiency occurs over the first few months. The stability problem is caused by the so called "Staebler-Wronski" degradation, the illumination by light with photon energies larger than the energy gap leads to new light-induced defect states. After that, the output stabilizes. Amorphous-Si based modules are generally rated by manufacturers in terms of such "stabilized" output. An improvement in efficiency can be achieved by utilizing tandem cells [1].

2.12.3 Microcrystalline silicon solar cells

Microcrystalline silicon solar cells formed by plasma CVD at low temperatures are assumed to have a shorter lifetime than single-crystal cells, and it is common to employ a p-i-n structure including an internal electric field in the same way as in amorphous solar cell. A p-i-n type microcrystalline silicon solar cell is formed by a process fairly similar to that of an amorphous solar cell. Strictly speaking, these cells can be divided into p-i-n and n-i-p types according to the film deposition order, although the window layer of the solar cell is the p-type layer in both cases.

The characteristics of a cell having a p-i-n structure were first reported by workers at Neuchiitel University. Unlike an amorphous solar cell, this cell does not deteriorate when exposed to light. The very first reports on the characteristics of an n-i-p cell were made by the Kaneka PV Research Division using the light trapping structure described below. These cells had an intrinsic conversion efficiency of 10.7% and an apparent efficiency of 10.1% for a film thickness of 2 μm (surface area 1 cm^2, measured by the Japan Quality Assurance Organization (JQA)) (Figure 2.30). Also, by subjecting the silicon film in the photoelectric layer of this cell to X-ray diffraction (XRD) measurements, it was found to have a preferential (110) orientation. The p-i-n and n-i-p cells have different characteristics due to their different fabrication sequences. A large difference is that the underlying layer of a p-i-n cell is the transparent electrode, whereas the underlying layer of a n-i-p cell is the back electrode.

As a general rule, transparent electrodes are made of oxides, and since there is a risk of these oxides being reduced by the hydrogen atoms that are needed to form microcrystalline

cells, there is a smaller process window in the cell formation conditions for the p-i-n type. From the viewpoint of the ease with which integrated structures can be formed, which is a characteristic of thin-film solar cells, an advantage of p-i-n cells is that they can be formed as superstrate modules using integration techniques similar to those used for amorphous silicon. Furthermore, it should be possible to make integrated structures of n-i-p cells by methods equivalent to those used for $Cu(InGa)Se_2$-based solar cells. At the present time, it is difficult to determine which is better, but it should become possible to arrive at a conclusion in terms of cost, performance and applications through the production of sub-modules in the future [8].

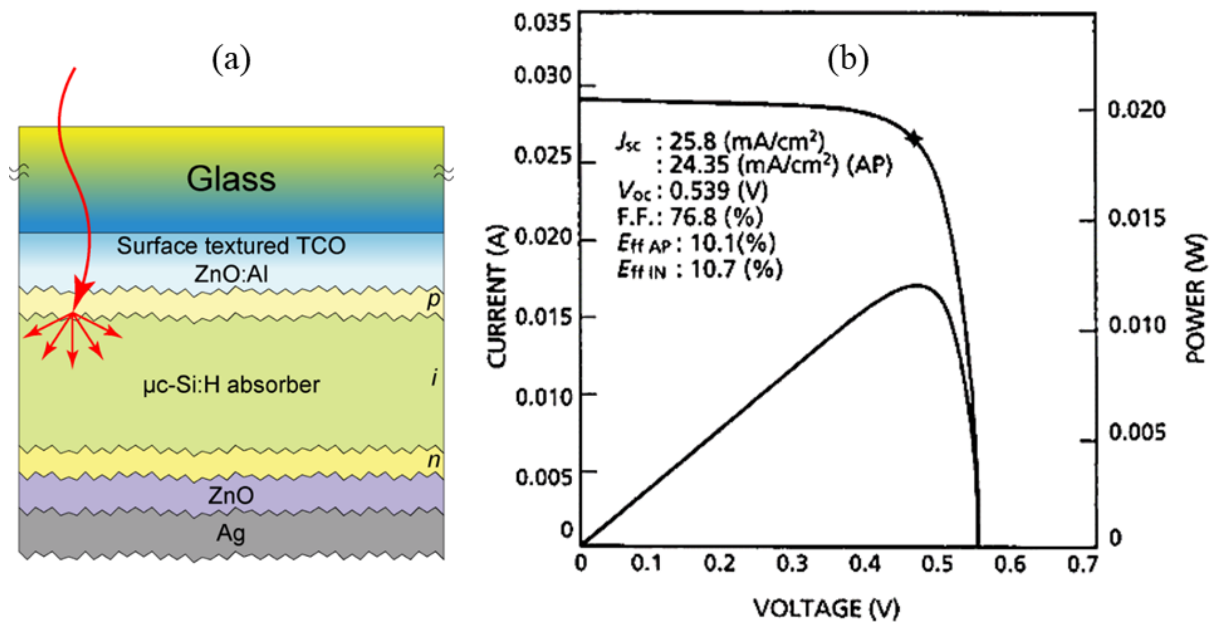

Figure 2.30 (a) Structure of a μc-Si:H solar cell, (b) Current-voltage characteristics of an n-i-p type microcrystalline silicon cell.

2.12.4 Multijunction solar cells

Because the solar spectrum is very wide from the ultraviolet to infrared, it is obvious that a semiconductor with a given bandgap cannot effectively use all of the solar energy. The photons with energy smaller than the bandgap cannot be absorbed, while the photons with energy higher than the bandgap can only use the part of energy equal to the bandgap and lose the portion of energy larger than the bandgap by thermal relaxation. Multijunction solar cells with different bandgaps in the component cells can resolve this issue with the wide bandgap

top cell absorbing the short wavelength photons, the middle cell absorbing the middle wavelength photons, and the bottom cell for the long wavelength ones [14].

The design and fabrication of multijunction solar cells are much more complicated than single-junction solar cells. First, additional attentions must be paid to the current matching because the Jsc of a multijunction solar cell takes the smallest photocurrent density among the individual component cells. A proper design, the component cell thicknesses, and selection of the bandgap of the absorber layers in each component cell should be optimized to give the desired current matching for the best stable efficiency [15].

In the ideal condition with no losses at the contacts, the voltage of the multijunction cell equals to the sum of the voltages of the subcells; the photocurrent takes the smaller one. One principle of designing multijunction solar cell is to have the component cell with the highest FF and the lowest light-induced degradation as the limiting cell (the smallest current density), which not only leads to a high initial efficiency but also an improved stability. Second, another important element in multijunction solar cells is the connection between two solar cells, where the n-layer of the top cell is directly deposited on the p-layer of the bottom cell, which is an invert n/p junction respecting to the main n-i-p junctions. The photo-electrons from the top cell need to recombine with the photoholes from the bottom cell to form a continuous current. Because the electrons and holes need to tunnel through a certain distance to meet each other, the n/p junction connecting the top and bottom cells is also called recombination tunnel-junction. If the carriers cannot tunnel into the opposite side, they accumulate in the n/p junction, cause a photo-voltage opposite to the main photo-voltage, and reduce the cell performance [14]. The connections between individual component cells need to be optimized to minimize the losses at the connection. A good tunnel-junction should have a minimum voltage loss for high V_{oc} and a low resistance for good FF. But as expected the multijunction solar cells provide higher efficiency than single-junction solar cells [15].

2.12.4.1 a-Si:H based double junction solar cells

Micromorph cells are thin film solar cells based on a multijunction architecture consisting of two solar cells that are stacked on top of each other. While the thin amorphous silicon top cell absorbs the blue light, the thicker microcrystalline silicon bottom cell absorbs the red and near infrared light, allowing this so-called tandem cell to cover a wider range of the solar spectrum. “Micromorph” tandem solar cells consisting of a microcrystalline silicon bottom cell and an amorphous silicon top cell are considered as one of the most promising new thin-film silicon solar-cell concepts. Their promise lies in the hope of simultaneously achieving

high conversion efficiencies at relatively low manufacturing costs. Since the bandgaps of amorphous Silicon (1.7eV) and microcrystalline Silicon (1.1eV) are well suited for tandem solar cells. One reason of the low costs of silicon thin film solar cells is its very low thickness (2 µm) compared to silicon wafer (200 µm). In the red and infrared wavelength range 2 µm of silicon are not enough to absorb all light and therefore light trapping is needed [9].

The structure shown in Fig. 2.31 consists of a microcrystalline bottom cell and a conventional amorphous top cell in tandem solar cell. The short-wavelength light is absorbed by the top amorphous cell and long-wavelength light is absorbed by the bottom microcrystalline cell. For micromorph tandem cell (of area 1.05cm^2) with a conversion efficiency of 11.5% is developed by TELSolar Lab SA [16] and tandem cells (a-Si:H/µc-Si:H) of conversion efficiencies of 12.63% and 12.69% are developed respectively by EPFL, Neuchâtel [17] and AIST, Tsukuba [18].

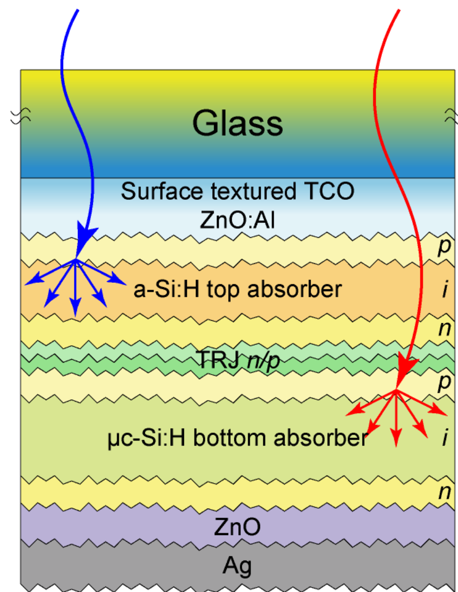

Figure 2.31 Schematic structure of a microcrystalline/ amorphous tandem cell.

2.12.4.2 a-Si:H based triple junction solar cells

The a-Si:H/a-SiGe:H/a-SiGe:H triple-junction solar cell has been studied since 1980s in Energy Conversion Devices, Inc. Similar to the double-junction solar cells, the a-Si:H/a-SiGe:H/a-SiGe:H triple-junction structure is deposited on SS/Ag/ZnO substrate (Figure 2.32 (a)). Figure 2.32 (b) shows the J-V characteristics curve of record efficiency solar cell. First, the triple-junction solar cell can use the wide solar spectrum effectively, which covers the wide range of 300–950 nm; second, the FF of the triple junction solar cell is much higher than single-

junction and double-junction solar cells because the current mismatch improves the FF. The a-Si:H top cell has less defect density than the a-SiGe:H middle and bottom cells, therefore, an optimized cell structure should be designed with a thin top cell such that the top cell is the current-limiting cell to achieve a high FF in the triple-junction structure. The a-Si:H/a-SiGe:H/a-SiGe:H triple-junction solar cell structure not only yields the highest efficiency, but also has the best stability [14].

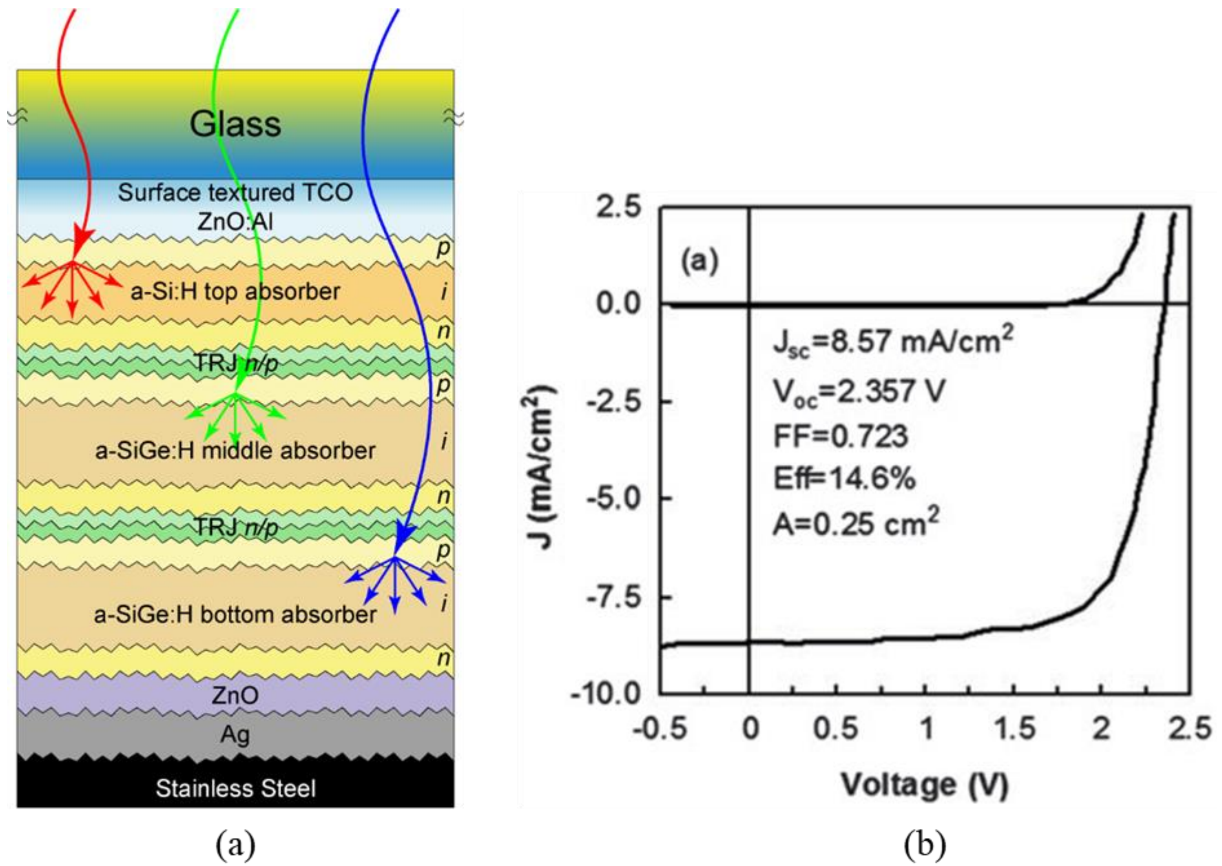

Figure 2.32 (a) Schematic structure of the a-Si:H/a-SiGe:H/a-SiGe:H triple-junction solar cell, (b) J-V characteristics of the a-Si:H/a-SiGe:H/a-SiGe:H triple-junction solar cell with an initial efficiency of 14.6% [19].

The advantage of μc-Si:H over a-Si:H and a-SiGe:H as the absorber layer in solar cells is the extended absorption spectrum to the long wavelength for high photocurrent. Using μc-Si:H as the middle and bottom cells in multijunction solar cells can absorb the sun light in a wide range and achieve high solar cell efficiency. Over the years, several multijunction solar cell structures have been extensively studied. For example, Fig. 2.33 shows the commonly used p-i-n multijunction solar cells [15].

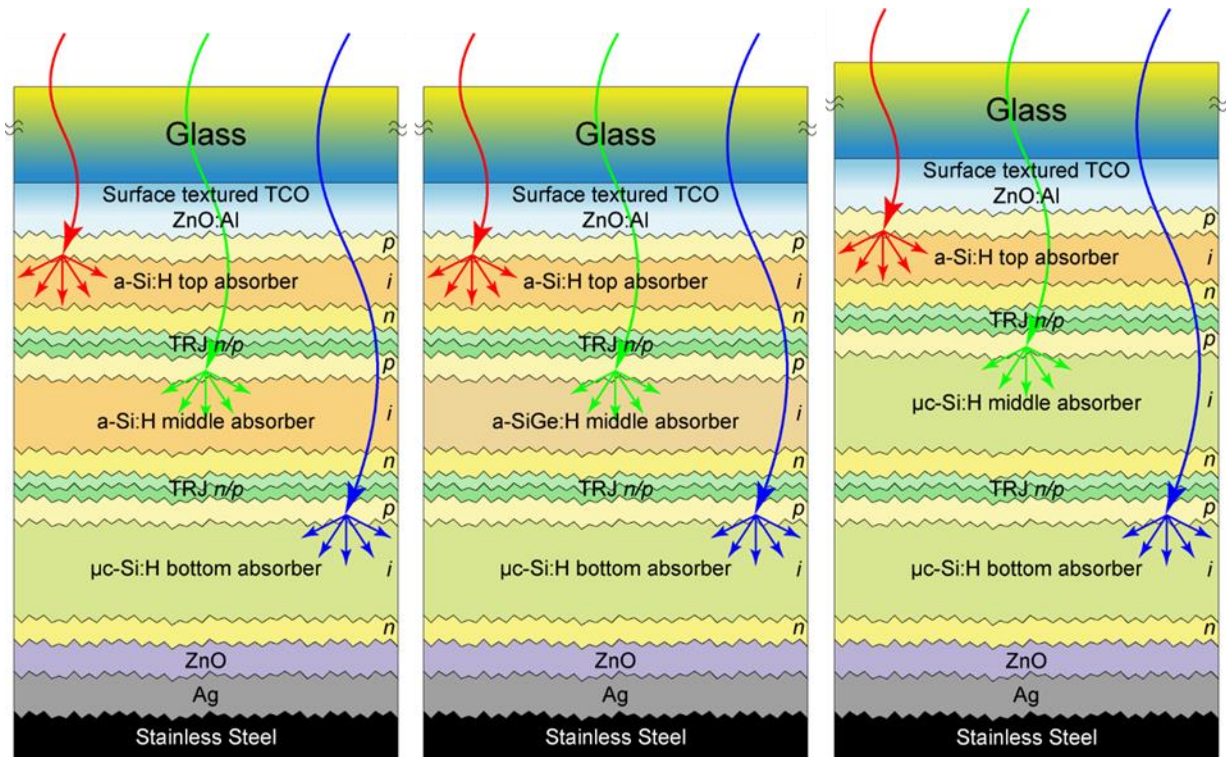

Figure 2.33 Schematics of p-i-n multijunction solar cells with µc-Si:H in the bottom cell.

The highest initial efficiency for thin film silicon solar cells is 16.3% achieved using an a-Si:H/a-SiGe:H/µc-Si:H triple-junction structure with the J-V characteristics and EQE curves in Fig. 2.34 [20].

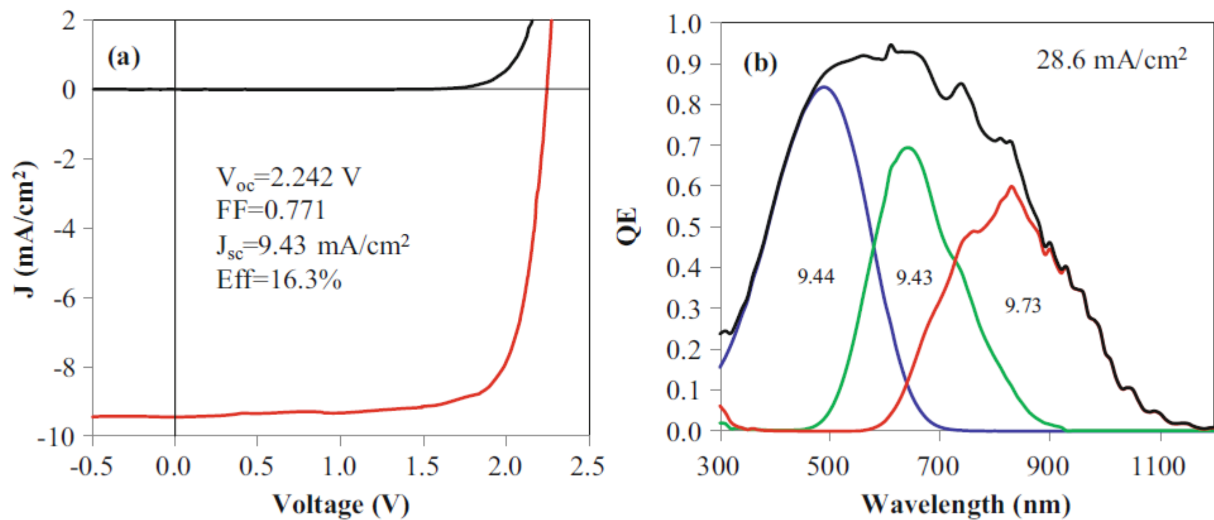

Figure 2.34 (a) J-V characteristics and (b) EQE spectra of an a-Si:H/a-SiGe:H/µc-Si:H triple junction solar cell with an initial efficiency of 16.3%.

Using an a-Si:H/μc-Si:H/μc-Si:H triple junction structure, LG Solar have demonstrated an NREL confirmed 13.44% stable efficiency with the results shown in Fig. 2.35 [21].

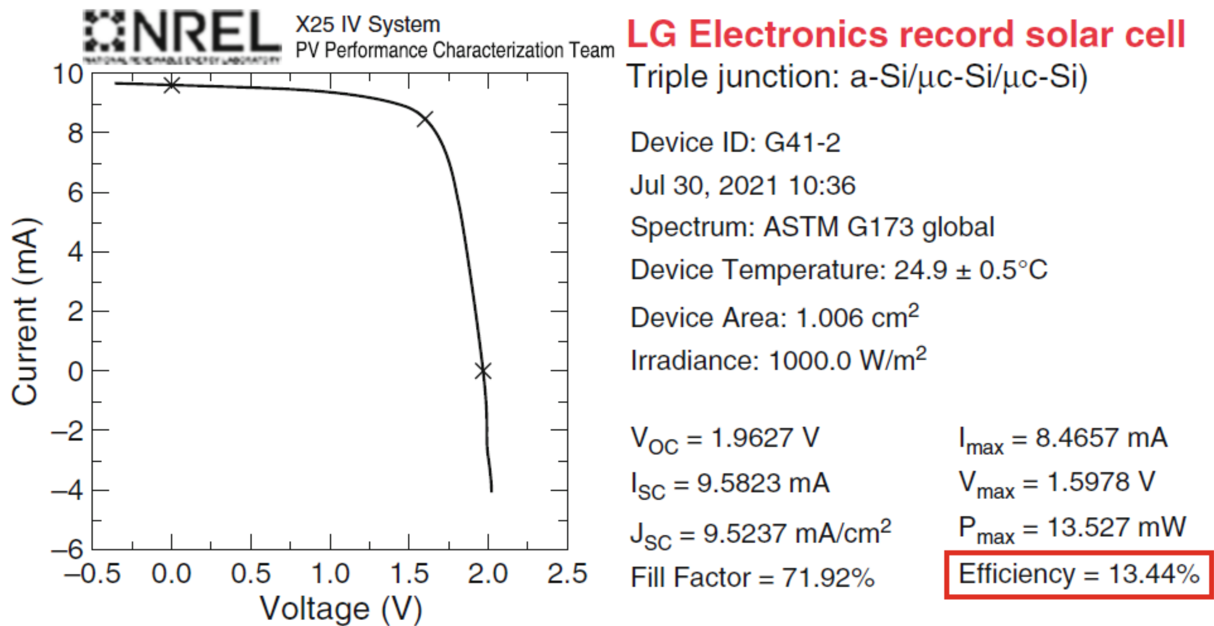

Figure 2.35 The established performance of the a-Si:H/μc-Si:H/μc-Si:H triple-junction solar cell after 1000 h light soaking. This new record was confirmed by NREL.

The progress of a-Si:H, a-SiGe:H and μc-Si:H multijunction solar cell efficiency made by the community is shown in Fig. 2.36. Although over 16% initial cell efficiencies have been achieved with both the n-i-p and p-i-n structures, the progress has been slowed down in recent years; especially the thin film silicon photovoltaic industry has been significantly shrunk. However, a remaining question for the thin film community is whether the thin film silicon solar cell efficiency has reached the upper limit. Simulation studies have shown that with quadruple structures, around 20% cell efficiencies could be attained [22].

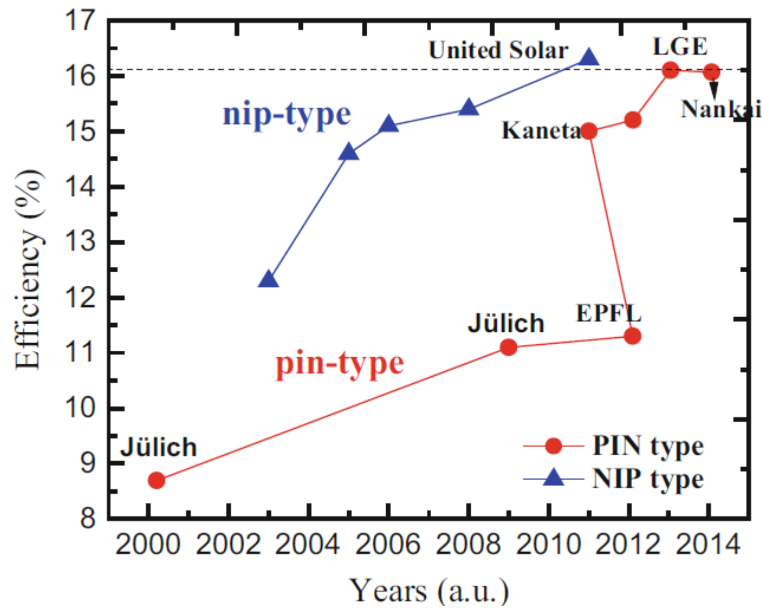

Figure 2.36 The highest efficiency of a-Si:H/a-SiGe:H/μc-Si:H triple-junction solar cells achieved in different research institutions.

a-Si:H and μc-Si:H multijunction solar cells have been also incorporated into production lines with increased module efficiency over a-Si:H and a-SiGe:H multijunction product. Large area module efficiency has been steady improved. A stable large area (1.43 m^2) efficiency of 12.34% has been achieved by TEL Solar and confirmed by ESTI as shown in Fig. 2.37 [23].

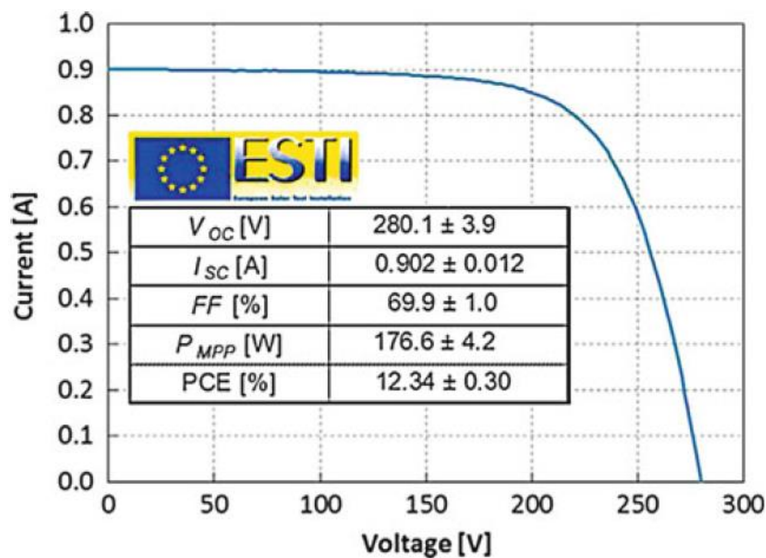

Figure 2.37 Stabilized I-V curve and parameters of the record module (1.43 m^2)) made by TEL Solar and certified by ESTI.

2.13 Conclusion

This chapter describes the basic elements needed to understand the solar cell. It begins by giving reminders about the solar radiation, and its application in the photovoltaic field. After that, explanations concerning the operation of the photovoltaic cells and their main characteristics such as the current characteristic voltage I-V, the spectral response RS (λ) and its photovoltaic parameters are covered. The different generations of the solar cells, the different classifications of the tandem solar cells and the a-Si:H based multijunction solar cells are also covered in this chapter.

Chapter 2 references

[1] S. M. Sze and M. K. Lee, "Semiconductor Devices: Physics and Technology Third." John Wiley & Sons, 2012.

[2] M. R. SERDOUK, "Etude par simulation numérique des propriétés électriques d'une cellule solaire en silicium amorphe hydrogéné (a-Si: H)." Université Mohamed Khider-Biskra, 2015.

[3] H. Mathieu and H. Fanet, *Physique des semiconducteurs et des composants électroniques-6ème édition: Cours et exercices corrigés*. Dunod, 2009.

[4] G. Barbarino, F. Barbato, and E. Nocerino, "The Semiconductor Multiplication System for Photoelectrons in a Vacuum Silicon Photomultiplier Tube (VSiPMT) and Related Front End Electronics."

[5] B. Van Zeghbroeck, "Principles of electronic devices," *Univ. Color.*, 2011.

[6] A. U. Manual, "Santa Clara, CA: Silvaco." Inc, 2017.

[7] S. M. Sze and K. K. Ng, *Physics of semiconductor devices*. John wiley & sons, 2006.

[8] T. Markvart, A. McEvoy, and L. Castaner, *Practical handbook of photovoltaics: fundamentals and applications*. Elsevier, 2003.

[9] A. M. Bagher, M. M. A. Vahid, and M. Mohsen, "Types of solar cells and application," *Am. J. Opt. Photonics*, vol. 3, no. 5, pp. 94–113, 2015.

[10] N. R. E. Laboratory, "Best Research-Cell Efficiency Chart." NREL Golden, CO, 2020.

[11] T. Todorov, O. Gunawan, and S. Guha, "A road towards 25% efficiency and beyond: perovskite tandem solar cells," *Mol. Syst. Des. Eng.*, vol. 1, no. 4, pp. 370–376, 2016.

[12] A. Shah and A. V. Shah, *Thin-film silicon solar cells*. EPFL press, 2010.

[13] J. Poortmans and V. Arkhipov, *Thin film solar cells: fabrication, characterization and applications*, vol. 5. John Wiley & Sons, 2006.

[14] Y. Zhao, X. Zhang, and B. Yan, "Hydrogenated Amorphous Silicon Thin Film," *Handb. Photovolt. Silicon*, pp. 639–692, 2019.

[15] Y. Zhao, X. Zhang, L. Bai, and B. Yan, "Hydrogenated Microcrystalline Silicon Thin Films," *Handb. Photovolt. Silicon*, pp. 693–756, 2019.

[16] U. Kroll *et al.*, "Recent Developments of High-Efficiency Micromorph Tandem Solar Cells in KAI-M/ Plasmabox PECVD Reactors," in *26th European Photovoltaic Solar Energy Conference and Exhibition (3BO.2.6)*, 2011, pp. 2340–2343.

[17] M. Boccard *et al.*, "High-stable-efficiency tandem thin-film silicon solar cell with low-refractive-index silicon-oxide interlayer," *IEEE J. photovoltaics*, vol. 4, no. 6, pp. 1368–

1373, 2014.

[18] T. Matsui *et al.*, “High-efficiency amorphous silicon solar cells: impact of deposition rate on metastability,” *Appl. Phys. Lett.*, vol. 106, no. 5, p. 53901, 2015.

[19] J. Yang, A. Banerjee, and S. Guha, “Triple-junction amorphous silicon alloy solar cell with 14.6% initial and 13.0% stable conversion efficiencies,” *Appl. Phys. Lett.*, vol. 70, no. 22, pp. 2975–2977, 1997.

[20] B. Yan, G. Yue, L. Sivec, J. Yang, S. Guha, and C.-S. Jiang, “Innovative dual function nc-SiOx: H layer leading to a> 16% efficient multi-junction thin-film silicon solar cell,” *Appl. Phys. Lett.*, vol. 99, no. 11, p. 113512, 2011.

[21] S. Kim, J.-W. Chung, H. Lee, J. Park, Y. Heo, and H.-M. Lee, “Remarkable progress in thin-film silicon solar cells using high-efficiency triple-junction technology,” *Sol. Energy Mater. Sol. Cells*, vol. 119, pp. 26–35, 2013.

[22] O. Isabella, A. H. M. Smets, and M. Zeman, “Thin-film silicon-based quadruple junction solar cells approaching 20% conversion efficiency,” *Sol. energy Mater. Sol. cells*, vol. 129, pp. 82–89, 2014.

[23] J. S. Cashmore *et al.*, “Improved conversion efficiencies of thin-film silicon tandem (MICROMORPH^{TM}) photovoltaic modules,” *Sol. Energy Mater. Sol. Cells*, vol. 144, pp. 84–95, 2016.

Chapter 3:
Simulation of a-Si:H, µ-Si:H and a-SiGe:H Based Multijunction Solar Cell: Silvaco-Atlas

3.1 Introduction

To simulate the electrical and optical characteristics of the solar cells, we used the Tcad-Silvaco software. The choice of physical models is important to achieve accurate numerical simulation results. For this, the Silvaco software provides a wide variety of physical models. The first difficulty for the user is to choose certain models compared to others that nevertheless describe the same physical phenomena. The other difficulty will be to choose the appropriate models with the physical mechanisms involved for the conditions of use of the device.

The purpose of this chapter is the theoretical study of the numerical simulation of multijunction solar cells by Silvaco-Atlas software. In the first part of this chapter, we will present the basic semiconductor equations (Poisson's equation, Carrier continuity equations and the transport equations), then physical model used for the simulation of density of states of a-Si: H, the steady-state trap recombination and the trap-assisted tunneling model for the tunnel recombination junction. In the second part of this chapter, we will present the simulation Silvaco-Atlas software and numerical simulations for thin film silicon solar cells of hydrogenated amorphous silicon.

3.2 Basic semiconductor equations

The mathematical models implemented in Atlas-Silvaco to simulate solar cell devices are based on fundamental physics. This model consists of a set of fundamental equations, which link together the electrostatic potential and the carrier densities, within some simulation domain. These equations, which are solved inside any general purpose device simulator consist of Poisson's equation, the continuity equations and the transport [1]. Poisson's equation relates variations in electrostatic potential to local charge densities. The continuity and the transport equations describe the way that the electron and hole densities evolve as a result of transport processes, generation processes, and recombination processes. The discretization of the equations is also performed so that they can be applied to the finite element grid used to represent the simulation domain.

3.2.1 Poisson's equation

Poisson's equation relates the electrostatic potential to the space charge density [1]:

$$div\,(\varepsilon \nabla \Psi) = -\rho \qquad (3.1)$$

where Ψ is the electrostatic potential, ε is the local permittivity, and ρ is the local space charge density. The reference potential is the intrinsic Fermi potential Ψ i. The local space charge density is the sum of contributions from all mobile and fixed charges, including electrons, holes, and ionized impurities.
The electric field is obtained from the gradient of the potential:

$$\vec{E} = -\nabla \psi \qquad (3.2)$$

3.2.2 Carrier continuity equations

The continuity equations for electrons and holes are defined by equations:

$$\frac{\partial n}{\partial t} = \frac{1}{q} div \overrightarrow{J_n} + G_n - R_n \qquad (3.3)$$

$$\frac{\partial p}{\partial t} = \frac{1}{q} div \vec{J}_p + G_p - R_p \qquad (3.4)$$

where n and p are the electron and hole concentrations, $\vec{J}_n$ and $\vec{J}_p$ are the electron and hole current densities, G_n and G_p are the generation rates for electrons and holes, R_n and R_p are the recombination rates for electrons and holes, and q is the charge of an electron.

3.2.3 The transport equations

Equations (3.1), (3.3), and (3.4) provide the general framework for device simulation. But further secondary equations are needed to specify particular physical models for: $\vec{J}_n$, $\vec{J}_p$, G_n, R_n, G_p and R_p.

The simplest model of charge transport that is useful is the Drift-Diffusion Model. This model has the attractive feature that it does not introduce any independent variables in addition to Ψ , n and p. Atlas supplies both drift-diffusion and advanced transport models.

3.2.4 Drift-diffusion transport model

The current densities in the continuity equations may be approximated by a drift-diffusion model and are expressed in terms of the quasi-Fermi levels ϕ_n and ϕ_p as:

$$\vec{J}_n = -q\mu_n n \nabla \phi_n \quad (3.5)$$

$$\vec{J}_p = -q\mu_p p \nabla \phi_p \quad (3.6)$$

where μ_n and μ_p are the electron and hole mobilities. The quasi-Fermi levels are then linked to the carrier concentrations and the potential through the two Boltzmann approximations:

$$n = n_{ie} \exp\left(\frac{-q(\psi - \phi_n)}{k_B T}\right) \quad (3.7)$$

$$p = n_{ie} \exp\left(\frac{-q(\psi - \phi_p)}{k_B T}\right) \quad (3.8)$$

where n_{ie} is the effective intrinsic concentration and T is the temperature. These two equations may then be re-written to define the quasi-Fermi potentials:

$$\phi_n = \psi - \frac{k_B T}{q} \ln \frac{n}{n_{ie}} \quad (3.9)$$

$$\phi_p = \psi + \frac{k_B T}{q} \ln \frac{p}{n_{ie}} \quad (3.10)$$

By substituting these equations into the current density expressions, the following adapted current relationships are obtained [1]:

$$\vec{J}_n = qD_n \nabla n - q\mu_n n \nabla \psi - \mu_n n k_B T \nabla \ln(\mathrm{n}_{ie}) \quad (3.11)$$

$$\vec{J}_p = qD_p \nabla p - q\mu_p p \nabla \psi - \mu_p p k_B T \nabla \ln(\mathrm{n}_{ie}) \quad (3.12)$$

The final term accounts for the gradient in the effective intrinsic carrier concentration, which takes account of bandgap narrowing effects. Effective electric fields are normally defined by:

$$\vec{E}_n = -\nabla\psi - \frac{k_B T}{q}\nabla \ln(\mathrm{n}_{ie}) \tag{3.13}$$

$$\vec{E}_p = -\nabla\psi + \frac{k_B T}{q}\nabla \ln(\mathrm{n}_{ie}) \tag{3.14}$$

which then allows the more conventional formulation of drift-diffusion equations as:

$$\vec{J}_n = qD_n\nabla n + q\mu_n n\vec{E}_n \tag{3.15}$$

$$\vec{J}_p = -qD_p\nabla p + q\mu_p p\vec{E}_n \tag{3.16}$$

It should be noted that this derivation of the drift-diffusion model has assumed that the Einstein relationship holds. In the case of Boltzmann statistics this corresponds to:

$$D_n = \frac{k_B T}{q}\mu_n \tag{3.17}$$

$$D_p = \frac{k_B T}{q}\mu_p \tag{3.18}$$

3.3 Density of states model of hydrogenated amorphous silicon

It is assumed that the total density of states (DOS) and *g(E)*, is composed of four bands: two tail bands (a donor-like valence band and an acceptor-like conduction band) and two deep level bands (one acceptor-like and the other donor-like) which are modeled using a Gaussian distribution [1].

$$N(E) = N_{ta}(E) + N_{td}(E) + N_{Ga}(E) + N_{Gd}(E) \tag{3.19}$$

Here, E is the trap energy, E_C is the conduction band energy, E_V is the valence band energy and the subscripts (T, G, A, D) stand for tail, Gaussian (deep level), acceptor and donor states respectively [1].

$$N_{ta}(E) = N_{TA}\exp\left[\frac{E - E_C}{W_{ta}}\right] \tag{3.20}$$

$$N_{td}(E) = N_{TD} \exp\left[\frac{E_V - E}{W_{td}}\right] \quad (3.21)$$

$$N_{Ga}(E) = N_{GA} \exp\left[-\left[\frac{EGA - E}{W_{ga}}\right]^2\right] \quad (3.22)$$

$$N_{Gd}(E) = N_{GD} \exp\left[-\left[\frac{E - EGD}{W_{gd}}\right]^2\right] \quad (3.23)$$

For an exponential tail distribution, the DOS is described by its conduction and valence band edge intercept densities (N_{TA} and N_{TD}), and by its characteristic decay energy (W_{ta} and W_{td}). For Gaussian distributions, the DOS is described by its total density of states (N_{GA} and N_{GD}), its characteristic decay energy (W_{ga} and W_{gd}), and its peak energy/peak distribution (E_{GA} and E_{GD}).

3.4 Amphoteric defects

In a-Si:H, the effect of dangling-bonds states on recombination can be significant. The dangling-bond states are amphoteric and located around the middle of the bandgap. The dangling-bond density of states for a-Si:H will be calculated using the defect-pool model as will the amphoteric defect density and recombination.

The amphoteric defects are given by [1]:

$$n^{+}_{AMP} = D(E) f^{+}_{AMP}(E) \quad (3.24)$$

$$n^{0}_{AMP} = D(E) f^{0}_{AMP}(E) \quad (3.25)$$

$$n^{-}_{AMP} = D(E) f^{-}_{AMP}(E) \quad (3.26)$$

Where:

$n^{+}_{AMP}(E)$ is the occupied density of the positive amphoteric traps.

$n^{0}_{AMP}(E)$ is the occupied density of the neutral amphoteric traps.

$n^{-}_{AMP}(E)$ is the occupied density of the negative amphoteric traps.

$f^{+}_{AMP}(E)$ is the probability of occupation of the positive amphoteric traps.

$f^{0}_{AMP}(E)$ is the probability of occupation of the neutral amphoteric traps.

$f^{-}_{AMP}(E)$ is the probability of occupation of the negative amphoteric traps.

D(E) is the dangling-bond density of states given by equation (3.28) [1].

The total charge caused by the presence of amphoteric traps is defined by [1]:

$$Q_{TAMP} = q\int_{E_V}^{E_C} (n^{+}_{AMP}(E) - n^{-}_{AMP}(E))dE \qquad (3.27)$$

$$D(E) = N_{TD}\left(\frac{H}{N_{SiSi}}\right)^{\frac{kT^*}{4W_{td}}}\left(\frac{2W_{td}^{\ 2}}{2W_{td}-kT^*}\right)\exp\left[-\frac{1}{2W_{td}}\left(E_P - E_V - \frac{\sigma^2}{4W_{td}}\right)\right]$$
$$\cdot\left(\frac{2}{f^{0}_{AMP_O}(E)}\right)^{\frac{kT^*}{2W_{td}}}\cdot\frac{1}{\sqrt{2\pi\sigma^2}}\exp\left[-\left(\frac{E+\frac{\sigma^2}{2W_{td}}-E_P}{2\sigma^2}\right)^2\right] \qquad (3.28)$$

where:

E_P is the most probable potential defect energy.

E_v is the valence band edge.

W_{td} is the characteristic energy.

H is the density of hydrogen.

N_{SiSi} is the density of Si-Si bonds.

N_{TD} is the density of states of the valance-band tail exponential region extrapolated to the valence-band edge.

σ is the defect pool width.

T^* is the freeze-in temperature.

$f^{0}_{AMP_0}(E)$ the equilibrium probability of occupation of the neutral amphoteric traps.

The probabilities of occupation can be calculated from the equilibrium probabilities of occupation $f^{+}_{AMP_0}(E)$,$f^{0}_{AMP_0}(E)$,$f^{-}_{AMP_0}(E)$ and the capture and emission rates [1]:

$$f^{+}_{AMP}(E) = \frac{1}{1+\left[\dfrac{e^{+}_{p}+nv_{n}\sigma^{+}_{n}}{e^{0}_{n}+pv_{p}\sigma^{0}_{p}}\right]\left[1+\dfrac{e^{0}_{p}+nv_{n}\sigma^{0}_{n}}{e^{-}_{n}+pv_{p}\sigma^{-}_{p}}\right]} \quad (3.29)$$

$$f^{0}_{AMP}(E) = \frac{1}{1+\left[\dfrac{e^{0}_{n}+pv_{p}\sigma^{0}_{p}}{e^{+}_{p}+pv_{p}\sigma^{+}_{n}}\right]\left[1+\dfrac{e^{0}_{p}+nv_{n}\sigma^{0}_{n}}{e^{-}_{n}+pv_{p}\sigma^{-}_{p}}\right]} \quad (3.30)$$

$$f^{-}_{AMP}(E) = 1 - f^{0}_{AMP}(E) - f^{+}_{AMP}(E) \quad (3.31)$$

where:

σ^{0}_{n} is the electron capture cross-section for neutral defects.

σ^{+}_{n} is the electron capture cross-section for positive defects.

σ^{0}_{p} is the hole capture cross-section for neutral defects.

σ^{-}_{p} is the hole capture cross-section for negative defects.

e^{0}_{n} is the electron emission coefficient for neutral defects.

e^{-}_{n} is the electron emission coefficient for negative defects.

e^{+}_{p} is the hole emission coefficient for positive defects.

e^{0}_{p} is the hole emission coefficient for neutral defects.

$$e^{0}_{n} = \frac{n_0 f^{+}_{AMP_0}(E) v_n \sigma^{+}_{n}}{f^{0}_{AMP_0}(E)} \quad (3.32)$$

$$e^{-}_{n} = \frac{n_0 f^{0}_{AMP_0}(E) v_n \sigma^{0}_{n}}{f^{-}_{AMP_0}(E)} \quad (3.33)$$

$$e^{0}_{p} = \frac{p_0 f^{-}_{AMP_0}(E) v_p \sigma^{-}_{p}}{f^{0}_{AMP_0}(E)} \quad (3.34)$$

$$e^{+}_{p} = \frac{p_0 f^{0}_{AMP_0}(E) v_p \sigma^{0}_{p}}{f^{+}_{AMP_0}(E)} \quad (3.35)$$

$$f^{+}_{AMP_0}(E) = \frac{1}{1+2\exp\left[\dfrac{E_F - E_T}{k_B T}\right]+\exp\left[\dfrac{2E_F - 2E_T - U}{k_B T}\right]} \quad (3.36)$$

$$f^{0}_{AMP_0}(E) = \frac{2\exp\left[\frac{E_F - E_T}{k_B T}\right]}{1 + 2\exp\left[\frac{E_F - E_T}{k_B T}\right] + \exp\left[\frac{2E_F - 2E_T - U}{k_B T}\right]} \tag{3.37}$$

$$f^{-}_{AMP_0}(E) = 1 - f^{+}_{AMP_0}(E) - f^{0}_{AMP_0}(E) \tag{3.38}$$

where:

n_0 is the equilibrium electron concentration.

p_0 is the equilibrium hole concentration.

E_F is the Fermi energy.

E_T is the trap energy.

U is the defect electron correlation energy.

The most common defect states in a-Si:H and a-SiGe:H semiconductors are dangling bonds (DB), for a-Si:H the DB states are often modeled by the Defect Pool Model (DPM) [2,3] which considers three Gaussian distributions with different charges, positively charged (D^+), neutral state (D^0) and negatively charged (D^-). For a-SiGe:H and μc-Si:H materials the DB states are modeled by the standard model consisting of two Gaussian distributions of donor- and acceptor-like mid-gap states [4]. The defect parameters of a-Si:H, μc-Si:H and a-SiGe:H materials are listed in Tables 3.1 and 3.2. The simulation parameters are taken from references [5–12] and are slightly modified.

Defect states parameters	**a-Si:H**	**μc-Si:H**	**a-SiGe:H**
Tail states			
N_{TA}, N_{TD} (cm^{-3}.eV^{-1})	10^{21}	$2\text{x}10^{20}$	10^{21}
W_{ta} (eV)	0.025	0.01	0.025
W_{td} (eV)	0.043	0.02	0.043
σ_{na} (cm^2)	10^{-17}	10^{-17}	10^{-17}
σ_{pa} (cm^2)	10^{-17}	10^{-17}	10^{-17}
σ_{nd} (cm^2)	10^{-17}	10^{-17}	10^{-17}
σ_{pd} (cm^2)	10^{-17}	10^{-17}	10^{-17}

Table 3.1. Defect states parameters of tail states [5 -8], [10] and [11].

Defect states parameters	**a-Si:H**	**μc-Si:H**	**a-SiGe:H**
Gaussian model			
N_{GA}, N_{GD}(cm^{-3})	-	10^{15}	10^{15}
E_{Ga} (eV)	-	0.8	0.52
E_{Gd} (eV)	-	0.8	0.68
W_{Ga} (eV)	-	0.2	0.188
W_{Gd} (eV)	-	0.188	0.188
σ_{nGa}(cm^2)	-	10^{-17}	10^{-17}
σ_{pGa}(cm^2)	-	10^{-17}	10^{-17}
σ_{nGd}(cm^2)	-	10^{-17}	10^{-17}
σ_{pGd}(cm^2)	-	10^{-17}	10^{-17}
Defect Pool Model			
U (eV)	0.2	-	-
σ (eV)	0.19	-	-
E_p (eV)	1.22	-	-
N_{SiSi} (cm^{-3})	2x10^{23}	-	-
H (cm^{-3})	10^{21}	-	-
σ_n^+ (cm^2)	2.3x10^{-15}	-	-
σ_n^0 (cm^2)	5x10^{-16}	-	-
σ_p^- (cm^2)	2.3x10^{-15}	-	-
σ_p^o (cm^2)	5x10^{-16}	-	-

Table 3.2. Defect states parameters of Defect pool model and Gaussian model [5 – 7], [9] and [12].

3.5 Steady-state trap recombination

For steady-state conditions, the net recombination/generation rate is identical for electrons (R_n) and holes (R_p). The Shockley-Read-Hall recombination/generation rate for Gaussian distribution defect states is given by [1]:

$$R_{n,p} = \int_{E_v}^{E_c} (np - n_i^2) \left\{ \left[\frac{v_n v_p \sigma_{na} \sigma_{pa} N_{ta}(E)}{v_n \sigma_{na} \left(n + n_i \exp\left[\frac{E - E_i}{k_B T} \right] \right) + v_p \sigma_{pa} \left(p + n_i \exp\left[\frac{E_i - E}{k_B T} \right] \right)} \right] + \left[\frac{v_n v_p \sigma_{nGa} \sigma_{pGa} N_{Ga}(E)}{v_n \sigma_{nGa} \left(n + n_i \exp\left[\frac{E - E_i}{k_B T} \right] \right) + v_p \sigma_{pGa} \left(p + n_i \exp\left[\frac{E_i - E}{k_B T} \right] \right)} \right] + \left[\frac{v_n v_p \sigma_{nd} \sigma_{pd} N_{td}(E)}{v_n \sigma_{nd} \left(n + n_i \exp\left[\frac{E - E_i}{k_B T} \right] \right) + v_p \sigma_{pd} \left(p + n_i \exp\left[\frac{E_i - E}{k_B T} \right] \right)} \right] + \left[\frac{v_n v_p \sigma_{nGd} \sigma_{pGd} N_{Gd}(E)}{v_n \sigma_{nGd} \left(n + n_i \exp\left[\frac{E - E_i}{k_B T} \right] \right) + v_p \sigma_{pGd} \left(p + n_i \exp\left[\frac{E_i - E}{k_B T} \right] \right)} \right] \right\} dE \quad (3.39)$$

where v_n is the electron thermal velocity and v_p is the hole thermal velocity, n_i is the intrinsic carrier concentration. σ_{na} and σ_{nGa} are the electron capture cross-section for the acceptor tail and Gaussian states respectively. σ_{pa} and σ_{pGa} are the hole capture cross-sections for the acceptor tail and Gaussian states respectively and σ_{nd} , σ_{nGd} , σ_{pd} , and σ_{pGd} are the equivalents for donors states.

In the case of defect pool distribution model, the recombination rate is given by [1]:

$$R_{n,p} = \int_{E_v}^{E_c} D(E)\left[nv_n\sigma_n^{+}f_{AMP}^{+}(E) - e_n^{0}f_{AMP}^{0}(E)\right]dE + \int_{E_v}^{E_c} D(E)\left[nv_n\sigma_n^{0}f_{AMP}^{0}(E) - e_n^{-}f_{AMP}^{-}(E)\right]dE$$

(3.40)

3.6 Trap-assisted tunneling model

The model for the tunnel recombination junction of the tandem solar cell is based on the trap-assisted tunneling recombination model. Trap-Assisted Tunneling models the trap-to-band phonon-assisted tunneling effects for Dirac wells. At high electric fields, tunneling of electrons from the valence band to the conduction band through trap or defect states can have an important effect on the current. Trap-assisted Tunneling is modelled by including field-effect enhancement terms (Γ_n and Γ_p) in the capture cross-sections terms of the recombination rate given by eq. 3.40. The electron capture cross-section (σ_{na}, σ_{nGa}, σ_{nd}, and σ_{nGd}) are modified by including the electron field-effect term (Γ_n^{DIRAC}). For example, the electron capture cross-section for acceptor tail states (σ_{na}) becomes:

The field-effect enhancement term for electrons is given by [1]:

$$\sigma_{na} \times (1 + \Gamma_n^{DIRAC}) \qquad (3.41)$$

σ_{nGa}, σ_{nd}, and σ_{nGd} are also modified in this way.

$$\Gamma_n^{DIRAC} = \frac{\Delta En}{k_B T}\int_0^1 \exp\left(\frac{\Delta En}{k_B T}u - K_n u^{3/2}\right)du \qquad (3.42)$$

While the field-effect enhancement term for hole is:

$$\Gamma_p^{DIRAC} = \frac{\Delta Ep}{k_B T}\int_0^1 \exp\left(\frac{\Delta En}{k_B T}u - K_p u^{3/2}\right)du \qquad (3.43)$$

The hole capture cross-sections (σ_{pa}, σ_{pGa}, σ_{pd}, and σ_{pGd}) are modified by including the hole field effect term (Γ_p^{DIRAC}). For example, σ_{pa} now becomes:

$$\sigma_{pa} \times (1 + \Gamma_p^{DIRAC}) \qquad (3.44)$$

σ_{pGa} , σ_{pd} , and σ_{pGd} are also modified in this way.

where u is the integration variable, ΔE_n is the energy range where tunneling can occur for electrons, ΔE_p is the tunneling energy range for holes, and k_n and k_p are given by [1]:

$$k_n = \frac{4}{3}\frac{\sqrt{2m_0 m_n \Delta E_n^3}}{q\hbar|F|} \tag{3.45}$$

$$k_P = \frac{4}{3}\frac{\sqrt{2m_0 m_p \Delta E_p^3}}{q\hbar|F|} \tag{3.46}$$

$\hbar$ is the reduced Planck's constant, F is the local electric field, m_0 is the rest mass of an electron, and m_n (m_p) is the relative effective mass for electrons (holes).

The trap assisted tunneling recombination rate is given by [1]:

$$\begin{aligned} R_{tat} = \int_{E_v}^{E_c} (np - n_i^2) \Bigg\{ & \left[\frac{v_n v_p \sigma_{na}\sigma_{pa}(1+\Gamma_n)(1+\Gamma_p) N_{ta}(E)}{v_n \sigma_{na}(1+\Gamma_n)\left(n + n_i \exp\left[\frac{E-E_i}{k_B T}\right]\right) + v_p \sigma_{pa}(1+\Gamma_p)\left(p + n_i \exp\left[\frac{E_i - E}{k_B T}\right]\right)} \right] \\ + & \left[\frac{v_n v_p \sigma_{nGa}\sigma_{pGa}(1+\Gamma_n)(1+\Gamma_p) N_{Ga}(E)}{v_n \sigma_{nGa}(1+\Gamma_n)\left(n + n_i \exp\left[\frac{E-E_i}{k_B T}\right]\right) + v_p \sigma_{pGa}(1+\Gamma_p)\left(p + n_i \exp\left[\frac{E_i - E}{k_B T}\right]\right)} \right] \\ + & \left[\frac{v_n v_p \sigma_{nd}\sigma_{pd}(1+\Gamma_n)(1+\Gamma_p) N_{td}(E)}{v_n \sigma_{nd}(1+\Gamma_n)\left(n + n_i \exp\left[\frac{E-E_i}{k_B T}\right]\right) + v_p \sigma_{pd}(1+\Gamma_p)\left(p + n_i \exp\left[\frac{E_i - E}{k_B T}\right]\right)} \right] \\ + & \left[\frac{v_n v_p \sigma_{nGd}\sigma_{pGd}(1+\Gamma_n)(1+\Gamma_p) N_{Gd}(E)}{v_n \sigma_{nGd}(1+\Gamma_n)\left(n + n_i \exp\left[\frac{E-E_i}{k_B T}\right]\right) + v_p \sigma_{pGd}(1+\Gamma_p)\left(p + n_i \exp\left[\frac{E_i - E}{k_B T}\right]\right)} \right] \Bigg\} dE \end{aligned} \tag{3.47}$$

μc-Si:H semiconductor is used for the tunnel recombination junction, the trap assisted tunneling recombination model parameters were set to the default values set by Atlas for Silicon and work well for all our simulation of the tandem solar cell.

3.7 Silvaco-Atlas simulation software

In present work the solar cell device Simulations are carried out using the Silvaco-Atlas simulator. Silvaco International produces a suite of software programs that together become a Virtual Wafer Fabrication tool. The DeckBuild run-time environment received the input files. Within the input files, Silvaco-Atlas was called to execute the code. And finally, TonyPlot was used to view the output of the simulation. Additionally, output log files were produced. The data extracted from the log files could then be displayed using Microsoft Excel or Matlab scripts. Figure 3.1 shows the inputs and outputs for Silvaco Atlas.

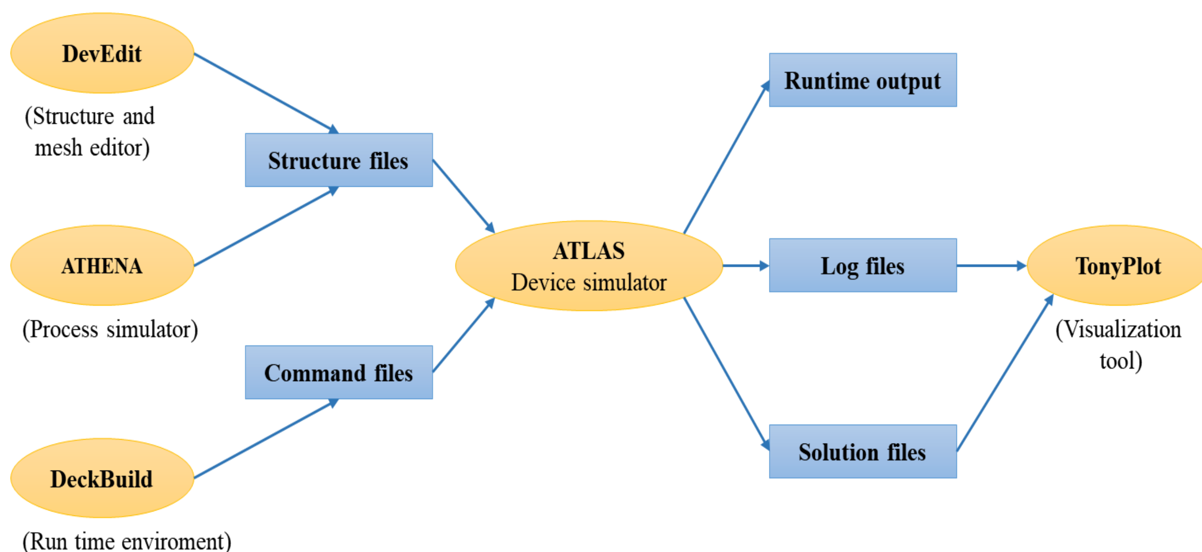

Figure 3.1 Atlas inputs and outputs.

3.8 Order of Atlas command groups

The order of Atlas command groups is listed in Table 3.3.

Group	**Statements**
Structure specification	Mesh Region Doping Electrode
Material models specification	Material Models Defects Light source Contact Interface
Numerical method selection	Method
Solution specification	Log Solve Load Save
Results analysis	Extract Tonyplot

Table 3.3 Atlas command groups with the primary statements in each group.

3.8.1 Structure specification

The structure specification is done by defining the mesh, the region, the electrodes and the doping levels.

a) Mesh

The mesh is a series of horizontal x and vertical y lines and spacing between them. The general format to define the mesh is:

```
x.mesh location=<value> spacing=<value>
y.mesh location=<value> spacing=<value>
```

Figure 3.2 illustrates the mesh used for a-Si:H solar cell simulated in Silvaco-Atlas.

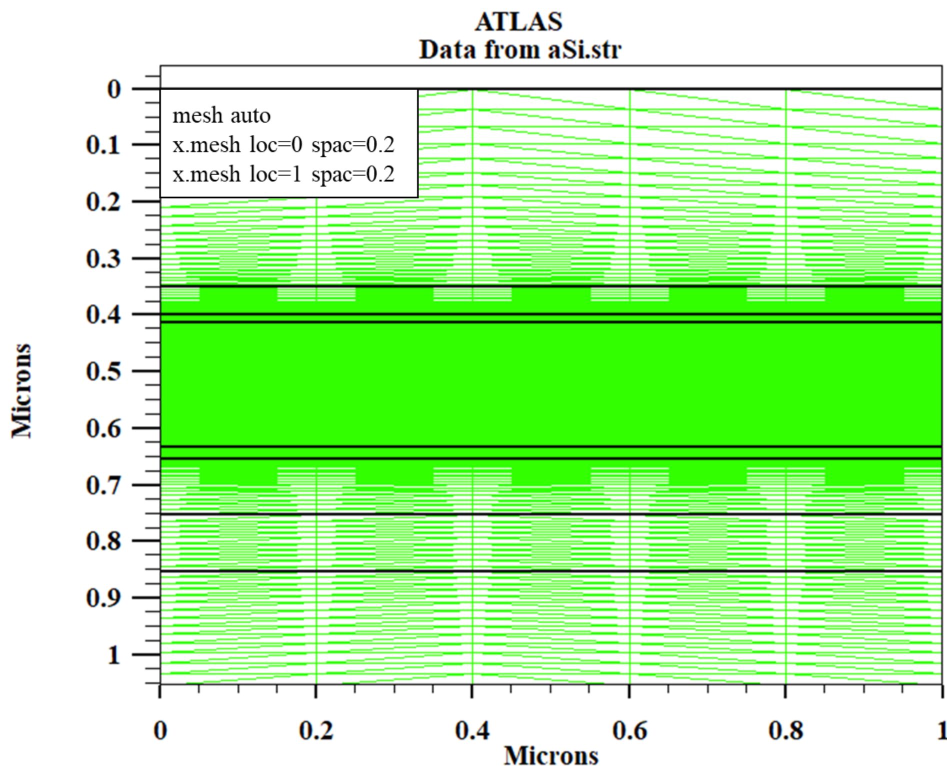

Figure 3.2 Non-uniform mesh creation using Atlas for a-Si:H solar cell.

A coarse or fine mesh determines the accuracy of the simulation. A coarse mesh allows a faster simulation, but less accurate results. A fine mesh produces a slower simulation, but more accurate results. The areas that have a finer mesh, therefore, are of greatest interest in the simulation. The most efficient way to work is to allocate a fine grid only in critical areas (around junctions and depletion regions, areas of high electric field, areas of current flow, base region of BJTs, areas of considerable recombination effects, areas of high impact ionization…etc.) and coarser grid elsewhere.

b) Region

After defining the mesh, it is necessary to define the regions. The format to define the regions is as follows:

region number=<integer> <material_type> <position parameters>

From Figure 3.3, the code that defines the regions is identified. There are eight regions defined. The regions must then be given a material.

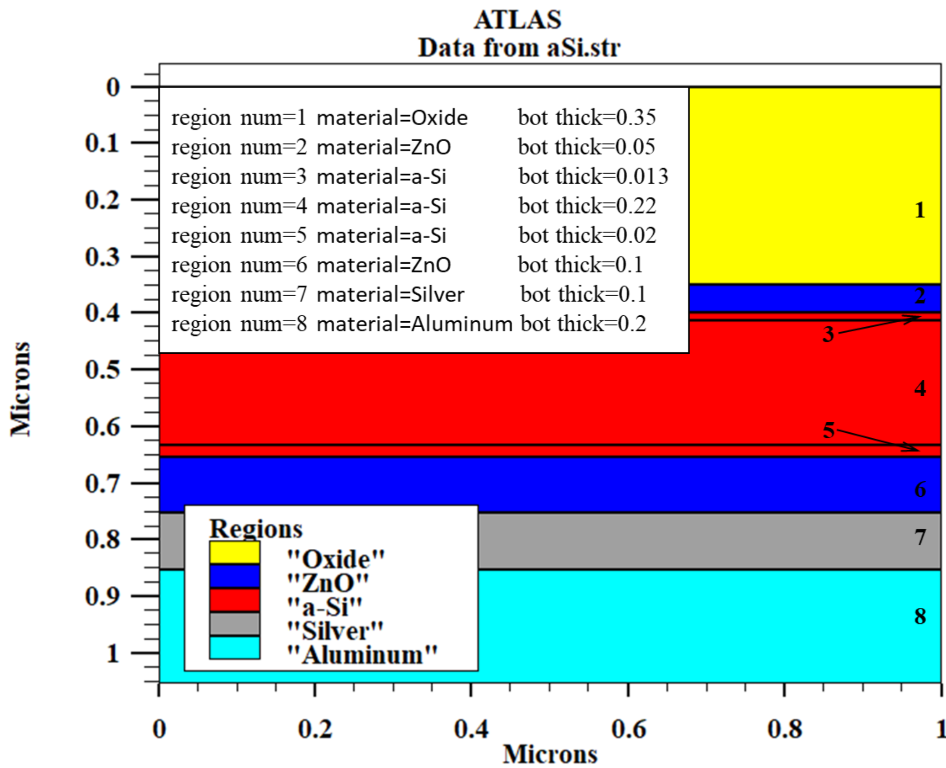

Figure 3.3 Regions of a-Si:H solar cell.

c) Electrodes

The next structure specification corresponds to electrodes. The electrodes defined are the anode and the cathode. However, Silvaco-Atlas has a limit of 50 electrodes that can be defined. The format to define electrodes is as follows:

electrode name=<electrode name> <position_parameters>

From Figure 3.4, the electrode statements are defined for the anode and the cathode. Note that the cathode is defined with aluminum and the anode is defined with ZnO.

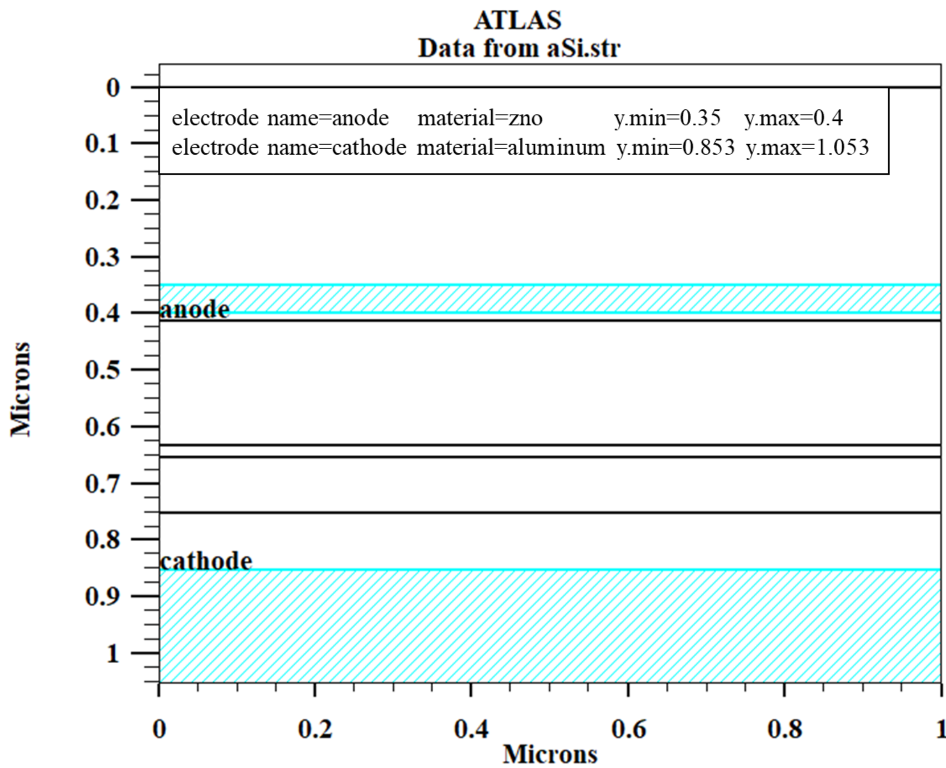

Figure 3.4 Electrodes of a-Si:H solar cell.

d) Doping

The last aspect of structure specification that needs to be defined is doping. The format of the Atlas statement is as follows:

doping <distribution type> <dopant_type> <position parameters>

From Figure 3.5, the doping types and the doping levels are defined. Doping can be n-type or p-type. The distribution type can be uniform or Gaussian.

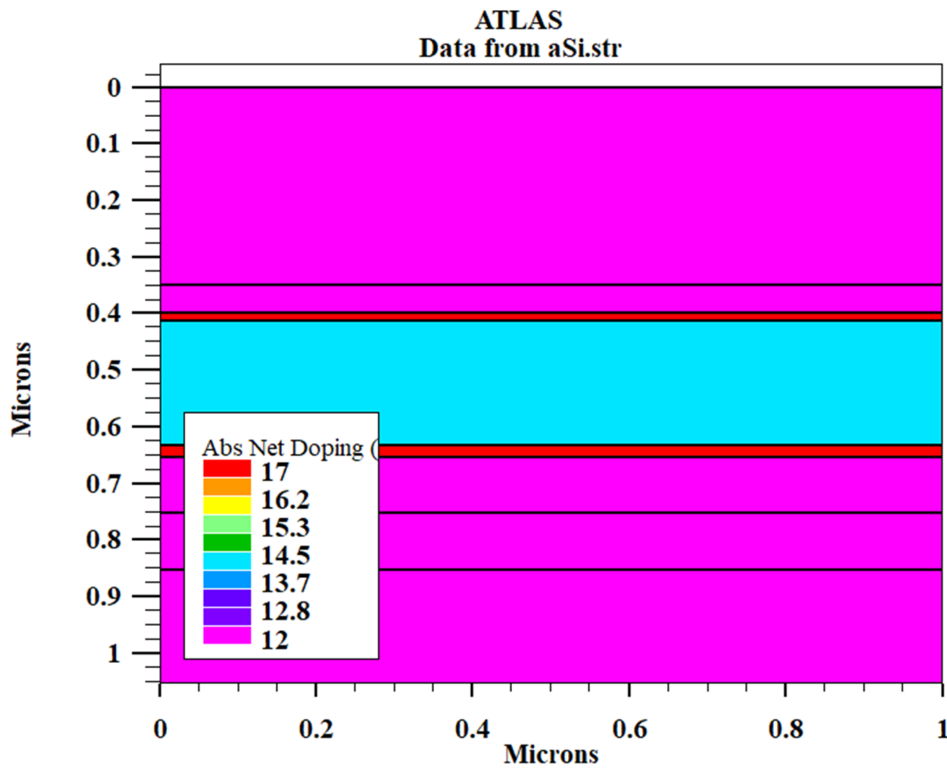

Figure 3.5 Doping of a-Si:H solar cell.

3.8.2 Materials model specification

After the structure specification, the materials model specification is next. the materials model specification is introduced into material, models, contact, and interface.

a) Material

The format for the material statement is as follows:

material <localization> <material_definition>

Below is an example of the material statement:

material region=3 eg300=1.71 nv300=1e21 nc300=1e21 permittivity=11.9 affinity=3.89 mun0=1 mup0=0.6

These parameters of semiconductors are the band gap at room temperature (EG300), electron mobility (MUN) and hole mobility (MUP), electron (TAUN0) and hole (TAUP0)

recombination lifetimes, conduction band density at room temperature (NC300), valence band density at room temperature (NV300), PERMITTIVITY, AFFINITY.

b) Defects

For aSi:H defect pool model, the syntax for a typical defect states definition is given below:

```
defect region=3 cont nta=1e21 ntd=1e21 wta=0.025 wtd=0.043 \
nga=0 ngd=0 ega=0.62 egd=0.78 wga=0.188 wgd=0.188 \
numa=100 numd=100 sigtae=1.e-17 sigtah=1.e-17 sigtde=1.e-17 sigtdh=1.e-17

defects region=3 amphoteric cont signp=2.3e-15 sign0=5e-16 sigp0=5e-16 sigpn=2.3e-15 \
hconc=1e21 nsisi=2e23 sigma=0.19 t0=500 ev0=0.043 eu=0.2 \
ep.amp=1.22 num.amp=100 nv0.amp=2e20
```

c) Light source

The illumination by solar spectrum is defined by the Beam statement. The origin and angle of incidence need to be defined. An angle of 90 degrees means normal incidence from the top. The parameter power.file points to an external file that contains a list of wavelengths vs. intensity. The file 'solarex12.spec' contains data for the Air Mass 1.5 Solar Spectrum. The intensity in the file can be considered just as relative intensity between the wavelengths [2].

```
beam num=1 x.orig=5 y.orig=-10 angle=90 power.file=solarex12.spec verbose back.reflect
reflect=2
```

The verbose command enables a higher level of diagnostic run-time printing. The back.reflect command specifies that back side reflections are to be taken into account while the reflect value specifies the number of reflections that will be traced.
It is possible to store the optical intensity of the illumination by specifying output file (opt.int) at any time before saving a structure file. The photogeneration rate will appear in the solution structure file by default.

d) Models

The physical models fall into five categories: mobility, recombination, carrier statistics, impact ionization, and tunneling. The syntax of the model statement is as follows:

models <model flag> <general parameter> <model dependent parameters>

The choice of model depends on the materials chosen for simulation.

The example below activates two recombination models SRH and trap tunneling.

model srh
model region=6 trap.tunnel

SRH is the Shockley-Read-Hall model and TRAP.TUNNEL is the trap assisted tunneling model.

e) Contact

Contact determines the attributes of the electrode. The syntax for contact is as follows:

contact number=<n> |name=<ename>

The following is an example of the contact statement.

contact number=1 name=anode

f) Interface

The semiconductor or insulator boundaries are determined with the interface statement. The syntax is as follows:

interface <parameters>

The following example shows the usage of the interface statement.

```
interface x.min=-4 x.max=4 y.min=-0.5 y.max=4 s.n=1e4 s.p=1e4
```

The max and min values determine the boundaries. The S.N and S.P values specify the electron and hole surface recombination velocities.

3.8.3. Numerical method selection

After the materials model specification, the numerical method selection must be specified. The only statement that applies to numerical method selection is method.

There are various numerical methods to calculate solutions to semiconductor device problems. There are three types of solution techniques used in Silvaco-Atlas:

- decoupled (GUMMEL)
- fully coupled (NEWTON)
- BLOCK

The GUMMEL method solves for each unknown by keeping all other unknowns constant. The process is repeated until there is a stable solution. The NEWTON method solves all unknowns simultaneously. The BLOCK method solves some equations with the GUMMEL method and some with the NEWTON method.

The GUMMEL method is used for a system of equations that are weakly coupled and there is linear convergence. The NEWTON method is used when equations are strongly coupled and there is quadratic convergence.

The following example shows the use of the method statement.

```
method newton
```

3.8.4 Solution specification

After completing the numerical method selection, the solution specification is next. Solution specification is grouped into log, solve, load, and save statements.

a) Log

LOG saves all terminal characteristics to a file. DC, transient, or AC data generated by a SOLVE statement after a LOG statement is saved.

The following shows an example of the LOG statement.

```
log outfile=myoutputfile.log
```

The example saves the current-voltage information into myoutputfile.log.

b) Solve

The SOLVE statement follows the LOG statement. SOLVE performs a solution for one or more bias points. The following is an example of the SOLVE statement.

```
solve b1=1
solve vanode=0.0 name=anode vstep=0.05 vfinal=1
```

c) Load and Save

The LOAD statement enters previous solutions from files as initial guess to other bias points. The SAVE statement enters all node point information into an output file.

The following are examples of LOAD and SAVE statements.

```
save outf=sol.str
```

In this case, SOL.STR has information saved after a SOLVE statement. Then, in a different simulation, SOL.STR can be loaded as follows:

```
load infile=sol.str
```

3.8.5 Results analysis

Once a solution has been found for a semiconductor device problem, the information can be displayed graphically with TonyPlot. Additionally, device parameters can be extracted with the EXTRACT statement.

In the example below, the EXTRACT statement gives the current and voltage characteristics of a solar cell. This information is saved into the I(V)curve.dat file. Then, TonyPlot plots the data in the I(V)curve.dat file (Figs. 3.6) and the power.dat file (Fig 3.7).

```
extract init infile="top_only.log"
extract name="I(V)" curve(v."anode", i."cathode"*1e8*1e3) outf=" I(V)curve.dat "
```

```
extract name="Jsc" max(i."cathode")
extract name="JscmAcm2" $Jsc*1e8*1e3
extract name="Voc" x.val from curve(v."anode", i."cathode") where y.val=0.0
extract name="P" curve(v."anode", (v."anode" * i."cathode"*1e8*1e3)) outf="power.dat"
extract name="Pm" max(curve(v."anode", (v."anode" * i."cathode")))
extract name="Vm" x.val from curve(v."anode", (v."anode"*i."cathode") ) where y.val=$"Pm"
extract name="Im" $"Pm"/$"Vm"
extract name="FF" $"Pm"/($"Jsc"*$"Voc")*100
extract name="Eff" (1e8*$Pm/(0.1*1))*100
tonyplot ivcurve.dat
tonyplot power.dat
```

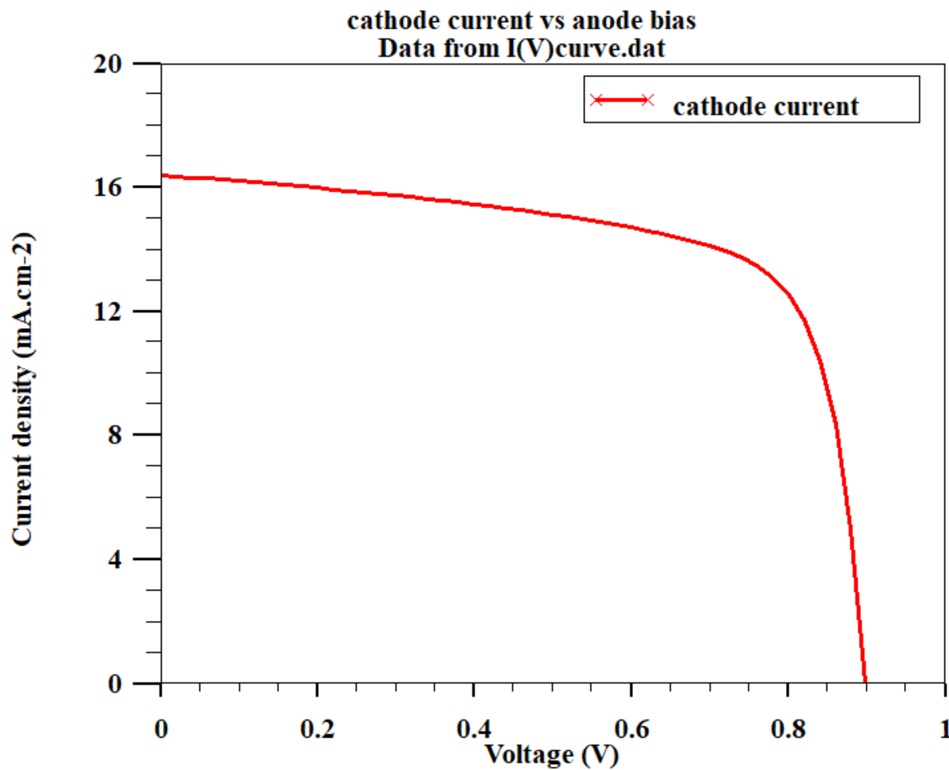

Figure 3.6 I-V characteristic plotted by the instruction TonyPlot.

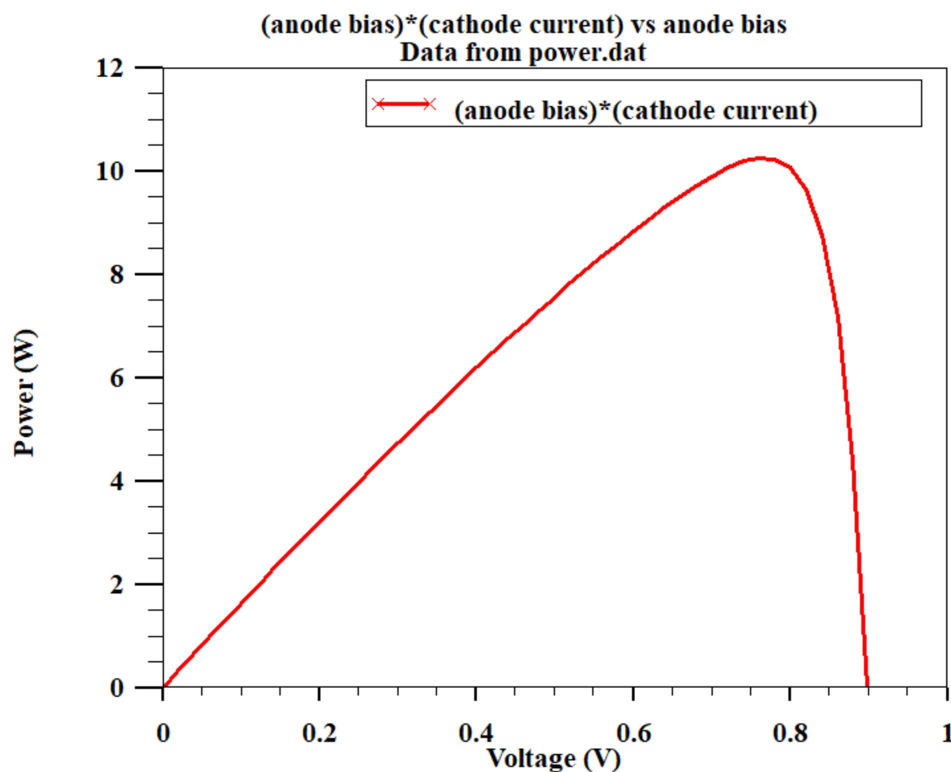

Figure 3.7 P-V characteristic plotted by the instruction TonyPlot.

3.9 Conclusion

This chapter concerns the mathematical model describing electronic devices such as solar cells, this model is formed by the basic semiconductor equations (Poisson's equation, Carrier continuity equations and the transport equations), physical model used for the simulation of the density of states of a-Si: H, steady-state trap recombination and trap-assisted tunneling models for the TRJ are also presented. In this work, the simulation software Silvaco-Atlas used for the simulation of the solar cells is also described by presenting the numerical simulation for a-Si:H solar cell as an example.

Chapter 3 references

[1] A. U. Manual, "Santa Clara, CA: Silvaco." Inc, 2017.

[2] M. J. Powell and S. C. Deane, "Improved defect-pool model for charged defects in amorphous silicon," *Phys. Rev. B*, vol. 48, no. 15, p. 10815, 1993.

[3] M. J. Powell and S. C. Deane, "Defect-pool model and the hydrogen density of states in hydrogenated amorphous silicon," *Phys. Rev. B*, vol. 53, no. 15, p. 10121, 1996.

[4] A. Kosarian and P. Jelodarian, "Modeling and Optimization of Advanced Single-and Multijunction Solar Cells Based on Thin-Film a-Si: H/SiGe Heterostructure," *ISRN Renew. Energy*, vol. 2011, 2011.

[5] S. T. Chang, M. Tang, R. Y. He, W.-C. Wang, Z. Pei, and C.-Y. Kung, "TCAD simulation of hydrogenated amorphous silicon-carbon/microcrystalline-silicon/hydrogenated amorphous silicon-germanium PIN solar cells," *Thin Solid Films*, vol. 518, no. 6, pp. S250–S254, 2010.

[6] R. van Swaaij, R. Kind, and M. Zeman, "Recombination efficacy in a-Si: H pin devices," *J. Non. Cryst. Solids*, vol. 358, no. 17, pp. 2190–2193, 2012.

[7] K. Ding *et al.*, "Characterization and simulation of a-Si: H/μc-Si: H tandem solar cells," *Sol. energy Mater. Sol. cells*, vol. 95, no. 12, pp. 3318–3327, 2011.

[8] S. T. Chang, B.-F. Hsieh, and Y.-C. Liu, "A simulation study of thin film tandem solar cells with a nanoplate absorber bottom cell," *Thin Solid Films*, vol. 520, no. 8, pp. 3369–3373, 2012.

[9] M. Riaz, A. C. Kadhim, S. K. Earles, and A. Azzahrani, "Variation in efficiency with change in band gap and thickness in thin film amorphous silicon tandem heterojunction solar cells with AFORS-HET," *Opt. Express*, vol. 26, no. 14, pp. A626–A635, 2018.

[10] K. Shaoying, W. Chong, P. Tao, Y. Jie, and Y. Yu, "Numerical simulation of the performance of the a-Si: H/a-SiGe: H/a-SiGe: H tandem solar cell," *J. Semicond.*, vol. 35, no. 3, p. 34013, 2014.

[11] A. Garcia-Rivera, E. Comesaña, A. J. Garcia-Loureiro, R. Valin, J. A. Rodríguez, and M. Vetter, "Simulation of a-Si: H dual junction solar cells," in *2013 Spanish Conference on Electron Devices*, 2013, pp. 373–376.

[12] M. Nawaz, "Computer analysis of thin-film amorphous silicon heterojunction solar cells," *J. Phys. D. Appl. Phys.*, vol. 44, no. 14, p. 145105, 2011.

Chapter 4:
Results and discussion

4.1 Introduction

a-Si:H and its alloys are important thin film silicon semiconductor materials for solar cells which have emerged as a source of renewable energy for large-scale terrestrial application due to the abundant material, lower cost and lower temperature of fabrication processes compared to other technologies [1].

The absorber materials for thin film silicon solar cells cover a big family of silicon-based alloys. a-Si:H is one of the earliest studied materials obtained by radio-frequency glow discharge [2, 3]. The direct bandgap is typically in the range of 1.7 to 1.9 eV; it strongly absorbs the light with wavelength shorter than 800 nm. An a-Si:H layer of a few hundred nanometers is enough to capture most of the relevant photons. On the contrary, μc-Si:H [4 – 6] is a very different absorber material from a-Si:H. μc-Si:H has an indirect bandgap of 1.12 eV, the narrower bandgap allows μc-Si:H to absorb the near-infrared light. The indirect bandgap results in much weaker absorption coefficient and much larger thickness needed to have adequate optical absorption. The thickness of μc-Si:H absorber layer can vary from 1 to 5 μm, the practical maximum of the thickness is decided by the electronic quality of the absorber material. Interestingly, by alloying the atoms of other elements with silicon and hydrogen, various bandgaps rather than that of a-Si:H or μc-Si:H can be obtained. Alloying with the large Ge atoms leads to the smaller bandgaps of hydrogenated amorphous silicon germanium (a-SiGe*x*:H) [7 – 9] in the range 1.4 to 1.7 eV. It has been reported that the band gap of a-Si:H can also be increased to 2 eV or more by incorporating oxygen at a concentration of only about 3% [10, 11] and with a good optoelectrical property. Alloying a-Si:H with carbon (a-SiC:H) allows increasing of the band-gap up to 2.7 eV [12]. All these alloys, presenting band gap values either above or below the one of pure a-Si:H, can be profitably used in thin-film silicon multi-junction solar cells as absorber, window or intermediate layers [13 – 16].

In this chapter, thin film silicon solar devices based on double and triple junction's concepts are investigated with the use of the Silvaco-Atlas software. This chapter will begin by defining the structure of the single and double junction solar cell a-Si: H/μc-Si:H incorporating n-p type μc-Si:H TRJ between the a-Si:H top and μc-Si:H bottom cells. The effect of donor and acceptor concentrations of the TRJ layers, and the effect of TRJ thickness on the photovoltaic parameters (V_{oc}, J_{sc}, FF, η) of the double junction solar cell are studied in order to optimize the μc-Si:H TRJ structure. a-Si:H/a-Si:Ge:H/μc-Si:H triple junction based solar cells incorporating optimized μc-Si:H TRJs between a-Si:H top, a-SiGe:H middle and μc-Si:H bottom cells have been extensively studied. Optimizations of thicknesses of triple junction solar cell active i-

layers and bandgaps, and the dependence of the triple junction solar cell performance on defect states are also detailed in order to explore the potential of such device structures to achieve high performances.

4.2 aSi:H/μc-Si:H double junction solar cell

The a-Si:H/μc-Si:H double junction solar cell with a-Si:H as the top cell and μc-Si:H as the bottom cell achieved the high conversion efficiency [17], which was proposed by the Institute of Microtechnique, Switzerland (IMT), in 1994, with an initial efficiency of 9.1% [18], and then has received much attention through the following decades. a-Si:H/μc-Si:H tandem solar cells of 12.63% and 12.69% are developed respectively by EPFL, Neuchâtel [19] and AIST, Tsukuba [20]. The a-Si:H/μc-Si:H tandem solar cell consists of two p–i–n solar cells connected in a serial configuration. This configuration leads to a junction between the n-type layer of the top cell to the p-type layer of the bottom one and acts as a reverse biased diode placed opposite to the p-i-n cell. Tunnel recombination junction diodes are typically used between the solar cells to solve this reverse bias problem.

4.2.1 Device structure of aSi:H/μc-Si:H double junction solar cell

The device structure which we simulated is an a-Si:H/μc-Si:H double junction solar cell with p-i-n configurations. The different band-gaps of 1.7 and 1.1 eV for a-Si:H and μc-Si:H can effectively absorb a wide solar spectrum (300-1000 nm), the a-Si:H component cell absorbs photons with energies above 1.7 eV, photons with lower energies, which pass through the a-Si:H top cell, get a chance to be absorbed by the μc-Si:H bottom cell. We simulated an experimental a-Si:H/μc-Si:H tandem solar cell reported in [20]. The thicknesses of the top a-Si:H and bottom μc-Si:H cells are 350 nm and 2.5 μm, respectively. The numerical simulations are performed for the tandem a-Si:H/μc-Si:H solar cell with the configurations: SiO_2 (370 nm)/ZnO (40 nm)/p-a-Si:H (13 nm)/i-a-Si:H (350 nm)/n-a-Si:H (20 nm)/n-μc-Si:H (5 nm)/p-μc-Si:H (5 nm)/p-μc-Si:H (20 nm)/i-μc-Si:H (2500 nm)/n-μc-Si:H (15 nm)/ZnO (40 nm)/Ag (100 nm)/Al (200 nm). The transparent conductive oxide (TCO) layer of ZnO serves as the front anode contact and Aluminum (Al) represents the back cathode contact of the tandem solar cell.

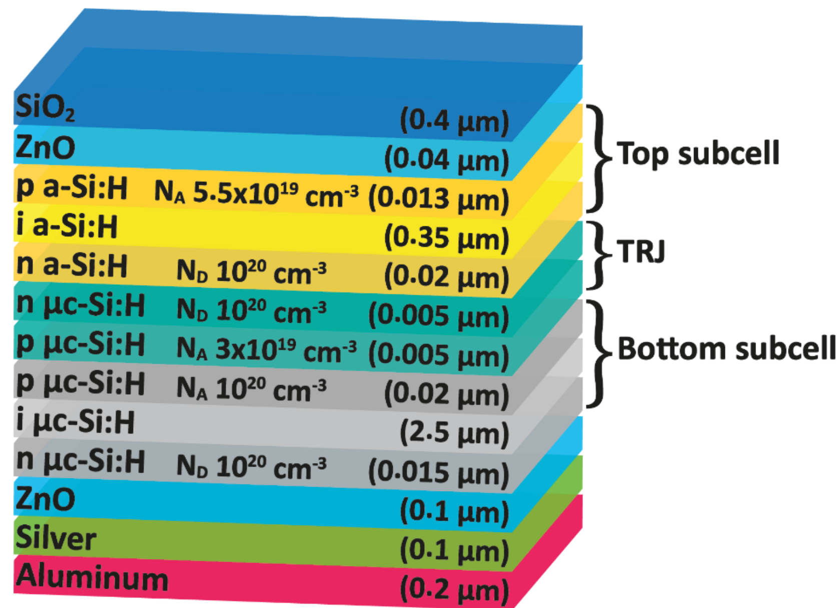

Figure 4.1 Structure used in the simulation of a p-i-n (a-Si:H)/p-i-n (µc-Si:H) tandem solar cell mechanically stacked with n-p (µc-Si:H) tunnel recombination junction cell.

The construction of this structure in the Atlas simulator is shown in Fig. 4.2.

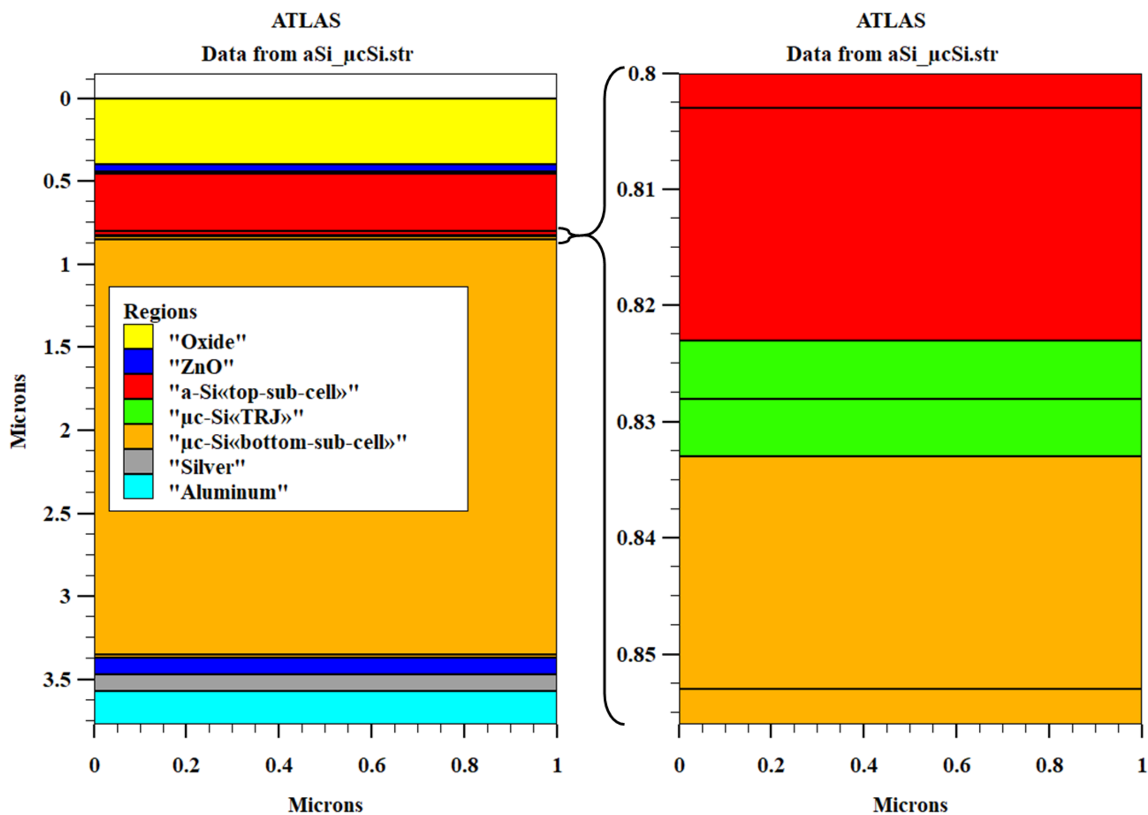

Figure 4.2 Two-dimensional simulated structure of the a-Si:H/µc-Si:H tandem solar cell with Atlas-Silvaco.

The definition of the structure in the Atlas simulator consists of four stages: definitions of mesh, regions, doping and electrodes. To proceed with the numerical simulation, it is necessary to define the mesh of the structure. The mesh divides the structure to simulate in small cells to allow the numerical resolution of the fundamental equations of the semiconductors (continuity and Poisson equations for the electrons and for the holes) in order to find the distribution of the carriers of charges, the electric potential and current. The mesh must be the finest possible for obtaining good simulation results. In our work, we used the mesh shown in figure 4.3

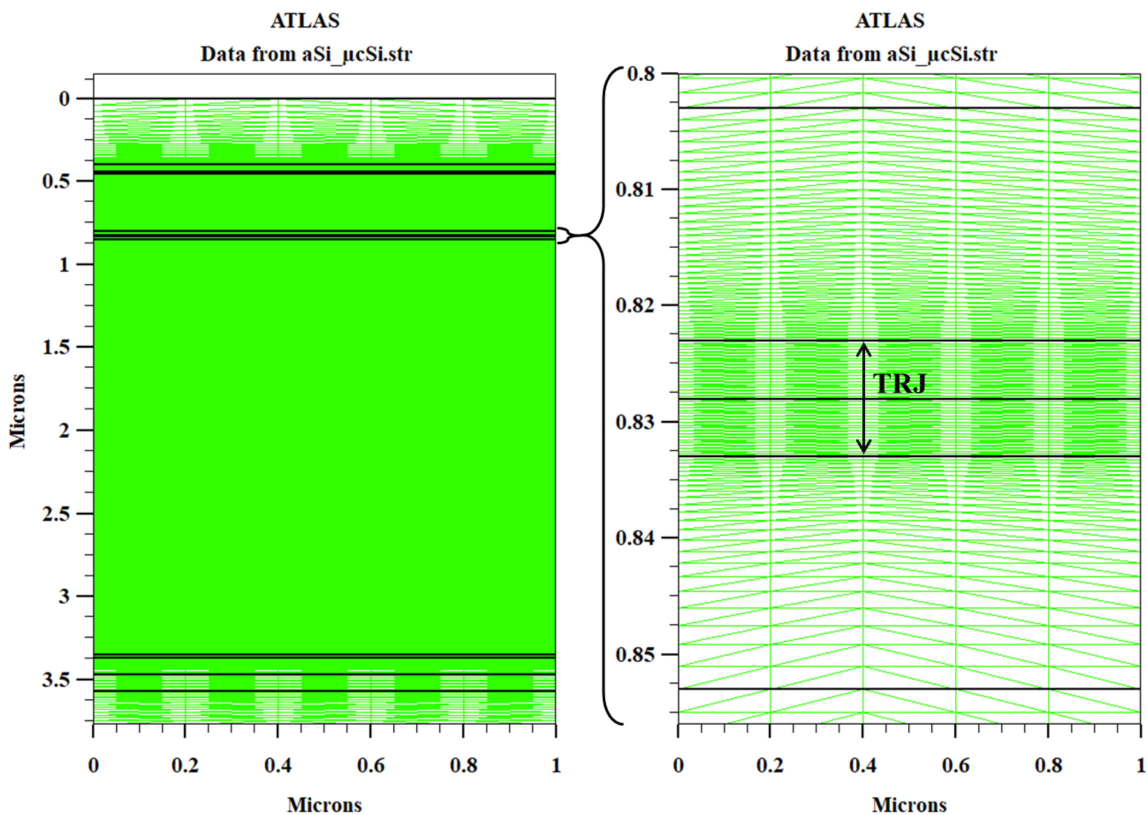

Figure 4.3 Mesh of the tandem solar cell with the zoom of the mesh in the TRJ part.

After the operation of the mesh, comes the step of definition of the regions. These determine the different layers forming the solar cell. We used rectangular regions while defining the material of each of them. The top cell has the a-Si:H material for each layer (p, i and n layers), the TRJ has the µc-Si:H material for n-type and p-type layers and the bottom cell has the µc-Si:H material for each layer (p, i and n layers). We also used a layer of silicon oxide (SiO_2) acting as an antireflection layer of the solar cell. After selecting the regions and the

materials, comes the step of defining the electrodes. The ZnO anode is located on the p a-Si:H layer, and the aluminum cathode is made on the bottom surface of the tandem solar cell. The a-Si:H p and n type layers of the top cell are doped with acceptor and donor concentrations of the order of 5.5×10^{19} and 10^{20} cm^{-3} respectively. The µc-Si: H n and p type layers of the TRJ are doped with donor and acceptor concentrations of the order of 10^{20} and 3×10^{19} cm^{-3} respectively. The µc-Si: H p and n type layers of the bottom cell are doped with acceptor and donor concentrations of the order of 10^{20} and 10^{20} cm^{-3} respectively.

4.2.2 Simulation models and parameters

The tandem cell parameters related to each layer and material are summarized in Table 4.1 and defect details parameters of a-Si:H and µc-Si:H are listed in Tables 4.2 and 4.3. Their detailed descriptions are listed as follows: (N_D and N_A) are the doping concentrations of donors and acceptors ; E_g is the mobility gap energy; (N_c and N_v) are the effective densities of states of the conduction and valence bands; χ is the affinity; ε is the relative permittivity; (μ_e and μ_h) are the electron and hole mobilities; (N_{TA} and N_{TA}) are the effective densities of sates at conduction and valence band edges. For the ZnO and µ-Si:H materials, the optical parameters such as the wavelength-dependent refractive index $n(\lambda)$ and extinction coefficient $k(\lambda)$ are obtained from [21] and [22], respectively. For the a-Si:H material, the Tauc-Lorentz dielectric function with Urbach Tail model was used for the calculation of n and k [23]. The optical constants for the layers Silver (Ag), Aluminum (Al) and silicon oxide (SiO_2) are included in the Silvaco-atlas sopra database where a set of optical constants of various materials are available. Reflection loss from the surface of the tandem cell has also been integrated into the model. The double junction solar cell simulated operates at a temperature set to 300 K and under a global AM1.5 spectrum with a power density of 100 mW.cm^{-2}.

Layer properties	a-Si:H top cell			μc-Si:H TJR		μc-Si:H bottom cell		
	p	i	n	N	p	P	i	n
Thikness (nm)	13	350	20	5	5	20	2500	15
N_D (cm^{-3})	-	-	10^{20}	10^{20}	-	-	-	10^{20}
N_A (cm^{-3})	5.5×10^{19}	-	-	-	3×10^{19}	10^{20}	-	-
E_g (eV)	1.71	1.71	1.71	1.16	1.16	1.16	1.16	1.16
N_c (cm^{-3})	10^{21}	10^{21}	10^{21}	3.5×10^{20}	3.5×10^{20}	3.5×10^{20}	3.5×10^{20}	3.5×10^{20}
N_v (cm^{-3})	10^{21}	10^{21}	10^{21}	3.5×10^{20}	3.5×10^{20}	3.5×10^{20}	3.5×10^{20}	3.5×10^{20}
χ (eV)	3.89	3.89	3.89	4.05	4.05	4.05	4.05	4.05
ε	11.9	11.9	11.9	11.9	11.9	11.9	11.9	11.9
μ_e (cm^2/Vs)	1	1	1	20	20	20	20	20
μ_h (cm^2/Vs)	0.6	0.6	0.6	4	4	4	4	4

Table 4.1 Electrical parameters for tandem solar cell used in this work [24 - 36].

Defect states parameters	a-Si:H top cell			μc-Si:H TJR		μc-Si:H bottom cell		
	p	i	n	n	p	P	i	n
Tail states								
N_{TA}, N_{TD} (cm^{-3}.eV^{-1})	10^{21}	10^{21}	10^{21}	2×10^{20}	2×10^{20}	2×10^{20}	2×10^{20}	2×10^{20}
W_{ta} (eV)	0.025	0.025	0.025	0.01	0.01	0.01	0.01	0.01
W_{td} (eV)	0.043	0.043	0.043	0.02	0.02	0.02	0.02	0.02
σ_{na}(cm^2)	10^{-17}	10^{-17}	10^{-17}	10^{-17}	10^{-17}	10^{-17}	10^{-17}	10^{-17}
σ_{pa}(cm^2)	10^{-17}	10^{-17}	10^{-17}	10^{-17}	10^{-17}	10^{-17}	10^{-17}	10^{-17}
σ_{nd}(cm^2)	10^{-17}	10^{-17}	10^{-17}	10^{-17}	10^{-17}	10^{-17}	10^{-17}	10^{-17}
σ_{pd}(cm^2)	10^{-17}	10^{-17}	10^{-17}	10^{-17}	10^{-17}	10^{-17}	10^{-17}	10^{-17}

Table 4.2 Defect states parameters of tail states [22, 30, 33, 37, 38].

Defect states parameters	a-Si:H top cell			μc-Si:H TJR		μc-Si:H bottom cell		
	p	I	N	n	P	p	i	n
Gaussian model								
N_{GA}, N_{GD}(cm^{-3})	-	-	-	10^{15}	10^{15}	10^{15}	10^{15}	10^{15}
$E_{Ga}\left(\text{eV}\right)$	-	-	-	0.8	0.8	0.8	0.8	0.8
$E_{Gd}\left(\text{eV}\right)$	-	-	-	0.8	0.8	0.8	0.8	0.8
$W_{Ga}\left(\text{eV}\right)$	-	-	-	0.2	0.2	0.2	0.2	0.2
$W_{Gd}\left(\text{eV}\right)$	-	-	-	0.188	0.188	0.188	0.188	0.188
$\sigma_{nGa}(\text{cm}^2)$	-	-	-	10^{-17}	10^{-17}	10^{-17}	10^{-17}	10^{-17}
$\sigma_{pGa}(\text{cm}^2)$	-	-	-	10^{-17}	10^{-17}	10^{-17}	10^{-17}	10^{-17}
$\sigma_{nGd}(\text{cm}^2)$	-	-	-	10^{-17}	10^{-17}	10^{-17}	10^{-17}	10^{-17}
$\sigma_{pGd}(\text{cm}^2)$	-	-	-	10^{-17}	10^{-17}	10^{-17}	10^{-17}	10^{-17}
Defect Pool Model								
$U\left(\text{eV}\right)$	0.2	0.2	0.2	-	-	-	-	-
σ (eV)	0.19	0.19	0.19	-	-	-	-	-
$E_p\left(\text{eV}\right)$	1.22	1.22	1.22	-	-	-	-	-
N_{SiSi} (cm^{-3})	2×10^{23}	2×10^{23}	2×10^{23}	-	-	-	-	-
H (cm^{-3})	10^{21}	10^{21}	10^{21}	-	-	-	-	-
$\sigma_n{}^{+}$ (cm^2)	2.3×10^{-15}	2.3×10^{-15}	2.3×10^{-15}	-	-	-	-	-
$\sigma_n{}^{0}$ (cm^2)	5×10^{-16}	5×10^{-16}	5×10^{-16}	-	-	-	-	-
$\sigma_p{}^{-}$ (cm^2)	2.3×10^{-15}	2.3×10^{-15}	2.3×10^{-15}	-	-	-	-	-
$\sigma_p{}^{o}$ (cm^2)	5×10^{-16}	5×10^{-16}	5×10^{-16}	-	-	-	-	-

Table 4.3 Defect states parameters of Gaussian and DPM distributions [22, 30, 37].

4.2.3 Single a-Si:H and μc-Si:H solar cells performances

The first simulation step consists of the simulation of single a-Si:H and μc-Si:H based p-i-n solar cells separately. The parameter values adopted in the simulation are given in Tables 4.1-3.

Simulation studies are carried out using an a-Si:H p–i–n structure consisting of ZnO/p-a-Si:H(13 nm)/i-a-Si:H(220 nm)/n-a-Si:H(20 nm)/ZnO/Silver/Al, which is shown in figure 4.4.

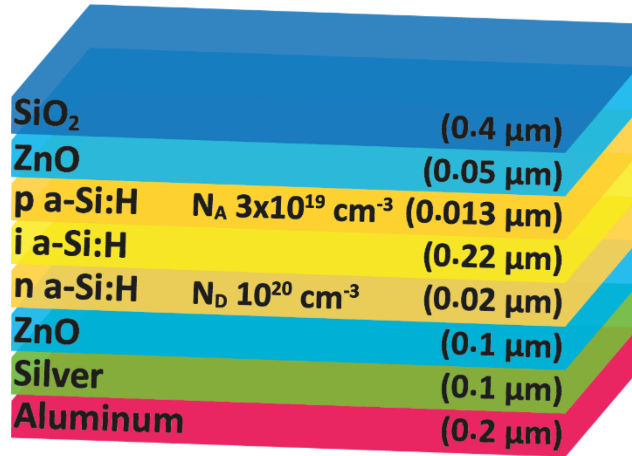

Figure 4.4 Schematic structure of single a-Si:H top-cell.

A transparent conductive oxide layer of ZnO is used as the front electrical contact. Between the thin p-type a-Si:H layer and thin n-type a-Si:H layer a thick intrinsic a-Si:H layer is deposited, which is used as an absorbing layer. ZnO/Silver/Al are used to reduce the light transmission loss through the back electrical contact. Acceptor (N_A) and donor (N_D) concentrations of 3×10^{19} cm^{-3} and 10^{20} cm^{-3} are used for the a-Si:H p-i-n solar cell. The band-gap of a-Si:H can range from 1.7 to 1.9 eV [39], the band gap of p-, i- and n-type a-Si:H layers are set to 1.7 eV. The 220 nm thickness i-layer of the simulated a-Si:H p-i-n solar cell is equal to the i-thickness of the a-Si:H p-i-n solar cell obtained experimentally by triode PECVD which shows a stabilized efficiency η of 10.226% (J_{sc}=16.36 mA/cm^2, V_{oc}=0.896V, and FF=69.8%) [20]. The normally incident light was assumed to be on the top face of the a-Si:H p–i–n solar cell. In a thin film a-Si:H or μc-Si p–i–n solar cell, electron-hole pairs are generated in the i-absorber layer. The electric field created along the i-layer by the p- and n-layers activates the separation of electron-hole pairs and drift electrons to the n-layer and holes to the p-layer. At the p- and n- layers, the charge carriers are collected by electrical contacts and this result in the flow of photocurrent in the cell. Figure 4.5 shows the structure of the single a-Si:H top-cell simulated by the Atlas-Silvaco software.

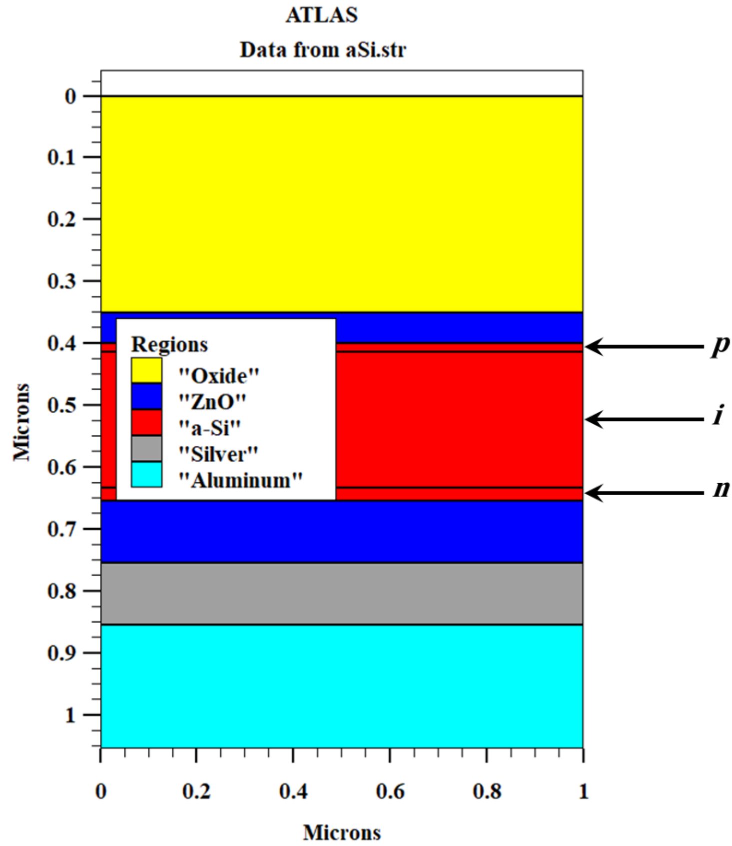

Figure 4.5 Schematic structure of single a-Si:H top-cell.

The simulation has been used to study a μc-Si:H p–i–n structure consisting of ZnO/ p-μc-Si:H (20 nm) / i-μc-Si:H (2500 nm)/ n-μc-Si:H (15 nm) /ZnO/Silver/Al as shown in figure 4.6.

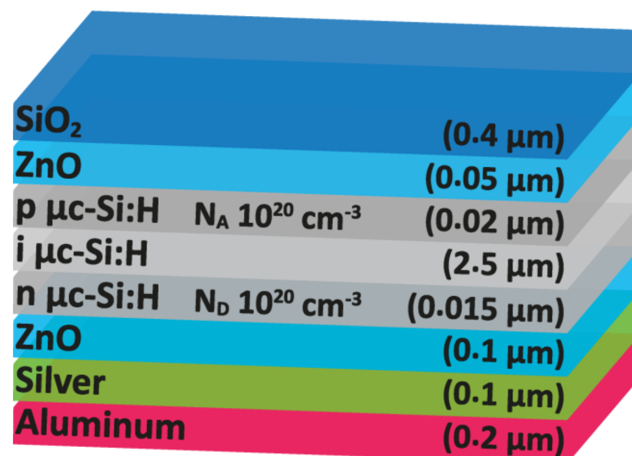

Figure 4.6 Schematic structure of single μc-Si:H bottom-cell.

A thin layer of p- type μc-Si:H was kept over the ZnO layer followed by a thick layer of intrinsic μc-Si:H and then a thin layer of n-type μc-Si:H. The light was assumed to be normally incident on the top face of the μc-Si:H p–i–n solar cell. The band gap of p-, i-, and n-layers are set to 1.16 eV, respectively. Acceptor and donor concentrations of 10^{20} cm^{-3} are used for the μc-Si:H p-i-n solar cell. Figure 4.7 illustrates the structure of the single μc-Si:H bottom-cell simulated by the Atlas Silvaco simulator.

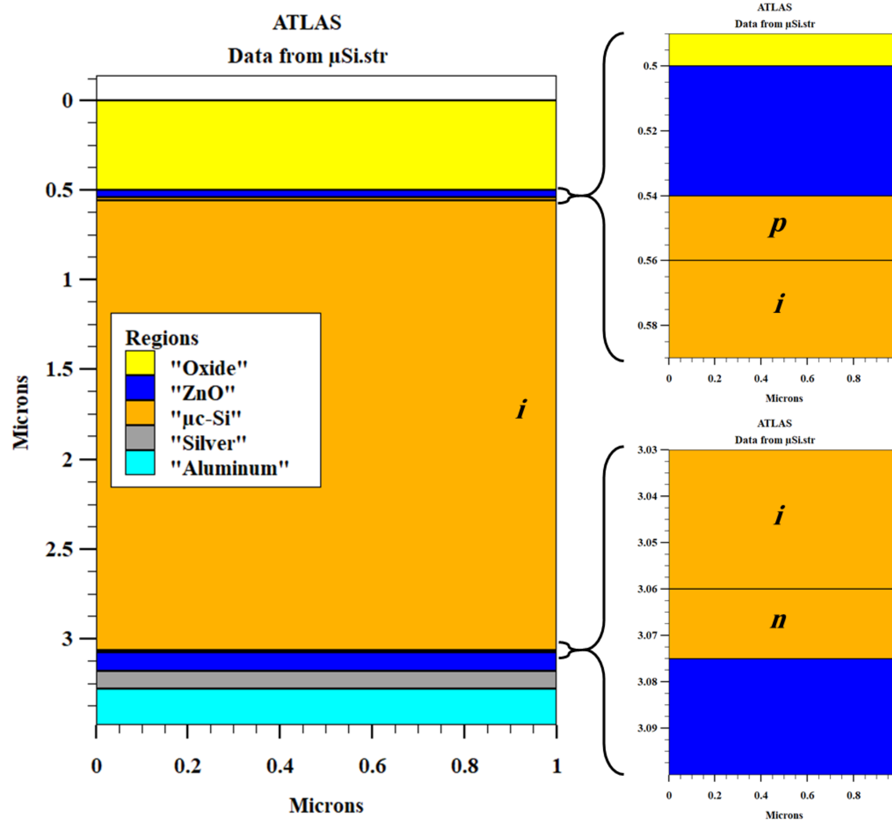

Figure 4.7 Schematic structure of single μc-Si:H bottom-cell.

The *J–V* characteristics simulated for the single a-Si:H and μc-Si:H solar cells are presented in figure 4.8. Table 4.4 shows the photo electrical parameters of the single a-Si:H solar cell extracted from the corresponding *J–V* characteristic together with experimental results for comparison. The present results indicate a good agreement with experimental record results for a-Si:H solar cells. The photo electrical parameters for the single μc-Si:H bottom-cell extracted from the corresponding *J–V* characteristic are summarized in Table 4.4. The simulation values of the short-circuit current and the fill factor are reasonable, but the open circuit voltage is low. The resulting conversion efficiency of 6.5% which is lower than that of the a-Si:H solar cell is mainly due to lower open-circuit voltage.

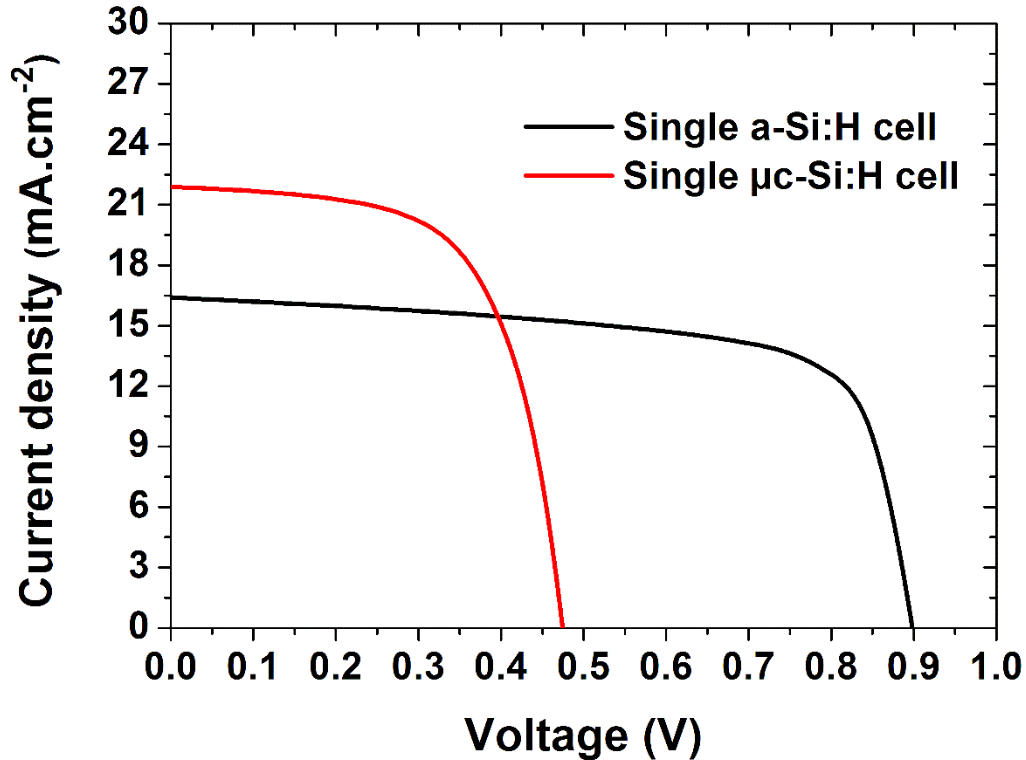

Figure 4.8 *J–V* characteristics for the single a-Si:H and µc-Si:H solar cells.

	J_{sc}(mA/cm^2)	V_{oc}(V)	*FF* (%)	η (%)
Single a-Si:H cell simulation	16.39	0.89	69.44	10.22
Single a-Si:H cell experiment [20, 40]	16.36	0.89	69.8	10.22
Single µc-Si:H cell simulation	21.89	0.47	63	6.50

Table 4.4 Simulation and experiment photovoltaic parameters of a-Si:H and µc-Si:H solar cells.

4.2.4 a-Si:H/µc-Si:H double junction solar cell performance

Matsui et al. [20] investigated a-Si:H/µc-Si:H tandem solar cells experimentally, top-cell thickness was increased to 350 nm by taking advantage of the improved metastability of the a-Si:H absorber deposited by triode PECVD. The thickness of the bottom cell was 2.5 µm. Such device shows a stabilized efficiency η of 12.696±0.4 % (J_{sc}=13.45 mA/cm^2, V_{oc}=1.342 V, and *FF*=70.2 %).

In our work, the a-Si:H/μc-Si:H tandem solar cell structure is shown in figure. 4.1. The *J-V* characteristics of the a-Si:H top-cell, the μc-Si:H bottom-cell and the whole a-Si:H/μc-Si:H tandem-cell are shown together in figure 4.9.

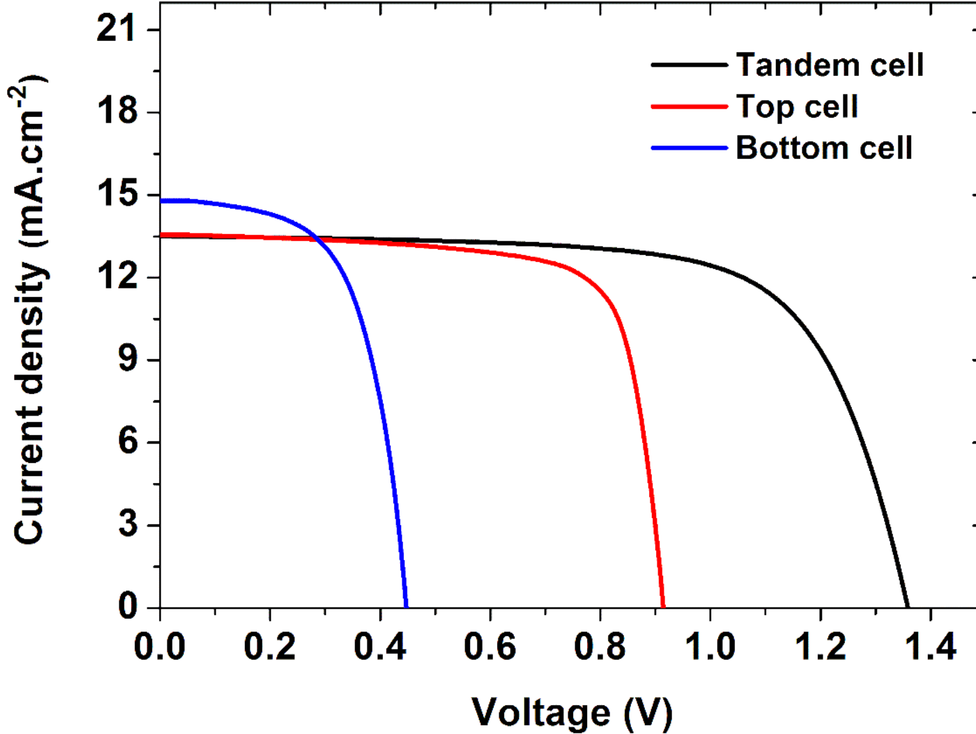

Figure 4.9 *J–V* characteristics for the a-Si:H top-cell, μc-Si:H bottom-cell and a-Si:H/μc-Si:H tandem solar cell.

The simulated photoelectrical parameters together with experimental results are indicated in Table 4.5. In order to plot the *J-V* curves of the top and bottom cells, two groups of anodes and cathodes contacts of the top and bottom cells were respectively placed on the top, and bottom layers of the top and bottom cells. In the tandem cell, the short-circuit current density (J_{sc}) is limited by the low short-circuit current density of the top cell, such that the tandem J_{sc} of 13.5 mA/cm^2 is about equal to the top-cell J_{sc} of 13.56 mA/cm^2. On the other hand, the tandem V_{oc} (1.353 V) is equal to the summation of the top-cell V_{oc} (0.907 V) and the bottom-cell V_{oc} (0.446 V). From these results, the correct operation of the series connected a-Si:H and μc-Si:H cells forming the tandem cell is demonstrated. In addition, the fill factor of the tandem cell (69.46%) lies within the fill factors of the top (74.93%) and of the bottom (60.41%) solar cells. Clearly, the increase of V_{oc} of the tandem cell is the cause of the efficiency improvement to 12.69% with respect to those of the single a-Si:H (10.22%) and μc-Si:H (6.5%)

cells. The simulation results with the tandem cell efficiency η of 12.69% show a good correlation with experimental record results in a-Si:H/µc-Si:H tandem solar cells, thus validating the simulation models and the parameters chosen for the simulation. The comparison between the results of the µc-Si:H single cell with those of the µc-Si:H bottom solar cell in the tandem solar cell is given, we notice that the photoelectrical parameters of the µc-Si:H bottom-cell have significantly decreased owing to the top layers absorbing some of the incident light. The photoelectrical parameters of the a-Si:H top solar cell in the tandem solar cell, as compared to those of the a-Si:H single cell, indicate small photoelectrical parameters reductions owing to smaller light absorption by the bottom layers.

	J_{sc}(mA/cm^2)	V_{oc}(V)	FF (%)	η (%)
a-Si:H top-cell simulation	13.56	0.907	74.93	9.22
µc-Si:H bottom-cell simulation	14.79	0.446	60.41	3.98
a-SiH/µc-Si:H tandem cell simulation	13.50	1.353	69.46	12.69
a-SiH/µc-Si:H tandem cell experiment [20, 40]	13.45	1.34	70	12.69

Table 4.5 Simulation photovoltaic parameters of the top, bottom and tandem solar cells together with experimental results of the tandem solar cell.

4.2.5 Effect of TRJ on double junction solar cell

The TRJ should be an Ohmic contact with no rectifying behavior to allow the electrons from the top cell and holes from the bottom cell to recombine and form a continue current flow [41]. If the TRJ cannot provide enough recombination, light-induced dipoles would be created, due to the accumulation of trapped electrons or holes, which would reduce the electrical field in the top and bottom cells, and then attain the open-circuit voltage and fill factor of the entire tandem solar cells [42]. Numerical simulations show that a low mobility gap and a highly defective layer inserted between the n-type layer of the top cell and the p-type layer of the bottom one is useful to recombination [43]. Furthermore, Rubinelli et al. [44] studied in detail by simulation using the computer code D-AMPS the kinetics controlling the electrical transport of a p-i-n µc-Si:H tunnel recombination junction inserted in a-Si:H/a-Si:H tandem solar cells yielding high conversion efficiencies. In our work, we used a TRJ having the simple n-µc-Si:H/p-µc-Si:H structure functions as an electrical connection between the a-Si:H top and µc-Si:H bottom cells and utilizes an internal carrier exchange effect. This effect can be

accomplished by the recombination between electrons photogenerated in the top cell with holes photogenerated in the bottom cell through the localised trap states at TRJ n/p interface. In the TRJ and by a tunneling mechanism, the carrier moves to the TRJ interface and reaches the recombination centers as it can be seen in figure 4.10.

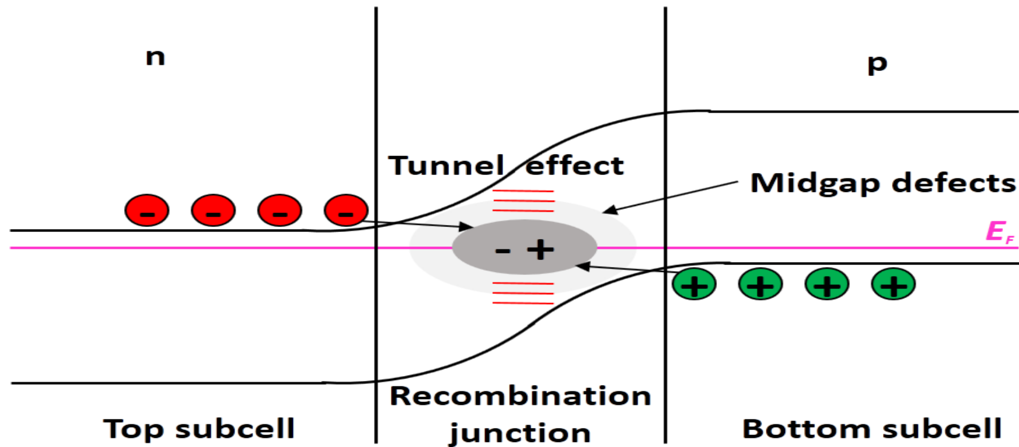

Figure 4.10 Band diagram explaining tunneling of electrons and holes to midgap states and their subsequent recombination.

The numerical simulation of the tandem solar cell performance is increasingly sensitive to the design of the TRJ structure and the model and it can easily diverge if the grid mesh size and the model are not selected adequately. The design of the TRJ and the setting of the adequate models and parameters in the simulation are, therefore, particularly important. According to the literature, the Shockley–Read–Hall (SRH) recombination model is not able to reproduce the experimentally observed characteristics of a-Si:H/a-Si:H tandem solar cells such as the open-circuit voltage and the fill factor [45, 46], the consideration of the trap-assisted tunneling model controlling the transport of carriers across the TRJ allowing to reproduce the experimental open-circuit voltage of a-Si:H/a-Si:H tandem solar cells [46, 47]. In our numerical simulation, we defined the recombination mechanism inside the tunnel recombination junction by the trap-assisted tunneling recombination model in the silvaco-atlas simulator. The following numerical simulation illustrates the influence of the dopant concentrations and thickness of the TRJ layers on the photoelectrical parameters of the a-Si:H/µc-Si:H tandem solar cell.

4.2.5.a Effect of donor and acceptor concentrations of the TRJ on double junction solar cell

The n-layer µc-Si:H of the TJR plays a very important role in the tandem solar cell as the recombination layer between electrons and holes photogenerated in the top and bottom cells, respectively. We have simulated the photovoltaic parameters of the tandem solar cell as a function of donor concentration N_D of the n-layer µc-Si:H of the TJR. During simulation, the acceptor dopant concentration N_A of the p-layer µc-Si:H of TJR is kept constant at 10^{19} cm^{-3} and all of the other parameters for a-Si:H/µc-Si:H tandem solar cell are set to the same values listed in Tables 4.1-4.3. The variations of the short-circuit current density, the open-circuit voltage, the fill factor and the conversion efficiency as a function of n-layer µc-Si:H dopant concentration N_D of the TRJ are shown in figure 4.11(a-d).

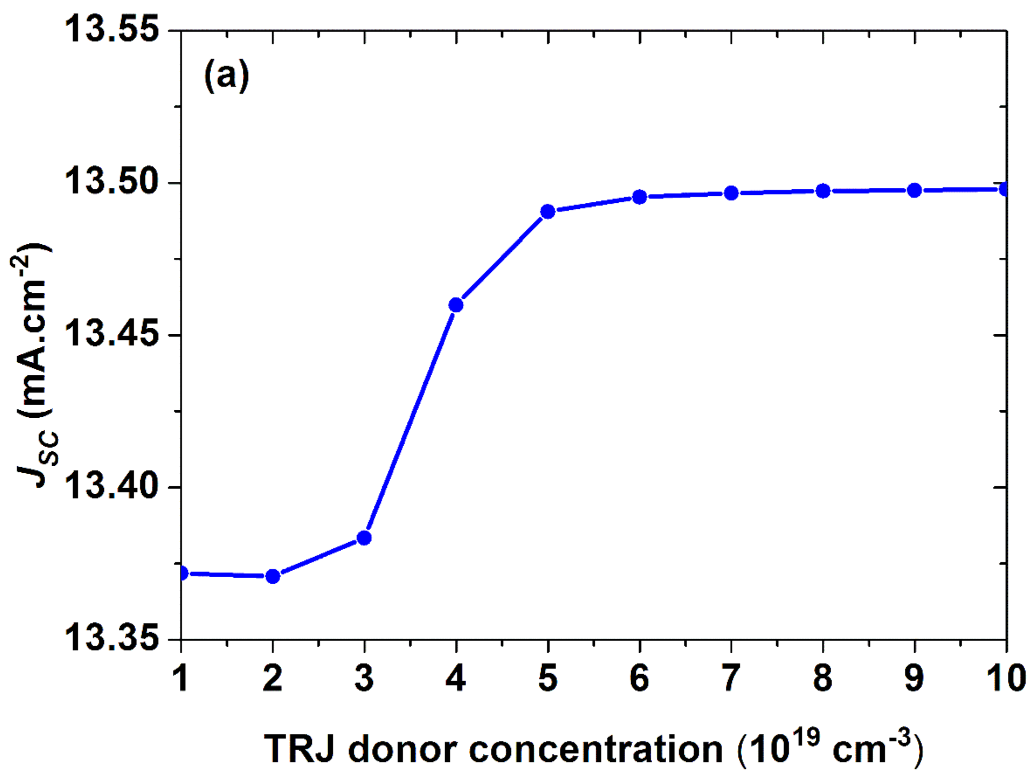

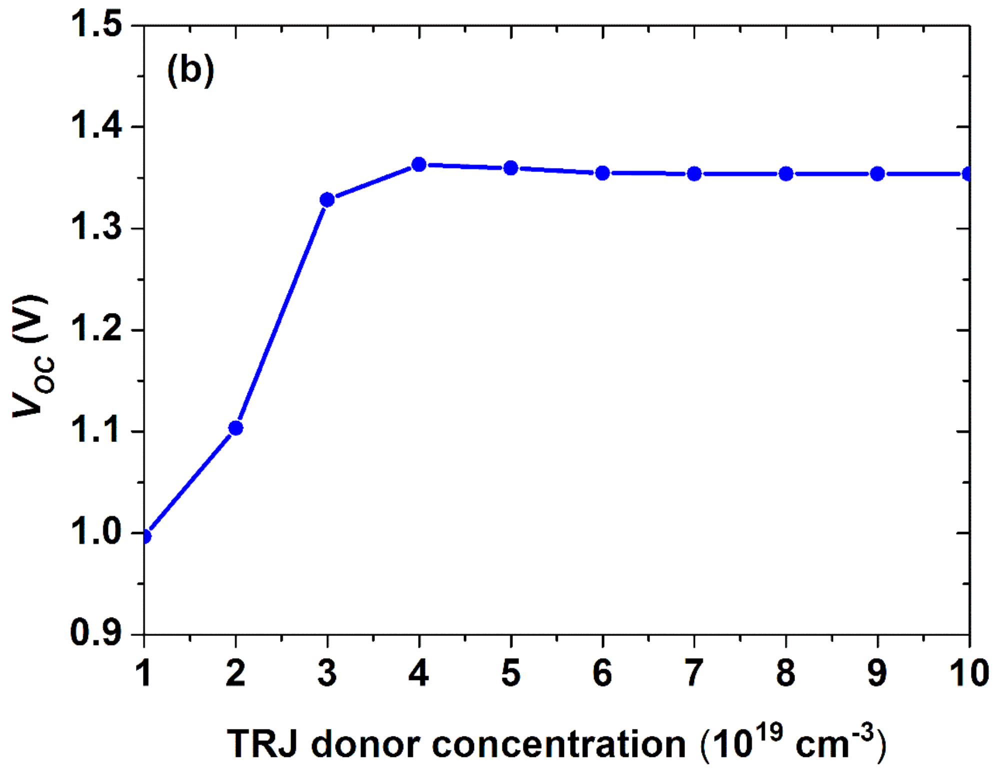
(b)
V_{OC} (V)
1.5
1.4
1.3
1.2
1.1
1.0
0.9
1
2
3
4
5
6
7
8
9
10
TRJ donor concentration (10^{19} cm^{-3})

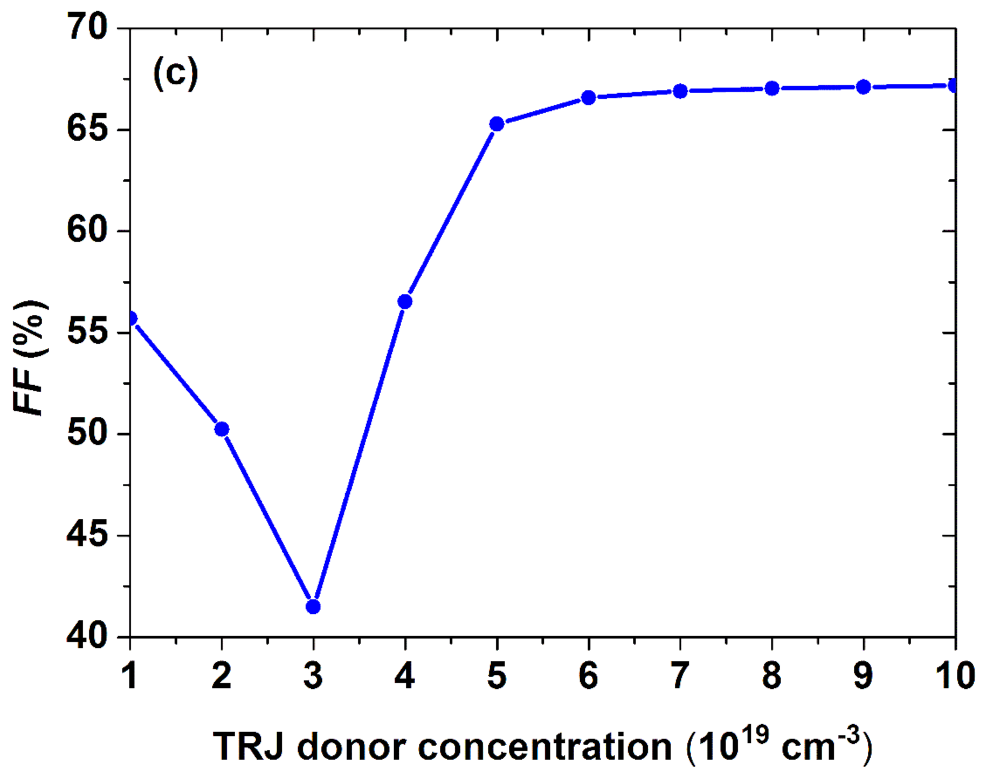
(c)
FF (%)
70
65
60
55
50
45
40
1
2
3
4
5
6
7
8
9
10
TRJ donor concentration (10^{19} cm^{-3})

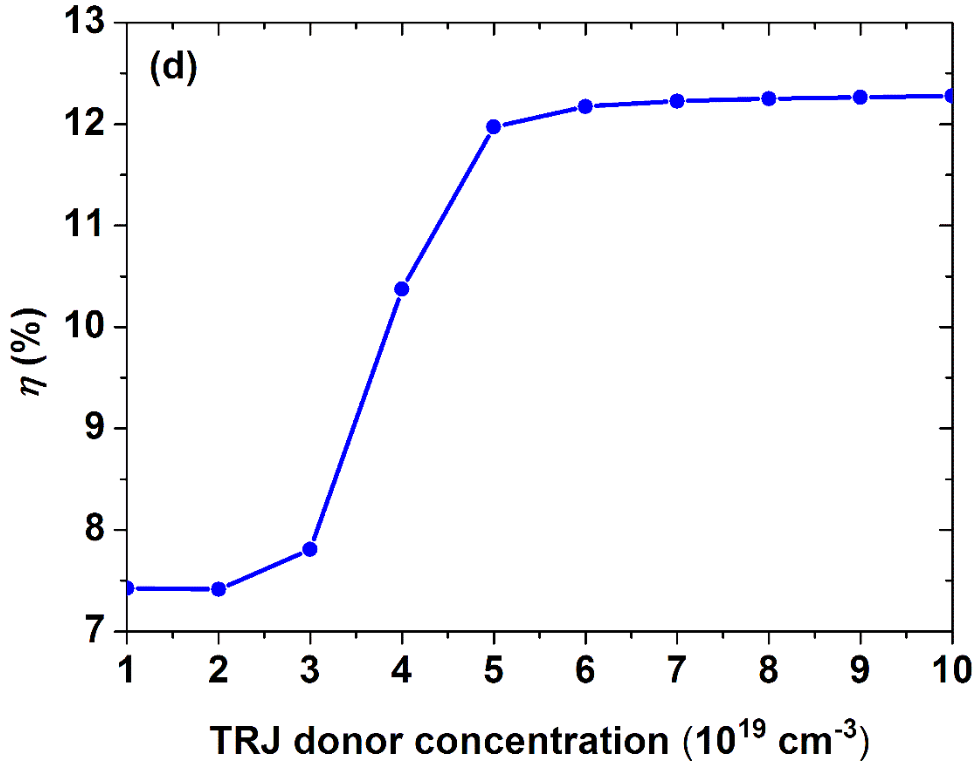

Figure 4.11 Simulated photovoltaic parameters of the a-Si:H/µc-Si:H tandem solar cell as function of the donor concentration N_D of the TRJ.

When the donor concentration N_D increased from 10^{19} cm^{-3} to 2×10^{19} cm^{-3}, J_{sc} remains nearly constant to a value of ~13.37 mA.cm^{-2}. However, with the increasing of the donor concentration N_D in the range 2×10^{19} – 10^{20} cm^{-3} J_{sc} increased slightly from 13.37 mA.cm^{-2} to 13.5 mA.cm^{-2}. Initially V_{oc} was found to continuously increase with the increasing of the donor concentration N_D in the range 10^{19} cm^{-3}–3×10^{19} cm^{-3} and then saturates to a value of 1.35 V. On the other hand, *FF* showed down behavior with the increasing of donor concentration N_D in the range 10^{19} – 3×10^{19} cm^{-3} and it attains minimum value of 41.47 % at 3×10^{19} cm^{-3} and then *FF* increased to 67.17% with the increasing of n layer concentration from 3×10^{19} cm^{-3} to 10^{20} cm^{-3}. The efficiency remains constant to a value of 7.42 % with the increase of the n layer concentration from $1\text{x}10^{19}$ cm^{-3} to 2×10^{19} cm^{-3} but drastically enhanced from 7.42 % to 12.28 % in the n layer concentration range from 2×10^{19} cm^{-3} to 10^{20} cm^{-3}; the conversion efficiency is constant to a value of 12.28 % in the n layer concentration range from 6×10^{19} cm^{-3} to 10^{20} cm^{-3}. The maximum values of J_{sc}, V_{oc}, *FF* and η were found to be 13.5 mA.cm^{-2}, 1.35 V, 67.17% and 12.28%, respectively at n layer concentration of 10^{20} cm^{-3}. The results indicate that the dopant concentration N_D enhances the short-circuit current, the open circuit voltage, the fill factor and

the conversion efficiency. The n-layer concentration of 10^{20} cm^{-3} may be considered an optimized value for getting efficient a-Si:H/μc-Si:H tandem solar cell. figure 4.12 shows the recombination rate around the TRJ for three TRJ n-layer concentrations N_D set to 10^{19}, 4×10^{19}, and 8×10^{19} cm^{-3} under short-circuit case. This figure clearly shows recombination peaks appearing at the tunnel recombination junction. The recombination rate is increased at the p-μc-Si:H region of the tunnel junction due to lower mobility gap of the microcrystalline layers. A closer simulation of the tandem solar cell structure for three concentrations N_D (10^{19}, 4×10^{19}, and 8×10^{19} cm^{-3}) of the TRJ n-layer under thermodynamic equilibrium conditions reveals that the recombination peaks are approximately located at the positions where the Fermi levels cross midgaps. The recombination rate in μc-Si:H tunnel recombination junction is completely dominated by midgap states due to tails in μc-Si:H are very steep and μc-Si:H has a low mobility gap.

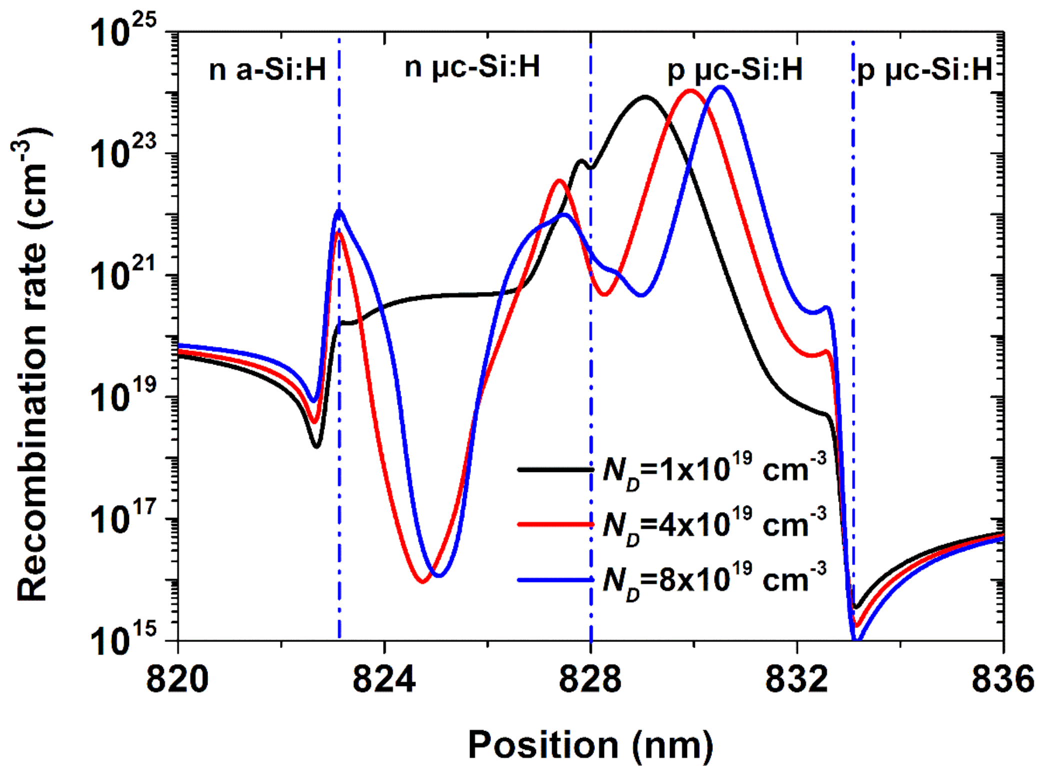

Figure 4.12 Recombination rate around the TRJ for various donor concentrations N_D of the TRJ under short-circuit condition.

This result indicates that a large number of carriers recombine in the tunnel junction, and to this can be attributed that thin recombination layers provide recombination centers for

the recombination of carriers and play an important role in the trapped assisted tunnelling process. The recombination peaks are shifted with TRJ n-layer donor concentration N_D assumed as 10^{19} cm^{-3}, 4×10^{19} cm^{-3}, 8×10^{19} cm^{-3} , respectively, from n/p interface to the inside of the TRJ p-layer and that lead to increasing the conversion efficiency η from 7.42% to 12.23% with increasing TRJ donor concentration N_D from 10^{19} to 8×10^{19} cm^{-3}. Improved recombination rate approximately at the middle of the p-layer of the microcrystalline junction reduces the competitive recombination in the i-layers of the tandem solar cell to improve carrier collection and efficiency of the tandem solar cell. This result agrees with the simulation result of Rath et al. [48] using the computer program AMPS. They simulated numerically an a-Si:H/a-Si:H tandem cell having a tunnel recombination junction (n) µc-Si:H/(p) µc-Si:H structure. A good recombination takes place in a region ~ 3.5 nm thick near the n/p interface and mainly located inside the (p) µc-Si layer. The increase of the conversion efficiency of the tandem solar cell with the donor concentration of the TRJ is explained through the simulated energy band diagrams. figure 13(a-c) show the energy band diagram around the TRJ for three different concentrations N_D (10^{19}, 4×10^{19}, and 8×10^{19} cm^{-3}) under short-circuit case, an enlarged view of the quasi-Fermi levels is inserted in figure 4.13(a-c).

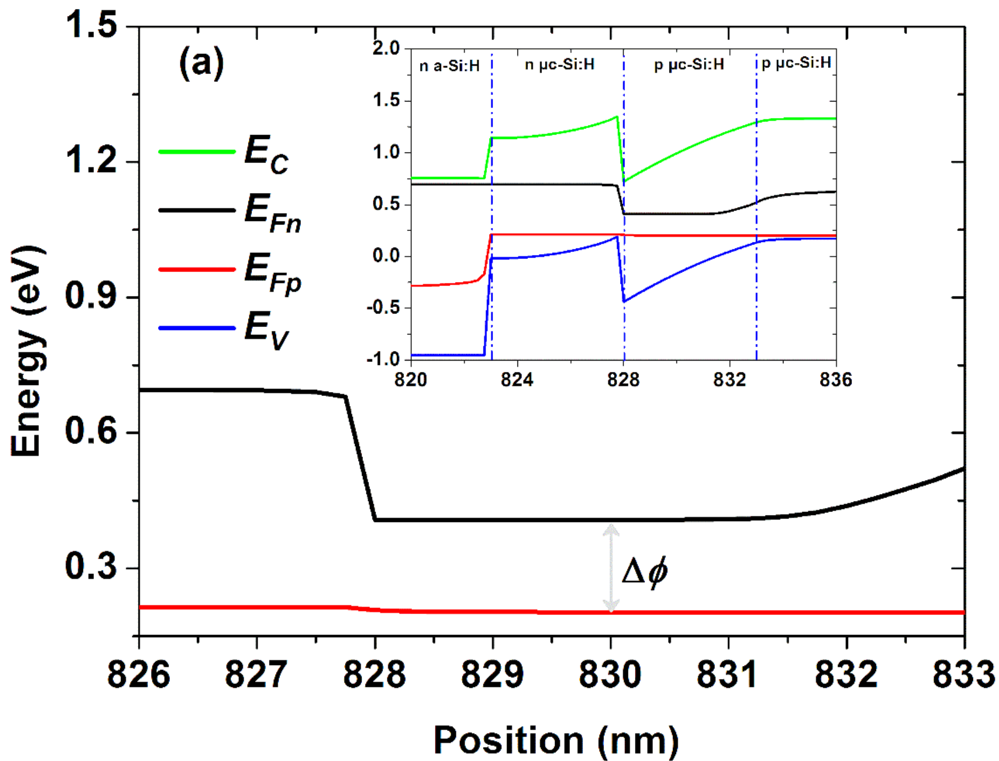

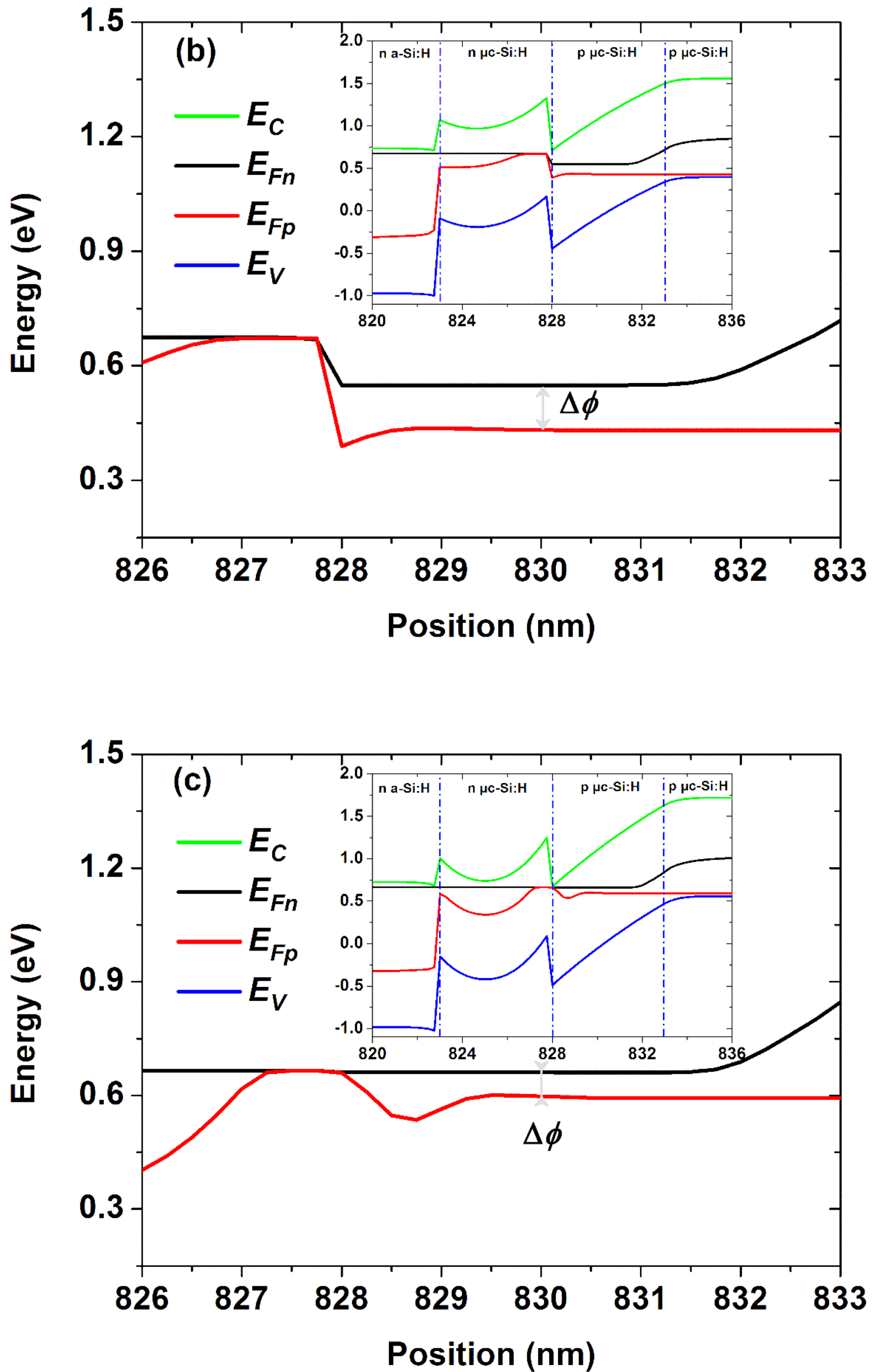

Figure 4.13 (a) Band diagram around the TRJ under short-circuit condition for a donor concentration N_D of (a) 10^{19} cm^{-3}, (b) 4×10^{19} cm^{-3} and (c) 8×10^{19} cm^{-3}.

$\Delta\phi$ is the quasi-Fermi level separation (the difference between hole and electron QFLs). When the donor concentrations of the TRJ n-layer value is low and equal to 10^{19} cm^{-3} (Fig. 4.13(a)), the difference between the quasi-Fermi levels $\Delta\phi = 0.195$ eV. This splitting of QFLS may decrease the recombination rate at the TRJ and lower the efficiency (η = 7.42%). When increasing the donor concentrations of the TRJ n-layer to 4×10^{19} cm^{-3} and once to 10^{20} cm^{-3}, the difference between the quasi-Fermi levels is reduced $\Delta\phi = 0.118$ eV (Fig. 4.13(b)) even to be negligible $\Delta\phi = 0.057$ eV (Fig. 4.13(c)). So, the value of the efficiency (η = 12.23%) was obtained with lower $\Delta\phi$. The donor concentration N_D shifts and pins the quasi-Fermi levels near midgaps, this is more advantageous for the transport and the tunneling-enhanced recombination mechanism of carriers. To obtain the largest efficiency of the tandem solar cell the quasi-Fermi levels in the n- and p- regions of the TRJ should be as close as possible to each other as illustrated in Fig. 4.13(c). The difference between the quasi-Fermi levels can be considered as the loss in the TRJ as illustrated in Fig. 4.13(a). In that case, a lower efficiency η of 7.42 % was found.

Moreover, after obtaining the best possible n-layer concentration of the TRJ as 10^{20} cm^{-3}, optimization of p-layer concentration N_A of the TRJ is performed by keeping the n-layer concentration of the TRJ as 10^{20} cm^{-3}. Fig. 4.14(a-d) shows variations of J_{sc}, V_{oc}, FF and η as the function of p-layer concentration N_A.

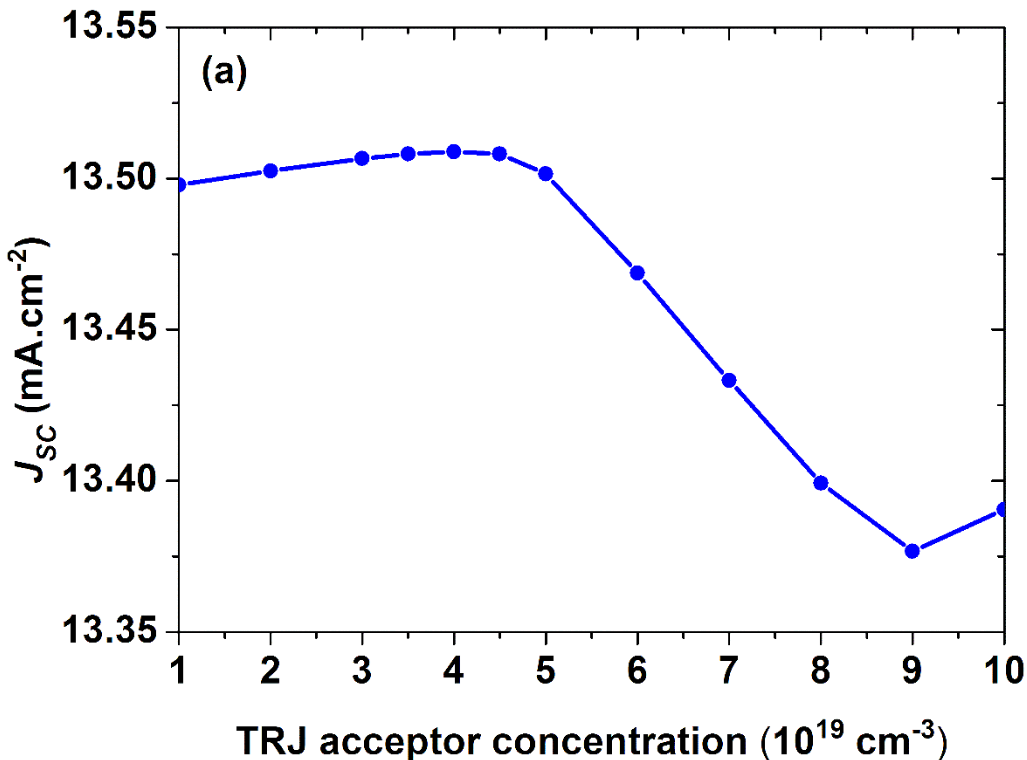

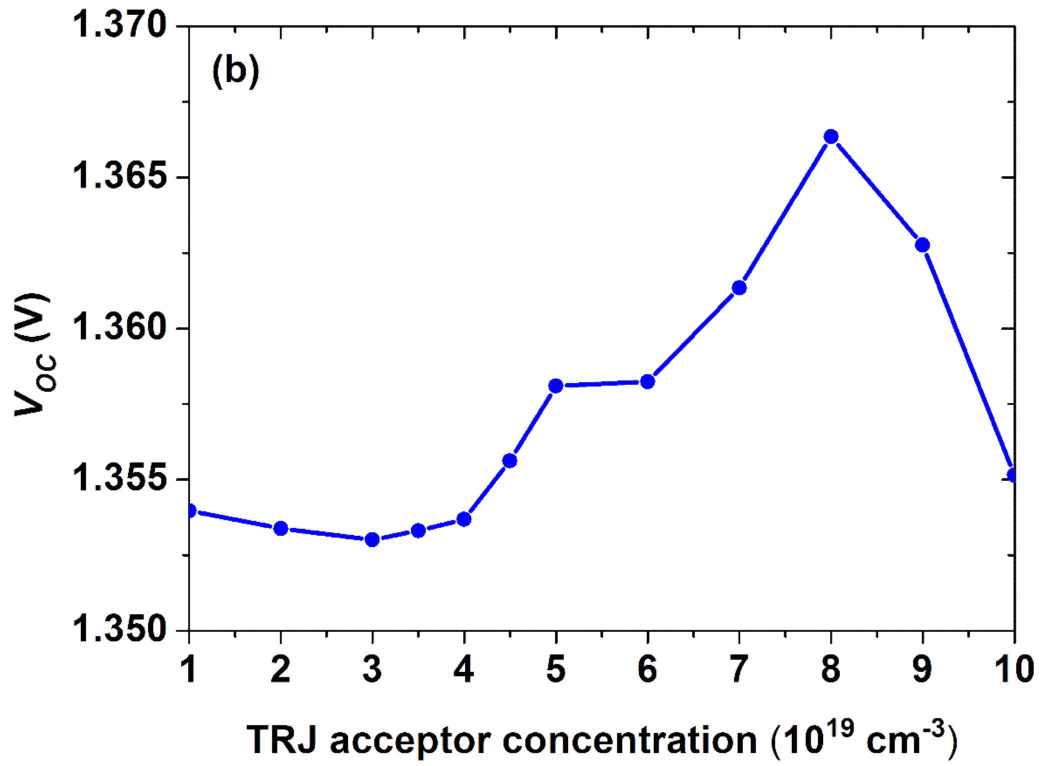
(b)
1.370
1.365
1.360
1.355
1.350
V_OC (V)
1
2
3
4
5
6
7
8
9
10
TRJ acceptor concentration (10^19 cm^-3)

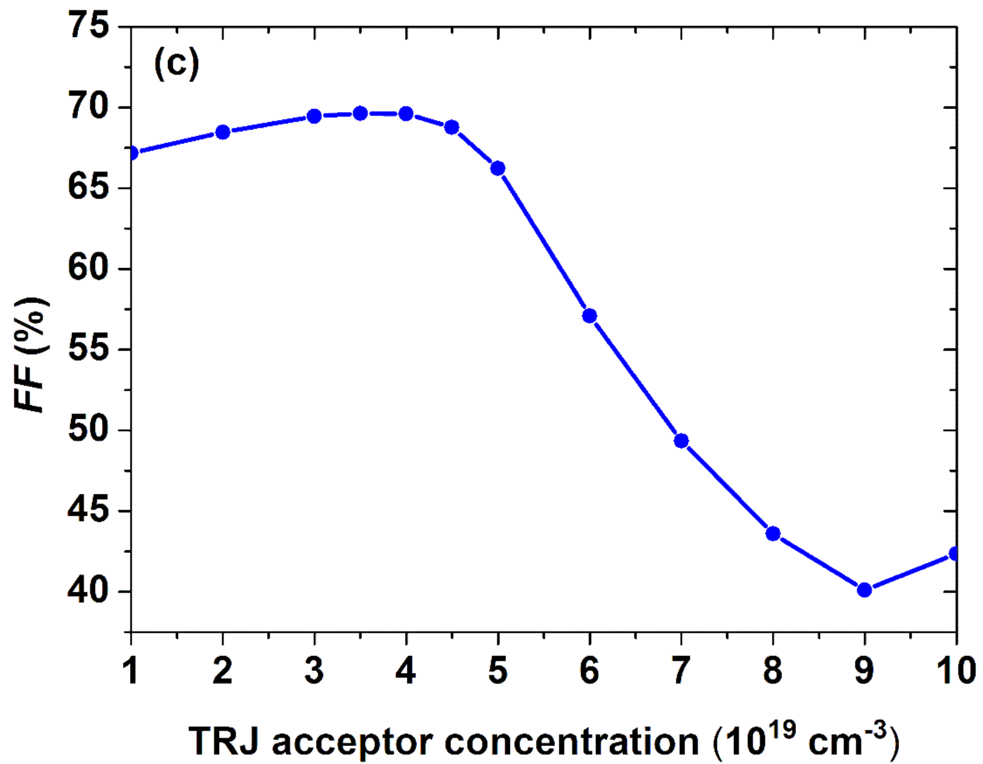
(c)
75
70
65
60
55
50
45
40
FF (%)
1
2
3
4
5
6
7
8
9
10
TRJ acceptor concentration (10^19 cm^-3)

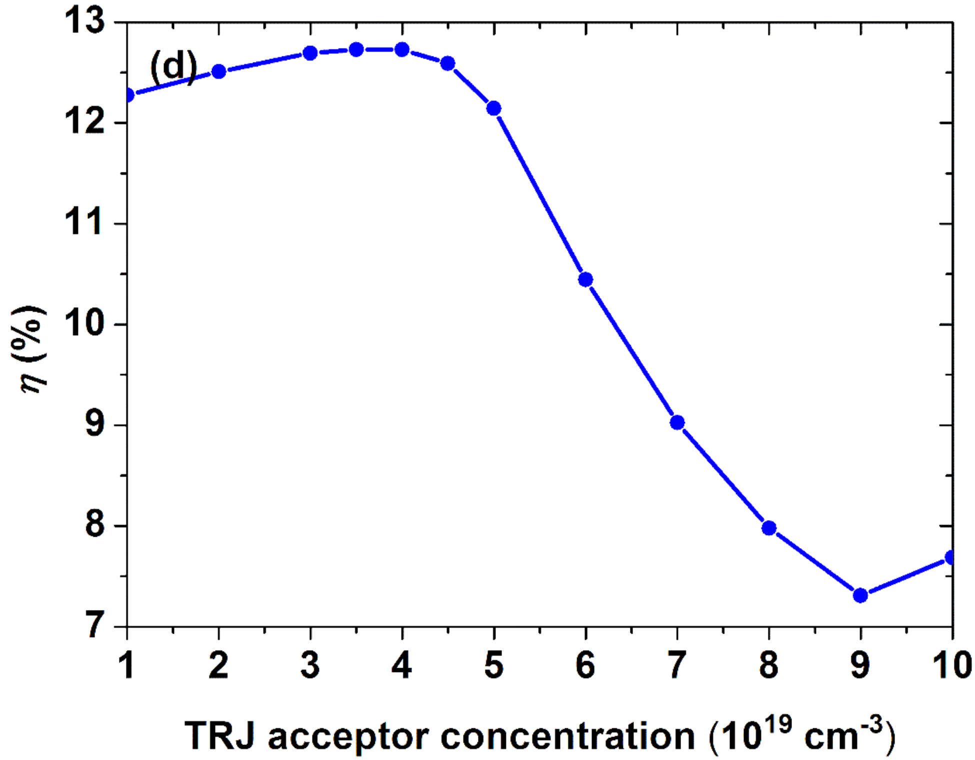

Figure 4.14 Simulated photovoltaic parameters of the a-Si:H/μc-Si:H tandem solar cell as function of the acceptor concentration N_A of the TRJ.

The short-circuit current of the tandem cell increases slightly from 13.49 mA.cm^{-2} to 13.5 mA.cm^{-2} with the increasing p-layer concentration from 10^{19} cm^{-3} to 4×10^{19} cm^{-3}. Then, it was found that J_{sc} is slightly reduced from 13.5 mA.cm^{-2} to 13.39 mA.cm^{-2} with increasing p-layer concentration from 4×10^{19} cm^{-3} to 10^{20} cm^{-3}. The open circuit voltage V_{oc} of the tandem cell is nearly constant (1.35 V) from 10^{19} cm^{-3} to 4x10^{19} cm^{-3} and then creases slightly from 1.35 V to 1.36 V for the range of the p-layer concentration between 4×10^{19} cm^{-3} and 8×10^{19} cm^{-3}. With further increase of the p-layer concentration from 8x10^{19} cm^{-3} to 10^{20} cm^{-3}, the V_{oc} is slightly reduced from 1.36 V to 1.35 V. The fill factor increases slightly from 67.17% to 69.59% with the increasing p-layer concentration from 10^{19} cm^{-3} to 4×10^{19} cm^{-3}, then it decreases drastically from 69.59% to 42.35% with increasing p-layer concentration from 4×10^{19} cm^{-3} to 10^{20} cm^{-3}.The simulated values of η showed the same behavior as observed in J_{sc} and FF. η was found to increase from 12.27% to 12.73% with increasing p-layer concentration from 10^{19} cm^{-3} to 4×10^{19} cm^{-3}. After that, it decreased from 12.73% to 7.68% with increasing p-layer concentration from 4×10^{19} cm^{-3} to 10^{20} cm^{-3}. The optimum conversion efficiency is about 12.73% (values of J_{sc}, V_{oc} and FF were found to be 13.5 mA.cm^{-2}, 1.35 V and 69.59%

respectively) at p-layer concentration of 4×10^{19} cm^{-3}. The results indicate that the dopant concentration N_A reduces the short circuit- current, the fill factor and the conversion efficiency while the open-circuit voltage is nearly constant. The p-layer concentration of 4×10^{19} cm^{-3} was optimized for getting efficient a-Si:H/µc-Si:H tandem solar cell. Fig. 4.15 shows the recombination rate around the TRJ obtained when the TRJ p-layer acceptor concentration N_A is set to 10^{19}, 4×10^{19}, and 10^{20} cm^{-3} under short-circuit conditions. This figure clearly shows recombination peaks appearing at the tunnel recombination junction. We then simulated the tandem solar cell structure for three concentrations N_A (10^{19}, 4×10^{19}, and 10^{20} cm^{-3}) of the TRJ p-layer under thermodynamic equilibrium conditions, we also found that the recombination peaks are approximately located at the positions where the Fermi levels positions cross midgaps. Our results show that the recombination peaks are shifting from the TRJ p-layer to the TRJ n-layer with increasing TRJ p-layer concentration N_A from 10^{19} cm^{-3} to 10^{20} cm^{-3}. In this case, the efficiency η of the tandem solar cell increases from 12.26 % to 12.73 % with the increasing p-layer concentration from 10^{19} to 4×10^{19} cm^{-3} then decreases to 7.68 % with increasing TRJ p-layer concentration N_A from 4×10^{19} to 10^{20} cm^{-3}.

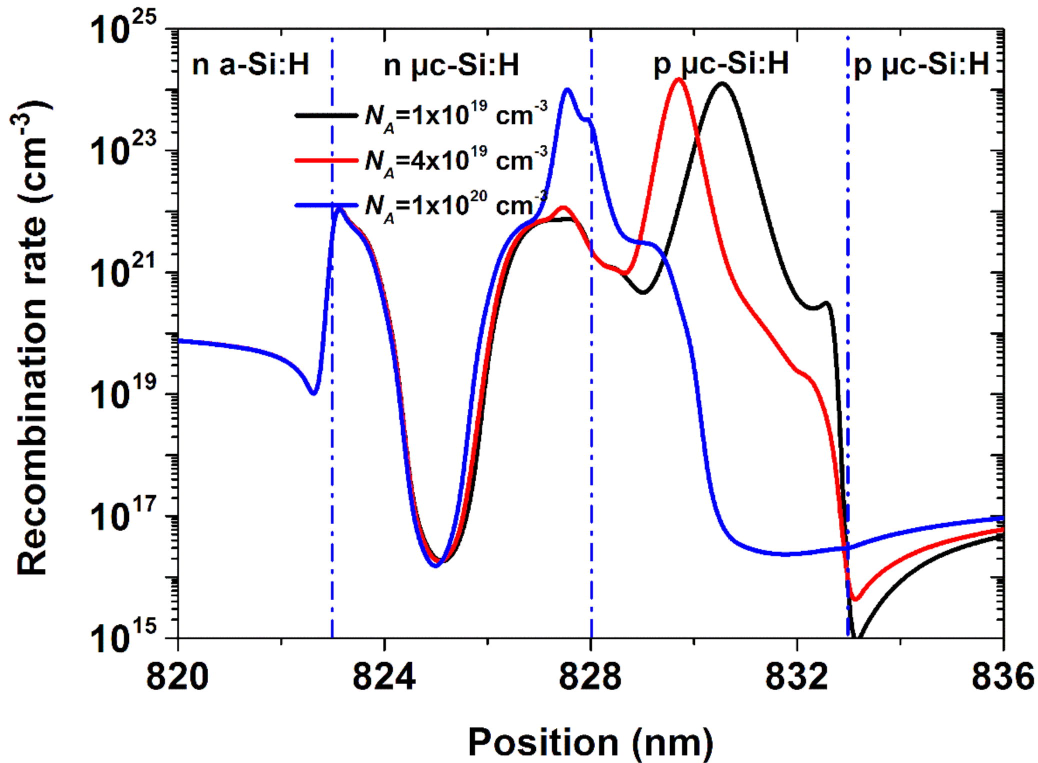

Figure 4.15 Recombination rate around the TRJ for various acceptor concentrations N_A of the TRJ under short-circuit condition.

Improved recombination rate approximately near the n/p interface of the TRJ enhances the competitive recombination in the i-layers of the tandem solar cell to reduce carrier collection and efficiency of the tandem solar cell. In order to explain the decrease of the conversion efficiency of the tandem solar cell with the TRJ acceptor concentration, we examined the energy band diagram inside the TRJ for various values of the TRJ p-layer concentrations N_A under short-circuit conditions. An enlarged view of the quasi-Fermi levels is inserted in Fig. 4.16(a-c).

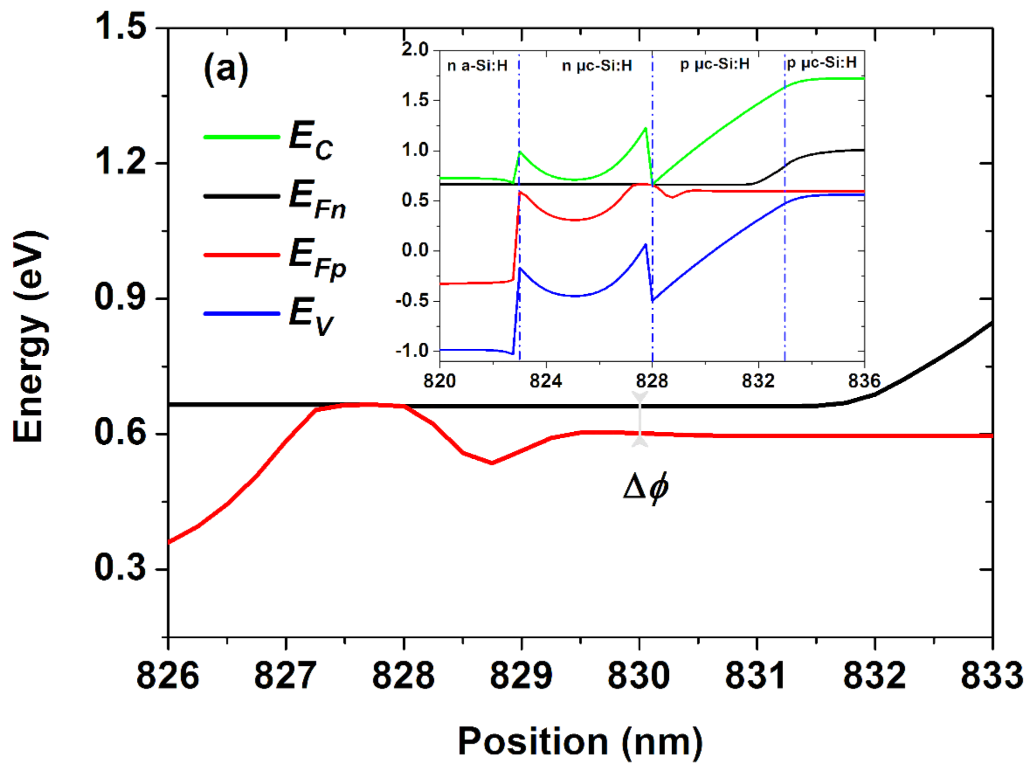

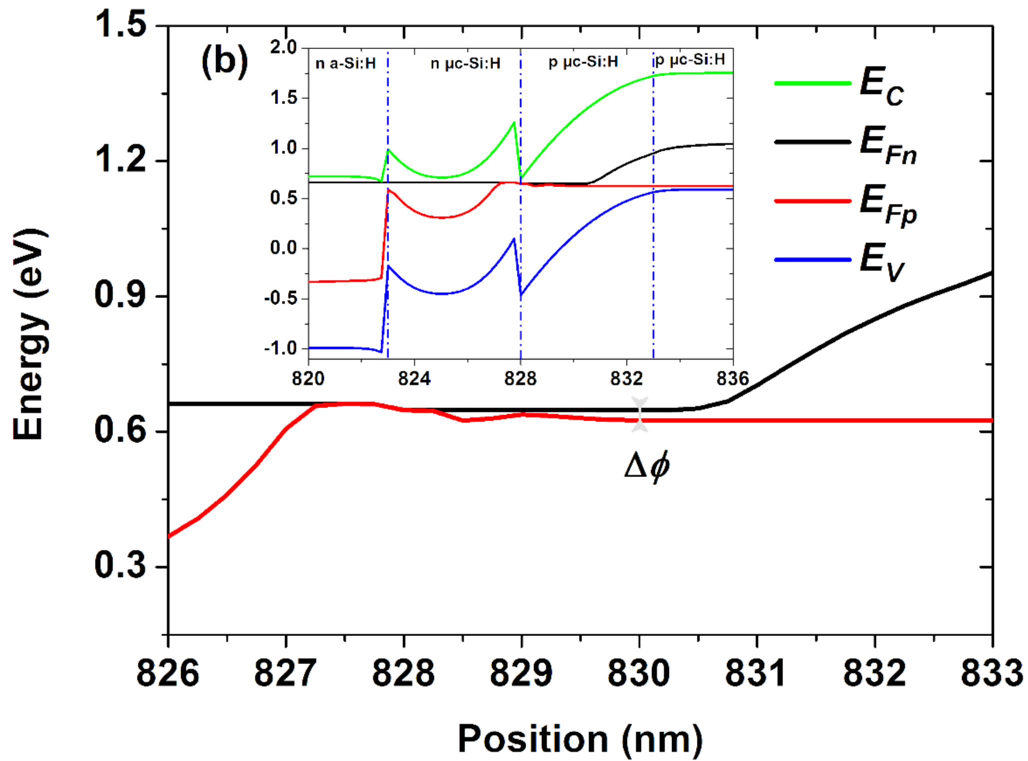

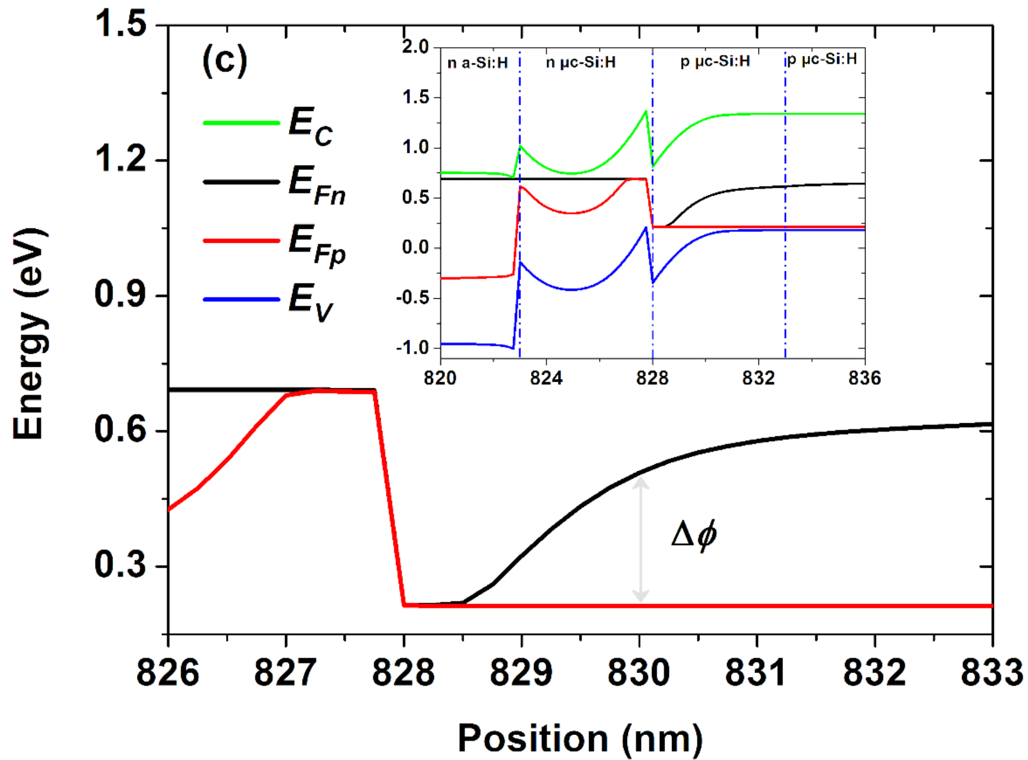

Figure 4.16 Band diagram around the TRJ under short-circuit condition for an acceptor concentration N_A of (a) 10^{19} cm^{-3}, (b) 4×10^{19} cm^{-3} and (c) 10^{20} cm^{-3}.

When the acceptor concentrations of the TRJ p-layer value is low and equal to 10^{19} cm^{-3} (Fig. 4.16(a)), the difference between the quasi-Fermi levels is small and $\Delta\phi = 0.061$ eV. When increasing the acceptor concentrations of the TRJ p-layer to 4×10^{19} cm^{-3}, the difference between the quasi-Fermi levels is reduced $\Delta\phi = 0.025$ eV (Fig. 4.16(b)). Then the difference between the quasi-Fermi levels is enhanced $\Delta\phi = 0.29$ eV when increasing the acceptor concentrations of the TRJ p-layer to 10^{20} cm^{-3} (Fig. 4.16(c)). The high value of the efficiency (η = 12.73 %) was obtained with lower $\Delta\phi$ and for an acceptor concentration of 4×10^{19} cm^{-3}. This is more beneficial for the transport and the tunneling-enhanced recombination process of carriers. The difference between the quasi-Fermi levels can be considered as the loss in the TRJ and the most recombination happens at the n-layer of TRJ as illustrated in Fig. 4.16(c). In that case, a lower efficiency η of 7.68 % was obtained [49].

4.2.5.b Effect of TRJ thickness on double junction solar cell

Once we obtained optimal dopant concentrations of the TJR by simulation, we performed studying the effect of the TRJ thickness on the photoelectrical parameters of the tandem solar cell. This study is carried out by taking constant dopant concentrations of µc-Si:H n- and p- layers of the TJR as 10^{20} cm^{-3} and 4×10^{19} cm^{-3}, respectively. In view of this, we have also examined the behaviours of J_{sc}, V_{oc}, FF and η as a function of TRJ thickness of µc-Si:H layers as shown in Fig. 4.17(a-d).

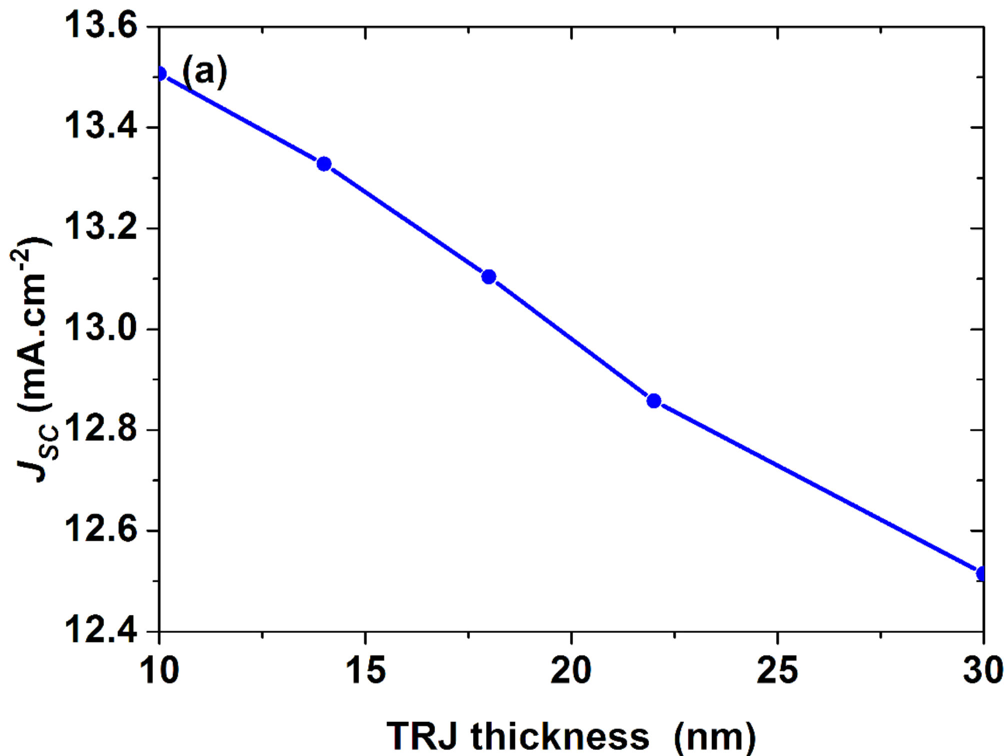

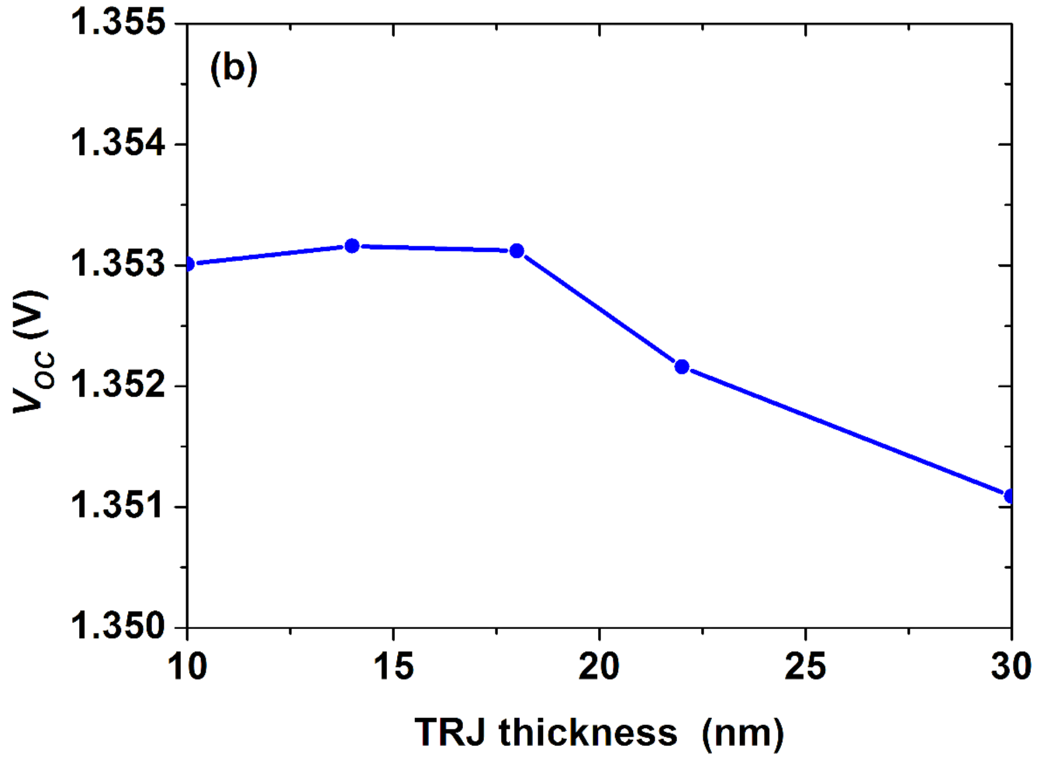
1.355
1.354
1.353
1.352
1.351
1.350
(b)
V_{OC} (V)
10
15
20
25
30
TRJ thickness (nm)

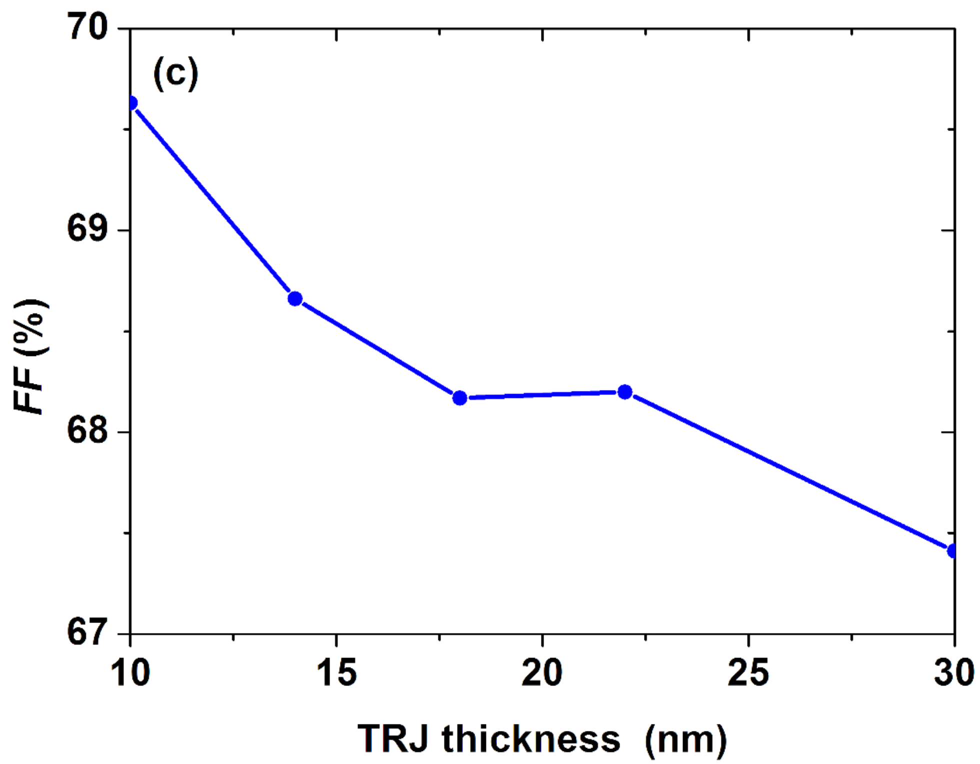
70
69
68
67
(c)
FF (%)
10
15
20
25
30
TRJ thickness (nm)

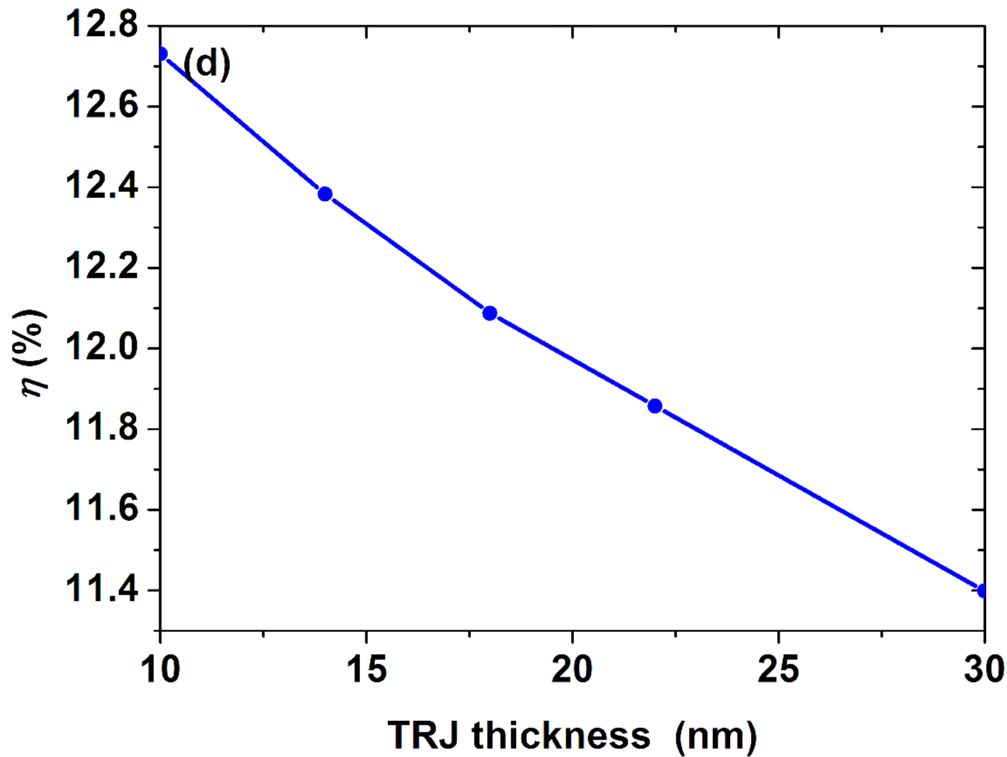

Figure 4.17 Simulated photovoltaic parameters of the a-Si:H/μc-Si:H tandem solar cell as function of thickness of the TRJ.

J_{sc} decreases from 13.5 mA.cm^{-2} to 12.51 mA.cm^{-2} with increasing TJR thickness from 10 nm to 30 nm but V_{oc} shows a very small variation value of 1.35 V. With increasing TRJ thickness from 10 nm to 30 nm. *FF* and η decreased from 69.63 % to 67.41 % and 12.73 % to 11.39 %, respectively. The TRJ thickness reduces the short-circuit current, the fill factor and the conversion efficiency, but the open circuit voltage is nearly constant. If the TRJ layer is too thick, it will lead to optical losses by absorption. It is worth noting that when TRJ thickness is too thin, the maximum efficiency of 12.73% is obtained at TRJ thickness of 10 nm. In order to explain the decrease of the conversion efficiency of the tandem solar cell with the TRJ thickness, we examined the recombination rate for tunnel junction thicknesses set to 10 nm and 30 nm as illustrated in Fig. 4.18(a-b). The recombination peak is approximately situated in the middle of the TRJ p-layer for a thickness of 10 nm while the recombination peak is moved toward the TRJ n-layer for a thickness of 30 nm. For a TRJ thickness of 10 nm, a good recombination peak is approximately located in the middle of the TRJ p-region where the Fermi level at thermodynamic equilibrium crosses midgap. The increase of the TRJ thickness to 30 nm causes a shift of the recombination peak toward the TRJ n-region. Improved recombination

rate approximately near the n/p interface of the microcrystalline junction enhances the competitive recombination in the i-layers of the tandem solar cell to reduce carrier collection and efficiency of the tandem solar cell. This behaviour can be considered as the loss in the TRJ and responsible for the decrease of the efficiency of the tandem solar cell from 12.73% to 11.39% with increasing the TRJ thickness from 10 nm to 30 nm, respectively.

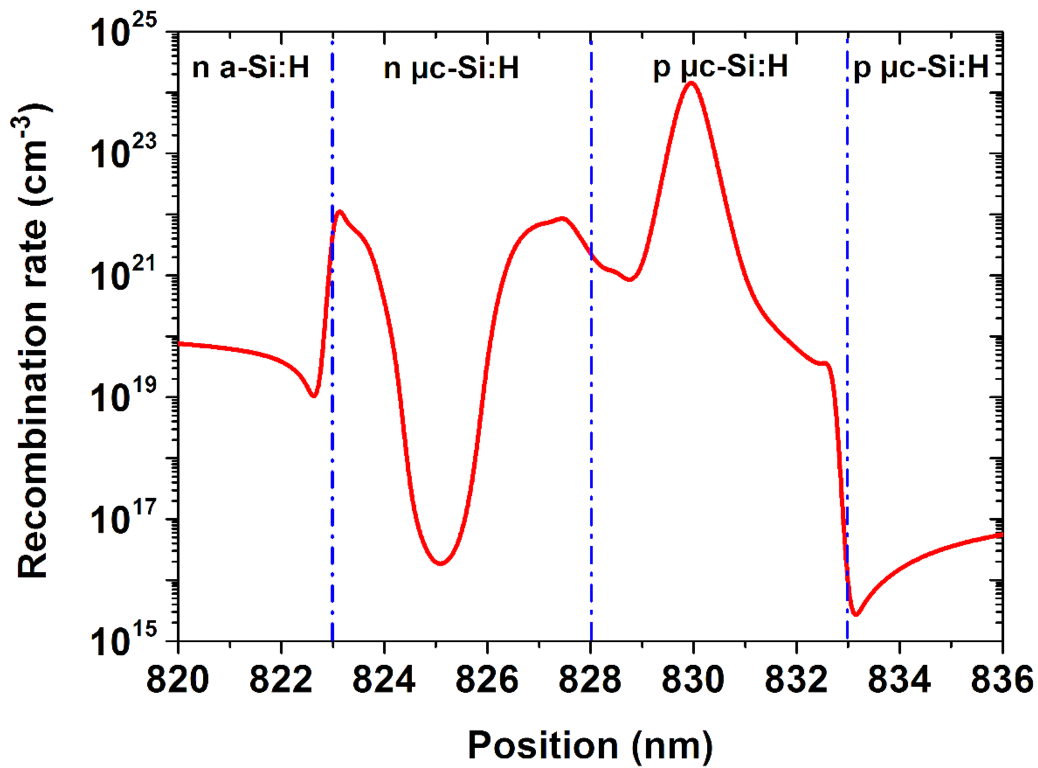

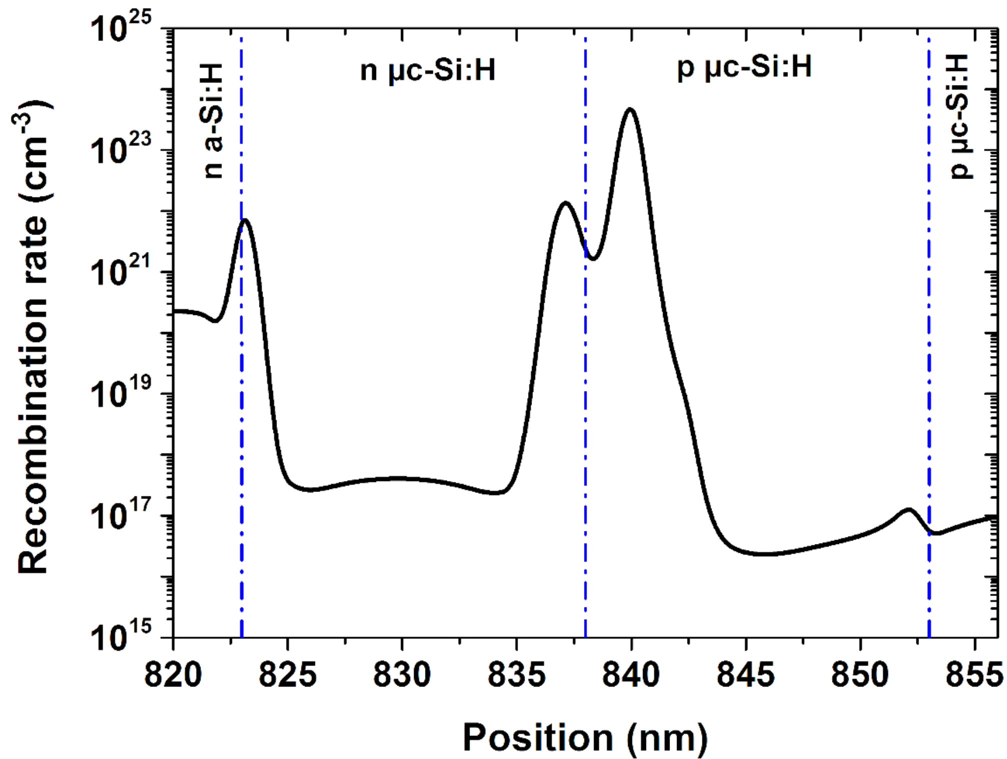

Figure 4.18 Recombination rate around the TRJ under short-circuit condition for tunnel recombination junction thickness of (a) 10 nm and (b) 30 nm.

4.3 a-Si:H/a-SiGe:H/μc-Si:H triple junction solar cell

4.3.1 Device structure and simulation details

As shown in Fig. 4.19, the triple junction solar cell is composed of three subcels with p-i-n configurations: namely, a-Si:H (top), a-SiGe:H (middle), and μc-Si:H (bottom) junctions stacked in series. Two tunnel recombination junctions (TRJ) (i.e., n-μc-Si:H/ p-μc-Si:H) are located between each pair of three subcells.

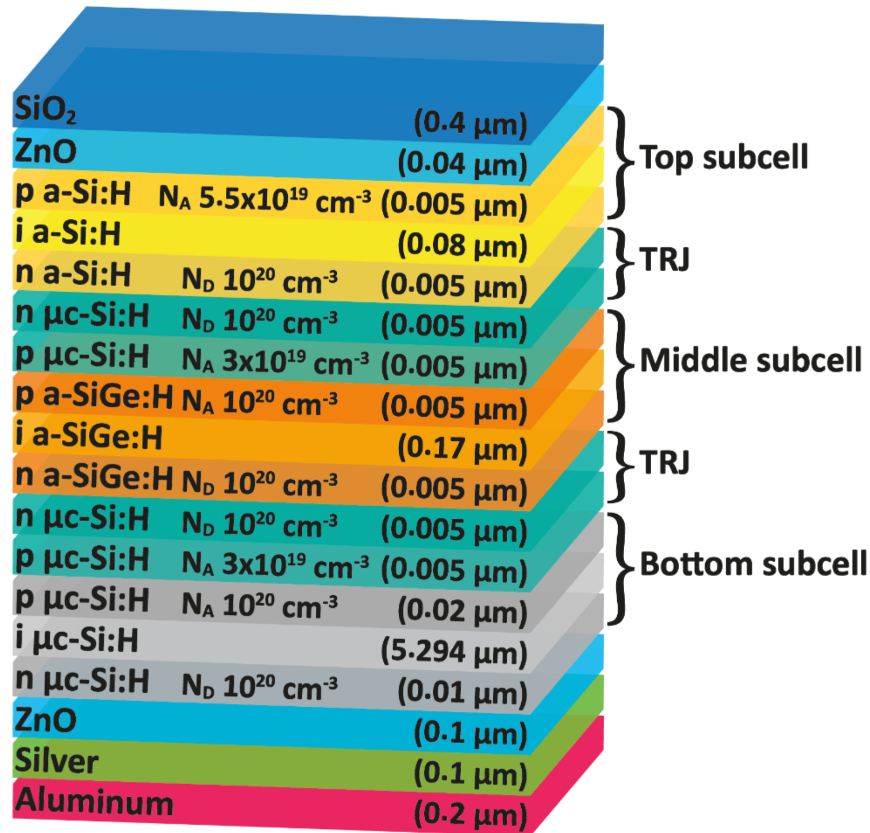

Figure 4.19 Structure used in the simulation of a p-i-n a-Si:H/a-SiGe:H/µc-Si:H triple junction solar cell with n-p µc-Si:H tunnel recombination junctions.

The TRJ plays a significant role in enhancing the conversion efficiency, the development and the design of the TRJ has been detailed in the double junction cell section. The different band gaps set to 1.7, 1.5 and 1.1 eV for a-Si:H, a-SiGe:H and µc-Si:H materials can effectively absorb a wide solar spectrum (300-1100 nm). The a-Si:H component cell absorbs photons with energies above 1.7 eV, photons with lower energies, which pass through the a-Si:H top cell get a chance to be absorbed by the a-SiGe:H middle and µc-Si:H bottom cells. The incident light enters through a glass (SiO_2) as a transparent superstrate which is covered with a transparent conductive oxide (TCO) layer of ZnO serves as the front anode contact and ZnO/Ag/Al represents the back cathode contact of the triple junction solar cell. The interfaces between the layers may not be just flat. A random texturization is usually introduced at front TCO / p-layer interface for p-i-n cells to scatter light in directions different than specular. In this way the path of light inside the i-layer (i.e. absorber layer) can be increased and absorption enhanced [50]. The doping concentrations and different thicknesses used in the simulation are indicated in Fig. 4.19. The structure and mesh of the triple junction solar cell by Atlas-Silvaco are presented in Figures 4.20 and 4.21.

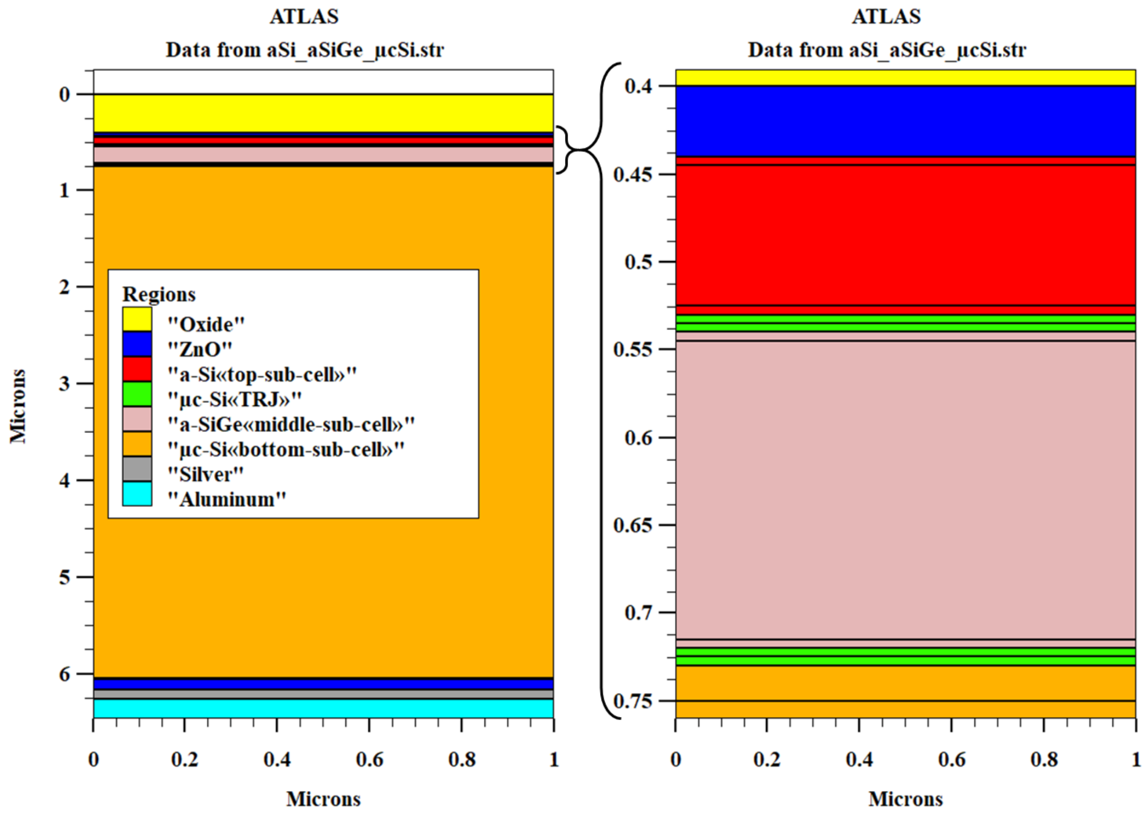

Figure 4.20 Two-dimensional simulated structure of the p-i-n a-Si:H/a-SiGe:H/µc-Si:H triple junction solar cell with Atlas-Silvaco.

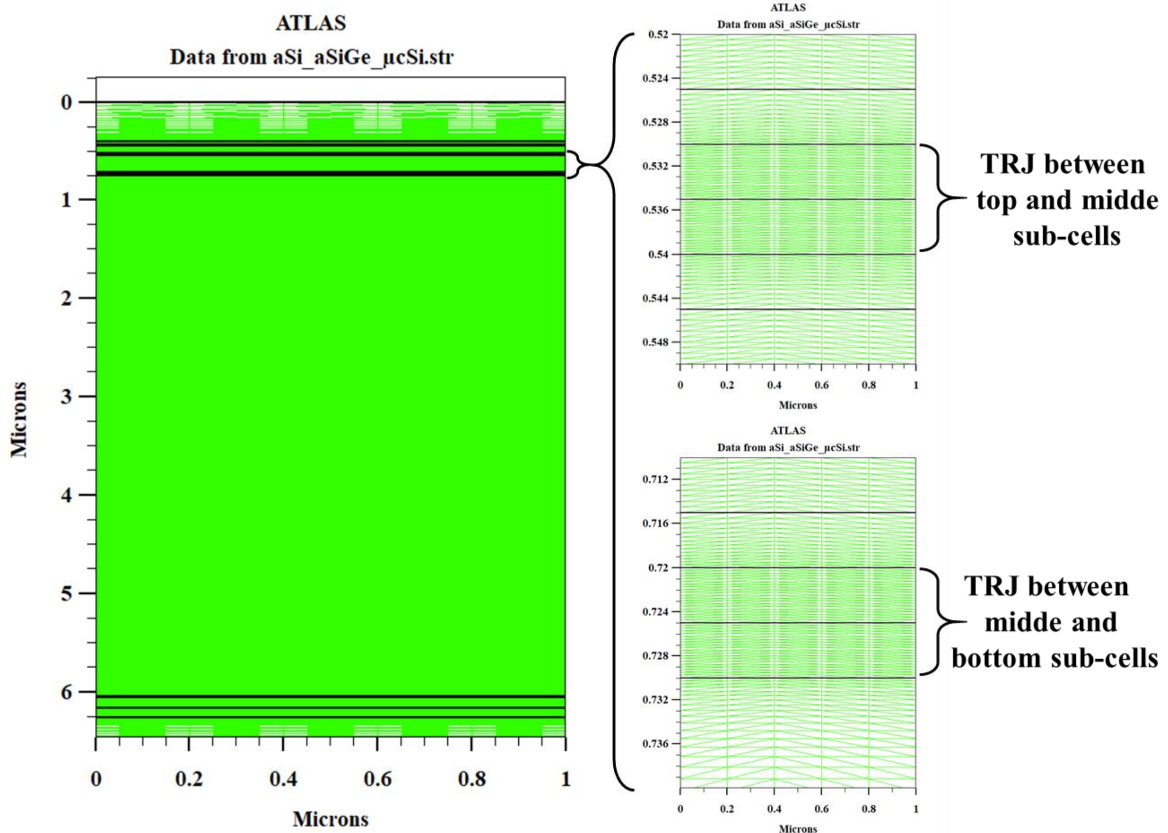

Figure 4.21 Mesh of the triple solar cell with the zoom of the mesh in the TRJ part.

The defect recombination is modeled by the Shockley-Read-Hall (SRH) model and the tunnel recombination junction model is based on the trap-assisted tunneling recombination model of Hurkx et al. [51] as described in the chapter 3. The input parameters of a-Si:H and μc-Si:H materials can be found in Tables 4.1-3. The a-SiGe:H material parameters are summarized in Table 4.6 and defect parameters are listed in Tables 4.7 and 4.8, the simulation parameters are taken from references [27 - 30] [36, 52] and [53].

Layer properties	a-SiGe:H solar cell		
	p	i	n
E_g (eV)	1.5	1.5	1.5
N_c (cm^{-3})	2.5x10^{20}	2.5x10^{20}	2.5x10^{20}
N_v (cm^{-3})	2.5x10^{20}	2.5x10^{20}	2.5x10^{20}
χ (eV)	4.17	4.17	4.17
ε	11.9	11.9	11.9
μ_e (cm^2/Vs)	10	10	10
μ_h (cm^2/Vs)	2	2	2

Table 4.6 Electrical parameters for a-SiGe:H solar cell [27, 30, 52, 53].

Defect states parameters	a-SiGe:H solar cell		
	p	i	n
Tail states			
N_{ta}, N_{td} (cm^{-3})	1e21	1e21	1e21
W_{TA} (eV)	0.025	0.025	0.025
W_{TD} (eV)	0.043	0.043	0.043
σ_{na} (cm^2)	1e-17	1e-17	1e-17
σ_{pa} (cm^2)	1e-17	1e-17	1e-17
σ_{nd} (cm^2)	1e-17	1e-17	1e-17
σ_{pd} (cm^2)	1e-17	1e-17	1e-17

Table 4.7 Defect states parameters of tail states [29].

Defect states parameters	a-SiGe:H solar cell		
	p	i	n
Gaussian model			
N_{Ga}, N_{Gd} (cm^{-3})	1e15	1e15	1e15
E_{Ga} (eV)	0.52	0.52	0.52
E_{Gd} (eV)	0.68	0.68	0.68
W_{Ga} (eV)	0.188	0.188	0.188
W_{Gd} (eV)	0.188	0.188	0.188
σ_{nGa} (cm^2)	1e-17	5e-15	1e-17
σ_{pGa} (cm^2)	1e-17	1e-16	1e-17
σ_{nGd} (cm^2)	1e-17	1e-16	1e-17
σ_{pGd} (cm^2)	1e-17	5e-15	1e-17

Table 4.8 Defect states parameters of Gaussian distributions [28, 36].

The optical parameters which are the refractive index *n* and extinction coefficient *k* as function of the wavelength for a-SiGe:H are obtained from [27]. The numerical simulations were performed at a temperature of 300 K and under a global AM1.5 (100 mW.cm^{-2}) spectrum.

Fig. 4.22 shows the triple junction solar cell energy band diagram simulated under thermodynamic equilibrium conditions. Around the tunnel recombination junctions, the energy Fermi level E_F of electrons and holes is situated close to the band edges E_C and E_V. This is advantageous for the transport and the tunneling enhanced recombination mechanism of carriers. Fig. 4.23 shows the recombination rate around the TRJs under short-circuit conditions. This figure clearly shows high recombination peaks appearing at the tunnel recombination junctions and are approximately located at the positions where the Fermi level at thermodynamic equilibrium crosses midgap. Improved recombination rates at the TRJs reduces the competitive recombination in the i-layers of the triple junction solar cell to improve carrier collection and efficiency of the triple junction solar cell.

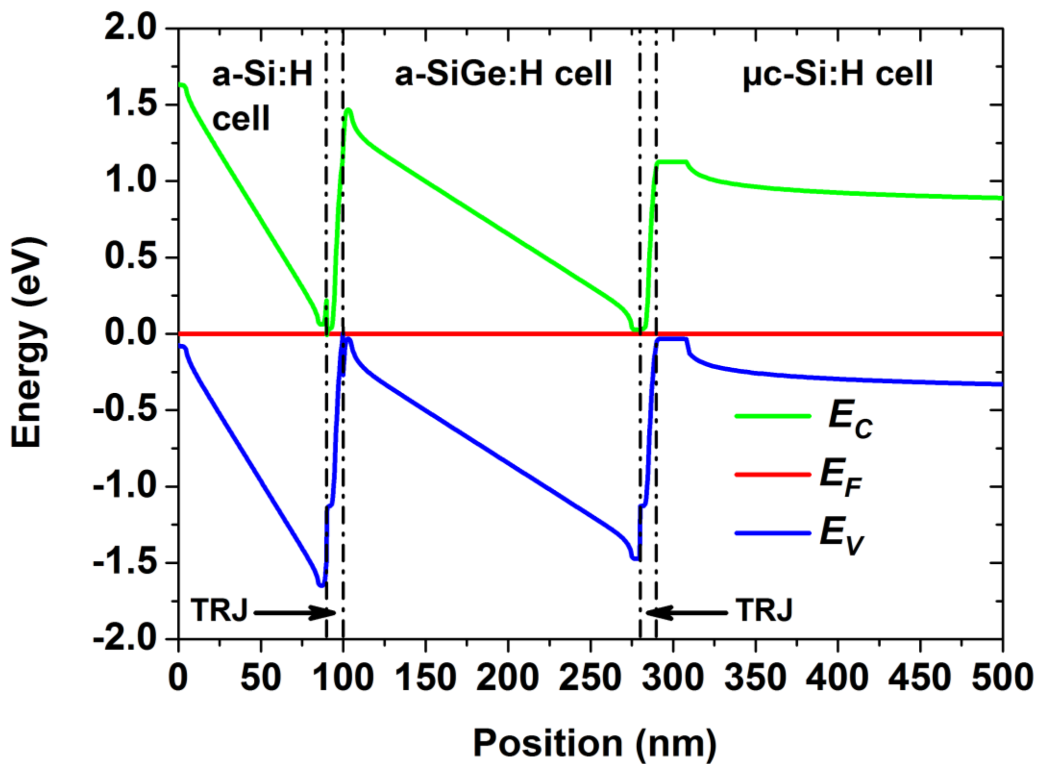

Figure 4.22 Energy band diagram of a-Si:H/a-SiGe:H/μc-Si:H triple junction solar cell simulated under thermodynamic equilibrium conditions.

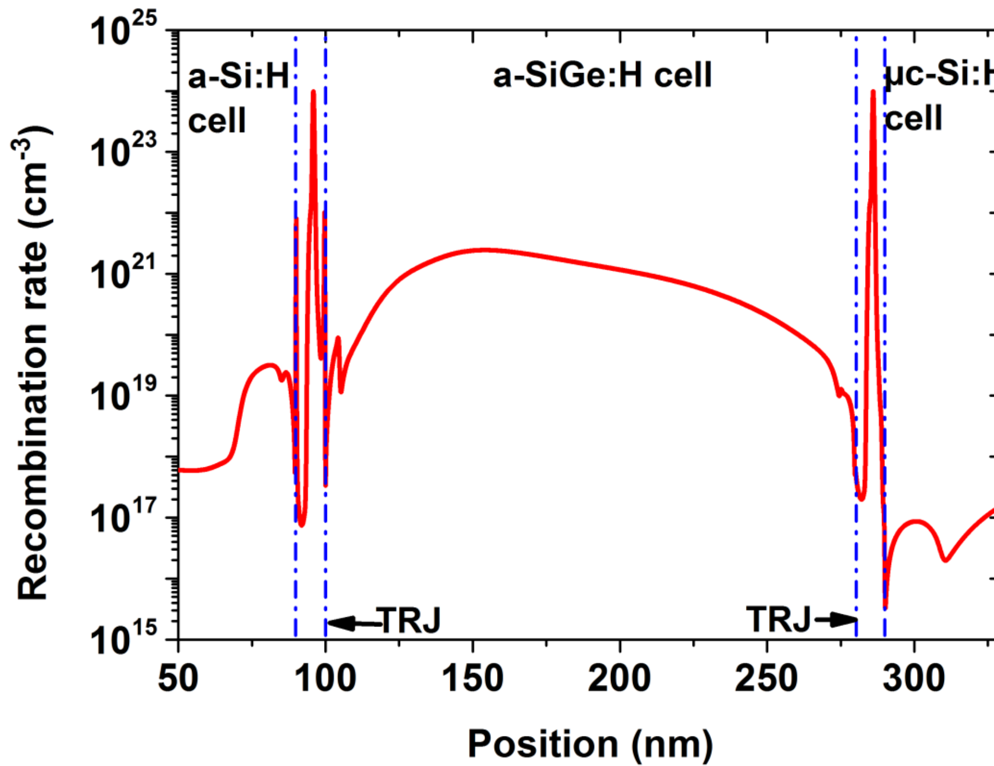

Figure 4.23 Recombination rate of a-Si:H/a-SiGe:H/µc-Si:H triple junction solar cell around the TRJs simulated under short-circuit condition.

4.3.2 Single a-Si:H, a-SiGe:H and µc-Si:H solar cells performances

We first simulated the performance of single a-Si:H, a-SiGe:H and µc-Si:H solar cells as illustrated in Figs (4.4, 4.6 and 4.24). The *J–V* characteristics simulated for the single a-Si:H, a-SiGe:H, and µc-Si:H solar cells are presented in Fig 4.25.

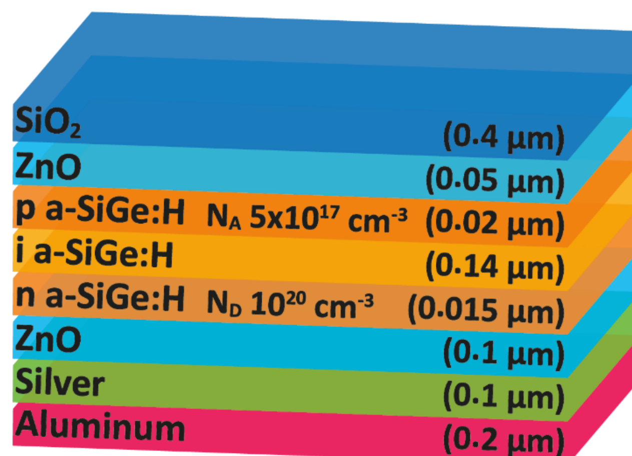

Figure 4.24 Schematic structure of single a-SiGe:H solar cell.

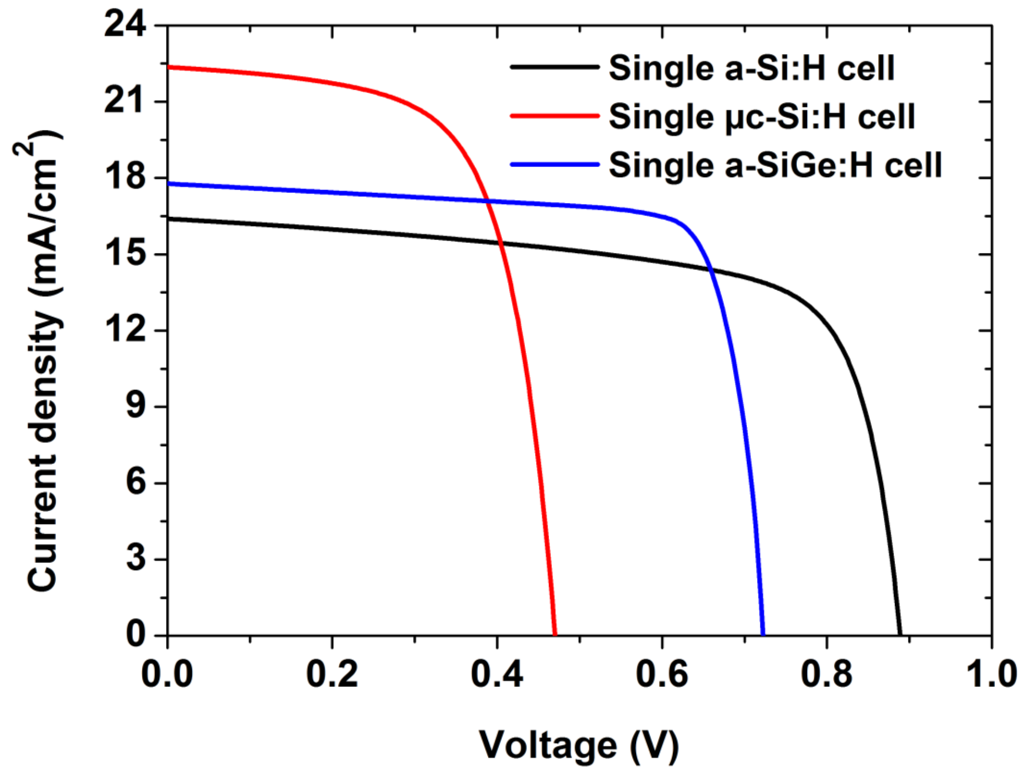

Figure 4.25 *J–V* characteristics simulated for the single a-Si:H, a-SiGe:H, and μc-Si:H solar cells.

Table 4.9 shows the photovoltaic parameters including the open-circuit voltage (V_{oc}), short circuit-current density (J_{sc}), fill factor (*FF*) and conversion efficiency (η) of solar cells extracted from the corresponding *J–V* characteristics. The a-Si:H and a-SiGe:H solar cells have conversion efficiencies of 10.22% (J_{sc}=16.39 mA/cm^2, V_{oc}=0.89 V, *FF*=69.44%) and 10.7% (J_{sc}=17.78 mA/cm^2, V_{oc}=0.73 V, *FF*=81.97%). These values are in good agreement with those obtained from experimental a-Si:H and a-SiGe:H cells published in Refs. [40] and [54], which supports the validation of the used models and the parameters in the simulation. The μc-Si:H solar cell has a lower conversion efficiency 6.5% (J_{sc}=21.89 mA/cm^2, V_{oc}=0.47 V, *FF*=63%) than that of the a-Si:H and a-SiGe:H solar cells mainly due to lower V_{oc} and *FF*.

	J_{sc}(mA/cm^2)	V_{oc}(V)	FF (%)	η (%)
Single a-Si:H cell simulation	16.39	0.89	69.44	10.22
Single a-Si:H cell experiment [40]	16.36	0.89	69.8	10.22
Single a-SiGe:H cell simulation	17.78	0.73	81.97	10.7
Single a-SiGe:H cell experiment [54]	17.9	0.795	70.9	10.1
Single μc-Si:H cell simulation	21.89	0.47	63	6.50

Table 4.9 Simulation photovoltaic parameters of single a-Si:H, a-SiGe:H and μc-Si:H solar cells.

4.3.3 a-Si:H/a-SiGe:H/μc-Si:H triple junction solar cell performance

The schematic structure of the initial triple junction solar cell is shown in Fig. 4.19. The different band-gaps are around 1.7, 1.5 and 1.1 eV for a-Si:H, a-SiGe:H and μc-Si:H layers. The *J-V* characteristics of the a-Si:H top-cell, a-SiGe:H middle-cell, μc-Si:H bottom-cell and the initial triple junction solar cell are shown in Fig. 4.26. The simulated photovoltaic parameters are indicated in Table 4.10.

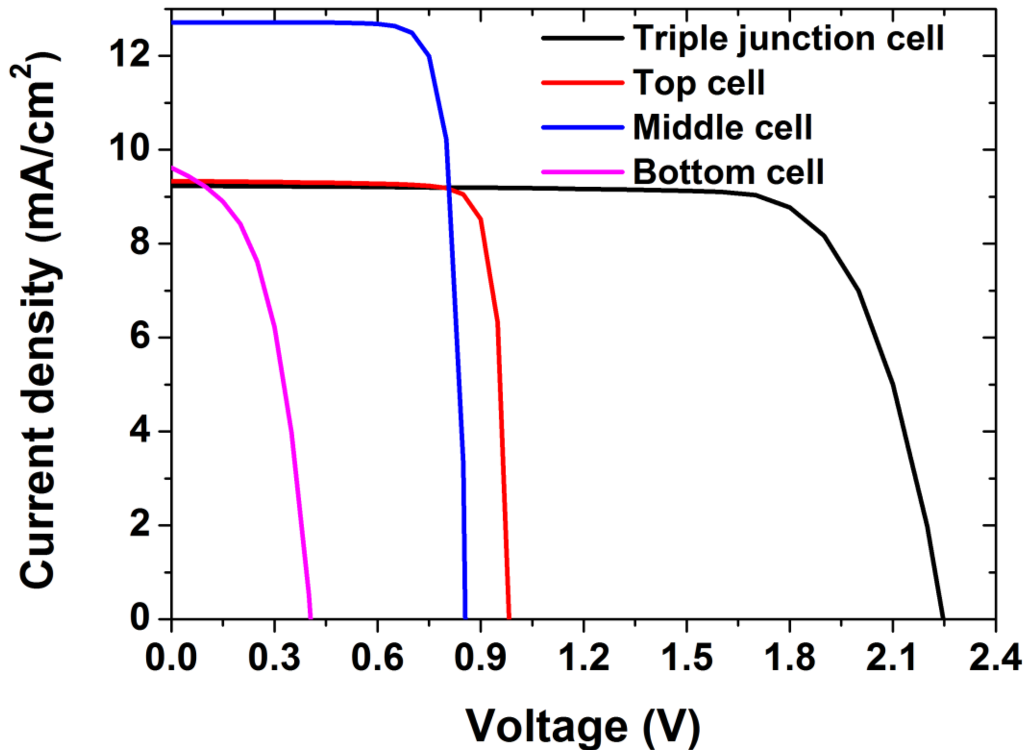

Figure 4.26 *J–V* characteristics for the a-Si:H top cell, a-SiGe:H middle cell, μc-Si:H bottom cell and initial triple junction solar cell.

	J_{sc}(mA/cm^2)	V_{oc}(V)	*FF* (%)	η (%)
a-Si:H top-cell	9.333	0.982	83.83	7.69
a-SiGe:H middle cell	12.71	0.855	82.68	8.99
µc-Si:H bottom-cell	9.61	0.404	48.88	1.90
a-SiH/ a-SiGe:H /µc-Si:H triple junction cell	9.234	2.246	76.11	15.79

Table 4.10 Simulation photovoltaic parameters of the top, middle, bottom and initial triple junction solar cells.

The J_{sc} of the triple junction solar cell is limited by the low current of the a-Si:H top cell. this result is consistent with the previous experimental results reported in Ref. [55]. The triple junction solar cell J_{sc} of 9.234 mA/cm^2 is about equal to the top-cell J_{sc} of 9.333 mA/cm^2. The sum of V_{oc} values of the three sub cells 2.241 V is equal to that of the triple junction solar cell 2.246 V. This demonstrates the correct operation of the series connected a-Si:H, a-SiGe:H and µc-Si:H solar cells forming the triple junction solar cell. However, a thick µc-Si:H bottom solar cell is required due to its weak infrared absorption [56]. A thick i-layer can induce a weak internal built in field, which reduces µc-Si:H bottom solar cell V_{oc} and *FF*. As listed in Table 4.10, It can be observed that the conversion of the µc-Si:H bottom subcell is much lower than those of the other two subcells. This is mainly due to lower V_{oc} and *FF*. The conversion efficiency of 15.79% (J_{sc}=9.234 mA/cm^2, V_{oc}=2.246 V, *FF*=76.11 %) is obtained for the initial triple junction solar cell. The J_{sc} of the triple junction solar cell is limited by the low J_{sc} of the a-Si:H top cell simply because the top, middle and bottom cells were current-mismatched, resulting in a relatively low triple junction cell conversion efficiency. In the next sections, we used the simulation to design an optimal a-Si:H/a-SiGe:H/µc-Si:H triple junction structure. We carried out investigations of the influences of several parameters on the a-Si:H/a-SiG:H/µc-Si:H triple junction solar cells (e.g. the thicknesses of the active i-layers of the top, middle and bottom subcells to enhance the overall short-circuit current and the band gaps of the layers of the top, middle and bottom subcells to enhance the open circuit voltage) and the conversion efficiency of the triple junction solar cell consequently improves.

4.3.3.a Optimization of thicknesses of triple junction solar cell active i-layers

The current produced by a single solar cell is directly related to the thickness of its absorber layer. As the absorber layer becomes thicker, the current produced becomes larger,

which is also true for multi-junction solar cells. However, the thicker the solar cell, the more photons it absorbs. Thus, fewer photons are allowed to pass through to the other cells bellow it. This shadowing can affect the lower cells and starve them of light. Therefore, a thick top cell will cause the currents produced by the lower cells to decrease. A short-circuit current can be used as one factor in overall power optimization. In order to find the maximum triple junction cell efficiency, a search for the optimum subcell layer thicknesses is carried out.

Many simulations are executed with the variations of the thicknesses of the top and middle cells. The first result shows the dependence of the short-circuit current density of the top cell on its thickness (Fig 4.27). The thickness of the bottom cell must be as high as possible to increase the triple junction cell current produced due to its position. However, the current of the bottom cell is greatly affected by the thickness of the middle cell, as shown in Fig 4.28. For this reason, a 5.294 µm thickness is chosen for the bottom cell i-layer.

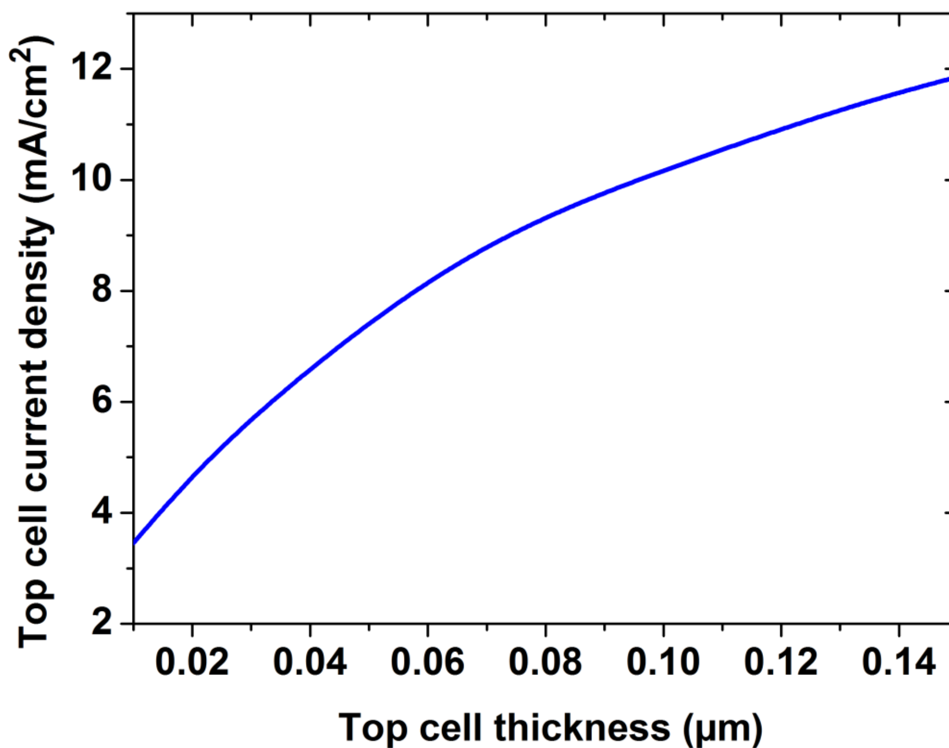

Figure 4.27 Top cell short-circuit current density as a function of top cell i-layer thickness.

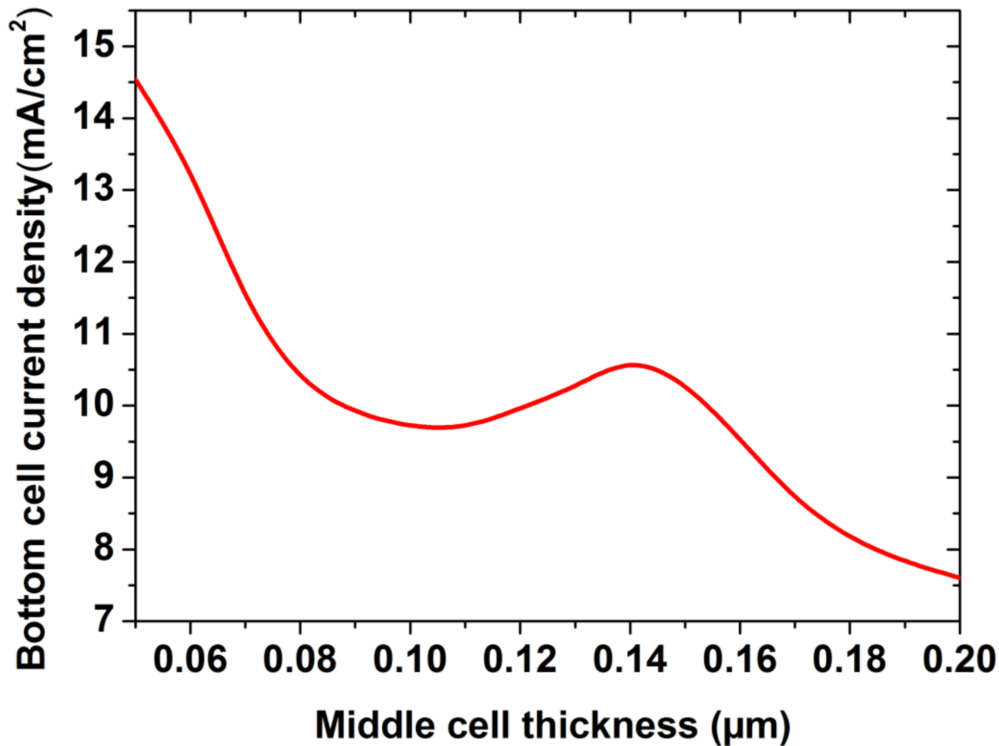

Figure 4.28 Bottom cell short-circuit current density as a function of middle cell i-layer thickness.

In Figs 4.29(a-c) are plotted the short-circuit current densities of the top, middle and bottom cells as a function of the thickness of the top layer, where strong dependence is shown for three current densities. The total current density produced by the triple junction solar cell is the current density produced by the triple junction combination of the three cells, due to their series connection. The triple junction short-circuit current density is the best indication of the efficiency of the triple junction solar cell and that is why it is also plotted. As the thickness of the i-aSi:H layer in the top cell increases, the top cell J_{sct} increases and the middle cell J_{scm} decreases. This is simply because the thick top cell absorbs more light, leaving transmitted less light to the middle cell and, in contrast, the thin top cell absorbs less light, leaving transmitted more light to the middle cell. With progressive increase of the a-Si:H layer in the top-cell, the increasing J_{sct}, and the decreasing J_{scm} cross one another. By appropriately adjusting the thickness of i-a-SiGe:H layer, the bottom cell J_{scb} can be equal to J_{sct} and J_{scm} under current matching conditions at the optimal i-a-Si:H, i-a-SiGe:H and i-µc-Si:H layer' thicknesses of 0.11 µm, 0.14 µm and 5.294 µm, respectively, where $J_{sct} = J_{scm} = J_{scb} = 10.55$ mA/cm^2, which is about

equal to the maximum short-circuit current density of 10.315 mA/cm^2 for the triple junction solar cell.

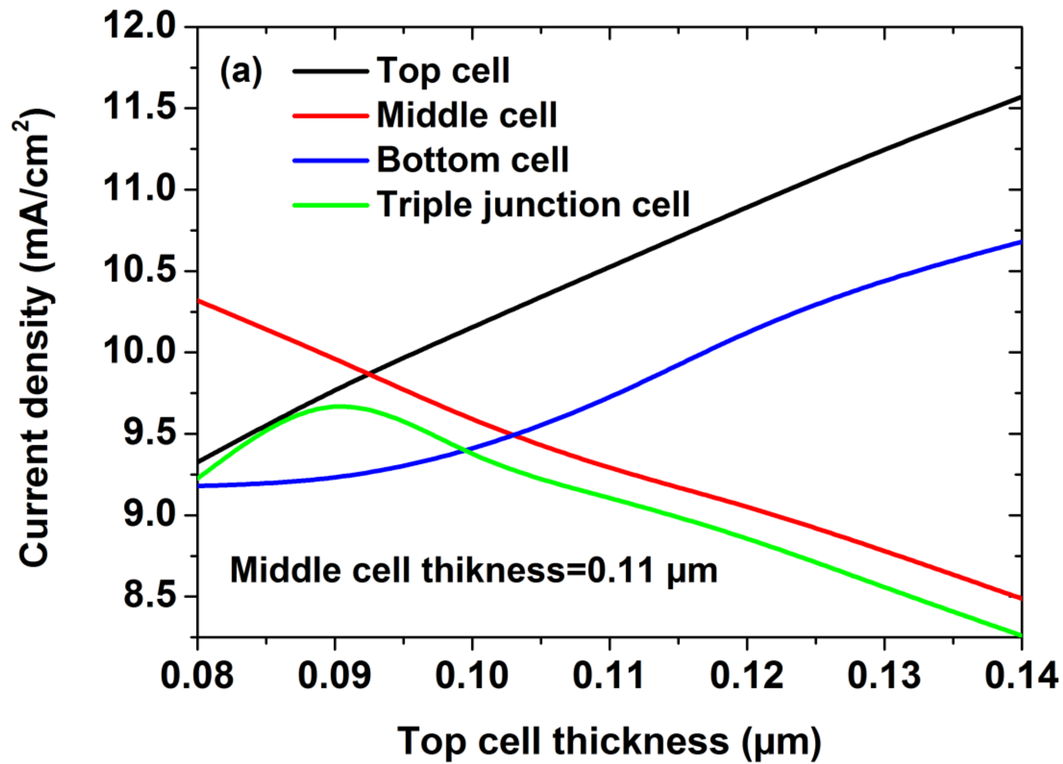

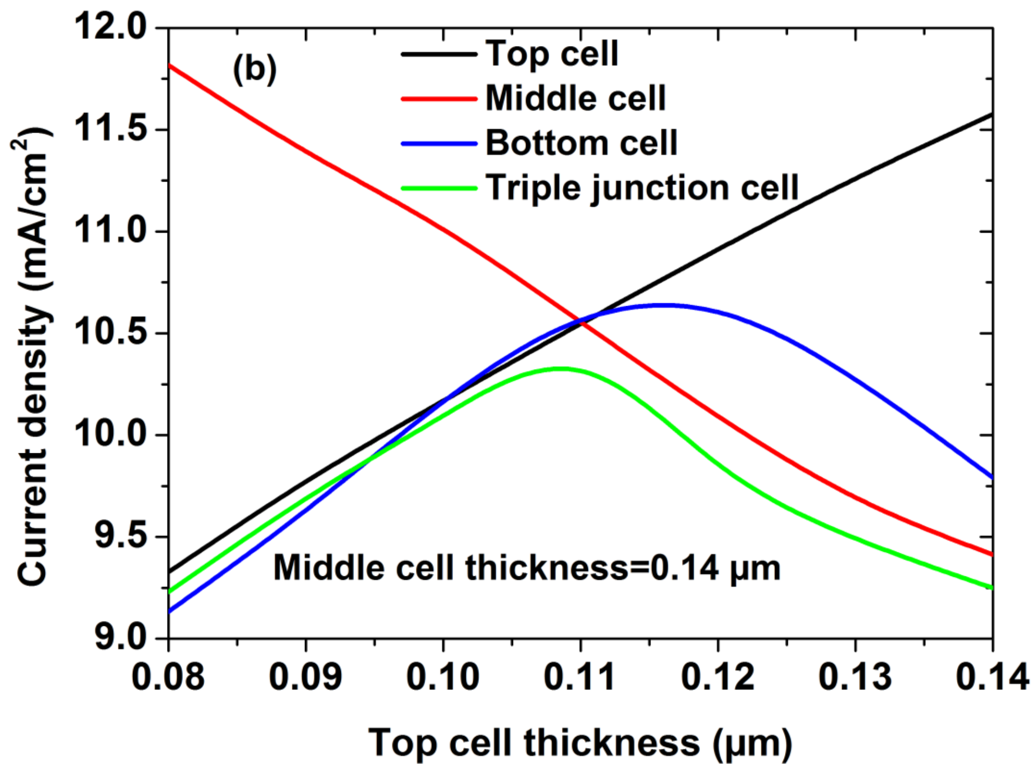

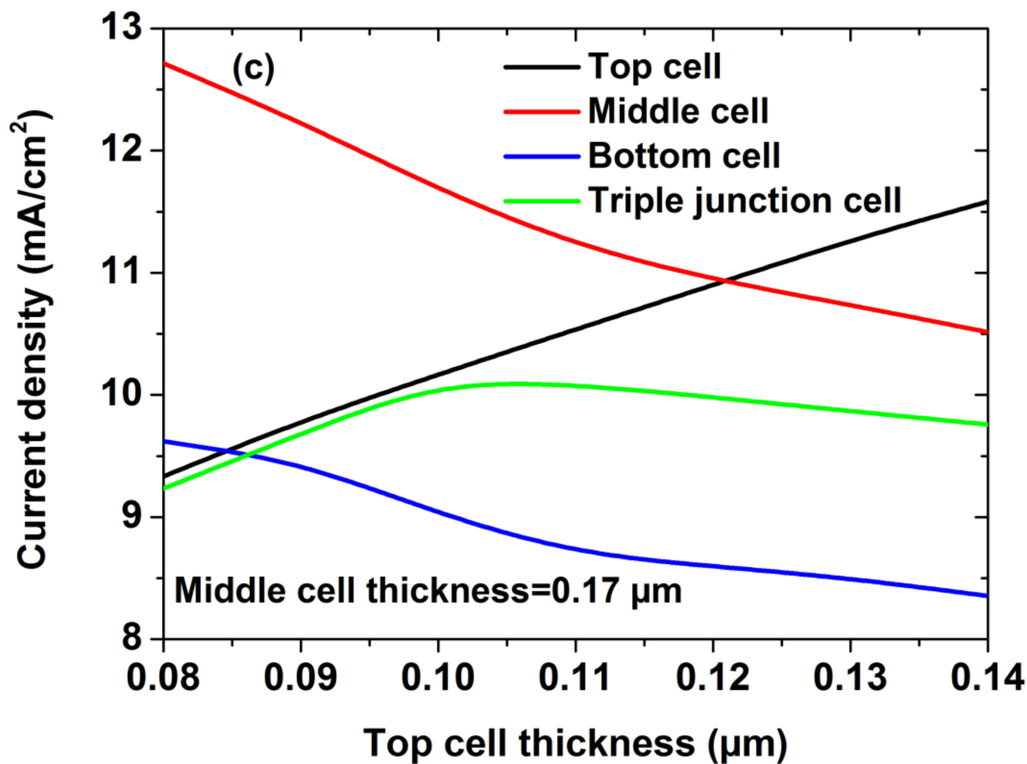

Figure 4.29 Short-circuit current densities of top, middle and bottom cells as a function of top i-layer thickness for (a) middle cell thickness=0.11 µm, (b) middle cell thickness=0.14 µm and (c) middle cell thickness=0.17 µm.

Note that the current matching point for the top cell thickness appears to be 0.11µm, whereas it is 0.14 µm for the middle cell. The same current matching point at the same combination of cell thicknesses is also found when we simulate all the current densities as functions of the middle cell thickness.

The *J–V* characteristics of the top, middle, bottom and triple junction cells are plotted in Fig 4.30. Matched photocurrents between the triple junction solar cell and subcells are observed with the photovoltaic parameters summarized in Table 4.11.

The open-circuit voltage V_{oc} of the triple junction solar cell (2.23 V) is equal to the sum of the V_{oc} values for the top (0.964 V), middle (0.856 V) and bottom (0.408 V) cells. The conversion efficiency of the triple junction solar cell working under current matching condition is improved to 16.95% due to the enhanced short-circuit current density, which has increased from 9.234 to 10.315 mA/cm^2.

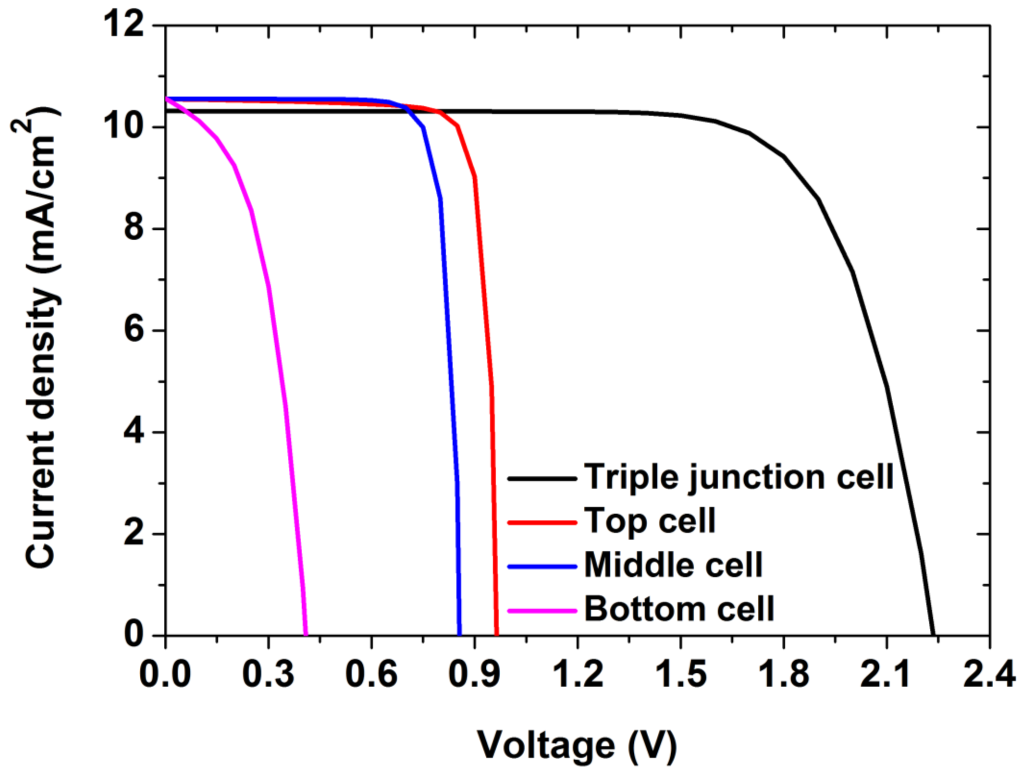

Figure 4.30 *J–V* characteristics for the a-Si:H top cell, a-SiGe:H middle cell, μc-Si:H bottom cell and the triple junction solar cell at current matching.

	J_{sc}(mA/cm^2)	V_{oc}(V)	*FF* (%)	η (%)
a-Si:H top-cell	10.546	0.964	83.829	8.525
a-SiGe:H middle cell	10.555	0.856	83.004	7.500
μc-Si:H bottom-cell	10.564	0.408	48.429	2.090
a-SiH/ a-SiGe:H /μc-Si:H triple junction cell	10.315	2.23	73.51	16.95

Table 4.11 Simulation photovoltaic parameters of the top, middle, bottom and triple junction solar cells at current matching point

4.3.3.b Optimization of bandgaps of triple junction solar cell layers

Next, we calculate the efficiencies of different bandgap energy combinations and evaluate the results graphically. Figure 4.31 shows the efficiency of the triple junction solar cell for top and middle cell band gap energies varying from 1.7 to 2 eV and 1.35 to 1.8 eV [36],

respectively. The bottom band gap energy is fixed at 1.18 eV. As shown, the optimum efficiency is 18.25% for top, middle and bottom cells band gap energies of 1.86, 1.71 and 1.18 eV, respectively.

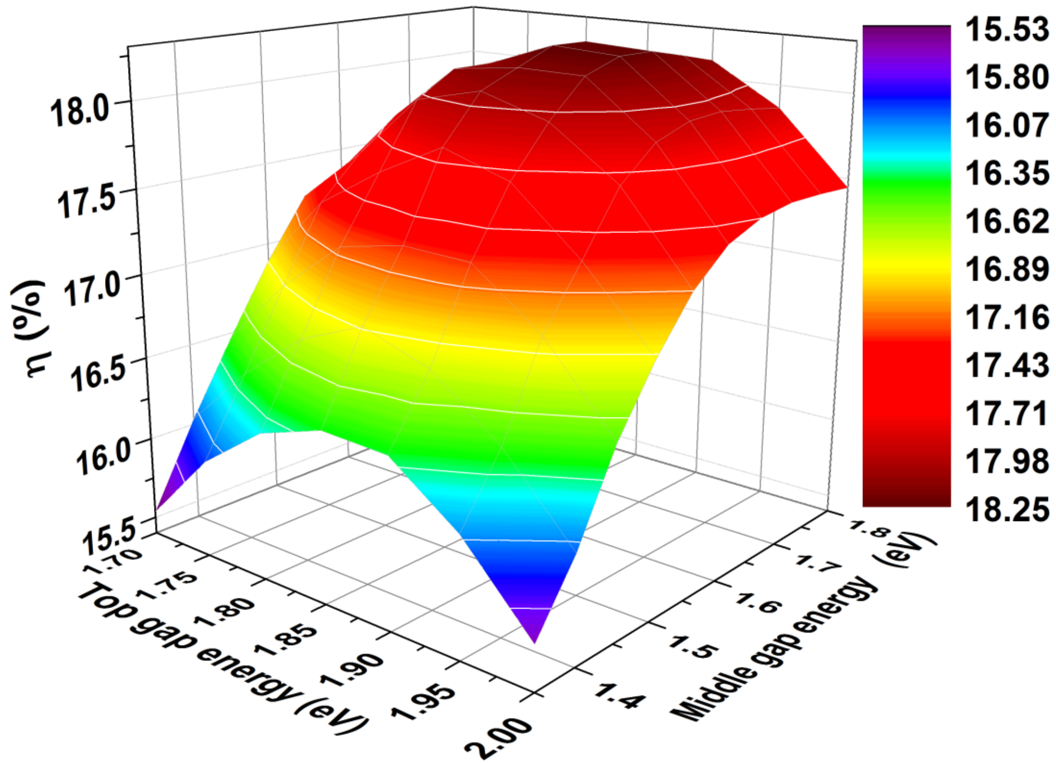

Figure 4.31 The variation in the efficiency with the band gap energies of the a-Si:H top and a-SiGe:H middle cells.

The *J*-*V* characteristics of the optimized triple junction solar cell as compared to the initial triple junction solar cell are illustrated in Fig 4.32. Increases in the J_{sc} (from 9.234 to 10.02 mA/cm^2) and the V_{oc} (from 2.246 to 2.41 V) are clearly observed.

A comparison of the photovoltaic parameters of the optimized triple junction solar cell and those of the initial triple junction solar cell is given in Table 4.12. The conversion efficiency increases from 15.79% to 18.25% due to the enhancement in both J_{sc} (from 9.23 to 10.02 mA/cm^2) and V_{oc} (from 2.246 to 2.41 V).

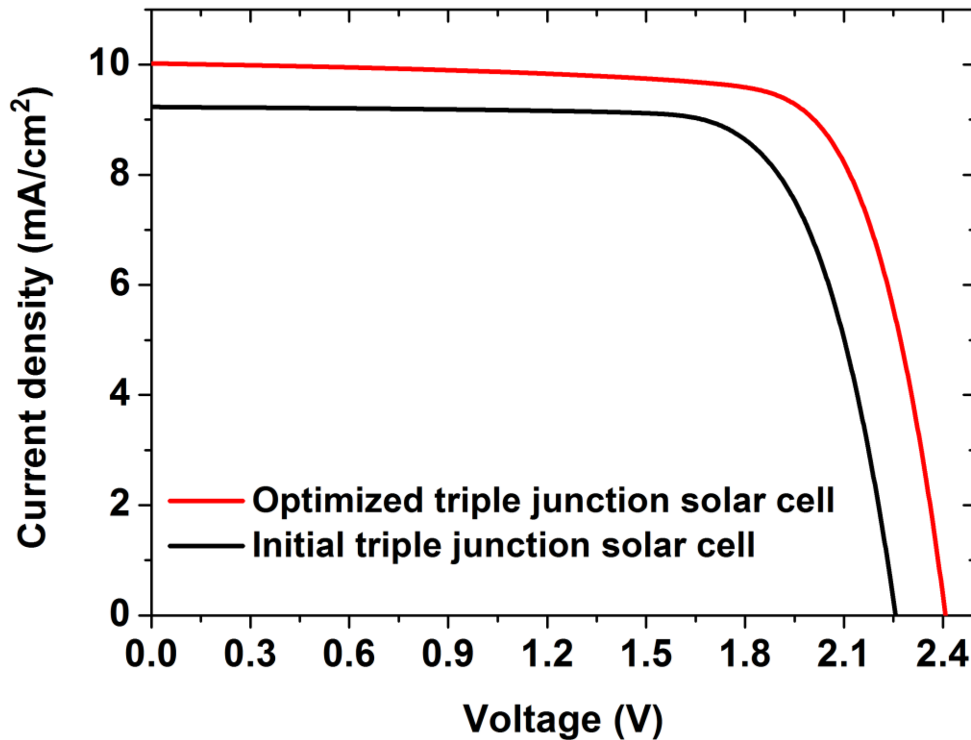

Figure 4.32 *J-V* characteristic of the improved triple junction solar cell as compared to the initial triple junction solar cell.

	J_{sc}(mA/cm^2)	V_{oc}(V)	*FF* (%)	η (%)
Initial triple junction solar cell	9.234	2.246	76.11	15.79
Improved triple junction solar cell	10.02	2.41	75.52	18.25

Table 4.12 Simulation photovoltaic parameters of the initial and improved triple junction solar cells.

Fig 4.33 illustrates the external quantum efficiencies (EQEs) of the top, middle and bottom subcells of the optimized triple junction solar cell when the transfer matrix method is used in the optical model to account for the coherent interference in thin films. In addition, the total of the triple junction solar cell EQE is presented. There is apparently a cutoff wavelength for each subcell corresponding to the absorption edge of its intrinsic layer. First, the top cell absorbs almost all the photons in the wavelength range 0.1- 0.55 µm. Next, the remaining photons enter the middle cell, where light is absorbed in the wavelength range 0.55-0.7 µm. Finally, the remaining photons in the wavelength range 0.7-1.1 µm are absorbed by the bottom

cell. This figure illustrates efficient absorption over the AM 1.5G solar spectrum, which ensures light distribution among all the subcells for the generation of currents [57].

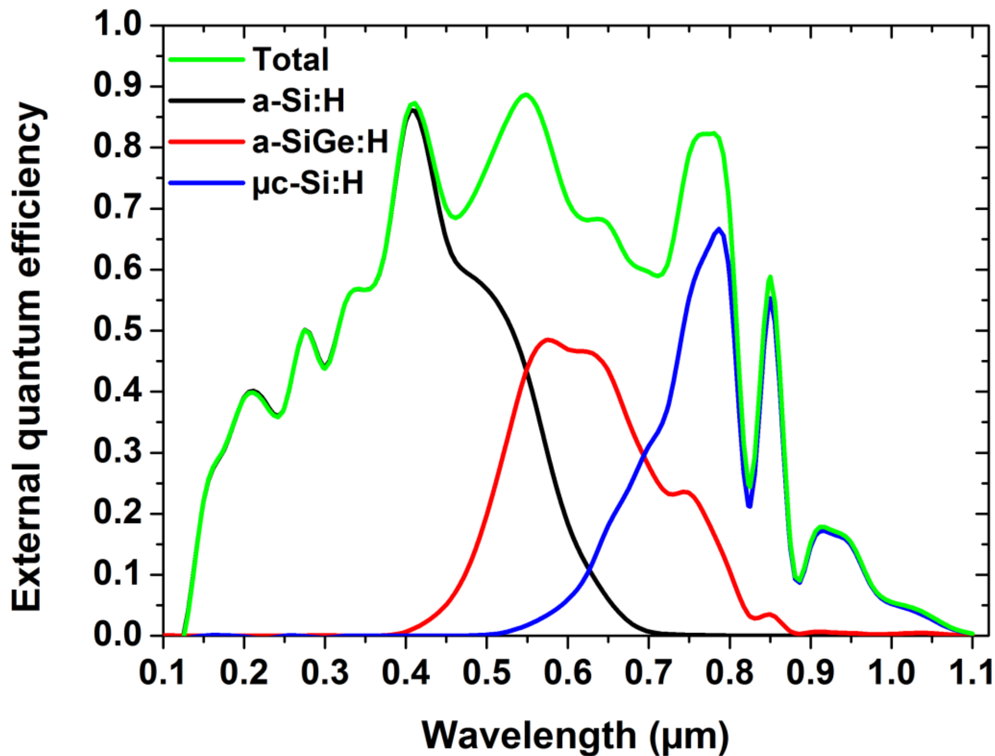

Figure 4.33 EQE curves of the a-Si:H/a-SiGe:H/μc-Si:H triple junction solar cell.

Fig. 4.34 shows the light absorptances (*A*) and the reflectances (*R* = 1-*A*) of the triple junction solar cell layers as a function of the wavelength of the incident light. Any colored area corresponds to the amount of incident light that is absorbed in the related layer. The absorptances in the i-layers of the top, middle and bottom cells are represented by the magenta area and the contributions from top, middle, and bottom i-layers are indicated by the black, red, and green dotted lines. There are significant parasitic absorption losses as well. The yellow and green areas represent the absorption losses in the SiO_2 layer and the combined absorption losses in the p- and n-layers. The white area represents the light that is reflected by the whole triple junction solar cell. The absorption losses originating from the other layers are negligible. The parasitic absorption is dominantly determined by the absorption in the SiO_2, the p- and n-layers. Note that the significant contribution to optical losses arises from the triple junction solar cell reflectance. Santbergen et al [58] simulated a triple junction thin-film silicon solar cell and tried

two approaches for reflection reduction. First, an MgF_2 antireflection coating reduced the reflectance and increased the triple junction solar cell current. Second, an antireflective foil with pyramid texture caused a reflection reduction that affected the top, middle, and bottom cells and increased the triple junction solar cell current. Future work could implement an MgF_2 antireflection coating and antireflective foil with pyramid texture to the triple junction solar cell to reduce the reflectance.

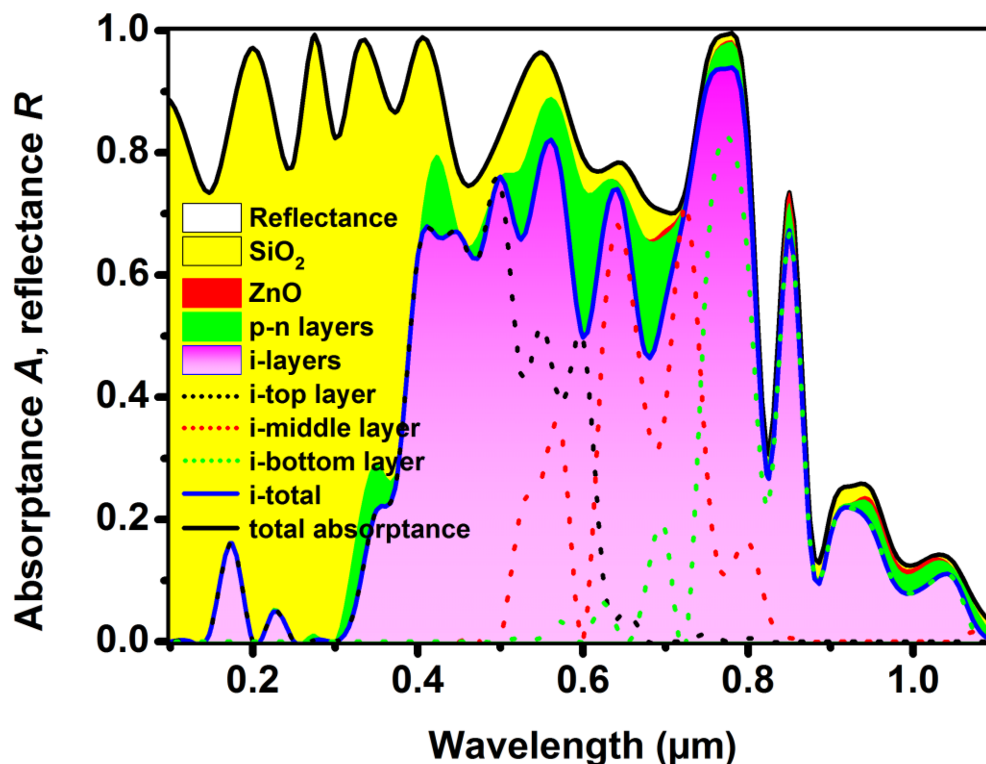

Figure 4.34 Absorptance *A* and reflectance *R* of the triple junction solar cell layers as a function of the wavelength of incident light. The colored areas illustrate the light absorption over the layers. The white area represents the reflected light.

4.3.3.c Dependence of triple junction solar cell performance on defect states

Amorphous silicon materials such as a-Si:H and a-SiGe:H contain a large number of defect states within the band gap. Numerical simulations of both a-Si:H and a-SiGe:H defect states effects have been investigated. Three cases have been considered. In the first and the second ones, the density of states of the a-Si:H top solar cell has been fixed at a low value (10^{13} cm^{-3}) while the density of states of a-SiGe:H middle solar cell was varied, and vice versa.

However, in the third case both densities of states of a-Si:H and a-SiGe:H solar cells of the triple junction solar cell have been varied. We have studied the influence of the defect densities of a-Si:H and a-SiGe:H materials on the conversion efficiency of the triple junction solar cell from 10^{13} cm^{-3} to 10^{17} cm^{-3}.

Fig 4.35 demonstrated the variation of the efficiencies as function of defect density only in the a-Si:H top solar cell, only in the a-SiGe:H middle solar cell, and in the two a-Si:H and a-SiGe:H solar cells of the triple junction solar cell to examine the relative impact of each of these cases. The triple junction solar cell efficiency is constant with the defect density until 10^{14} cm^{-3}. After that, it decreases due to the fact that the high recombination of photocarriers caused by the high defect density results in the reduction of the photocurrent and consequently the efficiency of the triple junction solar cell is decreased. The defect density has a low influence on the conversion efficiency as long as it stays below the threshold of 10^{14} cm^{-3}. It is shown that the triple junction solar cell efficiency depends strongly on the defect density of the a-Si:H top solar cell.

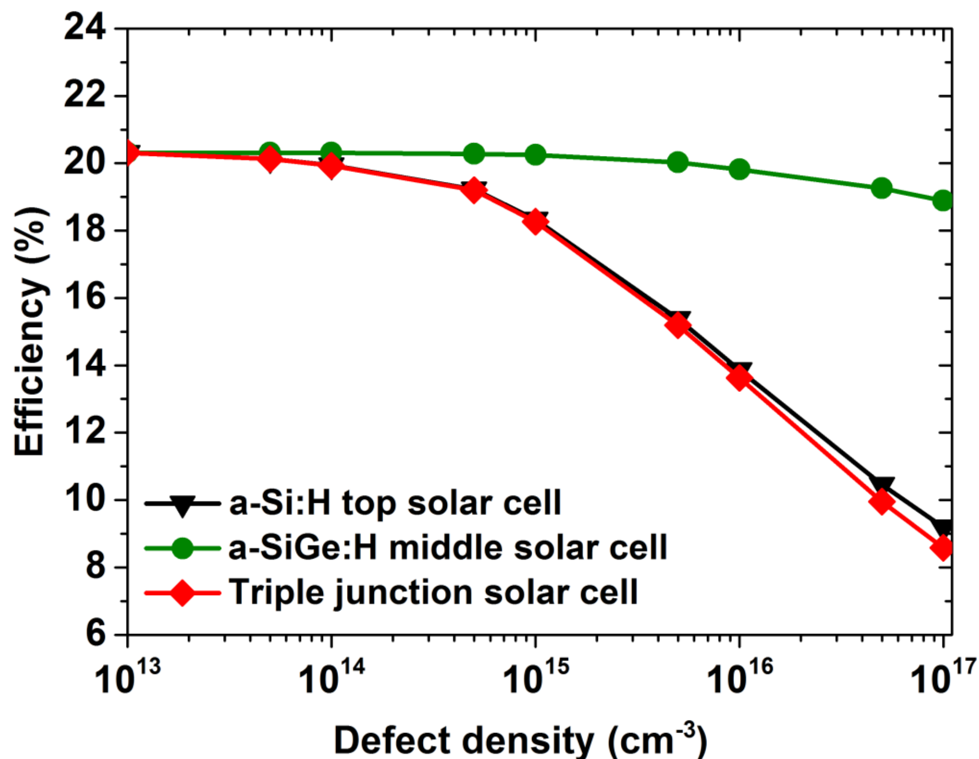

Figure 4.35 Conversion efficiency as a function of defect density in only a-SiGe:H middle cell, in only a-Si:H top cell, and in triple junction solar cell.

It is clear that the quality of the a-Si:H material is the dominant factor in determining the performance of the triple junction solar cell. However, the defect density of the a-SiGe:H middle solar cell has no significant effect on the conversion efficiency of the triple junction solar cell. For the a-Si:H top cell the band gap is larger, this means that the recombination mechanism of the photocarriers will be higher and therefore reducing the photocurrent of the a-Si:H top solar cell and then the conversion efficiency in the triple junction solar cell. These results show that a high efficiency of 20.3% is achieved with a low defect density of a-Si:H material in the range 10^{13} to 10^{14} cm^{-3} which is needed for the triple junction solar cell performance.

The proposed a-Si:H/a-SiGe:H/µc-Si:H triple junction solar cell yields a very promising device efficiency 20.3%. This performance is superior to the fabricated a-Si:H/a-SiGe:H/µc-Si:H triple junction solar cell efficiency 16.1% [59] under the illumination of one sun AM1.5G. The simulation results can be used to optimize a-Si:H/a-SiGe:H/µc-Si:H triple junction solar cells and to develop new designs of high efficiency a-Si:H/a-SiGe:H/µc-Si:H triple junction solar cells.

4.4 Conclusion

In this chapter, we investigated thin film silicon solar cells based on double and triple junction's concepts by using the Silvaco-Atlas software. The *J–V* characteristics and associated photovoltaic parameters were determined under AM1.5 G light spectrum. The electrical behavior of the double junction solar cell a-Si: H/µc-Si:H incorporating n-p type µc-Si:H TRJ between the a-Si:H top and µc-Si:H bottom cells is studied. a-Si:H and µc-Si:H single subcells of the tandem solar cell were first simulated and their simulated conversion efficiencies of 10.22% and 6.5%, respectively. However, the tandem solar cell provides an enhancement of the conversion efficiency to 12.69%, in good agreement with an experimentally published conversion efficiency. After that, we studied the effects of the donor and acceptor concentrations and thickness of the TRJ on the photovoltaic parameters of the tandem solar cell. The a-Si:H/µcSi:H double junction solar cell highest conversion efficiency of 12.73% is achieved for un optimal TRJ with donor, acceptor concentrations and thickness of 10^{20} cm^{-3}, $4x10^{19}$ cm^{-3} and 10 nm, respectively. Afterwards, the numerical simulation of a highly efficient triple junction solar cell was presented. The triple junction solar cell is composed of three subcels with p-i-n configurations: namely, a-Si:H (top), a-SiGe:H (middle), and µc-Si:H (bottom) junctions stacked in series with two optimal TRJs (i.e., n-µc-Si:H/ p-µc-Si:H) placed

between each pair of three subcells. We first simulated separately single junction a-Si:H, a-SiGe:H and μc-Si:H solar cells and their conversion efficiencies are of 10.22%, 10.63% and 6.5% respectively. Then we studied the performance of the triple junction solar cell and an initial conversion efficiency of 15.79% was obtained. We presented the optimization of the thicknesses of the intrinsic layers of top and middle cells for matching current. Under current matching conditions, the optimal i-a-Si:H, i-a-SiGe:H and i-μc-Si:H layers' thicknesses of 0.11 μm, 0.14 μm and 5.294 μm, respectively. The conversion efficiency of the triple junction solar cell working at current matching condition is improved to 16.95%. The optimization as the use of wide band gaps of top (1.86 eV), middle (1.71 eV) and bottom subcells (1.18 eV) is also presented. The conversion efficiency of the triple junction solar cell is increased to 18.25%. Finally, we studied the effects of defects of a-Si:H and a-SiGe:H subcells on the performance of the triple junction solar cell. Based on our simulation results, the optimized triple junction solar cell has a potential to deliver a high conversion efficiency of 20.3% with a low defect density of a-Si:H material in the range 10^{13} to 10^{14} cm^{-3} which is needed for the triple junction solar cell performance.

Chapter 4 references

[1] J. Poortmans and V. Arkhipov, *Thin film solar cells: fabrication, characterization and applications*, vol. 5. John Wiley & Sons, 2006.

[2] H. F. Sterling and R. C. G. Swann, "Chemical vapour deposition promoted by rf discharge," *Solid. State. Electron.*, vol. 8, no. 8, pp. 653–654, 1965.

[3] R. C. Chittick, J. H. Alexander, and H. F. Sterling, "The preparation and properties of amorphous silicon," *J. Electrochem. Soc.*, vol. 116, no. 1, p. 77, 1969.

[4] S. Vepřek and V. Mareček, "The preparation of thin layers of Ge and Si by chemical hydrogen plasma transport," *Solid. State. Electron.*, vol. 11, no. 7, pp. 683–684, 1968.

[5] P. Torres *et al.*, "Device grade microcrystalline silicon owing to reduced oxygen contamination," *Appl. Phys. Lett.*, vol. 69, no. 10, pp. 1373–1375, 1996.

[6] S. Hänni, "Microcrystalline silicon for high-efficiency thin-film photovoltaic devices," EPFL, 2014.

[7] W. Paul, D. K. Paul, B. Von Roedern, J. Blake, and S. Oguz, "Preferential attachment of H in amorphous hydrogenated binary semiconductors and consequent inferior reduction of pseudogap state density," *Phys. Rev. Lett.*, vol. 46, no. 15, p. 1016, 1981.

[8] B. Von Roedern, D. K. Paul, J. Blake, R. W. Collins, G. Moddel, and W. Paul, "Optical absorption, photoconductivity, and photoluminescence of glow-discharge amorphous Si 1− x Ge x alloys," *Phys. Rev. B*, vol. 25, no. 12, p. 7678, 1982.

[9] S. Guha, "Light-induced effects in amorphous silicon alloys-Design of solar cells with improved stability," *J. Non. Cryst. Solids*, vol. 77, pp. 1451–1460, 1985.

[10] S. Inthisang, K. Sriprapha, S. Miyajima, A. Yamada, and M. Konagai, "Hydrogenated amorphous silicon oxide solar cells fabricated near the phase transition between amorphous and microcrystalline structures," *Jpn. J. Appl. Phys.*, vol. 48, no. 12R, p. 122402, 2009.

[11] D. Y. Kim, E. Guijt, R. A. van Swaaij, and M. Zeman, "Development of a-SiOx: H solar cells with very high Voc× FF product," *Prog. Photovoltaics Res. Appl.*, vol. 23, no. 6, pp. 671–684, 2015.

[12] N. Andoh, H. Nagayoshi, T. Kanbashi, and K. Kamisako, "Characterization of high-quality a-SiC: H films prepared by hydrogen-radical CVD method," *Sol. energy Mater. Sol. cells*, vol. 49, no. 1–4, pp. 89–94, 1997.

[13] J. Meier *et al.*, "The'micromorph'solar cells: A new way to high efficiency thin film silicon solar cells," in *13th EC Photovoltaic Solar Energy Conference*, 1995, no. CONF,

pp. 1445–1450.

[14] H. Sai *et al.*, “High-efficiency microcrystalline silicon solar cells on honeycomb textured substrates grown with high-rate VHF plasma-enhanced chemical vapor deposition,” *Jpn. J. Appl. Phys.*, vol. 54, no. 8S1, p. 08KB05, 2015.

[15] B. Yan, G. Yue, L. Sivec, J. Yang, S. Guha, and C.-S. Jiang, “Innovative dual function nc-SiOx: H layer leading to a> 16% efficient multi-junction thin-film silicon solar cell,” *Appl. Phys. Lett.*, vol. 99, no. 11, p. 113512, 2011.

[16] H. Sai, T. Matsui, and K. Matsubara, “Stabilized 14.0%-efficient triple-junction thin-film silicon solar cell,” *Appl. Phys. Lett.*, vol. 109, no. 18, p. 183506, 2016.

[17] I. Tobias and A. Luque, “Ideal efficiency of monolithic, series-connected multijunction solar cells,” *Prog. Photovoltaics Res. Appl.*, vol. 10, no. 5, pp. 323–329, 2002.

[18] J. Meier, S. Dubail, R. Fluckiger, D. Fischer, H. Keppner, and A. Shah, “Intrinsic microcrystalline silicon (/spl mu/c-Si: H)-a promising new thin film solar cell material,” in *Proceedings of 1994 IEEE 1st World Conference on Photovoltaic Energy Conversion-WCPEC (A Joint Conference of PVSC, PVSEC and PSEC)*, 1994, vol. 1, pp. 409–412.

[19] M. Boccard *et al.*, “High-stable-efficiency tandem thin-film silicon solar cell with low-refractive-index silicon-oxide interlayer,” *IEEE J. photovoltaics*, vol. 4, no. 6, pp. 1368–1373, 2014.

[20] T. Matsui *et al.*, “High-efficiency amorphous silicon solar cells: impact of deposition rate on metastability,” *Appl. Phys. Lett.*, vol. 106, no. 5, p. 53901, 2015.

[21] M. Richter *et al.*, “Optical characterization and modeling of Cu (In, Ga)(Se, S) 2 solar cells with spectroscopic ellipsometry and coherent numerical simulation,” *Thin Solid Films*, vol. 535, pp. 331–335, 2013.

[22] K. Ding *et al.*, “Characterization and simulation of a-Si: H/μc-Si: H tandem solar cells,” *Sol. energy Mater. Sol. cells*, vol. 95, no. 12, pp. 3318–3327, 2011.

[23] M. Foldyna, K. Postava, J. Bouchala, J. Pistora, and T. Yamaguchi, “Model dielectric functional of amorphous materials including Urbach tail,” in *Microwave and Optical Technology 2003*, 2004, vol. 5445, pp. 301–305.

[24] N. Dwivedi, S. Kumar, A. Bisht, K. Patel, and S. Sudhakar, “Simulation approach for optimization of device structure and thickness of HIT solar cells to achieve∼ 27% efficiency,” *Sol. energy*, vol. 88, pp. 31–41, 2013.

[25] C. Feser, J. Lacombe, K. v. Maydell, and C. Agert, “A simulation study towards a new concept for realization of thin film triple junction solar cells based on group IV elements,” *Prog. Photovoltaics Res. Appl.*, vol. 20, no. 1, pp. 74–81, 2012.

[26] N. Selmane, A. Cheknane, M. Aillerie, and H. S. Hilal, “Effect of ZnO-based TCO on the performance of a-Si H (n)/a-Si H (i)/c-Si H (p)/Al BSF (p+)/Al heterojunction solar cells,” *Environ. Prog. Sustain. Energy*, vol. 38, no. 4, p. 13114, 2019.

[27] O. Isabella, A. H. M. Smets, and M. Zeman, “Thin-film silicon-based quadruple junction solar cells approaching 20% conversion efficiency,” *Sol. energy Mater. Sol. cells*, vol. 129, pp. 82–89, 2014.

[28] M. Riaz, A. C. Kadhim, S. K. Earles, and A. Azzahrani, “Variation in efficiency with change in band gap and thickness in thin film amorphous silicon tandem heterojunction solar cells with AFORS-HET,” *Opt. Express*, vol. 26, no. 14, pp. A626–A635, 2018.

[29] K. Shaoying, W. Chong, P. Tao, Y. Jie, and Y. Yu, “Numerical simulation of the performance of the a-Si: H/a-SiGe: H/a-SiGe: H tandem solar cell,” *J. Semicond.*, vol. 35, no. 3, p. 34013, 2014.

[30] S. T. Chang, M. Tang, R. Y. He, W.-C. Wang, Z. Pei, and C.-Y. Kung, “TCAD simulation of hydrogenated amorphous silicon-carbon/microcrystalline-silicon/hydrogenated amorphous silicon-germanium PIN solar cells,” *Thin Solid Films*, vol. 518, no. 6, pp. S250–S254, 2010.

[31] M. I. Kabir, Z. Ibrahim, K. Sopian, and N. Amin, “Effect of structural variations in amorphous silicon based single and multi-junction solar cells from numerical analysis,” *Sol. energy Mater. Sol. cells*, vol. 94, no. 9, pp. 1542–1545, 2010.

[32] M. Zeman, J. A. Willemen, L. L. A. Vosteen, G. Tao, and J. W. Metselaar, “Computer modelling of current matching in a-Si: H/a-Si: H tandem solar cells on textured TCO substrates,” *Sol. Energy Mater. Sol. Cells*, vol. 46, no. 2, pp. 81–99, 1997.

[33] A. Garcia-Rivera, E. Comesaña, A. J. Garcia-Loureiro, R. Valin, J. A. Rodríguez, and M. Vetter, “Simulation of a-Si: H dual junction solar cells,” in *2013 Spanish Conference on Electron Devices*, 2013, pp. 373–376.

[34] Y. Hishikawa, N. Nakamura, S. Tsuda, S. Nakano, Y. Kishi, and Y. Kuwano, “Interference-free determination of the optical absorption coefficient and the optical gap of amorphous silicon thin films,” *Jpn. J. Appl. Phys.*, vol. 30, no. 5R, p. 1008, 1991.

[35] A. M. K. Dagamseh, B. Vet, P. Šutta, and M. Zeman, “Modelling and optimization of a-Si: H solar cells with ZnO: Al back reflector,” *Sol. Energy Mater. Sol. Cells*, vol. 94, no. 12, pp. 2119–2123, 2010.

[36] M. Nawaz, “Computer analysis of thin-film amorphous silicon heterojunction solar cells,” *J. Phys. D. Appl. Phys.*, vol. 44, no. 14, p. 145105, 2011.

[37] R. van Swaaij, R. Kind, and M. Zeman, “Recombination efficacy in a-Si: H pin devices,”

J. Non. Cryst. Solids, vol. 358, no. 17, pp. 2190–2193, 2012.

[38] S. T. Chang, B.-F. Hsieh, and Y.-C. Liu, “A simulation study of thin film tandem solar cells with a nanoplate absorber bottom cell,” *Thin Solid Films*, vol. 520, no. 8, pp. 3369–3373, 2012.

[39] G. Beaucarne, “Silicon Thin-Film Solar Cells,” *Adv. Optoelectron.*, vol. 2007, p. 36970, 2007.

[40] M. A. Green, K. Emery, Y. Hishikawa, W. Warta, and E. D. Dunlop, “Solar cell efficiency tables (version 48),” *Prog. Photovoltaics Res. Appl.*, vol. 24, no. 7, pp. 905–913, Jul. 2016.

[41] X. Deng, E. A. Schiff, A. Luque, and S. Hegedus, “Handbook of photovoltaic science and engineering,” *A. Luque, John Wiley Sons, Chichester*, 2003.

[42] J. Kwak, S. W. Kwon, and K. S. Lim, “Fabrication of an–p–p tunnel junction for a protocrystalline silicon multilayer/amorphous silicon tandem solar cell,” *J. Non. Cryst. Solids*, vol. 352, no. 9–20, pp. 1847–1850, 2006.

[43] J. Y. Hou, J. K. Arch, S. J. Fonash, S. Wiedeman, and M. Bennett, “An examination of the’tunnel junctions’ in triple junction a-Si: H based solar cells: modeling and effects on performance,” in *The Conference Record of the Twenty-Second IEEE Photovoltaic Specialists Conference-1991*, 1991, pp. 1260–1264.

[44] F. A. Rubinelli, J. K. Rath, and R. E. I. Schropp, “Microcrystalline nip tunnel junction in a-Si: H/a-Si: H tandem cells,” *J. Appl. Phys.*, vol. 89, no. 7, pp. 4010–4018, 2001.

[45] A. Sturiale, H. T. Li, J. K. Rath, R. E. I. Schropp, and F. A. Rubinelli, “Exploring dark current voltage characteristics of micromorph silicon tandem cells with computer simulations,” *J. Appl. Phys.*, vol. 106, no. 1, p. 14502, 2009.

[46] M. Vukadinović, F. Smole, M. Topič, R. E. I. Schropp, and F. A. Rubinelli, “Transport in tunneling recombination junctions: A combined computer simulation study,” *J. Appl. Phys.*, vol. 96, no. 12, pp. 7289–7299, 2004.

[47] J. Hou, J. Xi, F. Kampas, S. Bae, and S. J. Fonash, “Non-local recombination in ‘tunnel junctions’ of multijunction amorphous Si alloy solar cells,” *MRS Online Proc. Libr. Arch.*, vol. 336, 1994.

[48] J. K. Rath, F. A. Rubinelli, and R. E. I. Schropp, “Microcrystalline n-and p-layers at the tunnel junction of a-Si: H/a-Si: H tandem cells,” *J. Non. Cryst. Solids*, vol. 227, pp. 1282–1286, 1998.

[49] M. N. Kateb, S. Tobbeche, and A. Merazga, “Influence of μc-Si: H tunnel recombination junction on the performance of a-Si: H/μc-Si: H tandem solar cell,” *Optik* , vol. 139, pp.

152–165, 2017.

[50] O. Isabella, "Light management in thin-film silicon solar cells," Ph.D. thesis, Delft University of Technology, 2013.

[51] G. A. M. Hurkx, D. B. M. Klaassen, M. P. G. Knuvers, and F. G. O'hara, "A new recombination model describing heavy-doping effects and low-temperature behaviour," in *International Technical Digest on Electron Devices Meeting*, 1989, pp. 307–310.

[52] J. F. Rasheed and V. S. Babu, "Performance evaluation of composition graded layer of aSi1-xGex: H in n+ aSi: H/i-aSi: H/p+ aSi1-xGex: H graded band gap single junction solar cells," *Mater. Today Proc.*, vol. 27, pp. 26–31, 2020.

[53] Q. H. Fan *et al.*, "Simulation of a-Si/a-SiGe thin film tandem junction solar cells," *J. Phys. D. Appl. Phys.*, vol. 43, no. 14, p. 145101, 2010.

[54] J.-W. Schuettauf *et al.*, "Amorphous silicon–germanium for triple and quadruple junction thin-film silicon based solar cells," *Sol. Energy Mater. Sol. Cells*, vol. 133, pp. 163–169, 2015.

[55] Y. Cao *et al.*, "Hydrogenated microcrystalline silicon germanium as bottom sub-cell absorber for triple junction solar cell," *Sol. energy Mater. Sol. cells*, vol. 114, pp. 161–164, 2013.

[56] R. E. I. Schropp *et al.*, "Nanostructured thin films for multibandgap silicon triple junction solar cells," *Sol. Energy Mater. Sol. Cells*, vol. 93, no. 6–7, pp. 1129–1133, 2009.

[57] M. N. Kateb and S. Tobbeche, "Numerical simulation and optimization of a-Si:H/a-SiGe:H/µc-Si:H triple junction thin film silicon solar cell designs for high conversion efficiency," *Opt. Quantum Electron.*, vol. 53, no. 11, p. 605, 2021.

[58] R. Santbergen, T. Meguro, T. Suezaki, G. Koizumi, K. Yamamoto, and M. Zeman, "GenPro4 optical model for solar cell simulation and its application to multijunction solar cells," *IEEE J. photovoltaics*, vol. 7, no. 3, pp. 919–926, 2017.

[59] S. Kim, J.-W. Chung, H. Lee, J. Park, Y. Heo, and H.-M. Lee, "Remarkable progress in thin-film silicon solar cells using high-efficiency triple-junction technology," *Sol. Energy Mater. Sol. Cells*, vol. 119, pp. 26–35, 2013.

Conclusion

Today's solar cells used multijunction structures for an effective use of the solar spectrum. In order to achieve higher efficiency on a-Si:H solar cells, double and triple junction solar cells are used for better use of the solar spectrum due to better absorption of different sunlight wavelengths in different layers with different band gaps and, thus, to obtain higher conversion efficiencies of the solar cells. There are two crucial requirements in the multi-junction structure: (i) the tunnel recombination junction between the component cells has to feature low electrical and optical losses and (ii) the current generated at the maximum power has to be equal in each component cell (current matching).

The structures of the multijunction solar cells are complex and the numerical simulation is needed to improve the detailed understanding of the device physics and hence optimize the design of the device for improving the multijunction solar cell efficiency.

The aim of this thesis was to investigate multijunction thin film silicon solar cells as well as to understand the influence of the different structural parameters on the cell performance. In this work, thin film silicon solar devices based on double and triple junction's concepts are investigated with the use of the Silvaco-Atlas software. The *J–V* characteristics and associated photovoltaic parameters were determined under AM1.5 G light spectrum.

In the first part of this thesis we investigated the implementation of a tunnel recombination junction in a double junction solar cell, µc-Si:H was chosen as a suitable material to form the TRJ and a n-p junction was suggested for designing an efficient TRJ for application in thin film silicon solar cells. The double junction solar cell is composed of two subcels with p-i-n configurations namely, a-Si:H (top) and µc-Si:H (bottom) junctions stacked in series and are optically and electrically connected by a tunnel recombination junction (i.e., n-µc-Si:H/ p-µc-Si:H). Influence of parameters such as dopant concentrations and thickness of the TRJ on the tandem solar cell are considered. We presented the results of the simulated a-Si:H and µc-Si:H single solar cells and their simulated conversion efficiencies of 10.22% and 6.5%, respectively, agree with experimental ones. However, the aSi:H/µc-i:H double junction solar cell provided an enhancement of the conversion efficiency to 12.69%, in good agreement with an experimentally published record conversion efficiency. The lower short-circuit current limitation and the open-circuit voltage superimposition characteristics of the series connection of the top and bottom cells are proved by simulation. After that, we studied the effects of the donor and acceptor concentrations and thickness of the TRJ on the photovoltaic parameters of

the double junction solar cell. The simulated results indicate that the short-circuit current, the open-circuit voltage, the fill factor and the efficiency of the tandem cell are improved by increasing the donor concentration of the TRJ. On the other hand, the acceptor concentration and the thickness of the TRJ reduce mainly the short-circuit current, the fill factor and the efficiency while the open-circuit voltage changes slightly. This study shows a strong recombination process occurred in the TRJ, the a-Si:H/µcSi:H double junction solar cell highest conversion efficiency of 12.73% is achieved for un optimal TRJ with donor, acceptor concentrations and thickness of 10^{20} cm^{-3}, $4x10^{19}$ cm^{-3} and 10 nm, respectively. We explained the influence of variations of the TRJ parameters on the double junction solar cell performance in terms of the sensitivity of internal quantities such as the recombination rate and the band diagram to the TRJ parameters. The highest conversion efficiency is achieved for a recombination rate peak approximately located in the middle of the TRJ p-layer where the quasi-Fermi levels are close to each other.

Afterwards, triple junction solar cells were investigated in order to find a solar cell capable to deliver an optimal conversion efficiency for thin film silicon solar cells. The numerical simulation of a highly efficient triple junction solar cell was presented. The triple junction solar cell is composed of three subcels with p-i-n configurations: namely, a-Si:H (top), a-SiGe:H (middle), and µc-Si:H (bottom) junctions stacked in series with two TRJs (i.e., n-µc-Si:H/ p-µc-Si:H) placed between each pair of three subcells. The optimal TRJ design in the a-Si:H/µc-Si:H double junction solar was used in the a-si:H/a-SiGe:H/µc-Si:H triple junction solar cell. We first simulated separately single junction a-Si:H, a-SiGe:H and µc-Si:H solar cells and their conversion efficiencies are of 10.22%, 10.63% and 6.5% respectively. Then we studied the performance of the triple junction solar cell and an initial conversion efficiency of 15.79% was obtained. We suggested to further improve the performance of the triple junction solar cell, the optimization is to obtain the maximum short-circuit current density corresponding to the current matching between the a-Si:H top, a-SiGe:H middle and µc-Si:H bottom subcells which can be determined by varying the thicknesses of the a-Si:H top, aSiGe:H middle and µc-Si:H bottom subcells. The current matching corresponds to determine the thicknesses where the top, middle, bottom and triple cells share the same short-circuit current density. A high conversion efficiency of 16.95% is achieved at a current matching. Further improvement in triple junction solar cell performance were expected with the implementation of wide band gaps of top, middle and bottom subcells. This leads to improved conversion efficiency up to 18.25%.

Finally, we investigated the effects which will likely degrade the performance of the triple junction solar cell, especially structural defects (dangling bounds) in the active a-Si:H and

a-SiGe:H layers. It is shown that the triple junction solar cell efficiency depends strongly on the defect density of the a-Si:H top solar cell. It is clear that the quality of the a-Si:H material is the dominant factor in determining the performance of the triple junction solar cell. However, the defect density of the a-SiGe:H middle solar cell has no significant effect on the conversion efficiency of the triple junction solar cell. For the a-Si:H top cell the band gap is larger, this means that the recombination mechanism of the photocarriers will be higher and therefore reducing the photocurrent of the a-Si:H top solar cell and then the conversion efficiency in the triple junction solar cell. These results show that a high efficiency of 20.3% is achieved with a low defect density of a-Si:H material in the range 10^{13} to 10^{14} cm^{-3} which is needed for the triple junction solar cell performance.

The proposed a-Si:H/a-SiGe:H/µc-Si:H triple junction solar cell yields a very promising device efficiency 20.3% under the illumination of one sun AM1.5G.

Perspectives

- Development and characterization of a triple junction solar cell to achieve the 20% conversion efficiency predicted by our studies.
- An important step is obtaining higher efficiency in multijunction a-Si:H alloy solar cells such as studying the performances of quadruple junction a-SiC_z:H/a-Si:H/a-$Si_{1-x}Ge_x$:H/µc-Si:H cell structure and quadruple junction a-Si:H/a-$Si_{1-x}Ge_x$:H/µc-Si:H/µc-$Si_{1-y}Ge_y$:H cell structure.
- This study may be extended to multijunction structures with heterojunction such as those associating a-Si:H material with $Cu(In_{(1-x)}Ga_x)Se_2$ (CIGS) thin film material or perovskite thin film material.

Publications and conferences

- M. N. Kateb and S. Tobbeche, "Numerical simulation and optimization of a-Si:H/a-SiGe:H/µc-Si:H triple junction thin film silicon solar cell designs for high conversion efficiency," *Opt. Quantum Electron.*, vol. 53, no. 11, p. 605, 2021. https://doi.org/10.1007/s11082-021-03259-2
- M. N. Kateb, S. Tobbeche, and A. Merazga, "Influence of µc-Si: H tunnel recombination junction on the performance of a-Si: H/µc-Si: H tandem solar cell," *Optik* , vol. 139, pp. 152–165, 2017. http://dx.doi.org/10.1016/j.ijleo.2017.03.099
- S. Tobbeche and M. N. Kateb, "Simulation and optimization of silicon solar cell back surface field," *Mater. Sci.*, vol. 21, no. 4, pp. 491–496, 2015. https://doi.org/10.5755/j01.ms.21.4.9565
- Science and Applications of Thin Films Conference and Exhibition (SATF 2016) with poster presentation entitled: "Effect of tunnel recombination junction µc-Si:H dopant concentrations and thickness on the performance of a-Si:H/µc-Si:H tandem solar cell" 2016.
- International Renewable Energy Congress (IREC 2012) with poster presentation entitled: "Effect of BSF on crystalline silicon solar cell using TCAD Silvaco Software" 2012.

Optik 139 (2017) 152–165

Contents lists available at ScienceDirect

Optik

journal homepage: www.elsevier.de/ijleo

Original research article

Influence of μc-Si:H tunnel recombination junction on the performance of a-Si:H/μc-Si:H tandem solar cell

M.N. Kateb [a], S. Tobbeche [a,*], A. Merazga [b]

[a] *Laboratoire des Matériaux Semiconducteurs et Métalliques (LMSM), Faculté des Sciences et de la Technologie, Département de Génie-Electrique, Université de Biskra, BP 145, 07000 Biskra, Algeria*
[b] *Physics Department, Faculty of Science, Taif University, Taif 21974, Saudi Arabia*

A R T I C L E I N F O

Article history:
Received 24 December 2016
Accepted 21 March 2017

Keywords:
a-Si:H solar cell
μc-Si:H solar cell
a-Si:H/μc-Si:H tandem solar cell
Tunnel recombination junction
Silvaco-Atlas simulation

A B S T R A C T

Numerical simulations of hydrogenated amorphous silicon (a-Si:H)/hydrogenated microcrystalline silicon (μc-Si:H) p-i-n type tandem solar cell with a μc-Si:H n-p type tunnel recombination junction (TRJ) between the a-Si:H top cell and the μc-Si:H bottom cell are carried out using the simulator Silvaco-Atlas. Photovoltaic characteristics of a-Si:H and μc-Si:H solar cells and a-Si:H/μc-Si:H tandem solar cell were simulated first and their efficiencies of about 10.22%, 6.5% and 12.69% respectively, agree well with experimental reported record efficiencies. Influence of parameters such as dopant concentrations and thickness of the TRJ on the tandem solar cell are then studied. The simulated results demonstrate that the short-circuit current, the open-circuit voltage, the fill factor and the efficiency of the tandem cell are improved by increasing the donor concentration of the TRJ. On the other hand, the acceptor concentration and the thickness of the TRJ reduce mainly the short-circuit current, the fill factor and the efficiency while the open-circuit voltage changes slightly. This study shows a strong recombination process occurred in the TRJ, the highest conversion efficiency of 12.73% is achieved when the peak of the recombination rate is approximately located in the middle of the TRJ p-layer where the quasi-Fermi levels are close to each other.

© 2017 Elsevier GmbH. All rights reserved.

1. Introduction

Thin-film solar cell technology has gradually increased for low production costs and acceptable efficiencies. Thin-film Si solar cells offer several inherent advantages such as the use of abundant materials, the possibility to fabricate solar cells on flexible and lightweight substrates [1,2] and low energy payback times due to the low material usage and fabrication temperature [3]. Furthermore, thin-film Si solar cells are designed for a low cost of the material and no toxic elements are employed compared to cadmium telluride (CdTe) and copper indium gallium diselenide (CIGS) thin-film technologies. μc-Si:H and a-Si:H semiconductors with band-gaps of about 1.1 eV and 1.8 eV, respectively, are frequently used for thin-film Si solar cells. More recently it has been reported that the band gap of a-Si:H can also be increased to 2 eV or more by incorporating oxygen at a concentration of only about 3% [4,5] and with a good optoelectrical property. This result has opened up new doors for the design of thin-film silicon based multi-junction solar cells. Alloying a-Si:H with carbon (a-SiC:H) allows increasing of the band-gap up to 2.7 eV [6] and it has been used as the p-window layer of single and multi-junction

* Corresponding author.
E-mail address: souad_tobbeche@yahoo.fr (S. Tobbeche).

http://dx.doi.org/10.1016/j.ijleo.2017.03.099
0030-4026/© 2017 Elsevier GmbH. All rights reserved.

SATF2016

SATF 2016

IZMIR INSTITUTE OF TECHNOLOGY

IZTECH

SCIENCE & APPLICATIONS OF THIN FILMS
CONFERENCE & EXHIBITION

This is to certify that

Mohamed Nadjib KATEB

has contributed **'Science and Applications of Thin Films Conference and Exhibition (SATF 2016)'** held in Cesme Ilica Hotel Spa & Wellness Thermal Resort Hotel between the dates of 19-23 September 2016, Izmir, Turkey

On behalf of the organizing committee, I would like to express my special gratitude.

SATF 2016

Prof. Dr. Lutfi OZYUZER
Chair of SATF 2016

Optical and Quantum Electronics (2021) 53:605
https://doi.org/10.1007/s11082-021-03259-2

Numerical simulation and optimization of a-Si:H/a-SiGe:H/μc-Si:H triple junction thin film silicon solar cell designs for high conversion efficiency

M. N. Kateb[1] · S. Tobbeche[1]

Received: 27 March 2021 / Accepted: 18 September 2021
© The Author(s), under exclusive licence to Springer Science+Business Media, LLC, part of Springer Nature 2021

Abstract
Thin film silicon solar cells based on hydrogenated amorphous silicon (a-Si:H), hydrogenated amorphous silicon–germanium (a-SiGe:H) and hydrogenated microcrystalline silicon (μc-Si:H) are promising candidates for low-cost photovoltaic technology due to their low costs and low- temperature processing. However, the conversion efficiency of a thin film silicon solar cell is low compared to that of a silicon solar cell. Conversion efficiency improvements can be obtained through the use of multi-junction solar cells consisting of series of connected subcells. This work focuses on a numerical investigation of triple junction solar cells consisting of a-Si:H top cells, a-SiGe:H middle cells and μc-Si:H bottom cells, with the goal of obtaining a high conversion efficiency. The initial conversion efficiency is 15.79%. After optimizing the top, middle and bottom subcell thicknesses at current matching, the conversion efficiency is enhanced to 16.95%. The band gaps of the top, middle and bottom subcells are then optimized, increasing the conversion efficiency to 18.25%. It is found that the triple junction solar cell is sensitive to defects in the a-Si:H top cell, the conversion efficiency can be improved to 20.3% when defects are reduced. The simulation results reported in this work can be used to optimize and develop thin film silicon solar cells.

Keywords Numerical simulation · Triple junction solar cell · a-Si:H · a-SiGe:H · μc-Si:H

1 Introduction

Thin film solar cells have been of great interest in recent years. Many types of semiconductor materials, such as copper indium gallium diselenide (CIGS) (Hedayati et al. 2020; Azizifar et al. 2020; Rasouli et al. 2020) and antimony selenosulfide (Sb_2Se_3) (Zhou et al. 2021; Cao et al. 2021, 2019,2020a, 2020b) have been applied as the absorption layers of thin film solar cells and achieved excellent device performance. Research has shown that

✉ S. Tobbeche
s.tobbeche@univ-biskra.dz

[1] Laboratoire des Matériaux Semiconducteurs et Métalliques (LMSM), Département de Génie-Electrique, Faculté des Sciences et de la Technologie, Université de Biskra, BP 145, Biskra 07000, Algérie

Published online: 13 October 2021